Synthesis, formulation and printing of nanoparticle-containing inks for electronics applications

Rehab Alhazmi

Thesis submitted for the degree of Doctor of Philosophy

University of East Anglia, School of Chemistry

Norwich, UK

March 2024

Abstract

Printing of conductive ink based on silver nanoparticles (Ag NPs) can be extensively applied for various applications in printed electronics (PE) and flexible electronic (FE) due to its high conductivity. The work presented in this study concentrates on the synthesis and characterization of NPs, ink formulation for inkjet printing technology, printing of Ag NPs inks on different substrates (photo paper and modified plastic substrates polyethylene terephthalate (PET) or polyimide (PI)) and investigates the effect of spontaneous room temperature sintering on the microstructure and electrical properties of the printed films.

In the present study, a number of methods have been proposed and tested for this purpose. Silver nanoparticles were successfully synthesized with a reasonable nano size about 4 nm. However, some of those synthesis methods did not produce nanoparticles with the desired size or narrow size dispersity, which caused serious problems in size distribution and the quality of ink formulation.

$AgNO_3$ was reduced in ethylene glycol (EG) or sodium borohydride ($NaBH_4$) in the presence of a polymer, which was acting as capping and dispersing agent, such as polyacrylic acid (PAA), polyvinyl pyrrolidone (PVP) or polyvinyl alcohol (PVOH), to ensure the stability of the Ag NPs solution. The prepared Ag NPs were characterized using various experimental techniques: dynamic light scattering (DLS), transmission electron microscopy (TEM), scanning electron microscopy (SEM), energy dispersive spectroscopy (EDS), thermogravimetric analysis (TGA) and these finding were then utilized to develop a stable aqueous printable ink formulation.

Printing materials cost effectively, with adequate conductivity and printability, has been attracting plenty of researchers and scientists as an alternative to using pure silver nanoparticles, due to their relatively high price from a commercial perspective. Therefore, using nickel or copper combined with silver in nanoparticles synthesis was tested, using core- shell and alloy configurations, since they are the most promising candidates for use as a conductive material as the replacement of Ag. Promising results were achieved, especially from the printing of copper in a core-shell system, which had a good particle distribution and achieved our goal while being more economical (at least in material cost – the increased synthetic cost would need to be evaluated). Both nickel and copper

nano inks are unstable, however, and are prone to oxidizing during the synthesis process. They usually require a reductive atmosphere or a special sintering method to ensure good conductivity. This contrasts with silver ink, where Ag does not require additional care during its formulation as it is chemically relatively stable, which is an advantage.

Conductive inks with 10, 20 and 30 wt.% silver content were formulated with the Ag NPs capped with PAA, PVP, or PVOH by using a combination of simple solvent mixtures. Similarly, the same method was applied to the alloy ink. However, for the synthesized copper–silver core-shell nanoparticles, due to the hydrophobic surface capping ligands, 10 wt% inks were formulated by dispersing these in a non-polar (xylene) solvent using probe sonication for 30 minutes to accomplish the formulation of the conductive ink.

The above formulations were then ready to print by using a Jet Lab 4 inkjet printer, with different nozzles (size 80 or 50 µm) on a suitable substrate. This approach offered simple, flexible, low cost and rapid prototyping alternatives, compared with other conventional printing techniques. The printed conductive ink is able to sinter at room temperature and that makes it possible to print onto a flexible paper or even a plastic substrate in order to get conductive patterns. The ink stored under ambient conditions was stable against aggregation for more than six months.

The investigation of the printed tracks was carried out using different techniques such as optical microscopy and SEM for the quality and morphology of the printed silver layers, profilometry for thickness measurements, and a Beha-Amprobe (Glotteral, Germany) Digital Multimeter for the electrical properties. The mechanical stability of tracks was also evaluated using a custom-designed bending rig.

The results showed that in the case of Ag/PAA and Ag/PVP ink, excellent conductivity was observed, and the performance approaches a remarkable resistivity of only 2 times that of bulk silver. Using Ag Ni alloy-based ink, we obtained better resistivity compared with Ag @Ni CS NPs ink. For alloy inks, the lowest resistivity of (Ag 75: Ni 25), (Ag 40: Ni 60) w/w% inks were 2 times and 29 times bulk nickel, respectively after printing 5 layers on photo paper, resulting in spontaneous room temperature sintering. The formulated ink from the as-

synthesized Cu–Ag core–shell nanoparticles was printed onto a PVOH coated PET substrate using an inkjet printer. The film was sintered using chemical sintering, since the strongly bound hydrophobic capping ligands prevented spontaneous Cl^-based sintering. The lowest resistivity of the Cu–Ag core–shell conductive inks was approximately 129 times the resistivity of bulk Cu.

The second part of this thesis examines how a plastic substrate surface (PET or PI) can be developed by applying a PVOH coating formula with different Cl^- concentrations, in order to improve its surface properties to make it suitable for inkjet printing and room temperature sintering.

The printed silver patterns showed great mechanical stability on both plastic and paper substrates, in tensile and compressive mode bending after 500 bending cycles on the plastic substrate and up to 1000 bending cycles on photo paper, suggesting it may be suitable for flexible electronic applications. This work potentially provides a promising route toward the large-scale fabrication of low-cost yet flexible printed electronic devices.

Having successfully printed and investigated these materials, the nano-silver ink was employed to fabricate a prototype pattern for a simple resistive temperature sensor device. This was generated and tested across a range of temperatures (20 -130 °C). The conducted tests demonstrate that the Ag printed sensor on photo paper, PET/PVOH and PI/PVOH was altered after being exposed to the oven heat. Generally, they showed good linear response range/resistance behaviour. However, the pre-heated devices that were printed on PI/PET were transformed into excellent devices by heating them again and showed much lower resistance. After heat treatment, the temperature sensor printed on PI/ PET showed clearly some cracks and voids formed within the track. This is attributed to the instability of the coated PVOH layer over the substrate under the printed layer (because it is chemically altered when heated to high temp) so that actually, the temperature sensor is still only stable to about 100 °C, even though the base substrates are stable at a much higher temperature.

Table of Contents

Abstract ..... **ii**

List of Abbreviations ..... **x**

List of figures ..... **xii**

List of Tables ..... **xxii**

Acknowledgements ..... **xxvii**

Chapter 1. Introduction **1**

1.1 Nanoparticles (NPs) **1**

1.2 Colloidal nanoparticles (NPs) **1**

1.2.1 The concepts of colloidal stability 2

1.2.1.1 Electrostatic stabilisation 2

1.2.1.2 Steric stabilisation 3

1.2.2 Metal colloidal growth 3

1.2.3 Synthetic methods for colloidal nanoparticles 4

1.2.3.1 Aqueous methods 6

1.2.3.2 Non-aqueous methods 7

1.3 Core-shell or bimetallic system (alloy, core -shell nanoparticles) 8

1.3.1 Hot-injection method 12

1.4 Printing electronics **13**

1.5 Printing techniques **14**

1.5.1 Screen printing 14

1.5.2 Rotary printing 15

1.5.3 Inkjet printing 17

1.6 Principles of inkjet printing **18**

1.6.1 Droplet ejection and flight 19

1.6.2 Droplet impact and spreading 21

1.6.3 Solidification 21

1.6.4 Satellite droplets 22

1.6.5 Coffee ring formation and effect 23

1.7 Conductive inks **25**

1.7.1 Nanoparticle ink 25

1.7.2 Organometallic ink 27

1.7.3 Conductive polymer 27

1.7.4 Other types of conductive ink 28

1.7.5 Properties of inks 28

1.8 Substrates for additive printing **29**

1.8.1 Interaction of droplets with the substrate 30
1.9 Sintering 30
1.9.1 Thermal sintering 31
1.9.2 Microwave sintering 31
1.9.3 Photonic sintering 31
1.9.4 Electrical sintering 32
1.10 Characterisation of printed tracks 34
1.11 Applications for inkjet printing of conductive materials 35
1.12 The aim of this study 35
Chapter 2: Experimental Methodology 45
2.1 Chemicals and materials 45
2.1.1 Inorganic salts and solvents: 45
2.1.2 Polymers: 45
2.1.3 Modifying plastic substrates materials : 45
2.2 Synthesis of nano particles by aqueous method 46
2.2.1 Synthesis of silver nanoparticles (Ag NPs) by chemical reduction method in an aqueous solution 46
2.2.2. Synthesis of silver nanoparticles by co-reduction of Ag and Ni metal precursors at room temperature 47
2.2.3. Synthesis of silver nanoparticles- polyvinyl alcohol (Ag/PVOH) composites 47
2.2.4. Synthesis of Ni-Ag /PAA core-shell NPs 48
2.3. Synthesis of nano particles by non-aqueous method 48
2.3.1. Synthesis of silver-polyvinyl pyrrolidone (Ag/PVP) by a modified polyol process 48
2.3.2. Synthesis of Ni-Ag /PAA core-shell NPs by polyol method 49
2.4. Synthesis of nanoparticles by hot-injection method 50
2.4.1. Synthesis of core-shell silver / nickel nanoparticles by solvothermal hot injection method 50
2.4.2 Synthesis of copper @ silver core-shell NPs by thermal decomposition and galvanic displacement 51
2.4.3 Synthesis of nickel @ silver /PAA core-shell nanoparticles 51
2.5 Nanoparticle characterization 52
2.5.1 Dynamic light scattering (DLS) 52
2.5.2 Transmission electron microscopy (TEM) 53
2.5.3 Scanning electron microscopy (SEM) 53
2.5.4 Thermogravimetric analysis (TGA) 53
2.6 Ink formulation 54
2.6.1 Typical ink formulation 54
2.6.2 Ink formulation of the Cu@ Ag NPs for conductive inks 55

2.6.3 Rheological properties of silver inks 56
2.7 Substrate materials 56
2.8 Ink jet printer 56
2.8.1 Principles of operation of a drop on demand (DOD) printer 56
2.8.2 Inkjet printing setup 58
2.8.3 Ink deposition 60
2.9 Characterization of deposited films 61
2.9.2 Sintering 63
2.10 Preparation of coating solution 65
Chapter 3. Pure silver nanoparticles results and discussion 68
3.1 Characterisation of Ag-PAA NPs formed by chemical reduction method in an aqueous solution. 68
3.1.1. Characterisation of 30%, 20% and 10% AgPAA standard ink 74
3.1.2 Ink viscosity measurement 76
3.1.3 The Effect of printing AgPAA patterns on photo paper with different parameters 77
3.1.4 Morphology of AgPAA ink and printed track film 77
3.1.5 Effect of print pitch on geometry, electrical and mechanical properties of Ag patterns printed on photo paper with room temperature sintering 83
3.1.6 Comparison of layer overprinting and print pitch variation on electrical and mechanical properties 89
3.2 Characterisation of Ag-PVOH NPs 91
3.3 Characterization of silver nanoparticles – polyvinyl alcohol (Ag/PVOH) composition 93
3.4 Characterisation of Ag-PVP NPs 95
3.5 Characterization of silver- polyvinyl pyrrolidone (Ag/PVP) by a modified polyol process 96
3.5.2 The effect of printing AgPVP patterns on photo paper with different parameters 100
3.5.3 Morphology of AgPVP ink printed patterns on photo paper 101
3.5.4 Effect of print pitch on geometry, electrical and mechanical properties with room temperature sintering of AgPVP ink 107
3.5.5 Comparison of layer overprinting and print pitch variation on properties of AgPVP ink 109
3.6 Conclusion 111
References 113
Chapter 4. Alloy silver – nickel nanoparticle results and discussion 115
4.1 Synthesis and characterization of silver nanoparticles by co-reduction of Ag and Ni metal precursors at room temperature 115
4.2 Characterisation of 10% Ag-Ni/PAA (50:50 w/w%) standard ink 121
4.2.1 Morphology of printed patterns 123

4.2.2 Effect of Print Pitch on Geometry and Electrical Properties with Room Temperature Sintering....128
4.2.3 Comparison of layer overprinting and print pitch variation on properties 130
4.2.4 Analysis of the elemental composition of printing film surface and dried formulated alloy ink....132
4.3 Effect of using different nozzle size (80 µm) on the physical diameter of droplets and electrical properties of tracks with room temperature sintering 139
4.3.1 Comparison of layer overprinting and print pitch variation on properties 144
4.4 Effect of printing 10% AgNi /PAA (75:25 w/w%) alloy ink on photo paper on geometry and electrical properties with room temperature sintering....146
4.5 Characterisation of 10, 20, 30 wt.% Ag-Ni/PAA alloy standard ink....149
4.6 Characterisation of 10% Ag-Ni/PAA (40:60 w/w%) alloy standard ink 153
4.7 Conclusion 155
References....157
Chapter 5. Core- shell results and discussion....158
5.1 Formation and characterisation of nickel @silver / PAA core-shell nanoparticles 158
5.2 Synthesis and characterization of nickel-silver /PAA core-shell NPs by Polyol Method 161
5.2.1 Ink formulation and inkjet printing of Ni@ Ag core-shell....165
5.3 Formation and characterization of silver @ nickel core-shell nanoparticle by solvothermal hot injection method....166
5.4 Synthesis and characterization of copper@ silver core-shell NPs by thermal decomposition and galvanic displacement 168
5.4.1 Sintering, ink formulation and inkjet printing....173
5.5 Conclusion 179
References....181
Chapter 6. Developing flexible plastic substrates for room temperature silver sintering results and discussion 183
6.1 Aim of this chapter 185
6.2 Fabrication of PVOH /KCl coated film....185
6.3 Assessment of electrical performance of printed tracks 187
6.4 Testing the robustness of the produced silver tracks on flexible substrates....188
6.4.1 Mechanics of bending /stretching-mode....189
6.4.2 Assessment of electrical properties of tracks on PVOH-KCl substrate after bending test....192
6.5 Conclusion 205
References....207
Chapter 7. Design and characterization of a simple temperature sensor obtained by inkjet printing on photo paper /flexible substrate results and discusion....209

7.1 Fabrication process 209

7.2 Theory and fabrication of temperature sensor inkjet printed on paper substrate 212

7.3 Resistive temperature sensor on PVOH/KCl coted polyester substrate (PET) 217

7.4 Resistive behaviour of pre-heated temperature sensor on PVOH/PET substrate 220

7.5 Resistive temperature sensor on PVOH/KCl coated polyimide substrate (PI) 224

7.6 Resistive behaviour of pre-heated temperature sensor on PVOH/PI substrate 226

7.7 Conclusion 236

References 238

Chapter 8. Conclusion and recommendations for future research 240

8.1 Conclusion 240

8.2 Recommendations for future research 243

Chapter 9. Appendix 249

A. More examples of "cross- sectional" scans of the stylus profilometer trace across a printed track 249

B. SEM images of the surface of the 30 wt.% AgPAA printed tracks at different pitch size (a)75 µm; (b) 55 µm; (c) 35 µm; (d) 15 µm; (e) overprinting 2x(65 µm); and (f) overprinting 4x (65 µm) at room temperature 251

List of Abbreviations

Abbreviation	Descriptions
COOH	Carboxylic acid
°C	Celsius
CIJ	Continuous inkjet printing
Cu	Copper
A	Cross-sectional Area
DOD	Drop on demand
DLS	Dynamic Light Scattering
EDL	Electric Double Layer
R	Electrical Resistance
EG	Ethylene glycol
Au	Gold
Hz	Hertz
HIFU	High-intensity Focused Ultrasound
ICP-MS	Inductively coupled plasma mass spectrometry
K/min	Kelvin per minute
L	Length of Printing Trace
µm	Micrometre
µs	Microsecond
MEA	Monoethanolamine
NPs	Nanoparticles
Ni	Nickel
$Ni(acac)_2$	Nickel acetate
Ω	Ohm
OAM	Olylamine
PAA	Poly acrylic acid
PVOH	Polyvinyl alcohol
PDI	Polydispersity index
PET	Poly(ethylene terephthalate)
PI	Poly imide
PVP	Polyvinyl pyrrolidone
KCl	Potassium chloride

ρ	Resistivity
SEM	Scanning Electron Microscopy
SEM/EDS	Scanning Electron Microscopy / Energy Dispersive X-Ray Spectroscopy
Ag	Silver
AgCl	Sliver chloride
$AgNO_3$	Sliver nitrate
$NaBH_4$	Sodium borohydride
NaOH	Sodium hydroxide
SFS	Sodium formaldehyde sulfoxylate dehydrate
T	Temperature
TGA	Thermogravimetric Analysis
h	Thickness of the printing Pattern
TSA	Thiosalicylic acid
TEM	Transition Electron Microscopy
TEA	Triethanolamine
UV-vis	Ultraviolet- visible
V	Volt
w/w %	Weight/weight %
W	Width of the Printing Pattern

List of figures

Figures No.	Figures Caption	Pages
1.1	Schematic of the generalised mechanism of nanoparticle growth due to coalescence.	3
1.2	Structure of the polymers polyvinylpyrrolidone, poly (vinyl alcohol) and poly (acrylic acid).	6
1.3	Screen printing schematic diagram.	15
1.4	Gravure printing schematic diagram.	16
1.5	Flexographic printing schematic diagram.	17
1.6	Schematic of DOD inkjet printing systems.	19
1.7	Examples of printed line morphologies.	21
1.8	Satellite drop formation during printing.	23
1.9	Schematic process of the coffee ring effect.	24
2.1	Schematic diagram showing the principle of a piezoelectric inkjet printer.	57
2.2	(a &b) Inkjet printer image, (c) panel control, (d) stage & nozzle control, (e) parameter control & ink droplet.	58
2.3	Typical unipolar waveforms for piezoelectric inkjet print-head	59
2.4	Drop generation from inkjet printer (a) with satellite, (b) mist and (c) stable ejection.	60
2.5	SEM images of (a) poor-quality printing on photo paper, (b) good quality printing on photo paper.	60
2.6	Nozzle, syringe and holder image.	61
2.7	(a) Diamond stylus profilometer in contact with the printed track; (b) area markers showing the region to be scanned.	61
2.8	Stylus profilometer trace across a printed track.	62
2.9	Schematic diagram showing the chemical sintering process	64
3.1	Schematic sketch of the mechanism of polymer protection.	69
3.2	The DLS graphs of as-synthesised Ag-PAA NPs.	70

3.3	TEM image of an Ag-PAA NPs powder.	72
3.4	SEM image of the Ag-PAA NPs powder.	73
3.5	TGA of the Ag-PAA NPs powder.	74
3.6	Viscosity of Ag NPs formulated ink.	76
3.7	Optical microscope images comparing different line widths produced at different print pitch size settings for the inkjet printer (a) 95 µm, (b) 55 µm, (c) 35 µm, and (d) 15 µm.	77
3.8	SEM images of printing paper surface at different magnifications. (a) 10,000 kx, (b) 20,000 kx, (c) 40,000 kx, (d) 80,000 kx.	78
3.9	SEM images of un-sintered AgPAA standard ink before printing (a) 10 wt.%; (b) 20 wt.% AgPAA ink.	79
3.10	SEM images of 10 wt.% AgPAA printed tracks with (a) 95 µm and (b) 15 µm pitch size at 25 ˚C.	79
3.11	SEM images of 10 wt.% AgPAA printed tracks with (95 µm) pitch size (a) at 42 °C and (b) 60 °C.	80
3.12	SEM images of 20 wt.% AgPAA printed tracks with (a) 95 µm;(b) 65 µm; (c) 45 µm; and (d)15 µm pitch size at 25 °C.	81
3.13	SEM images of the surface of the 30 wt.% AgPAA printed tracks at different pitch size (a)75 µm; (b) 55 µm; (c) 35 µm; (d) 15 µm; (e) overprinting x2 (65 µm); and (f) overprinting x4 (65 µm) at room temperature.	82
3.14	Results for lines printed of 30% AgPAA on glossy paper with a 50 µm nozzle diameter at room temperature (a) effect of print pitch on the line width/thickness, (b) effect of print pitch on resistance/RBS. Error bars show the resistivity/ RBS ± error.	86
3.15	Results of printed lines of 20% AgPAA on glossy paper with a 50 µm nozzle diameter at room	88

	temperature (a) effect of print pitch on the line width /thickness (b) effect of print pitch on resistance / RBS.	
3.16	Properties of room-temperature overprinted features on photo paper from a 50 μm nozzle at 65 μm print pitch, (a) effect of layers printed on line width /thickness, (b) effect of layers printed on resistance /RBS.	90
3.17	Microscope images of printing passes for 30% AgPAA at the same pitch size 65 μm with different numbers of printed layers (a) single layer, (b) five layers.	91
3.18	TEM images of Ag-PVOH NPs.	93
3.19	The DLS graph of Ag-PVOH NPs.	94
3.20	The DLS graph of Ag- PVP NPs made by a modified polyol process.	97
3.21	TGA of the Ag-PVP NPs powder.	98
3.22	Viscosity measurement of 30% AgPVP ink.	100
3.23	Optical microscope images showing different line widths at different pitch size (a) 85 μm; (b) 65 μm; (c) 35 μm; and (d)15 μm.	101
3.24	SEM images of the surface of the 10 wt.% AgPVP patterns at different pitch size (a) 85 μm, (b) 45 μm, (c) 15 μm.	102
3.25	SEM images of the surface of the 20 wt. % AgPVP patterns at different pitch size (a) 85 μm, (b) 45 μm, (c) 15 μm, (d) 45 μm (overprinting x5).	103
3.26	SEM of un-sintered 30% AgPVP ink .	104
3.27	SEM images of the surface of the 30 wt.% Ag PVP patterns at different pitch size (a) 95 μm, (b) 85 μm, (c) 65 μm and (d) 45 μm at room temperature.	105
3.28	SEM images of the surface of the 30 wt.% AgPVP patterns at 45 μm pitch size (e) overprinting (x3), (f) (overprinting x5) at room temperature.	106

3.29	SEM images of the surface of the 30 wt.% AgPVP printing film with size measurements.	107
3.30	Characteristics of printed lines on glossy photo paper with a 50 μm nozzle diameter at room temperature (a) effect of print pitch on the line width/ thickness (b) effect of print pitch on resistance /RBS.	109
3.31	Properties of room-temperature overprinted features on photo paper from a 50 μm nozzle at 45 μm print pitch. (a) Effect of number of printed layers on line width/thickness,(b)effect of number of printed layers on resistance /RBS.	110
3.32	Microscope images of printing passes for 30%AgPVP at same pitch size 45 μm with different numbers of printing layers (a) 1 layer, (b) 2 layers, (c) 3 layers and (d) 5 layers.	111
4.1	Average alloy nanoparticle size for Ag/Ni particles, plotted against the ratio used in particle synthesis.	118
4.2	SEM of Ag/Ni alloy NP (a) 50:50, (b) 75:25, (c) 40:60 and (d) 25:75 w/w%.	119
4.3	(a) TEM image of Ag-Ni (50-50 w/w%)-PAA, (b) Ag-Ni (25-75 w/w %)-PAA.	120
4.4	TGA of the Ag-Ni/PAA (50:50) w/w% alloy NPs powder.	121
4.5	10% Ag-Ni/PAA Alloy (50:50 Ag:Ni) ink viscosity.	123
4.6	Optical microscope images of 10% alloy Ag: Ni (50:50) w/w% ink showing the different line widths at different pitch size (a) 95 μm, (b) 65 μm, (c) 45 μm, (d) 15 μm.	123
4.7	SEM of 10% Ag-Ni/PAA alloy ink without sintering (a) (50:50), (b) (75:25), (c) (40:60), (d) (25:75) w/w%.	124
4.8	SEM images of the surface of the 10 % Ag-Ni/PAA (50:50 wt.%) alloy printed patterns at different pitch	126

	size (a) 75 μm, (b) 45 μm, (c) 25 μm and (d) 15 μm at room temperature.	
4.9	SEM images of the surface of the 10% Ag-Ni/PAA (50:50 w/w%) alloy overprinting patterns at pitch size (45 μm) (a) 3 layers, (b) 5 layers.	127
4.10	SEM images for 10 wt% Ag-Ni/PAA printing alloy after sintering with size measurements at room temperature.	128
4.11	Characteristics of printed lines of 10% AgNi/PAA (50:50) w/w% alloy ink on glossy photo paper with a 50μm nozzle diameter at room temperature. (a) Effect of print pitch on the line width/ thickness, (b) effect of print pitch on resistivity.	130
4.12	Properties of room-temperature overprinted features of 10% AgNi/PAA (50:50) w/w% alloy ink on photo paper from a 50 μm nozzle at 45 μm print pitch (a) effect of number of printed layers on line width/thickness, (b) effect of number of printed layers on resistivity.	132
4.13	Optical microscope images of over printing pattern of 10% alloy Ag:Ni (50:50 w/w%) at pitch size 45 μm (a) 3 layers, (b) 5 layers.	132
4.14	(a) EDS analysis results of printed Ag: Ni/PAA alloy film, (b)element distribution map.	133
4.15	EDS results of the substrate (photo paper) prior to printing.	135
4.16	(a) EDS results of 10% Ag-Ni/PAA dried ink on SEM metal stub, (b) element distribution map.	136
4.17	Comparison the effect of nozzle size on physical dimension and electric properties of printed lines on glossy photo paper at room temperature (a) on line width, (b) on line thickness, (c) resistivity shown	142

	relative to bulk silver, and (d) resistivity shown relative to bulk nickel.	
4.18	Comparison of SEM images of the surface of the 10 wt.% Ag-Ni/PAA (50:50 w/w%) alloy patterns at different pitch size (a) 50 μm nozzle (75), (45), (25) and 15 μm, (b) 80 μm nozzle (75), (45), (25) and 15 μm at room temperature respectively.	143
4.19	Comparison the effect of nozzle size on physical dimension and electric properties of overprinted lines on glossy photo paper at room temperature (a) on line width, (b) line thickness, (c) resistivity shown relative to bulk silver, and (d) resistivity shown relative to bulk nickel.	146
4.20	SEM images of the film surface of the 10% Ag-Ni/PAA (75:25 w/w%) alloy at different pitch size (a) (45 μm), (b) (25 μm), and (c) (15 μm) at room temperature.	147
4.21	SEM images of the surface of the 10% Ag-Ni/PAA (75:25 w/w%) alloy overprinting patterns at pitch size (45 μm) (a) 3 layers, and (b) 5 layers.	148
4.22	Properties of room-temperature overprinted features on photo paper from a 50 μm nozzle at 45 μm print pitch. (a) Effect of number of printed layers on line width/thickness, (b) effect of number of printed layers on resistivity.	149
4.23	SEM images of the surface of the 10% Ag-Ni/PAA (75:25), and (40:60) w/w% printed film on photo paper substrate.	151
4.24	Characteristics of printed lines on glossy photo paper with a 50 μm nozzle diameter at room temperature (a) effect of print pitch on the line width/ thickness, (b) effect of print pitch on resistivity.	154

4.25	Properties of room-temperature overprinted features on photo paper from a 50 μm nozzle at 45 μm print pitch. (a) Effect of number of printed layers on line width/thickness, (b) effect of number of printed layers on resistivity.	155
5.1	TEM image of Ni-Ag (1:1 w%).	160
5.2	The DLS graphs of nickel- silver core-shell nanoparticles.	161
5.3	TGA of the Ni@ Ag core-shell nanoparticles.	162
5.4	SEM images of the Ni@ Ag core-shell.	163
5.5	EDS results of as-synthesised Ni@ Ag core-shell composite.	164
5.6	TEM images of Ag-Ni core-shell NPs (a) (50:50), (b) (75:25).	167
5.7	The DLS graphs of (a) copper (core) nanoparticle, (b) Cu@ Ag core-shell nanoparticles.	170
5.8	(a) SEM images of the Cu@ Ag core-shell nanoparticles (Mag = 428.0 kx), (b) thickness of ligands between particles (Mag = 326.6 kx).	171
5.9	TGA of the Cu@ Ag core-shell nanoparticles.	172
5.10	EDS results of Cu@ Ag core-shell composite.	173
5.11	Characteristics of printed lines on coated PET at 90 °C by 50 μm nozzle (a) effect of print pitch on the line width/ thickness, (b) effect of print pitch on resistivity.	179
6.1	Photograph of bending rig (novel and custom built) with the parts labelled.	190
6.2	Simple drawing/images of forces in (a) compressive (printed track on top surface) and (b) tensile (printed track on bottom surface) bending.	190
6.3	Optical microscope image of the inkjet silver track on PVOH/KCl coated PET substrate.	191

6.4	(a) Illustration of bitmap creating steps, (b) example of a script file for printing.	191
6.5	A simple illustration of bending software setting, using Mach 3 software to control the motion of the micro engraving rig. (a) Overall software, (b) axes (X, Y) control, (C) load / control cycle.	192
6.6	The electrical resistance vs the change in resistance between the initial resistance and the resistance after number of bending cycles on (a) PET, (b) PI, (c) photo paper(wide line), and (d) photo paper (narrow line).	198
6.7	The electrical resistance of the printed silver vs bendability on (a) PET (tension, compression); (b) PI (tension , compression); (c) photo paper (wide line, tension, compression); (d) photo paper (narrow line, tension) bending. Error bars show the resistance S.D. for the 5 tracks tested simultaneously side by side in a bending test.	199
6.8	SEM images (a) before, (b) after bending test on coated PET.	202
6.9	SEM image after compressive bending for printed silver track on photo paper, showing a catastrophic crack right across the narrow track.	203
7.1	Images showing the setup for the temperature cycling experiments. The close-up images show the digital multimeter connected to the printed pads using wire connects attached with conductive silver epoxy. The aluminium block was coated with plastic packaging tape to insulate it electrically and avoid short-circuits.	212
7.2	Photograph of the temperature sensor design for photo paper.	213

7.3	Image of a test device on photo paper showing the effect of high temperature on photo paper causing yellowing.	214
7.4	Resistance versus temperature (during a 30 min heating ramp) of the printed temperature sensor on photo paper (a) cycle 1, (b) cycle 2. R^2 is the linearity, which was calculated using only the data points up to approximately 100 °C (orange data points on the graph).	215
7.5	SEM images of printed temperature sensor on photo paper (a) before heating, (b) after heating in oven for 30 min.	216
7.6	Resistance versus temperature (during a 30 min heating ramp) of the printed temperature sensor on PVOH/PET substrate (a) cycle 1; (b) cycle 2; and (c) cycle 3. R^2 is the linearity, which was calculated using only the data points up to approximately 100 °C (orange data points on the graph).	219
7.7	Resistance versus temperature (during a 30 min heating ramp) of the , how pre-heated printed temperature sensor on PVOH/PET substrate (a) cycle 1; (b) cycle 2; (c) cycle 3; (d) cycle 4. R^2 is the linearity, which was calculated using only the data points up to approximately 100 °C (orange data points on the graph).	221
7.8	SEM images of printed temperature sensor on PVOH/PET (a) before heating, (b) after pre-heating in oven for 1h/ 190 °C, then heating cycle for 30 min reaching a temperature of 130-137 °C for testing.	223
7.9	Resistance versus temperature (during a 30 min heating ramp) of the printed temperature sensor on	225

	PVOH/PI substrate (a) cycle 1; (b) cycle 2; and (c) cycle 3. R^2 is the linearity, which was calculated using only the data points up to approximately 100 °C (orange data points on the graph).	
7.10	Resistance versus temperature (during a 30 min heating ramp) of the pre- heated printed temperature sensor on PVOH/PI substrate (a) cycle 1; (b) cycle 2; and (c) cycle 3. R^2 is the linearity, which was calculated using only the data points up to approximately 100 °C (orange data points on the graph).	227
7.11	SEM images of printed temperature sensor on PVOH/PI (a) before heating, (b) after heating in oven for 1h/ 190 °C, then heating cycle for 30 min reaching a temperature of 130-137 °C for testing.	229
7.12	Thermogravimetric analysis for polyvinyl alcohol.	230
7.13	images of Ag printed device on coated PI substrate (a) printed device on pre-heated PI/PVOH substrate, (b) printed device on non-heat-treated PI/PVOH, substrate then heated afterwards.	232
7.14	FT-IR spectra of PVOH coated on PET /PI film (a) spectrum of the sample before heating, (b) after heating for 1 h, 190 °C.	233
7.15	FT-IR spectra of polyethylene terephthalate (PET) Films.	235
7.16	FT-IR spectra of Polyimide Films.	236

List of Tables

Table No.	Tables Caption	Pages
2.1	Different ink contents ratios.	55
3.1	The DLS data of prepared 30% standard silver ink.	75
3.2	The DLS data of prepared 20% standard silver ink.	75
3.3	The DLS data of prepared 10% standard silver ink.	76
3.4	Effect of pitch size on line width, thickness and resistivity for printed lines of 30% AgPAA ink on glossy paper with a 50 μm nozzle diameter, printed at room temperature.	84
3.5	Effect of pitch size on line width, thickness and resistivity for printed lines of 20% AgPAA ink on glossy paper with a 50μm nozzle diameter, printed at room temperature.	87
3.6	Summary of properties of room-temperature overprinted features of 30% AgPAA ink on photo paper from a 50 μm nozzle at 65 μm print pitch.	90
3.7	DLS data of Ag-PVOH NPs with the different PVOH chain lengths.	92
3.8	DLS data for Ag-PVP NPs with different PVP treatments.	95
3.9	DLS size distributed during period of time.	99
3.10	Effect of pitch on width, thickness and resistivity of printed lines. 30% AgPVP ink was printed with a 50 μm nozzle diameter on glossy photo paper at room temperature.	108
3.11	Summary of properties for room-temperature overprinted line features of 30% AgPVP on photo paper from a 50 μm nozzle at 45 μm print pitch.	110
4.1	Summary of metal composition and the size distribution results.	116

4.2	DLS size distribution of 10% Ag-Ni/PAA alloy ink after different periods of storage time and the resistance from manual “smear test “.	122
4.3	Effect of pitch on width, thickness and resistivity of printed lines. 10% AgNi/PAA (50:50) w/w% alloy ink was printed with a 50 µm nozzle diameter on glossy photo paper at room temperature. The first five print pitches showed no conductivity, so their other parameters were not measured.	129
4.4	Summary of properties of room-temperature overprinted features on photo paper from a 50 µm nozzle at 45 µm print pitch.	131
4.5	EDS elemental analysis results from printed film on photo paper.	134
4.6	EDS elemental analysis results from dried ink.	137
4.7	ICP-MS elements analysis results from Ag: Ni /PAA nanoparticles.	137
4.8	Composition of metals in Ag–Ni alloy samples as obtained by ICP-MS and from EDS analyses.	138
4.9	Comparison of electric properties of printed lines 10% AgNi /PAA (50:50 w/w %) alloy ink on glossy photo paper with a 50 µm / 80 µm nozzle at room temperature.	140/141
4.10	Summary of properties of room-temperature overprinted features on photo paper from a 50 /80 µm nozzle at 45 µm print pitch.	145
4.11	Summary of properties of room-temperature 10% AgNi /PAA (75:25) w/w% alloy ink overprinted features on photo paper from a 50 µm nozzle at 45 µm print pitch.	148
4.12	Summary of characterisation of Ag-Ni/PAA alloy standard ink.	150
4.13	Ag- Ni/PAA alloy ink behaviour applied on different substrate by a smear test and inkjet printing.	152

4.14	Effect of pitch on width, thickness and resistivity of printed lines with Cl^- spray sintering. 10% AgNi /PAA (40:60) w/w% alloy ink was printed with a 50μm nozzle diameter on glossy photo paper at room temperature.	153
4.15	Summary of properties of room-temperature 10% AgNi /PAA (40:60) w/w% alloy ink overprinted features on photo paper from a 50 μm nozzle at 45 μm print pitch.	154
5.1	Summary of the particle size of Ni-Ag-PAA core- shell NPs with different metal molar ratio.	160
5.2	ICP-MS elemental analysis results.	164
5.3	The DLS data and size distribution of Ag-Ni NPs prepared with hot injection method.	167
5.4	ICP-MS elemental analysis results.	173
5.5	Cu@ Ag core-shell ink behaviour applied on different substrates by a smear test.	176
5.6	Effect of pitch on width, thickness and resistivity of printed lines. 10% Cu Ag /xylene core-shell ink was printed with a 50 μm nozzle diameter on coated PET at 90 °C.	178
6.1	Bar metering application chart.	186
6.2	30 wt% AgPAA ink on PET coated substrate (tension) with 0.055 mm print pitch.	193
6.3	30 wt% AgPAA ink on PET coated substrate (compression) with 0.055 mm print pitch.	193
6.4	30 wt% AgPAA ink on PI coated substrate (tension) with 0.055 mm print pitch.	194
6.5	30 wt% AgPAA ink on PI coated substrate (compression) with 0.055 mm print pitch.	194
6.6	30 wt% AgPAA ink on photo paper/ wide line (2 mm) (compression) with 0.055 mm print pitch.	195

6.7	30 wt% AgPAA ink on photo paper/ wide line (2 mm) (tension) with 0.055 mm print pitch.	196
6.8	30 wt% AgPAA ink on photo paper/ narrow line (1 mm) (tension) with 0.055 mm print pitch.	197
6.9	30 wt% AgPAA ink on photo paper/ narrow line (1 mm) (compression) with 0.055 mm print pitch.	197
7.1	Summary of the measured resistance, temperature, and temperature coefficient (with SD in brackets) on photo paper over 30 min time.	214
7.2	Summary of the assessment of electrical properties of a temperature device on photo paper.	215
7.3	Overview of the characteristics of all tested sensors on photo paper.	216
7.4	Summary of the measured resistance, temperature, and temperature coefficient on PVOH/PET substrate over 30 mintime.	218
7.5	Summary of the assessment of electrical properties of temperature device on coated polyester (PET).	218
7.6	Summary of the measured resistance, temperature, and temperature coefficient for pre-heated temperature sensor on coated polyester (PET) over 30 min time.	220
7.7	Summary of the assessment of electrical properties of the pre-heated temperature sensor on PVOH/PET substrate.	220
7.8	Summary of the measured resistance, temperature, and temperature coefficient on coated Polyimide (PI) (during a 30 min temperature ramp).	224

7.9	Summary of the assessment of electrical properties of temperature device on PVOH/PI substrate.	224
7.10	Summary of the measured resistance, temperature, and temperature coefficient on pre-heated temperature sensor on coated (PI) over 30 min time.	226
7.11	Summary of the assessment of electrical properties of the pre-heated temperature device on PVOH/PI. substrate over 30 min time.	226
7.12	Assessment of IR spectroscopy functional groups of PVOH coated on PET /PI film before and after heating.	233
7.13	Assessment of IR spectroscopy functional groups PET substrate.	235
7.14	Assessment of IR spectroscopy functional groups PI substrate.	236

Acknowledgements

I would like to take this opportunity to first thank my primary supervisor, Professor Andrew Mayes for his expert guidance, enthusiastic encouragement, useful critiques and advice that made this project successful. An additional thanks goes for his moral support and understanding of my difficult circumstances. I could not have wished for a better supervisor.

I am especially indebted to Dr Andrew for his constant help and support even after his retirement.

A special thanks goes to my secondary supervisor, Dr Sonia Melendi-Espina for accepting to be my second supervisor on very short notice at the end of my journey and offering her help and support.

Thank you to my secondary supervisor Dr Mattew Alexander for all his guidance and suggestions in my first year of Ph.D.

My deepest appreciation goes to my husband Abdullah who supported me with love, helped me to be here and made my life enjoyable. His extraordinary love, respect and care are appreciated. Thank you for always believing in me, even when I didn't believe in myself.

Last but not least, my biggest gratitude goes to my family. I want to thank my mum and all of my family for all of their immeasurable love and support, both emotionally and financially throughout the journey and always. Thank you for the video calls, the WhatsApp conversations, the parcels with much-missed Arabic food, the reminders of home and for always keeping my feet on the ground. I would not have come this far if it wasn't for you all and I will be forever grateful.

Special thank you to my sisters, who always provided a fun distraction from the worries of the PhD life, for the nostalgic memories of our days together.

I am very grateful to my beloved children, (Wissam, Qusai, Milad and Jawad) and my little princess (Cadi) whose existence and unconditional love kept me strong and made this journey possible.

I am grateful to all of my friends (Masoomeh Bazzar), thank you for the useful discussions and for kindly introducing me to the research life and making my first steps easier. (Nahla Sindi) thank you for your friendship, your help and

for always keeping a smile on my face and spreading your positivity and your moral support.

All my hard time here alone abroad with my children has made me realise my hidden strengths and I came up even stronger to achieve my goals.

A special thanks goes to the invaluable technical assistance given by Dr Bertrand Leze, Dr Colin Macdonald and Graham Chilvers is hugely appreciated.

Finally, a special thanks goes to my Saudi Cultural Bureau, this thesis would not have been possible without their financial support and their always support throughout the journey.

Chapter 1. Introduction

1.1 Nanoparticles (NPs)

The field of nanoscience has blossomed in recent decades. The need for nanoparticles increases as miniaturisation becomes more important in advanced nanotechnology and engineering technology, with applications such as sensors, opto-electronics, information storage, computing, other electronic devices, use as catalysts for many photochemical reactions and biomedical applications. The attraction of nanoparticles is due to their high surface area, small dimensions, quantum effect [1,2,3], and excellent chemical and physical properties, including intriguing optical, electrical, magnetic and thermal characteristics. It is these properties, which are demonstrated by this intermediate state of matter and generally different from properties of bulk materials, that give nanomaterials their particular interest [3,4,5].

Nanoscale silver particles play an important role in a wide range of applications because of their unique properties. They have the highest electrical and thermal conductivities of any metal [5,6] and show desirable optical reflectivity and biological characteristics [7]. Their intriguing properties make them a priority material for use in a variety of applications, from electrical and thermal conduction in the electronic industry, to hygiene applications in medical devices, due to their antibacterial properties [4,8,9]. Silver NPs have recently been used in such diverse areas as medical applications, analytical sensing, chemical catalysis and electrically conductive inks for printing [10,11,12].

1.2 Colloidal nanoparticles (NPs)

Colloidal NPs are small in diameter, but large in surface area, and display interesting and unique optical, electrical, magnetic and chemical properties, which are different from their bulk equivalents. These properties give them enormous potential for application in medicine, catalysis and biotechnology, and can be specified by varying one of the parameters such as size, structure, shape or composition [13].

The use of silver nanoparticles (Ag NPs) in a number of applications is steadily increasing. However, the ability of Ag NPs to aggregate controls what

happens to them in any given environment. Stabilisation therefore becomes essential to the potential further application of colloidal NPs. The inherent structural variation of polymers coating NPs plays a significant part in colloidal stability. Improved colloidal stability is seen when polymers are inserted into or adsorbed onto the particle surface, via interaction with the electrostatic and steric stability of the coated colloidal particles [14,15].

1.2.1 The concepts of colloidal stability

One of the most significant parts of colloid science is the mechanism of NP stabilisation in the dispersing medium. Generally, nanoscale particles are unstable and tend to agglomerate or undergo coalescence, without any counteractive repulsive forces, as the distance between particles decreases. They are attracted to each other by various forces: van der Waals, magnetic or electrostatic. As a result, there is a need for repulsive forces, which can be provided by steric or electrostatic stabilisation [13].

1.2.1.1 Electrostatic stabilisation

To obtain stable NPs there is a need for forces which counter van der Waals attraction. In metal NPs, this is always supplied by the particle's surface charge, resulting in repulsive forces between particles.

In solution, solvated ions are all around the particles and cover their surface charge. As a result, the surface potential decreases in two layers, known as the electric double layer (EDL): the outer diffuse layer and a compact inner layer [13].

The interaction of electric surface potential within the EDL determines colloidal stability. The resulting Coulomb repulsion forces between the particles decay exponentially with distance between particles. The forces due to the EDL result from the overlapping electric potential distribution, also the overlapping ion concentration (osmotic pressure). If the electrostatic repulsion is adequately high, it prevents the particles coagulating [13].

1.2.1.2 Steric stabilisation

Steric stabilisation is a process in which a large molecule adsorbs onto the surface of the colloidal particles preventing them from aggregation, like polymers or surfactants that provide a protective layer. The process works because the density of the adsorbed molecules in the space between particles increases significantly as the distance between particles is reduced, causing an increase in osmotic repulsion. This results in reduced entropy and an increase in the Gibbs free energy, which is thermodynamically not appropriate [13].

1.2.2 Metal colloidal growth

This section explains the general mechanism and growth concept for the typical synthesis of colloidal metal NPs in the presence of mild reducing agents such as sodium citrate (Figure 1.1). For more understanding, the particle growth mechanism can be illustrated in three steps [16]:

Firstly, there is a rapid reduction of the metal ions to small-size atoms. Secondly, these free metal atoms tend to bind with other atoms and form dimers, trimers, etc and small clusters. These clusters start to coalesce until they achieve a certain stability, causing the process of coalescence to stop. As a result, the concentration of the particles decreases. Thirdly, the particles experience a phase called an intermediate phase of stability when particles that are bigger than 1 nm stop growing. However, during the synthesis, a decrease in the colloidal suspension stability occores. This step leads to further growth because of the particle's coalescence and produces larger particles. The particles are stable for days and the colloidal solution does not require stirring.

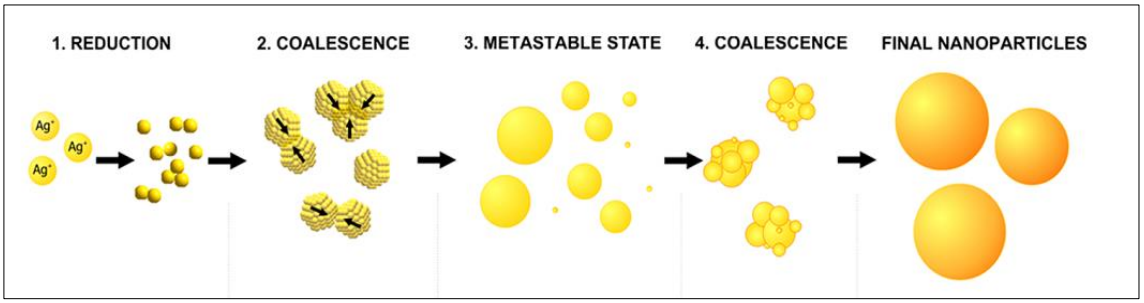

Figure 1.1 Schematic of the generalised mechanism of nanoparticle growth due to coalescence [16].

Indeed, the growth mechanism of the metal colloidal nanoparticles happens because of the coalescence and is governed by the electrostatic stabilization of the nanoparticles. In contrast, adding a steric stabilizer to the colloidal system will affect the growth mechanism by affecting the particle stability.

In comparison, synthesis in the presence of a steric stabilizing agent, such as a polymer will not affect the reduction process and the growth mechanism, but it will affect the duration of each step. Thus, the colloidal suspension shows long-term stability with more reliable monodispersed metal nanoparticles. Both systems have similar steps of the growth process, however, the third step is a metastable state, and it lasts for a longer time (30 - 90 min) compared with the nanoparticle without steric stabilizing. In the period after (the final step), the coalescence of the present particles happens and then stops when the particles reach a size at which the colloidal stability is enough to prevent particle aggregation and coalescence. It usually happens when almost 100 particles merge together to form a new stable nanoparticle and that leads to a decrease in particle contraction by approximately 1/80 of the previous particle amount [13,16,17,18].

Without electrostatic or steric stabilization, the collision between particles is very high due to their Brownian motion and the van der Waals attraction between particles. However, the presence of aggregation barriers like stabilizing agents will cause repulsion forces between particles and slow the particles' growth. Indeed, the growth mechanism of nanoparticles with a fast reduction process is mostly connected with colloidal stabilization [16,19].

The mechanism of NP growth discussed here is based on aggregation and finalised with coalescence.

1.2.3 Synthetic methods for colloidal nanoparticles

The aim of this section is to cover the development of the synthesis of silver nanoparticles including the trends and challenges that have led to the present project. Numerous NP synthetic methods have been reported in the literature, including physical, biological and chemical methods, which were elaborated to prepare the metal nanoparticles. For example, chemical reduction, photochemical reduction, electrochemical reduction, thermal decomposition in an

organic solvent, heat evaporation and so on [2,3,20,21]. Unfortunately, all of these approaches have some ingrained disadvantages. As a result, the choice of an appropriate method depends on the nature of the NP application [5].

To be more specific, physical methods usually need a vacuum, costly equipment and a high temperature, around 1000 °C. These requirements make physical methods less important and attractive in general than chemical methods [22]. To overcome these disadvantages with simple equipment and convenient operation, chemical methods are used, and these are considered to be some of the most popular methodologies for the synthesis of colloidal Ag NP in solution.

Although there are multiple chemical methods for silver NP synthesis, the chemical reduction process is continually chosen due to its ease and simplicity of handling for achieving the desired size of NP [2,21]. A typical process always requires a reducing agent, which acts as an electron donor and reduces silver ions to their metal form. Popular choices include sodium citrate [21,23], sodium borohydride [24,25], polyols [26], hydrazine [27], ascorbic acid [28] or polyethylene glycol [29,30]. The choice of appropriate synthesis conditions and reducing agent can affect the stability and size of the Ag NP produced significantly [31].

During the synthesis of Ag NP, it is necessary to modify the surface of the particles by coating or capping the metal with polymer or small molecule stabilisers, to prevent them from agglomeration and to determine the behaviour and size distribution [32,33]. These capping agents have a specific functional group to attach them on the surface of the NPs but otherwise show variation in their chemical and physical characteristics. Within this group of capping agents, adsorption of polymers such as PVP [34,1,4], PVOH and PAA [21] are effective at reducing the surface energy and preventing grain growth and agglomeration (Figure 1.2). These agents function either by covering the nanoparticles, forming a protective layer to avoid agglomeration by steric means, or by causing electrostatic repulsion between the particles [21].

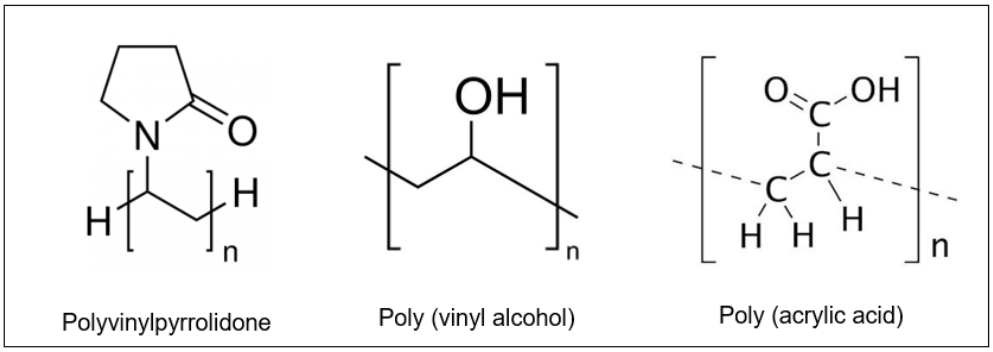

Figure 1.2 Structure of the polymers polyvinylpyrrolidone, poly (vinyl alcohol) and poly (acrylic acid).

Generally, the chemical synthetic methods can be divided into two groups depending on the medium.

1.2.3.1 Aqueous methods

Wang H. *et al.* [4] synthesised well-dispersed Ag NPs by a chemical reduction method in aqueous solution, using PVP as a capping agent in the presence of glucose and sodium hydroxide. The PVP as a dispersant helps to stabilise the silver nanoparticles by coordinating the N and O in PVP with the Ag particles and preventing their agglomeration.

Guo L. *et al.* [25] synthesized stable silver nanoparticles by the reduction of silver ions with $NaBH_4$ in the presence of poly (N-isopropyl acrylamide) in an aqueous solution. The results revealed that the Ag NPs were very stable at room temperature in a spherical shape and reasonably uniform in size between 16.2 ± 3.3nm and no aggregation was observed in aqueous solution.

Chou K. *et al*. [35] found that varying the ratio of PVP to $AgNO_3$ by weight from 0.05 to 1.5 allowed control of the size of the particles in an aqueous synthesis. They mainly used a continuous precipitation method, with $AgNO_3$, PVP, and $NaBH_4$ as a reducing agent, at room temperature. As a result, they obtained nanoparticles with an average size varied from 130 to 13 nm with high purity and the particles showed a perfect crystalline structure.

Bose S. *et al.* [36] synthesised nearly mono-dispersed Ag NPs, with size distributed in the range between 90-120 nm, by chemical reduction methods based on a medium of water and ethylene glycol, in the presence of PVP as a capping agent. The PVP stabilised colloidal suspension of Ag NPs in water/ethylene glycol medium was used as a conductive ink and showed

excellent desired properties, with a low sintering temperature, around 100 °C, and low viscosity, of 6.5 cP.

Milardovic S. *et al.* [21] synthesised Ag NPs with a mean size of 2.5 nm, by the reduction of $AgNO_3$ using a different reducing agent. They used an aqueous hydrazine solution and a mixed solution of PAA and silver nitrate. The resulting nano-silver ink, with a silver metal content of 25%, was printed at room temperature on flexible plastic and paper substrates. These tracks showed a resistivity of 8.0×10^{-8} Ω.m, after sintering at 105 °C for 20 minutes. The properties of this silver nanoink were examined by SEM, TEM, DLS and UV-Vis measurements. The results demonstrate the applicability of this approach for the successful preparation of an Ag NP-based ink with a good stability of approximately seven months.

1.2.3.2 Non-aqueous methods

In previous investigations by Wu R. *et al.* [37], stable and highly concentrated suspensions of Ag NPs have been prepared by using the chemical reduction method from silver nitrate in a formaldehyde reductant using an organic base, triethylamine, as the reaction promoter, with thiosalicylic acid (TSA), as the protecting agent. The obtained Ag NPs were prepared successfully, with an average size less than 10 nm. They showed low-temperature sintering and a good resistivity of about 4.29×10^{-5} Ωcm. The viscosities of the prepared suspensions, which ranged from 1.60 to 6.29 cP, made them suitable for use in ink-jet printers.

Another study by Tang Y. *et al.* [38] reported a stable colloidal solution of Ag NPs was prepared with an average size around 90 nm by using PVP as a capping and stabilising agent, in the presence of ethylene glycol by a polyol reduction method. The colloidal solution of Ag NPs was stable and was successfully formulated to ink and printed by screen printing on FR-4 epoxy class cloth substrate. The silver pattern showed a low electrical resistance and revealed significant conductivity, reaching 16% of that of bulk silver.

Wang Z. *et al.* [39] fabricated monodisperse Ag NPs, with a size of 118 nm, via a modified polyol process with a low mass ratio of PVP to $AgNO_3$, using EG as a reducing agent. The Ag NPs produced were very stable and successfully formulated into conductive inks that required a low sintering temperature of about

220 °C for 30 minutes under air atmosphere. The conductive patterns were produced by screen printing on PI substrate and had a comparatively low resistivity of 8.3 x 10^{-6} Ω.cm, which makes it usable for various applications.

1.3 Core-shell or bimetallic system (alloy, core -shell nanoparticles)

In recent years, huge research effort has been invested in new types of NP comprising a core-shell architecture of two different nano-size materials or mixed nano-alloys, both used for device fabrication in a variety of applications. The focus of this study is to achieve a substantial economic benefit by replacing an expensive and/or reactive metal in the particles, like silver and gold, with other, low-cost metals. These bimetallic NPs are more suitable for magnetic, sensing, optical, electrical contact, catalyst, switching and conductor applications, and much broader applications, than their mono-metallic counterparts [40]. Bimetallic NPs exhibit physicochemical properties that are unique compared with the individual metals and that provide a broader space for engineering materials and give new and enhanced capabilities. Also, for some combinations, it shows stability and functionality similar to noble metals but with lower cost [41,42]. There is abundant literature confirming that the synthesis of bimetallic nanoparticles with different metals and the same method give quite different results, since nucleation, growth rates and surface properties are different for each metal [3].

Our goal is to obtain a nanometallic-based conductive ink for inkjet printing. In this context, the conductive inks based on silver NPs hit the goal; they are stable against the oxidation process, have high electrical conductivity and ease of processing. However, it has some drawbacks due to its high price which is a hindrance to its use for commercial products [43]. Further, using silver NP ink could lower the reliability of an electrical circuit by the electro-migration process. This process happens, when silver comes in contact with insulating materials under electrical potential, so it is removed ionically from its initial location, and it is redeposited as metal at some other location. This process makes silver easily oxidized and reduced, and it is not passivated, while other metals do not present a practical migration hazard [44,45]. Silver migration changes the dielectric

properties, reduces the resistance, and causes short circuits, causing device failure, mostly under high humidity environments [46].

Among the various alternative metallic materials for replacing silver and other noble metals with cheaper ones are copper [47], nickel [48,49], aluminium [50] and tin [51,52]. The most common examples are Ni and Cu. They have a great attraction because of their outstanding properties. Nickel shows a good conductive property, reduced tendency for electro-migration process and is considerably cheaper than other candidates, such as silver and gold. Copper is much cheaper than silver too and has relatively high conductivity (only 6% less than that of Ag) and catalytic activity [53,54]. However, there is a serious challenge in using Ni or Cu in the synthesis of NPs, due to their immediate oxidation on exposure to air, which is coupled with losing their electrical conductivity (since the metal oxides are poor conductors). Oxidation is a particularly acute problem with NPs, due to the high surface to volume ratio. This limits their application in printed electronic fabrication.

To solve the problem of Ag high cost and the low oxidation stability of Ni and Cu, many approaches have been suggested to mitigate oxidation by simply alloying them together and forming a bimetallic nanoparticle structure such as alloy (mixing patterns) with another high oxidation resistance material such as Ag. Otherwise, they need to be protected from oxidation by coating the individual particles with a dense layer of capping agents, such as polymers and surfactants [55]. However, this process will not assure its stability against oxidation, it only minimizes the oxygen penetration to the metal NPs. The more effective and fast method is to deposit a thin layer of a non-oxidizing metal like silver metal [56,57]. This coating results in the formation of a core-shell system, and this retards the oxidation process of the Ni /Cu core [58]. The resultant surface should be capable of protecting the bulk core from oxidation.

Researchers have developed a diversity of ways to synthesise alloy, and core-shell nanoparticles, for example, chemical reduction methods [59,60,61], polyol method [59], solvothermal hot injection method [38], galvanic displacement [58].

From these, two common methods have been explored as effective routes to the synthesis of bimetallic nanoparticles, the most highly effective method is

transmetalation or galvanic displacement for the fabrication of core-shell NPs. In this method, the surface of the core acts as a reducing agent for the second metal with higher reduction potential. This process causes the formation of solely metal shells on the surface of the metallic core due to huge differences between the reduction of noble metals (Ag or Au) and non-noble metals like Cu and Ni [56]. Alternatively, the solvothermal reduction and co-reduction method is considered the most advantageous method in the preparation of the alloy nanoparticles, particularly if it is carried out in long-chain alkyl amines, such as octylamine, decyl amine, dodecyl amine or oleylamine. These amines can act as reducing agents and surface capping species at the same time. These alkylamines have an effect on NP properties and provide well-dispersed, mono-dispersed NPs of metal alloys and pure metals [59].

There are numerous reports on the synthesis of bimetallic nanoparticles: Bala T. *et al*. [63] prepared oleic acid-capped Ni NPs in an aqueous foam, in size 10-20 nm for the core. Afterwards, these Ni NPs were coated with silver shells by a simple transmetallation reaction, and the shell thickness was 2-4 nm. Chen D. *et al*. [61] reported the synthesis of Ni-Ag core-shell NPs in the presence of hydrazine reduction of metal salts in ethylene glycol. They have achieved Ni cores that were fully covered by Ag nano shells.

Tsuji M. *et al*. [42] successfully synthesized Ag/Cu alloy and novel Ag/Cu@ Cu particles. Their method is based on reducing a mixture of $AgNO_3$ and $Cu(OAC)_2.H_2O$ in a hot ethylene glycol solution in the presence of PVP. Modifying the Ag:Cu molar ratio or the reaction time could control the obtained particle structures. The same researchers, in a previous study [62], reported a simple one-pot preparation method to synthesize Ag@Cu core-shell NPs using a polyol method. They used a similar metal salts and polymer ($Cu(OAc)_2.H_2O$, $AgNO_3$,PVP) under bubbling Ar gas and ethylene glycol as reducing agent.

Guo H. *et al.* [64] synthesised mono-disperse Ag@Ni core-shell NPs using a facile one-pot method in the presence of oleylamine, which acts as a solvent and reducing agent. These NPs showed a narrow size distribution of 14.9 ±1.2 nm, and a tunable shell thickness. Their study showed that the formation of a Ni shell on Ag core exhibited a superparamagnetic behaviour at room temperature and excellent catalytic properties. It is the wrong orientation for our intended use, however, since the Ag is not protecting the Ni from oxidation.

Shankar R. *et al.* [65] reported the results of non-aqueous synthesis of Ag NPs with tin (II) acetate as a reducing agent in a toluene medium, which gave high conductivity for ink formulation in printed electronics. This method allows for easy scaling up to the manufacture of grammes of NPs and dispersal in an abundant non-aqueous solvent (hydrocarbon and organic solvents) making it a suitable method for several applications. This method results in particles with a 5-20 nm size range at room temperature, with a silver metallic core confirmed by x-ray diffraction. However, TGA proved the existence of the amine shell. A conductive ink formulation was generated by aerosol jet to achieve a good conductive track applied on many substrates, such as polyimide and photo paper.

Santhi K. *et al.* [66] synthesised Ag -Ni alloy NPs by a chemical reduction method with an average size of 30-40 nm. The precursor mixture of nickel sulphate and silver nitrate salts was reduced using sodium borohydride in the presence of PVP as a capping agent. The molar ratio of $NaBH_4$ to the metal ions in the precursor was kept at 10:1 to ensure the complete reduction of Ag and Ni ions. The resultant metal composition of the samples was in very good agreement with the precursor composition, and that was determined by Perkin Elmer Optima 5300 DV Inductively coupled plasma optical emission spectroscopy (ICP-OES) analysis and EDS analyses.

Tsai C. *et al.* [67] synthesized Cu-Ag core-shell in a typical procedure of one-pot sequential reduction. First, the metal salt solution containing $CuCl_2$ and PVP as a capping agent was dissolved in water. Then, the reducing agent solution $NaBH_4$ (1wt.%) and trisodium citrate dehydrate (1 wt.%) were added. In order to obtain Cu@Ag core-shell structure, the $AgNO_3$ salts were added after the reducing agents. This experiment was done at 100 °C under N_2 gas atmosphere. The obtained core-shell NPs had an average particle diameter of 25 ± 2.7 nm and an Ag/Cu atomic ratio of 1/8.

Kim N. *et al.* [54] succeeded in synthesizing Ag-Cu bimetallic NPs with a simple thermal decomposition method. The obtained NPs were in a narrow size distribution and the experimental and theoretical studies confirmed they were less prone to oxidation compared to pure Cu NPs. That significantly happened because of the electron transfer from Cu to Ag within these bimetallic NP structures and that caused the resistance improvement.

Yan S. *et al*. [68] synthesised Ag-Ni NPs with chemical reduction methods at room temperature. PVP was used as a stabilizing agent and sodium borohydride as the reducing agent for the precursor's mixed solutions of silver nitrate and nickel sulfate hexahydrate. Five Ag/Ni ratios were investigated and revealed that all NPs were in quasi-spherical morphology. XRD results showed all peaks of as-prepared NPs were close to pure Ag peaks and no peaks of pure Ni, however, with increasing the Ni content, in atom scale, small clusters of atoms are incorporated in the Ag matrix leading to an increase of free energy for the alloy structures.

Pajor-Świerzy A. *et al.* [69] have used a simple, fast and low-cost method to prepare Ni@Ag core-shell NPs in two effective steps to get a conductive material: 1) formation of Ni NPs in the presence of sodium borohydride as a reduction agent by the wet chemical method; and 2) synthesis of an Ag shell by the galvanic displacement reaction. The size of the obtained Ni core was about 50 and 210 nm -diameter coated with a thin Ag shell ~10–20 nm. Ni @Ag NPs in this study were prepared consistently and effectively, with long-term stability and blocking from Ni oxidation. Thus, these particles are much more acceptable for conductive materials, such as inks and pastes.

1.3.1 Hot-injection method

A different approach in the synthesis of the CS system, an Ag@Ni core-sell system, was successfully synthesised by using a practical hot-injection method. This result was obtained by Vykoukal V. *et al.*, [59] who synthesised Ag@Ni core-shell NPs by a solvothermal hot injection method from $AgNO_3$ and $Ni(acac)_2$ in a hot mixture of dry oleylamine and 1-octadecene at 230 °C, where a thin amorphous Ni layer covers Ag nuclei. AgNi nanoparticles were prepared with different Ag/Ni stoichiometric compositions. From the results obtained, by small angle X-ray scattering (SAXS), there is no dependence of the particle size (13-21 nm) on the Ag/Ni stoichiometric ratio. The NPs produced were spherical in shape with a size distribution of 23-31 nm. In this kind of reaction, the temperature and the injection rate were substantial factors in order to control the particle size.

Sopoušek J. *et al.* [70] have synthesised Ag-Cu NPs by solvothermal coreduction of silver acetate and copper acetylacetonate in a mixture of organic

solvents (oleylamine and 1-octadecene) at 230 °C under an inert atmosphere of nitrogen. The obtained NPs were measured by DLS, and the hydrodynamic average sphere diameters of the NPs size were between 20-40 nm. The atomic arrangements inside individual nanoparticles were studied by HRTEM. It was confirmed that Ag and Cu form a substitutional solid solution with the face-centered cubic lattice. The disturbances in the crystal lattice are boundaries of twin crystals. No oxides were observed on the Ag Cu nanoparticle surface. This confirms that the thermal synthesis in organic solvent with a minimum solubility of oxygen is a suitable method for the preparation of oxide-free metallic nanoparticles.

In summary, there is considerable literature precedent for synthesising Ni/Ag and Cu/Ag alloys and core shells that might be suitable for printing applications. Some of the materials were explicitly produced for this purpose and tested in various ways. Others were not, but their properties appear to be suitable for such use, based on the published characterisation. Based on this review, there appears to be a lot of opportunity to explore and optimise materials and processes in this area.

1.4 Printing electronics

In the last few years, growing interest has been devoted to the development of Printed Electronic (PE) technology, to benefit from the convenience, low cost, low ink consumption and flexibility of this approach. Also, it is becoming more accessible for manufacture of electronic devices on assorted substrates using printing methods such as aerosol printing, screen printing, spraying, stencil printing, gravure printing, and ink-jet printing [31,38].

Printed electronics is an example of the emerging theme of “additive manufacturing”, which has advantages in minimising waste, improving sustainability and environment-friendliness, high productivity, a simple fabrication process and simplicity of design changes [72]. To capture these benefits, it needs to use nanoparticles for the inkjet printing with stable and printable inks. Thus, the preparation of NPs for ink formation is a serious procedure that needs to deliver a desired size, shape and morphology [31]. The scale required also needs to be considered at the preparation stage, since methods that are unduly complex

or expensive to scale up are unlikely to be cost effective for general use, though they might still be relevant for high-value applications. For instance, hot injection methods are unlikely to be cost-effective for mass production of conductive tracks but might be acceptable to produce high quality quantum dots for display screen technology.

1.5 Printing techniques

A number of techniques were suggested for the fabrication of electronic devices which give high control of the deposition and pattern of the nanomaterials. The key points to select between these techniques is their ability to deliver simple, high throughput, low-cost mass production capability and produce nanosize features [73].

1.5.1 Screen printing

Screen printing is considered a thick film printing technology. The obtained films typically have a thickness between 20-100 μm, compared to other printing technologies in the range of 0.5-2 μm film thickness. In contrast, it has the largest availability for ink choices over other methods. The conductive ink should contain three main constituents: a metal conductor such as silver, carbon, gold and platinum or non-metallic like graphite with a proper solvent (ethylene glycol, cyclohexanone) and organic binders (glass powder, cellulose) while ensuring the balance between the solid content and liquid solvent. This will provide suitable viscosity and volatility for thermal curing. This technology has been widely used as the basis of electrode strip manufacture and fabrication of biosensors, such as those used for diabetic blood sugar monitoring [73,74].

Screen printing is a process that works by forcing an ink through a screen. The screen-printing plate is a combination of screen and stencil as illustrated in Figure 1.3. The printing procedure starts with imprinting or transferring the ink onto the screen and then moving the ink by the squeegee blade to penetrate the screen through an image-specific open mesh. The printable inks must have high viscosity when not under sheer, because when it is forced through the mesh screen with the squeegee blade it undergoes sheer thinning. This will allow the ink to pass through the stencil and to contact the substrate, then return to its viscous state, forming a sharp image with well-defined boundaries [74].

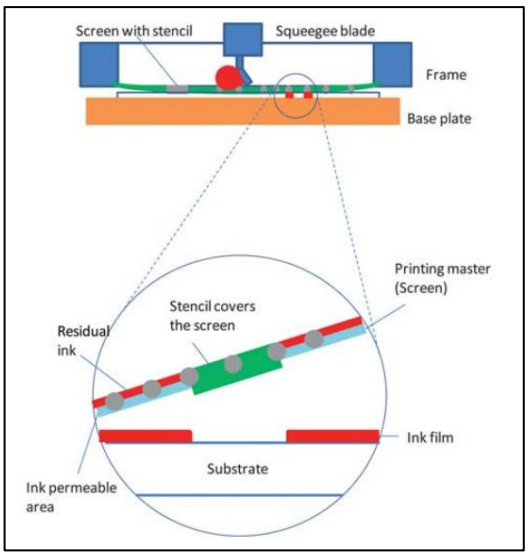

Figure 1.3 Screen Printing schematic diagram [74].

1.5.2 Rotary printing

Gravure, offset printing and flexographic are all printing methods used for roll-to-roll printing, such as magazines, newspapers and packages. They are considered the most powerful techniques for the fabrication of organic electronics, in terms of its excellent resolution, thin film deposition and the amount of material produced - up to 100 m min^{-1}. The film has a minimum line width in a range of tens of microns beside a couple of microns for line thickness [74].

Nevertheless, these techniques have some drawbacks as they are difficult to use on a research and development scale because of their large equipment requirements and design constraints around the complexity and expense of roller production. They are widely used for the purpose of scaling up the production of wide-area printing, however.

Gravure printing technology has high throughput, long print runs, uniformity, and versatility in operation. An engraved cylinder is rolled over a moving substrate, typically paper or plastic. The printing pattern is made up of recessed cells below the roll surface (Figure 1.4). These cells are then filled with ink and the excess ink will be removed by a flexible blade called a doctor blade. The pattern is typically pixelated into individual square cells. Finally, the ink on the printing roll is deposited onto a substrate when the roll is in contact with it in a single print step. Typically, it needs a high pressure (~3 MPA) to move ink from the carved cells on the cylinder to the substrate and a viscosity around (0.05-

0.2 Pa.s). These craved cells' depth and density would define the printed layers' thickness. The gravure cylinders are made from metals such as copper with a chromium coating. This results in excellent dimensional stability, roll durability and pattern fidelity as well as compatibility with a wide range of solvents. The main challenge with gravure is overcoming the non-idealities of the flexible blade wiping process [74,75,76]. However, it is typically only of use for longer print run processes (e.g. magazines, postage stamps) as the cost of the cylinders makes it expensive for short runs [73,74].

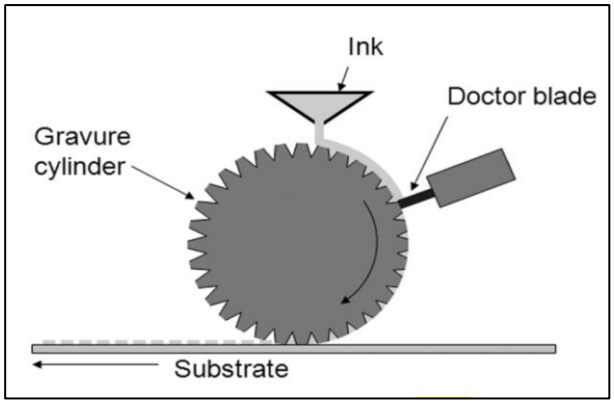

Figure 1.4 Gravure printing schematic diagram [76].

Flexographic printing techniques(Figure 1.5) produces a uniform film by applying the ink to the raised portion of the patterned flexography rubber which covers the surface of the printing roll. After that, it transfers the images onto the substrate when it comes in direct contact with it [73,74]. Thus, this is better than gravure for low-absorbency substrates since the ink is at the surface whereas in gravure it is in "pits" and has to be "pulled out" by surface tension and substrate deformation (hence the higher pressure needed), and the resolution is also marginal better (20 µm) in flexographic printing.

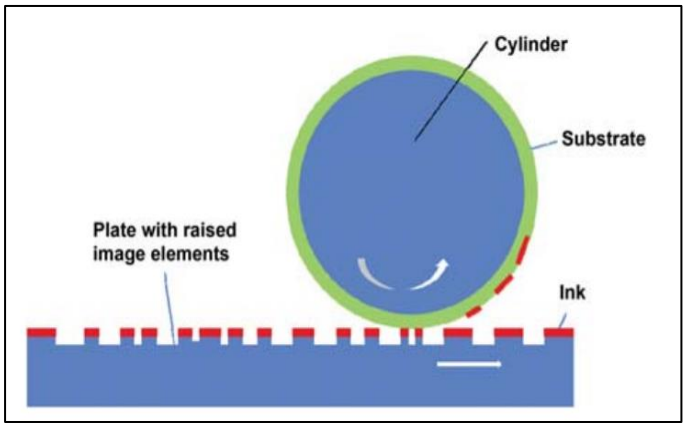

Figure 1.5 Flexographic printing schematic diagram [74].

1.5.3 Inkjet printing

In the electronics industry, the production of flexible, low-cost, lightweight, large-area, optically transparent and easy to manufacture electronic circuitry and devices is necessary, especially in the area of research and prototyping in science and engineering. As a consequence, the need for convenient and quick processing techniques to produce conductive lines at low cost has recently attracted attention to the new technology. For instance, inkjet printing offers the ability to print electronic circuits on a variety of substrates, such as paper, plastic or even rubber, in a simple and low-cost way [77].

Above all, the inkjet printing technique offers a way of manufacturing the device with digital control to get better quality, printing speed and precise deposition of material on the substrate. It also has the ability to print multiple layers – either of the same material to increase thickness, or different materials to make more complex structures, to improve device manufacturing [72,78]. This technique has recently been used to produce various bendable and transparent devices for such applications as solar cells [79], sensors [80], thin-film transistors [81], electronic displays [82] and supercapacitors [78,83].

The inkjet printing approach that is used in this study is known as the non-contact method. The nozzle head has a non-mechanical contact with the surface of the substrate, which allows the printing process to be more flexible in printing patterns and using many sensitive substrates such as photo paper and polyimide (PI) [31]. It allows the use of inviscid fluids (e.g., diluted polymer solution) and reduces metal wastage. Consequently, it has been shown to be applicable to the manufacturing of electro-optic devices, electro-chromic devices and gas sensors,

among others. It is obviously a good alternative to conventional printing approaches for electronic devices [84,85].

There are two substantial components of the inkjet printing technology: the mechanical system (printer) and the conductive material (ink). There are plenty of studies focused on the formation of droplets, jetting parameters and control of dropping location on the substrate, as will be discussed later in more detail [77].

1.6 Principles of inkjet printing

An inkjet printer can generate a droplet by two different mechanisms: drop on demand (DOD) and continuous inkjet (CIJ). CIJ mostly prints a drop diameter about 100 µm, as compared to a drop diameter of approximately 20-50 µm in DOD. The problem with CIJ is that it is wasteful of materials, as a huge amount of unwanted ink is used in the printing [78].

However, this obstacle can be averted by DOD. DOD is considered more economical as the printer produces individual drops to achieve the printing requirements. The drops are ejected from the nozzle when there is pressure in the fluid. In the absence of pressure, the liquid is held in the nozzle by surface tension [78]. Generating drops in the nozzle necessitates a pulse of pressure, which can be achieved by a thermal process or by using a piezoelectric transducer. Figure 1.6 displays a schematic DOD printed design. In the piezoelectric method, the drop ejection at the printhead nozzle is achieved through contraction of a piezoelectric element in response of an external voltage. In the thermal process, an electric current is passed through a small thin-film heater that heats the fluid to just above its boiling point to generate small bubbles. When the current is removed, no heat is transferred, so the bubbles disappear. This rapid expansion and collapse of bubbles creates a pulse of pressure [78, 86].

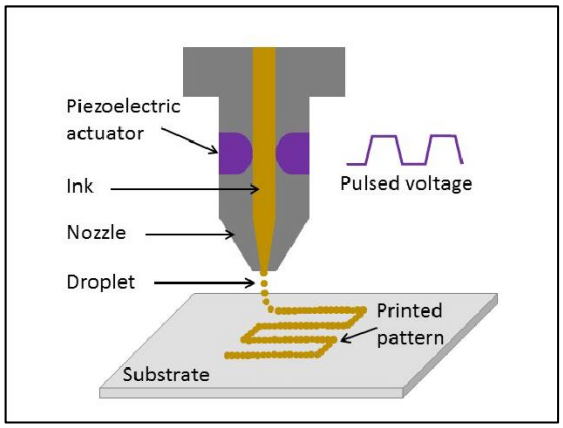

Figure 1.6 Schematic of DOD inkjet printing systems [87].

DOD is one of the most promising technologies in inkjet, due to its potential for printing conductive lines on the substrate in one step, thereby reducing waste in production, and time and space requirements [38]. As it is considered to be a simple methodology, cheap and eco-friendly, it is the most appropriate and effective process for the fabrication of various conductive tracks on flexible substrates. Furthermore, this technique allows flexible electronics to be made with roll-to-roll processing [77,88,89,90].

1.6.1 Droplet ejection and flight

Droplet ejection involves the production and separation of the droplet from the nozzle. Droplets are generated when an electrical current is applied to a piezoelectric element inside the ink reservoir. To form a droplet, a sudden change in volume raised by the flexing element creates a transient pressure wave that travels along the capillary to the nozzle, where the flow is pushed outward from the nozzle forming a droplet. The droplet breaks away from the nozzle plate when the kinetic energy transported by the pressure wave exceeds the surface tension that keeps it attached to the nozzle. The velocity of the droplet is defined by the amount of kinetic energy imparted. It should be more than multiple metres per second between 1 and 30 ms^{-1} to get over the drag caused by air [86,91]. An overly high velocity causes splashing of the droplet upon impact with the substrate, but low velocity allows the droplet to be decelerated by air drag before it contacts the surface [91].

The effectiveness of the droplet ejection process is characterised by many parameters, including droplet velocity, consistency, shape and volume. These

parameters are influenced by other factors such as fluid properties, nozzle geometry and waveform design [91,92,93,94,95,96,97]. On the other hand, the size, shape and volume of the ejected droplets are controlled by nozzle size, fluid surface tension and viscosity [91].

The viscosity of the fluid affects the operational jetting frequency and printing speed. For highly viscous ink, the reservoir filling rate is reduced and so therefore is the jetting frequency. However, if the viscosity of the ink is too low, high-frequency jetting occurs, causing unstable droplet ejection [98]. There are other factors that may affect the viscosity of the ink at the nozzle. Viscosity can increase when the nozzle is idle due to evaporation of volatile components in the ink. This can be avoided by regular cleaning and capping the nozzle head when not in use [91].

Smaller diameter nozzles make droplets with lower volumes. As droplets get smaller, the energy needed for them to break away from the nozzle increases as a result of increased inertial and capillary forces. They also decelerate quicker, so that the distance between the print head and substrate has to be reduced. These small droplets are optimal for applications that need high resolution and small dimensions. In contrast, larger droplets help in printing speed for large-area applications. The printhead geometry can be a reason for poor print quality by controlling the waveform design that affects the formed droplet. The incorrect waveform design causes multiple undesirable phenomena like puddle formation on the nozzle plate. The optimal design leads to the production of droplets with a diameter less than the print head orifice [91].

The path of the droplets should be perpendicular to the substrate for accurate and reproducible droplet positioning and should be one-tenth of the line width. The distance between the substrate and the nozzle is the throw distance. A long throw distance leads to inaccurate droplet placement due to air currents [91].

The droplet should be almost spherical in shape. Sometimes the droplet ejection condition may affect the droplet formation by forming a long-tail droplet. This tail could collapse back to the main droplet, or it may break forming a stream of smaller droplets and the unwanted phenomenon called "satellite droplets". This phenomenon will be discussed later in section 1.6.4 [91].

1.6.2 Droplet impact and spreading

Droplet deposition happens in two stages. In the beginning the droplet impact driven stage of less than 1 ms^{-1} duration due to the kinetic energy is partially dissipated by viscous forces. The rest of this energy is transformed into surface energy that spreads the droplet to a diameter defined by the relative surface energy between ink and the substrate in the second step of the deposition process. If the initial kinetic energy of the droplet is high, then the droplet could overshoot the desired diameter, causing the diameter to oscillate until the energy is dissipated, at which point it stabilises [91].

The print head velocity and the diameter, pitch and contact angle of the droplet are essential parameters in ensuring good coalescence of the droplets. When the droplet pitch is larger than the diameter of the droplets on the substrate, a train of separate, isolated droplets will be formed (Figure 1.7a). When the droplet pitch is decreased the droplets start to overlap and coalesce, forming a scalloped line (Figure 1.7b). With decreasing droplet pitch, the edges of the line become smoother, and the width of the line becomes more uniform (Figure 1.7c). Figure 1.7d shows a bead of ink with a circular cross-section, formed by a train of droplets coalescing [99].

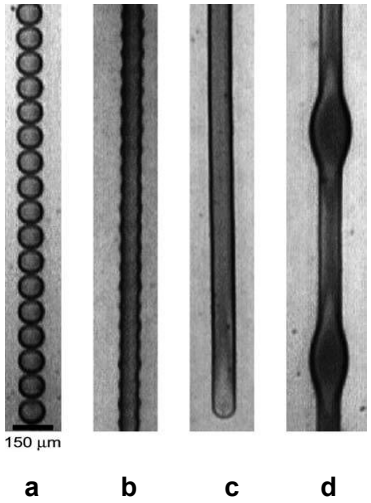

Figure 1.7 Examples of printed line morphologies [99].

1.6.3 Solidification

Solid deposition happens due to the phase change of the ink from a liquid to a solid phase by two mechanisms (solidification or evaporation). The type of the ink and the deposition process will determine which mechanism will take

place. If the deposition process is an impact-driven process solidification will happen. Otherwise, if the deposition process is surface energy dominated, an evaporation mechanism occurs [91,100].

Solidification of the droplet always happens alongside a significant reduction in volume especially when solidification occurs due to solvent evaporation. That solvent evaporation can affect the solidified process of the droplet depending on the solute distribution. For instance, when the edge of evaporated droplets has a higher solute concentration with lower concentrations elsewhere in the droplet, that is called a "coffee ring" and commonly happens with nanoparticle inks [91,101]. More details will be illustrated in section 1.6.5.

1.6.4 Satellite droplets

At all stages of printing, the formation of satellite drops is a constraint on the morphology of the printed line. This needs to be controlled for the sake of resolution and accuracy. The droplet shape should be nearly spherical, but following separation from the nozzle, the velocity of the droplet varies, resulting in the formation of a long tail behind the drop. This tail may either collapse back into the body of the main droplet or separate and break up into a stream of smaller droplets. The tail grows when the speed of the droplet is greater than the speed of the tail and the viscosity of the ink is high. As the difference in speeds increases, the tail breaks down into smaller, satellite droplets (Figure1.8) [78,91].

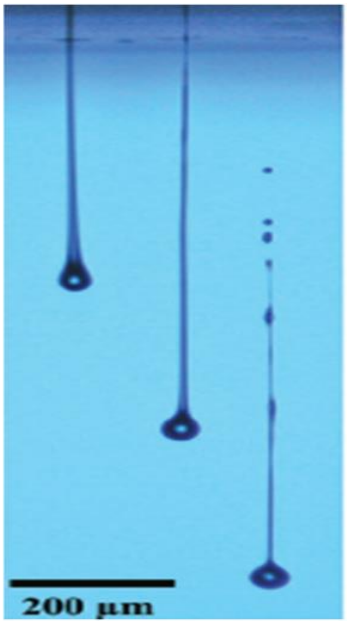

Figure 1.8 Satellite drop formation during printing [102].

A highly viscous ink displays a long, symmetrical tail shape. Tail length and symmetry decrease with decreasing viscosity. Viscosity is a parameter that has the power to influence the shape of the tail that is formed during printing [78]. Satellite droplets are a challenge to overcome in the droplet ejection and flight stage of printing. They are unwanted and can cause poor-quality phenomena including blurring of line edges and extraneous spotting [91].

1.6.5 Coffee ring formation and effect

A coffee ring is formed when the solvent in the ink evaporates after a droplet is deposited on a substrate, when most of the particles will gather at the periphery of the droplet during the drying process. This happens as the contact line of the drop is pinned on the substrate due to physical roughness or chemical heterogeneities, the evaporation produces a solvent capillary flow from the centre of the droplet to the contact line of the droplet, causing the suspended particles to accumulate at the periphery, resulting in the coffee ring effect (Figure 1.9). [78,103,104].

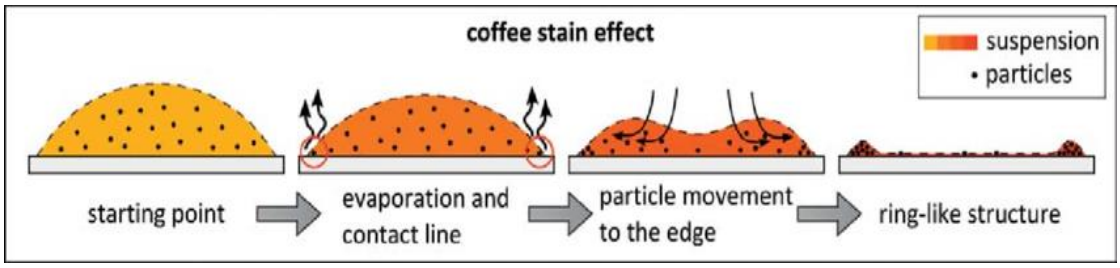

Figure 1.9 Schematic process of the coffee ring effect [105].

The coffee ring effect can be controlled by understanding the concentration, size and shape of solute particles. A higher concentration of suspended particles creates a wider ring, while the size of the particles affects the shape of the ring edge as smaller particles are transported to the outer edge of the ring with respect to the larger particles [103]. Typically, the coffee ring effect happen when the size of the drop is larger than the threshold limit . While the threshold diameter depends on the particles concentration, size and relative humidity of the environment of evaporation. At a higher humidity with constant concentration, the threshold diameter is lower, and a higher concentration results in a lower threshold diameter too [78]. Experimentally Shen X. *et al.*, [106] found that the coffee ring effect happens when the size of the drop is larger than the threshold limit.

For most manufacturing applications, the coffee ring effect is an unfavourable phenomenon that needs to be overcome, as it affects the electrical conductivity on the track on the substrate after the ink has dried. The lower concentration of particles in the middle of the track and the accumulation of particles at the edge lower the conductivity of the printed track [107].

Overcoming the coffee ring effect is very important for printing technology, as it is not easy to control the capillary flow of the suspended particles, because the evaporation of drops is non-linear and complex. One of the ways to stop the coffee ring effect is by controlling the surface tension of the solvents in the ink, a technique known as Marangoni flow. As a result, particles flow from areas of lower surface tension to those of higher surface tension within the droplet [99 ,108]. The surface tension is determined by the chemical composition of the liquid and the temperature or by the surfactant in the solvent [109]. There is a

temperature gradient across the droplet during evaporation, which promotes a corresponding surface tension gradient, resulting in the Marangoni effect [78].

1.7 Conductive inks

A major challenge in using inkjet for metallization is the formulation of suitable inks. Ink composition is crucial since it defines how the ink can be jetted. Typically, the inks should include the appropriate metal precursors and a carrier vehicle. The content of that metal precursor in the ink needs to be modified to obtain the resolution with the required electric properties for the printed film [110, 111].

Reactive inks allow different materials to be formed or removed selectively in inkjet printing techniques. They also provide an alternative means of metallising a surface by utilising inkjet printing with the deposition of two inks. They have been used effectively to fabricate silver/silver chloride electrodes [91,111].

Conductive inks include various active components: colloidal suspensions of NPs, conductive polymers or organometallic compounds in solution [111]. Whatever the conductive materials or solvent used, these inks frequently have other components as well, such as surfactants, dispersants, adhesion promoters, thickeners, stabilising agents and other additives depending on the particular application.

Out of these options, metal NPs are considered the best because of their high conductivity. There are many procedures for the preparation of inks based on monodisperse metal NPs, including electrochemical reduction, chemical reduction and microwave-assisted reduction. Of these, chemical reduction is most appropriate for several reasons, such as its simplicity, suitability for large-quantity production and cost-effectiveness [38].

1.7.1 Nanoparticle ink

There is interest in inks that contain dispersed nano-sized metal particles for creating electronic circuits and displays due to the small size of the metal particles, chemical stability and consistency. The printed circuit can be sintered at low temperatures to achieve low resistivity [112] and an appropriate print pitch can be obtained very easily.

Nano-sized metal particle ink has been used widely in different applications, such as catalysis and photonics, because nanoparticles can be produced in large quantities, dispersed in high concentration and show desired electrical conductivities. In particular, silver nanoparticles are the most used in the electronics field as thick film conductors in integrated circuits due to their low resistivity [91,112]. It is important to create appropriate inks from a suspension of nanoparticles in water or an organic solvent like ethylene glycol, toluene or cyclohexanone. The solvent should evaporate once it deposits but not so fast that it dries out at the nozzle when not in use for a short time and causes blockages [91].

The content of the nanoparticle in the ink itself should be appropriate, otherwise, some quality problems would arise because of the non-reproducibility of the ink batch performance. As reported by Lai Ch. *et al.* [31] some batches of inks may contain too much silver nanoparticle content and that increases the ink viscosity and increases the chance of blocking the nozzle head. Nevertheless, if the nanoparticles are insufficient and the ink becomes liquid, an inadequate printed track thickness will be obtained, and an electrical conductivity decrease may result. Therefore, maintaining the consistency of the nanoparticle ink quality is needed.

The high surface area to volume ratio of these nanoparticles allows sintering at lower temperatures than with the bulk material. For instance, gold NPs with a diameter of about 5 nm melt at 300-500 °C, whereas in its normal state gold melts at 1063 °C [91]. Likewise, particles with a diameter less than 100 nm are most likely to offer a notable reduction in melting temperature, to around 300 °C [113]. That makes them suitable for use in printed electronics, although even this temperature is beyond the stability of most plastic substrates.

On the other hand, NP ink is more likely to agglomerate the suspended particles, which causes increased viscosity, leading to clogging of the nozzle head. To avoid this phenomenon, coating the NPs with polymer or other capping agent to ensure its stability and dispersion is necessary. However, removing these capping agents is a challenge. It could be done by applying a high sintering temperature (“burning them off”), but this makes them inappropriate to use with flexible substrates, which cannot withstand the required temperatures. There is another possibility to remove them at a lower temperature by using a microwave

flash or a photonic sintering step together with thermal sintering [91], where the heating would be highly localised. In our study, we have managed to “remove them” (actually reposition them) at room temperature and that will be discussed later in detail.

Among the materials that have received attention for NP-based inks are gold [114], silver [12], copper [115], and nickel [12]. However, inks containing silver or gold NPs have attracted broad interest for their excellent properties: high conductivity, low chemical reactivity, high chemical stability and oxidation resistance [72]. Copper and nickel inks have been used, but their tendency to oxidise can impact the lifetime of the ink, necessitating the use of additional specialised coating layers or printing in inert atmospheres to minimise this risk [116].

1.7.2 Organometallic ink

Organometallic inks can be reduced to metallic species either optically or thermally. The advantage of these inks is that they are in the form of a solution, which removes the danger of particle agglomeration and nozzle blocking. Compared to NP inks, organometallic inks have higher conductivity [91].

It was demonstrated in a previous study [91] that the conductivity of silver inks after sintering at a temperature of 150 °C is only 11 to 53 per cent of that of the conventional metal, but organometallic ink can be sintered and reduced at a lower temperature. Silver is one of the commonest organometallic inks produced because it is able to form a wide range of compounds soluble in organic solvents. As shown by Smith P. *et al.* [117] using silver-containing organometallic ink printed by inkjet printer onto a different substrate, the printed tracks showed resistivity about 2 times bulk silver after being thermally treated at 150 °C. Other metals which can be used include copper, gold, aluminium [50], nickel [117] and platinum [91].

1.7.3 Conductive polymer

Many conductive polymers have been used with inkjet printing, like polypyrrole, polythiophenes such as poly(3,4-ethylenedioxythiophene) and polyaniline. A common characteristic of these polymers is the existence of a conjugated pi-electron system along the polymer, which gives them their conductive properties [91]. These polymers were used in many fields including

sensing applications [74], electrochemical displays [118], batteries [119], platforms for tissue engineering [120] and fuel cells [121]. Their use in sensing applications can be attributed to their inherent features wherein the electronic and/or electrochemical properties of the conducting polymers can react to specific species or properties of the environment [74].

These polymers have lower conductivities compared with metallic inks, high reactivity with oxygen, and susceptibility to humidity. Therefore, inert atmospheres for the printing process are an essential requirement in this case [122].

1.7.4 Other types of conductive ink

Graphene oxide has been used for inks as it is easily dispersed in water. The high electrical conductivity of graphene can be retrieved by thermal or chemical reduction [123]. The reduction of graphene oxide to graphene only makes a difference in the surface layer of graphene oxide [124]. Thermal reduction of graphene oxide can be more efficient than chemical reduction, but it needs a high temperature, preventing its use for flexible substrates [125]. The printed film using graphene oxide has unique properties by forming a polycrystalline film using the individual graphene oxide flakes that were previously in suspension. Consequently, it has been widely used in solution processing-based applications, for example, chemical and biological sensors [126] and transparent conductors [126].

Carbon nanotubes have been used as a conductive material and are considered a good alternative to copper for future interconnects because of their tolerance of higher current density and thermal conductivity [91]. The challenging problem with using this kind of material for inkjet printing or any solution-based processing technique is that the nanotubes have a tendency to stick together and make large bundles because of their high aspect ratios, making them susceptible to large van der Waals forces [127].

1.7.5 Properties of inks

In the field of electronic applications, inkjet printing is identified as an advanced economical type of device for industrialized usage, as it uses small, adjustable drops of fluid on a substrate to obtain higher quality and is reproducible. Consequently, the ink should be formulated to achieve the

requirements of specific fluid dynamics and parameters controlling the droplet formation for inkjet printing.

Understanding the fluid properties of ink, the medium carrier, adhesion promoter and dispersing agent used for ink formulation are essential factors for the realisation of droplet formation, shape, size, as well as determining the effect of wetting ink on the substrate after ejection and the presence of satellite droplets [31,84].

The most important aspect for selecting an ink is the physical properties, such as viscosity, surface tension and density of its liquid phase, which certainly influence the performance of the conductive ink. Viscosity is responsible for drop formation, especially the separation and corresponding tail. Meanwhile, surface tension creates the spherical shape of the liquid droplets emerging from a nozzle. To use a wide variety of fluids successfully in jets, viscosity should be in the range of 8-15 cP, surface tension should be between 25 and 50 $mN \cdot m^{-1}$, and typical fluids used for inkjet printing have a density close to 1000 kg m^{-3} [84,91].

The viscosity of the ink affects the operational jetting frequency and the printing speed. The reservoir filling rate is reduced when the viscosity is high, which decreases the jetting frequency. Relatively low viscosity, along with high resistance to precipitation and excellent dispersion of metal particles in the ink, is a primary characteristic that is needed to obtain printable fluid and guarantee its performance, as the low viscosity allows the expulsion of a droplet from the nozzle by the transient pressure pulse. However, because the NPs tend to cluster and agglomerate, viscosity increases with storage [84]. Consequently, it is important to keep measuring the viscosity during storage, to maintain performance and to understand the dynamics of agglomeration. In addition, the surface tension should be high enough to prohibit unwanted dripping from the nozzle, but low enough to ensure the ejected droplet can break away from the nozzle [91].

1.8 Substrates for additive printing

To date, many substrates have been used in printing electronic, such as polymeric material, glass, plastic packages, thin silicon chips and paper. However, there are many problems with printing electrical circuits on the above-

mentioned substrates by distributing nano-structured metals, because it requires a relatively high temperature (above approximately 200 °C) in a sintering process to fuse the metal particles together and achieve high conductivity. Therefore, there is still a need for development in nanomaterial printing, because such substrates as plastic and paper cannot tolerate the high temperature. Fortunately, these problems can be settled by a special sintering method, that the sintering process could be carried out at room temperature and effectively avoid these limitations as it will be discussed later in this work Chapter 2 (section 2.9.2) [38].

Herein, photo paper was used the most in this study due to its low cost and its was known to allow spontaneous room temperature sintering of silver inks from previous work in the group and other published work. Fortunately, these temperature problems were overcome by carrying out the sintering process at room temperature.

1.8.1 Interaction of droplets with the substrate

After depositing ink on the substrate, solidification of the droplet occurs. Evaporation of solvent, cooling through the transition temperature and chemical reaction are all complex multi-step processes that may happen depending on the properties of the liquid as well as the substrates, following the droplet ejection from the nozzle [78].

When the droplet contacts the substrate, the distortion of the droplet starts due to the effect of kinetic energy, and then the spreading of the droplet happens to reach equilibrium in a few seconds. Some of the kinetic energy is absorbed by the ink viscous dissipation. In contrast, if splashing is not found at the time of impact, the drop may recoil followed by expansion and oscillate for dissipating energy. When the droplet is in the equilibrium point, the higher surface tension value dominates over the smaller value of the fluid bond and the spherical structure formed [78].

1.9 Sintering

In the production of the electronic circuit, sintering is a key step in the fabrication of conductive tracks as it boosts grain growth, formation and coalescence within printed metal features. It requires eliminating the dispersing

agents to make contact between neighbouring particles to form a sintered neck. Consequently, electrical conductivity and mechanical adhesion are improved. Sintering is mostly carried out by increasing temperature to obtain fully fused NPs conductive path. However, in industrial and commercial concepts, it is advisable to use low temperatures for better results [91,128,129]. Below will be explained different sintering methods in detail:

1.9.1 Thermal sintering

Thermal oven sintering involves long sintering times. Typically, the printed track is treated for 30-60 minutes at a high temperature of 150-260 °C [91,130]. This limits the use of low-cost flexible substrates like most plastics, and any other substrates that cannot endure the high temperature [84,128].

Thermal sintering requires the entire substrate to be heated and that could lead to warping/rippling and/or shrinking of some substrates. Cracks may also occur in the printed line because of the large reduction in volume during sintering [126,131,132]. There are many sintering methods that have been developed to handle this issue, for example, laser radiation, microwave [128], argon plasma [134], flash-light and electrical sintering [135].

1.9.2 Microwave sintering

Microwave heating is like thermal sintering in an oven except it uses microwaves as the heat source. It is a rapid sintering method, using microwave radiation while reducing the sintering time to about 2 min [85]. However, the process is limited by the temperature of the reactor vessel in the microwave reaching 200 °C during the sintering and the penetration depth of about 2 µm (at 2.54 GHz), which limits the thickness of the film that can be sintered successfully [91,130].

1.9.3 Photonic sintering

Using flash lamps, lasers or other light sources for sintering is known as photonic sintering [133,136]. This technique can target the conductive tracks and sinters without destroying the substrate. It works when the printed material absorbs light, and that causes heating through the dissipation of non-radiative energy and exothermic photochemical reaction. This heat is restricted inside the NPs and transferred to the next particles causing rapid heating within the film. As

a result, the solvent is evaporated, and the particles are sintered [91]. The short sintering time by emitting millisecond high-intensity pulses reduces the problems of oxidation of metal NPs in air and exposure of the plastic substrate to heat. Thus, flash lamp sintering is perfect for large areas on a wide selection of substrates [133].

Gu X. *et al.* [130] have developed and studied the sintering method by using camera flash sintering.This simple, fast sintering method was successfully used to sinter inkjet-printed silver nanoparticle tracks on a polymer substrate at room temperature. The obtained resistivity was low about $8.4x10^{-8}$ Ωm and that was five times the RBS. Kang J. *et al.* [137] used intense pulsed light to sinter a conductive silver pattern and the resistivity was three times higher than that of bulk silver, which is enough to be used for electronic device printing.

Compared with thermal sintering, photonic sintering is preferable due to the reduced sintering time and the smaller affected zone affected by heat, which can minimise damage to low-temperature substrates [91,138]. However, laser sintering is better used for a small area, due to the spot size in most cases between 20 and 40 µm and the scan speed can be as low as 0.2 $mm \cdot s^{-1}$ [91].

1.9.4 Electrical sintering

Electrical sintering is the use of Joule heating to sinter the printed NP film [139]. A voltage applied across the NP film causes a current through the film which generates heat. This technique has many advantages, it needs less time for sintering, less than one minute, based on the geometry of the printed feature. It also minimises the damage to the substrate because of the area-specific heating and the ability to observe progress during the sintering process [91]. However, electrical sintering is a less useful production method. It requires contact with the printed film, which is not perfect for some applications. It is also limited to use in small areas and with narrow features such as interconnectors as a result of its localised action [140]. From the above, it is clearly necessary to develop a technique for sintering ink-jet printed tracks, based on metal NPs, that is low cost, has a low sintering temperature and high production potential [130].

All the techniques presented above require costly equipment, complex procedures and require considerable experimentation. Therefore, the development of chemical sintering at low temperature (ideally <100 °C) is a

potential solution. It has even been demonstrated that it is possible to achieve chemical sintering of NPs at room temperature and avoid these limitations [135]. Fortunately, there are two keys approaches that can be applied to solve the problems: use of a sintering agent, which could be a simple electrolyte like NaOH, HCl, NaCl or $MgCl_2$, or protection of the metallic NPs before use with a suitable stabilising agent [38].

As an illustration of this chemical sintering, a halide can detach the anchoring groups of stabilisers attached to the NPs to enable the particles to accumulate and eventually become connected, allowing them to be sintered. Several strategies have been used to introduce the sintering agents, in particular, dipping and dual printing. However, these methods are limited in their use since they can only be used to create 2D patterns on the substrate, which makes them much less applicable in those cutting-edge applications which usually require 3D geometry [135]. Wakuda and co-workers [141] treated the Ag NPs sintered at room temperature with dodecyl amine as a dispersant by dipping the film into a methanol bath, but the resistance of the product was very high. Magdassi S. *et al.* [142] triggered the room temperature sintering of Ag NPs stabilized by PAA with poly (diallyldimethylammonium chloride). That led to a spontaneous coalescence process of the NPs and a highly conductive film was obtained. Grouchko M. *et al.* [143] found that chloride ions detached the anchoring groups of the stabilizing agent PAA from the Ag NPs surface and that caused their coalescence and film sintering. The obtained conductive film showed 41% of the conductivity of bulk silver by a single printing step and room temperature sintering.

We are currently using a similar but more desirable strategy, which employs a surface coating or post-printing coating, to ensure the sintering process for the printed tracks afterward. Herein, the sintering of Ag NPs at room temperature has been achieved on various substrates, a successful substitute for conventional technology. On this basis, we have found that PAA/ or PVP were competent to stabilize Ag NPs by adsorbing on their surface and could be facilely detached by Cl^-, which leads to a spontaneous coalescence between particles to realize sintering. Typically, this sintering mechanism depends on two spontaneous behaviours of Ag NPs after they have been destabilized: coalescence and Ostwald ripening are driven by the surface-to-volume energy of

the very small nanoparticles [144,145]. As a result, we envision that this sintering at room temperature could serve as an adaptive method for the sintering of AgNP conductive patterns on different substrates at room temperature and promote the manufacture of printed electronics.

1.10 Characterisation of printed tracks

The printed conductive ink forms a conductive track after drying through solvent evaporation, achieved by performing an appropriate sintering process for heating and decomposing the organic insulating material, until it possesses enough interconnected conductive pathways and has fused to form the dense structure that shows electrically conductive properties. Once this track is created, it needs to be characterised to understand its bulk dimensions, micro/nanostructure and electrical properties. This then allows key material properties such as resistivity to be calculated and compared with reference values, such as the resistivity of the bulk metal. A variety of different analytical tools are needed to achieve this.

Optical microscopy images were captured from the printed tracks using a microscope with CCD camera. The direct imaging offers more accurate measurements of the physical dimensions of the ink pattern, which are required to calculate its resistivity. The resistivity of the sample printed pattern was calculated by using the equation (1.1) below, where ρ is resistivity, L is the length of the printing trace from end to end, A is the cross-sectional area of the ink and R is the electrical resistance which is obtained usually from a Digital Multimeter:

$$\rho = \frac{\mathrm{RA}}{\mathrm{L}} \qquad (1.1)$$

The cross-sectional area (A) is calculated by multiplying the width (w) of the printing pattern by the thickness (h), which is measured using a Profiler (equation 1.2):

$$\mathrm{A} = \mathrm{h} \cdot \mathrm{W} \qquad (1.2)$$

The profilometer measures the physical dimension (width and thickness) of the silver track on different substrates, based on the deflections of a diamond stylus tip and is evaluated by Vision 64 analysis software. It takes

electromechanical measurements by moving the diamond stylus vertically over the printed pattern surface.

Resistivity is a measure of how strongly a printed track opposes the flow of electric current in resistors or conductors with a uniform cross-section, where current flows uniformly. As a reciprocal quantity, conductivity is a fundamental property to measure of how easy a material permits the flow of electric current.

This are calculated by (equation 1.3 [145]):

$$\rho = \frac{1}{\sigma} \qquad (1.3)$$

Where σ = conductivity and ρ= resistivity

1.11 Applications for inkjet printing of conductive materials

Inkjet printing of conductive materials has been used in a great number of applications, ranging from the manufacture of display backplanes [82,147], electronic packaging [148], bendable devices [149], sensors [7], supercapacitors [13], printed circuits [112], thin-film transistors [81] and solar cells [11,78,130,150]. Recently, it has made noticeable progress in printed biological and pharmaceutical devices and their applications [73,129]. The use of inkjet printing offers the great advances in such fields, which is still in its infancy, and there is still considerable scope for use of this technology in other advanced applications. It is considered the most promising technique for emerging new technology in these areas [90].

1.12 The aim of this study

As the above literature summary demonstrates, there are many different methods for obtaining Ag NP colloids. Our work has focused on the scalable synthesis and coating of NPs with a polymer stabiliser layer to obtain a stable and concentrated dispersion of Ag NPs. Aqueous chemical, non-aqueous chemical, galvanic displacement and hot injection methods were used for the synthesis of colloidal silver NPs and also dual-metal particles with altered material composition or geometry. The particles produced were used in the fabrication of conductive inks.

This study aims to develop nano-inks for novel printing approaches, to be able to print small-scale conductive features and patterns that can be sintered at low temperatures and are suitable for printed electronics, sensors, device materials, etc in large scale commercial use. The success (or otherwise) of various formulated inks was tested by inkjet printing of model structures and detailed characterisation of the physical and electrical properties of them. Most of the printed structures were sintered at low temperature using Cl^- ion induced processes, though alternative strategies were adopted where necessary. An effective strategy was developed to transfer the successful Cl^- ion sintering approach from photo-paper to more useful flexible and thermo-resistant plastic substrates. The properties, including flexing and thermal behaviour, were explored using a range of strategies.

References

(1) Melillo, J. M.; Bowles, F. P.; Melillo, J. M.; Steudler, P. A.; Rayment, M.; Trumbore, S. E.; Amundson, R.; Bergh, J.; Linder, S.; Lundmark, T.; Elfving, B.; Jarvis, P.; Linder, S.; Harte, J.; Luo, Y.; Wan, S.; Hui, S.; Wallace, L.; Merriam, J.; Mcdowell, W. H.; Currie, W. S. Shape-Controlled Synthesis of Gold and Silver Nanoparticles. *Science*. **2002**, *298 (13),* 2176–2180.

(2) Toshlma, N.; Yonezawa, T.; Kushihashi, K. Polymer-Protected Palladium-Platinum Bimetallic Clusters : Preparation , Catalytic Properties and Structural Considerations. *J. CHEM. SOC. FARADAY TRANS.* **1993**, *89 (14),* 2537–2543.

(3) Liz-marzn, L. M.; Philipse, A. P. Stable Hydrosols of Metallic and Bimetallic Nanoparticles Immobilized Imogolite Fibers. *J. phys. Chem.* **1995**, *99 (15),* 15120–15128.

(4) Wang, H.; Qiao, X.; Chen, J.; Wang, X.; Ding, S. Mechanisms of PVP in the Preparation of Silver Nanoparticles. *Materials Chemistry and Physics.* **2005**, *94 (10),* 449–453.

(5) Jr, D. D. E.; Chumanov, G. Synthesis and Optical Properties of Silver Nanoparticles and Arrays. *Chem. Phys. Chem.* **2005**, *6 (2)* , 1221–1231.

(6) Murphy, C. J.; Sau, T. K.; Gole, A. M.; Orendorff, C. J.; Gao, J.; Gou, L.; Hunyadi, S. E.; Li, T.; April, R. V; Final, I.; May, F. Anisotropic Metal Nanoparticles : Synthesis , Assembly , and Optical Applications. *J. Phys. Chem.* **2005**, *109 (6),* 13857–13870.

(7) Yeung, K. L.; Gavriilidis, A.; Varma, A.; Bhasin, M. M. Effects of 1, 2 Dichloroethane Addition on the Optimal Silver Catalyst Distribution in Pellets for Epoxidation of Ethylene. *Journal of Catalysis.* **1998**, *174 (3),* 1–12.

(8) Hu, L.; Hecht, D. S.; Gru, G. Percolation in Transparent and Conducting Carbon Nanotube Networks. *NANO LETTERS*. **2004**, *4 (12),* 2513-2517.

(9) Tolaymat, T. M.; El Badawy, A. M.; Genaidy, A.; Scheckel, K. G.; Luxton, T. P.; Suidan, M. An Evidence-Based Environmental Perspective of Manufactured Silver Nanoparticle in Syntheses and Applications: A Systematic Review and Critical Appraisal of Peer-Reviewed Scientific Papers. *Sci. Total Environ.* **2010**, *408 (5),* 999–1006.

(10) Li, Y.; Wu, Y.; Ong, S. Facile Synthesis of Silver Nanoparticles Useful for Fabrication of High-Conductivity Elements for Printed Electronics. *J. AM. CHEM. SOC.* **2005**, *127 (2),* 3266–3267.

(11) Madaria, A. R.; Kumar, A.; Zhou, C. Large Scale, Highly Conductive and Patterned Transparent Films of Silver Nanowires on Arbitrary Substrates and. *Nanotechnology.* **2011**, *22 (7),* 0957-4484.

(12) Teerasong, S.; Jinnarak, A.; Chaneam, S.; Wilairat, P. Talanta Poly (Vinyl Alcohol) Capped Silver Nanoparticles for Antioxidant Assay Based on Seed-Mediated Nanoparticle Growth. *Talanta.* **2017**, *170 (3),* 193–198.

(13) Polte, J. Fundamental Growth Principles of Colloidal Metal Nanoparticles – a New Perspective. *CrystEngComm.* **2015**, *17 (22),* 6809–6830.

(14) El, A. M.; Scheckel, K. G.; Suidan, M.; Tolaymat, T. Science of the Total Environment The Impact of Stabilization Mechanism on the Aggregation Kinetics of Silver Nanoparticles. *Sci. Total Environ.* **2012**, *429 (15),* 325–331.

(15) Ghosh, S.; Mashayekhi, H.; Bhowmik, P.; Xing, B. Colloidal Stability of Al_2O_3 Nanoparticles as Affected by Coating of Structurally Different Humic Acids. *Langmuir.* **2010**, *26 (2),* 873–879.

(16) Tuaev, X.; Wuithschick, M.; Fischer, A.; Thuenemann, A. F.; Rademann, K.; Kraehnert, R.; Emmerling, F. Formation Mechanism of Colloidal Silver Nanoparticles : Analogies and Differences to the Growth of Gold Nanoparticles. *Acs NANO*. **2012**, *6 (7),* 5791–5802.

(17) Ahner, T. T.; Delissen, F.; Sokolov, S. Mechanism of Gold Nanoparticle Formation in the Classical Citrate Synthesis Method Derived from Coupled In Situ XANES and SAXS Evaluation. *J. AM. CHEM. SOC*. **2010**, *132 (9),* 1296–1301.

(18) Wuithschick, M.; Witte, S.; Kettemann, F.; Rademann, K.; Polte, J. Illustrating the Formation of Metal Nanoparticles with a Growth Concept Based on Colloidal Stability. *Phys. Chem. Chem. Phys.* **2015**, *17 (8),* 19895–19900.

(19) Schmidt, W.; Bussian, P.; Linde, M. Accessing Ultrashort Reaction Times in Particle Formation with SAXS Experiments : ZnS Precipitation on the Microsecond Time Scale. *J. AM. CHEM. SOC.* **2010**, *132 (4),* 6822–6826.

(20) Esumi, K.; Tano, T.; Torigoe, K.; Meguro, K. Preparation and Characterization of Bimetallic Pd-Cu Colloids by Thermal Decomposition of Their Acetate Compounds in Organic Solvents. *Chem. Mater.* **1990**, *2 (5),* 564–567.

(21) Milardović, S.; Ivaniševic, I.; Rogina, A.; Kassal, P. Synthesis and Electrochemical Characterization of AgNP Ink Suitable for Inkjet Printing. *Int. J. Electrochem. Sci.* **2018**, *13 (11),* 11136–11149.

(22) Smetana, A. B.; Klabunde, K. J.; Sorensen, C. M. Synthesis of Spherical Silver Nanoparticles by Digestive Ripening , Stabilization with Various Agents, and Their 3-D and 2-D Superlattice Formation. *Colloid and Interface Science.* **2005**, *284 (20),* 521–526.

(23) Zhou, G.; Wang, W. Synthesis of Silver Nanoparticles and Their Antiproliferation against Human Lung Cancer Cells In Vitro. *Orient. J. Chem*. **2012**, *28 (2),* 651-655.

(24) Hyning, D. L. Van; Zukoski, C. F. Formation Mechanisms and Aggregation Behavior of Borohydride Reduced Silver Particles*. Langmuir.* **1998**, *14 (4),* 7034–7046.

(25) Guo, L.; Nie, J.; Du, B.; Peng, Z.; Tesche, B. Thermoresponsive Polymer-Stabilized Silver Nanoparticles. *Colloid and Interface Chemistry.* **2008**, *319 (19)*, 175–181.

(26) Lin, J.; Hsueh, Y.; Huang, J. The Concentration Effect of Capping Agent for Synthesis of Silver Nanowire by Using the Polyol Method. *J. Solid State Chem.* **2014**, *214 (27)* , 2–6.

(27) Gohsh, D.; Dasgupta, S. Synthesis of Submicron Silver Powder by the Hydrometallurgical Reduction of Silver Nitrate with Hydrazine Hydrate and a Thermodynamic Analysis of the System. *Metallurgical and Materials Transactions.* **2008**, *39 (5)*, 35-45.

(28) Steinigeweg, D.; Schlu, S. Monodispersity and Size Control in the Synthesis of 20 – 100 Nm Quasi-Spherical Silver Nanoparticles by Citrate and Ascorbic Acid Reduction in Glycerol – Water Mixtures W. *ChemComm*. **2012**, *48 (11),* 8682–8684.

(29) Sun, Y.; Yin, Y.; Mayers, B. T.; Herricks, T.; Xia, Y. Uniform Silver Nanowires Synthesis by Reducing AgNO 3 with Ethylene Glycol in the Presence of Seeds and Poly (Vinyl Pyrrolidone). *Chem. Mater.* **2002**, *14 (6),* 4736–4745.

(30) Hasell, T.; Yang, J.; Wang, W.; Brown, P. D.; Howdle, S. M. A Facile Synthetic Route to Aqueous Dispersions of Silver Nanoparticles. *Materials Letter.* **2007**, *61 (21)*, 4906–4910.

(31) Lai, C. Y.; Cheong, C. F.; Mandeep, J. S.; Abdullah, H. B.; Amin, N.; Lai, K. W. Synthesis and Characterization of Silver Nanoparticles and Silver Inks : Review on the Past and Recent Technology Roadmaps. *Materials Engineering and Performance.* **2014**, *23* (10), 3541–3550.

(32) Chen, M; Feng, Y; Wang, X; Li, T; Zhang, J; Qian, D. Silver Nanoparticles Capped by Oleylamine: Formation, Growth, and Self-Organization. *Langmuir.* **2007**, *23 (3),* 5296–5304.

(33) Li, C.; Chang, S.; Su, F.; Lin, S.; Chou, Y. Effects of Capping Agents on the Dispersion of Silver Nanoparticles. *Colloids Surfaces A Physicochem. Eng. Asp.* **2013**, *419 (11)*, 209–215.

(34) Sun, Y; Xia, Y. Large-Scale Synthesis of Uniform Silver Nanowires Through a soft, self-seeding, polyol process. *Adv. Mater*. **2002**, *14 (11),* 833–837.

(35) Chou, K.; Chang, Y.; Chiu, L. Studies on the Continuous Precipitation of Silver Nanoparticles. *Ind. Eng. Chem. Res*. **2012**, *51 (3)*, 4905−4910

(36) Bose, S.; Chakraborty, S.; Sanyal, D. ScienceDirect Water-Ethylene Glycol Mediated Synthesis of Silver Nanoparticles for Conductive Ink. *Mater.* **2018**, *5* (3), 9941–9947.

(37) Wu, R. T.; Hsu, S. L. C. Preparation of Highly Concentrated and Stable Suspensions of Silver Nanoparticles by an Organic Base Catalyzed Reduction Reaction. *Mater. Res. Bull.* **2008**, *43* (5), 1276–1281.

(38) Tang, Y.; He, W.; Zhou, G.; Wang, S.; Yang, X. A New Approach Causing the Patterns Fabricated by Silver Nanoparticles to Be Conductive without Sintering. *Nanotechnology.* **2012**, *23 (3)*, 1-6

(39) Wang, Z.; Liang, X.; Zhao, T.; Hu, Y.; Zhu, P.; Sun, R. Facile Synthesis of Monodisperse Silver Nanoparticles for Screen Printing Conductive Inks. *J. Mater. Sci. Mater. Electron.* **2017**, *28* (22), 16939–16947.

(40) Alruqi, S. S.; Al-Thabaiti, S. A.; Malik, M. A.; Khan, Z. Role of Surfactants: One Step Facile Synthesis of Hetero Structured Ag-Ni Alloy by Seed Less Approach. *Colloids Surfaces A Physicochem. Eng. Asp.* **2018**, *540 (11*), 36–47.

(41) Shin, K.; Kim, H.; Mo, H. Catalytic Characteristics of AgCu Bimetallic Nanoparticles in the Oxygen Reduction Reaction. *Chem Cun Chem.* **2013**, *6*, 1044–1049.

(42) Tsuji, M.; Hikino, S.; Tanabe, R.; Sano, Y. Syntheses of Ag / Cu Alloy and Ag / Cu Alloy Core Cu Shell Nanoparticles Using a Polyol Method . *Cryst Eng Comm*. **2010**, *12 (5)*, 3900–3908.

(43) Pajor-Świerzy, A.; Pawłowski, R.; Warszyński, P.; Szczepanowicz, K. The Conductive Properties of Ink Coating Based on Ni–Ag Core–Shell Nanoparticles with the Bimodal Size Distribution. *J. Mater. Sci. Mater. Electron.* **2020**, *31* (15), 12991–12999.

(44) Kohman, G. T.; Hermance, H. W.; Downes, G. H. Silver Migration in Electrical Insulation. *Bell Syst. Tech. J.* **1955**, *34* (6), 1115–1147.

(45) Wang, S.; Gao, L.; Li, M.; Huang, D.; Qian, K.; Chiu, H. Electro-Migration of Silver Alloy Wire with Its Application on Bonding. *Conf. Electron. Packag. Technol. ICEPT.* **2013**, *978 (1)*, 789–793.

(46) Vu, K. Silver Migration–The Mechanism and Effects on Thick-Film Conductors. *Mater. Sci. Eng.* **2003**, *234,* 1–21.

(47) Bochicchio, D.; Ferrando, R. Structure and Thermal Stability of AgCu Chiral Nanoparticles. *Eur. Phys. J. D.* **2012**, *66 (115)*, 1-7

(48) Park, S.; Kim, H. Flash Light Sintering of Nickel Nanoparticles for Printed Electronics. *Thin Solid Films.* **2014**, *550 (11)*, 575–581.

(49) Lee, C. C.; Cheng, Y. Y.; Chang, H. Y.; Chen, D. H. Synthesis and Electromagnetic Wave Absorption Property of Ni-Ag Alloy Nanoparticles. *J. Alloys Compd.* **2009**, *480* (2), 674–680.

(50) Zulfiqar, S.; Zaidi, A.; Khan, U.; Ahmed, N. Heat Transfer Enhancement in H_2O Suspended by Aluminium Alloy Nanoparticles over a Convective Stretching Surface. *Advance in Mechanical Engineering.* **2020**, *12* (9), 1–11.

(51) Branco, A. J.; Dawes, S. S.; Mason, N. L.; Fonseca, M. V; Melissa, E.; Michael, B.; Branco, A. J.; Dawes, S. S.; Mason, N. L.; Guzman, M. V. F.; King, M. E.; Ross, M. B. Synthesis of Gold – Tin Alloy Nanoparticles with Tunable Plasmonic Properties. *STAR Protoc.* **2023**, *4 (3)*, 1-12.

(52) Chen, H.; Li, Z.; Wu, Z.; Zhang, Z. A Novel Route to Prepare and Characterize Sn – Bi Nanoparticles. *Journal of Alloy and Compoun*. **2005**, *394 (10)*, 282–285.

(53) Tan, S.; Zu, X.; Yi, G.; Liu, X. Synthesis of Highly Environmental Stable Copper–Silver Core–Shell Nanoparticles for Direct Writing Flexible Electronics. *J. Mater. Sci. Mater. Electron.* **2017**, *28 (21)*, 15899–15906.

(54) Kim, N. R.; Shin, K.; Jung, I.; Shim, M.; Lee, H. M. Ag − Cu Bimetallic Nanoparticles with Enhanced Resistance to Oxidation : A Combined Experimental and Theoretical Study. *J. Phys. Chem. C.* **2014**, *118 (10)*, 26324−26331.

(55) Magdassi, S.; Grouchko, M.; Kamyshny, A. Copper Nanoparticles for Printed Electronics: Routes Towards Achieving Oxidation Stability. *Materials.* **2010**, *3 (9)*, 4626–4638.

(56) Swierzy, A. P.-; Szczepanowicz, K.; Kamyshny, A.; Magdassi, S. Metallic Core-Shell Nanoparticles for Conductive Coatings and Printing. *Advance Colloid and Interface Science*. **2022**, *299 (11)*, 1-15

(57) Pajor-Świerzy, A.; Socha, P.; Pawlowski, R.; Warszynski, P.; Szczepanowicz, K. Application of Metallic Inks Based on Nickel-Silver Core – Shell Nanoparticles for Fabrication of Conductive Film. *Nanotechnology.* **2019**, *30 (2)*, (1-8).

(58) Jing, J. J.; Xie, J.; Chen, G. Y.; Li, W. H.; Zhang, M. M. Preparation of Nickel – Silver Core – Shell Nanoparticles by Liquid-Phase Reduction for Use in Conductive Paste. *J. Exp. Nanosci.* **2015**, *10* (17), 1347–1356.

(59) Vykoukal, V.; Bursik, J.; Roupcova, P.; Cullen, D. A.; Pinkas, J. Solvothermal Hot Injection Synthesis of Core-Shell AgNi Nanoparticles. *J. Alloys Compd.* **2019**, *770 (8)*, 377–385.

(60) Yuan, Y.; Xia, H.; Chen, Y.; Xie, D. One-Step Synthesis of Oxidation-Resistant Cu @ Ag Core – Shell Nanoparticles. *Micro and Nano Letters*. **2018**, *13 (6)*, 171–174.

(61) Chen, D.; Wang, S. Protective Agent-Free Synthesis of Ni – Ag Core – Shell Nanoparticles. *Materials Chemistry and Physics.* **2006**, *100 (1)*, 468–471.

(62) Tsuji, M. Synthesis of Ag @ Cu Core – Shell Nanoparticles in High Yield Using a Polyol Method. *Chem. Lett*. **2010**. *39 (12)*, 334-336.

(63) Bala, T.; Bhame, S. D.; Joy, P. A.; Prasad, B. L. V; Sastry, M. A Facile Liquid Foam Based Synthesis of Nickel Nanoparticles and Their Subsequent Conversion to Ni Core Ag Shell Particles : Structural Characterization and Investigation of Magnetic Properties. *J. Mater. Chem.* **2004**, *14 (8),* 2941–2945.

(64) Guo, H.; Chen, Y.; Chen, X.; Wen, R.; Yue, G.; Peng, D. Facile Synthesis of Near-Monodisperse Ag @ Ni Core – Shell Nanoparticles and Their Application for Catalytic Generation of Hydrogen. *Nanotechnology*. **2011**, *22 (2)*, 1-8.

(65) Chem, J. M.; Shankar, R.; Groven, L.; Amert, A.; Whites, W.; Kellar, J. J. Non-Aqueous Synthesis of Silver Nanoparticles Using Tin Acetate as a Reducing Agent for the Conductive Ink Formulation in Printed Electronics. *J. Mater. Chem*. **2011**, *21 (5)*, 10871–10877.

(66) Santhi, K.; Karthick, E. T. S. N. Synthesis , Structure Stability and Magnetic Properties of Nanocrystalline Ag – Ni Alloy. *J Nanopart Res.* **2012**, *14 (4)*, 1-12.

(67) Tsai, C.; Chen, S.; Song, J.; Chen, I.; Lee, H. Thermal Stability of Cu @ Ag Core – Shell Nanoparticles. *Corrosion Science.* **2013**, *74 (4)*, 123–129.

(68) Yan, S.; Sun, D.; Tan, Y.; Xing, X.; Yu, H.; Wu, Z. Synthesis and Formation Mechanism of Ag–Ni Alloy Nanoparticles at Room Temperature. *J. Phys. Chem. Solids* **2016**, *98 (6)*, 107–114.

(69) Pajor-Świerzy, A.; Gaweł, D.; Drzymała, E.; Socha, R.; Parlińska-Wojtan, M.; Szczepanowicz, K.; Warszyński, P. The Optimization of Methods of Synthesis of Nickel – Silver Core – Shell Nanoparticles for Conductive Materials. *Nanotechnology*. **2019**. *30 (10)*, 1-8.

(70) Sopoušek, J.; Pinkas, J.; Brož, P.; Buršík, J.; Vykoukal, V.; Škoda, D.; Stýskalík, A.; Zobač, O.; Vřešťál, J.; Hrdlička, A.; Šimbera, J. Ag-Cu Colloid Synthesis: Bimetallic Nanoparticle Characterisation and Thermal Treatment. *J. Nanomater.* **2014**, *2014 (2), 1-13*.

(71) Nie, X.; Wang, H.; Zou, J. Inkjet Printing of Silver Citrate Conductive Ink on PET Substrate. *Appl. Surf. Sci.* **2012**, *261 (8)*, 554–560.

(72) Lee, K. J.; Jun, B. H.; Kim, T. H.; Joung, J. Direct Synthesis and Inkjetting of Silver Nanocrystals toward Printed Electronics. *Nanotechnology*. **2006**, *17 (3)*, 2424–2428**.**

(73) Gonzalez-macia, L.; Morrin, A.; Smyth, M. R.; Killard, A. J. Advanced Printing and Deposition Methodologies for the Fabrication of Biosensors and Biodevices. *Analyst*. **2010**, *135 (12)*, 845–867.

(74) B. Weng, B.; Shepherd, R,; Crowley, K.; Killardb, A.; Wallace, G. Printing Conducting Polymers. *Analyst*. **2010**, *135* (11). 2745-3012.

(75) Grau, G.; Cen, J.; Kang, H.; Kitsomboonloha, R.; Scheideler, W. J.; Subramanian, V. Gravure-Printed Electronics: Recent Progress in Tooling Development, Understanding of Printing Physics, and Realization of Printed Devices. *Flex. Print. Electron.* **2016**, *1 (5)*, 1-24.

(76) Sung, D.; De La Fuente Vornbrock, A.; Subramanian, V. Scaling and Optimization of Gravure-Printed Silver Nanoparticle Lines for Printed Electronics. *IEEE Trans. Components Packag. Technol.* **2010**, *33* (1), 105–114.

(77) Lee, H.; Chou, K.; Huang, K. Inkjet Printing of Nanosized Silver Colloids. *Nanotechnology*. **2005**, *16 (9)*, 2436–2441.

(78) Nayak, L.; Mohanty, S.; Nayak, S. K. A Review on Inkjet Printing of Nanoparticle Inks For. *J. Mater, Chem. C.* **2019**, *7 (9),* 8771–8795.

(79) Peng, X.; Yuan, J.; Shen, S.; Gao, M.; Chesman, A. S. R.; Yin, H.; Cheng, J.; Zhang, Q.; Angmo, D. Perovskite and Organic Solar Cells Fabricated by Inkjet Printing: Progress and Prospects. *Adv. Funct. Mater.* **2017**, *27 (41)*, 1-27.

(80) Komuro, N.; Takaki, S.; Suzuki, K.; Citterio, D. Inkjet Printed (Bio)Chemical Sensing Devices. *Anal. Bioanal. Chem.* **2013**, *405*(*17)*, 5785–5805.

(81) Chung, S.; Cho, K.; Lee, T. Recent Progress in Inkjet-Printed Thin-Film Transistors. *Adv. Sci.* **2019**, *6 (6)*, 1-27.

(82) Mizukami, M.; Cho, S. Il; Watanabe, K.; Abiko, M.; Suzuri, Y.; Tokito, S.; Kido, J. Flexible Organic Light-Emitting Diode Displays Driven by Inkjet-Printed High-Mobility Organic Thin-Film Transistors. *IEEE Electron Device Lett.* **2018**, *39* (1), 39–42.

(83) Sun, J.; Cui, B.; Chu, F.; Yun, C.; He, M.; Li, L.; Song, Y. Printable Nanomaterials for the Fabrication of High-Performance Supercapacitors. *Nanomaterials.* **2018**, *8* (7), 1–24.

(84) Kosmala, A.; Wright, R.; Zhang, Q.; Kirby, P. Synthesis of Silver Nano Particles and Fabrication of Aqueous Ag Inks for Inkjet Printing. *Mater. Chem. Phys.* **2011**, *129 (3)*, 1075–1080.

(85) Perelaer, J.; De Gans, B. J.; Schubert, U. S. Ink-Jet Printing and Microwave Sintering of Conductive Silver Tracks. *Adv. Mater*. **2006**, *18 (16)*, 2101–2104.

(86) Derby, B. Inkjet Printing of Functional and Structural Materials: Fluid Property Requirements, Feature Stability, and Resolution. *Annu. Rev. Mater. Res.* **2010**, *40 (3)*, 395–414.

(87) Jabari, E.; Ahmed, F.; Liravi, F.; Secor, E. B.; Lin, L.; Toyserkani, E. 2D Printing of Graphene: A Review. *2D Mater.* **2019**, *6 (25)*, 1-26.

(88) Perelaer, J.; De Laat, A. W. M.; Hendriks, C. E.; Schubert, U. S. Inkjet-Printed Silver Tracks: Low Temperature Curing and Thermal Stability Investigation. *J. Mater. Chem.* **2008**, *18* (27), 3209–3215.

(89) Hao, Y.; Gao, J.; Xu, Z.; Zhang, N.; Luo, J.; Liu, X. Preparation of Silver Nanoparticles with Hyperbranched Polymers as a Stabilizer for Inkjet Printing of Flexible Circuits. *New J. Chem.* **2019**, *43* (6), 2797–2803.

(90) Singh, M.; Haverinen, H. M.; Dhagat, P.; Jabbour, G. E. Inkjet Printing-Process and Its Applications. *Adv. Mater.* **2010**, *22* (6), 673–685.

(91) Cummins, G.; Desmulliez, M. P. Y. Inkjet Printing of Conductive Materials: A Review. *Circuit World.* **2012**, *38* (4), 193–213.

(92) Kwon, K. S. Experimental Analysis of Waveform Effects on Satellite and Ligament Behavior via in Situ Measurement of the Drop-on-Demand Drop Formation Curve and the Instantaneous Jetting Speed Curve. *J. Micromechanics Microengineering.* **2010**, *20 (15)*, 1-15.

(93) Shin, P.; Sung, J. The Effect of Driving Waveforms on Droplet Formation in a Piezoelectric Inkjet Nozzle. *Proc. Electron. Packag. Technol. Conf. EPTC.* **2009**, *978 (1)*, 158–162.

(94) Gan, H. Y.; Shan, X.; Eriksson, T.; Lok, B. K.; Lam, Y. C. Reduction of Droplet Volume by Controlling Actuating Waveforms in Inkjet Printing for Micro-Pattern Formation. *J. Micromechanics Microengineering.* **2009**, *19 (9)*, 1-9.

(95) Liou, T. M.; Chan, C. Y.; Shih, K. C. Effects of Actuating Waveform, Ink Property, and Nozzle Size on Piezoelectrically Driven Inkjet Droplets. *Microfluid. Nanofluidics.* **2010**, *8 (5)*, 575–586.

(96) Wijshoff, H. Structure and Fluid-Dynamics in Piezo Inkjet Printheads; *Herman Wijshoff, Oc´e Technologies B.V., Venlo*. **2008**, 1-185.

(97) Tekin, E.; Smith, P. J.; Schubert, U. S. Inkjet Printing as a Deposition and Patterning Tool for Polymers and Inorganic Particles. *Soft Matter.* **2008**, *4 (4)*, 703–713.

(98) Antohe, B. V.; Wallace, D. B. Acoustic Phenomena in a Demand-Mode Piezoelectric Ink-Jet Printer. *Int. Conf. Digit. Print. Technol.* **2001**, *17 (1)*, 885–889.

(99) Soltman, D.; Subramanian, V. Inkjet-Printed Line Morphologies and Temperature Control of the Coffee Ring Effect. *Langmuir.* **2008**, *24 (5)*, 2224–2231.

(100) Stringer, J.; Derby, B. Limits to Feature Size and Resolution in Ink Jet Printing. *J. Eur. Ceram.Soc.***2009**, *29 (5)*, 913–918.

(101) Fukai, J.; Ishizuka, H.; Sakai, Y.; Kaneda, M.; Morita, M.; Takahara, A. Effects of Droplet Size and Solute Concentration on Drying Process of Polymer Solution Droplets Deposited on Homogeneous Surfaces. *Int. J. Heat Mass Transf.* **2006**, *49 (20)*, 3561–3567.

(102) Martin, G. D.; Hoath, S. D.; Hutchings, I. M. Inkjet Printing - The Physics of Manipulating Liquid Jets and Drops. *J. Phys. Conf. Ser.* **2008**, *105 (15)*, 1-15

(103) Wong, T. S.; Chen, T. H.; Shen, X.; Ho, C. M. Nanochromatography Driven by the Coffee Ring Effect. *Anal. Chem.* **2011**, *83* (6), 1871–1873.

(104) Yunker, P. J.; Still, T.; Lohr, M. A.; Yodh, A. G. Suppression of the Coffee-Ring Effect by Shape-Dependent Capillary Interactions. *Nature.* **2011**, *476 (7360)*, 308–311.

(105) Mikolajek, M.; Friederich, A.; Bauer, W.; Binder, J. R. Requirements to Ceramic Suspensions for Inkjet Printing. *CFI Ceram. Forum Int.* **2015**, *92 (3)*, E25–E29.

(106) Shen, X.; Ho, C. M.; Wong, T. S. Minimal Size of Coffee Ring Structure. *J. Phys. Chem. B.* **2010**, *114 (16)*, 5269–5274.

(107) Kaya, D.; Belyi, V. A.; Muthukumar, M. Pattern Formation in Drying Droplets of Polyelectrolyte and Salt. *J. Chem. Phys.* **2010**, *133 (11)*, 1-10

(108) Gugliotti, M.; Baptista, M. S.; Politi, M. J.; Quimica, I. De; S, B.; Paulo, U. D. S.; Prof, A.; Prestes, L.; Paulo, S.; Silverstein, T. P.; Slater, C. D. JCE DigiDemos : Tested Demonstrations Surface Tension Gradients Induced by Temperature : The Thermal Marangoni Effect Submitted By : *J. Chem. Educ.* **2004**, *81* (6), 824–826.

(109) Mayer, S. W. A Molecular Parameter Relationship between Surface Tension and Liquid Compressibility. *J. Phys. Chem.* **1963**, *67* (10), 2160–2164.

(110) Curtis, C.; Rivkin, T.; Miedaner, a; Alleman, J.; Perkins, J.; Smith, L.; Ginley, D. Metallizations by Direct-Write Inkjet Printing. *Conference Paper.* **2001**, 1-6.

(111) Bidoki, S. M.; Lewis, D. M.; Clark, M.; Vakorov, A.; Millner, P. A.; McGorman, D. Ink-Jet Fabrication of Electronic Components. *J. Micromechanics Microengineering.* **2007**, *17 (5)*, 967–974.

(112) Natsuki, J.; Abe, T. Synthesis of Pure Colloidal Silver Nanoparticles with High Electroconductivity for Printed Electronic Circuits: The Effect of Amines on Their Formation in Aqueous Media. *J. Colloid Interface Sci.* **2011**, *359 (1)*, 19–23.

(113) Mafuné, F.; Kohno, J. Y.; Takeda, Y.; Kondow, T. Dissociation and Aggregation of Gold Nanoparticles under Laser Irradiation. *J. Phys. Chem. B.* **2001**, *105 (38)*, 9050–9056.

(114) Anto, B. T.; Sivaramakrishnan, S.; Chua, L. L.; Ho, P. K. H. Hydrophilic Sparse Ionic Monolayer-Protected Metal Nanoparticles: Highly Concentrated Nano-Au and Nano-Ag 'Inks' That Can Be Sintered to near-Bulk Conductivity at 150°C. *Adv. Funct. Mater.* **2010**, *20 (2)*, 296–303.

(115) Pulkkinen, P.; Shan, J.; Leppänen, K.; Känsäkoski, A.; Laiho, A.; Järn, M.; Tenhu, H. Poly(Ethylene Imine) and Tetraethylenepentamine as Protecting Agents for Metallic Copper Nanoparticles. *ACS Appl. Mater. Interfaces.* **2009**, *1 (2)*, 519–525.

(116) Mohammadi, M. M.; Gunturi, S. S.; Shao, S.; Konda, S.; Buchner, R. D.; Swihart, M. T. Flame-Synthesized Nickel-Silver Nanoparticle Inks Provide High Conductivity without Sintering. *Chem. Eng. J.* **2019**, *372 (8)*, 648–655.

(117) Smith, P. J.; Shin, D. Y.; Stringer, J. E.; Derby, B.; Reis, N. Direct Ink-Jet Printing and Low Temperature Conversion of Conductive Silver Patterns. *J. Mater. Sci.* **2006**, *41 (13)*, 4153–4158.

(118) Mortimer, R. J.; Dyer, A. L.; Reynolds, J. R. Electrochromic Organic and Polymeric Materials for Display Applications. *Displays.* **2006**, *27 (1)*, 2–18.

(119) Ryu, K. S.; Jeong, S. K.; Joo, J.; Kim, K. M. Polyaniline Doped with Dimethyl Sulfate as a Nucleophilic Dopant and Its Electrochemical Properties as an Electrode in a Lithium Secondary Battery and a Redox Supercapacitor. *J. Phys. Chem. B.* **2007**, *111 (4)*, 731–739.

(120) Razal, J. M.; Kita, M.; Quigley, A. F.; Kennedy, E.; Moulton, S. E.; Kapsa, R. M. I.; Clark, G. M.; Wallace, C. C. Wet-Spun Biodegradable Fibers on Conducting Platforms: Novel Architectures for Muscle Regeneration. *Adv. Funct. Mater.* **2009**, *19 (21)*, 3381–3388.

(121) Singh, K.; Ohlan, A.; Saini, P.; Dhawan, S. K. Poly (3,4- Ethylenedioxythiophene) Fe_2O_3 Polymer Composite – Super Paramagnetic Behavior and Variable Range Hopping 1D Conduction Mechanism – Synthesis and Characterization. *Polym. Adv. Technol.* **2008**, *19 (11)*, 229–236.

(122) Gamerith, S.; Klug, A.; Scheiber, H.; Scherf, U.; Moderegger, E.; List, E. J. W. Direct Ink-Jet Printing of Ag-Cu Nanoparticle and Ag-Precursor Based Electrodes for OFET Applications. *Adv. Funct. Mater.* **2007**, *17 (16)*, 3111–3118.

(123) Gamerith, S.; Klug, A.; Scheiber, H.; Scherf, U.; Moderegger, E.; List, E. J. W. Direct Ink-Jet Printing of Ag-Cu Nanoparticle and Ag-Precursor Based Electrodes for OFET Applications. *Adv. Funct. Mater.* **2007**,*17 (16)*, 3111–3118.

(124) Li, X.; Zhang, G.; Bai, X.; Sun, X.; Wang, X.; Wang, E.; Dai, H. Highly Conducting Graphene Sheets and Langmuir-Blodgett Films. *Nat. Nanotechnol.* **2008**, *3 (9)*, 538–542.

(125) Eda, G.; Fanchini, G.; Chhowalla, M. Large-Area Ultrathin Films of Reduced Graphene Oxide as a Transparent and Flexible Electronic Material. *Nature nanotechnology*. **2008**, *3 (5)*, 1–5.

(126) Hecht, D. S.; Kaner, R. B. Solution-Processed Transparent Electrodes. *MRS Bull.* **2011**, *36 (10)*, 749–755.

(127) Hu, L.; Hecht, D. S.; Grüner, G. Carbon Nanotube Thin Films: Fabrication, Properties, and Applications. *Chem. Rev.* **2010**, *110 (10)*, 5790–5844.

(128) Tobjörk, D.; Aarnio, H.; Pulkkinen, P.; Bollström, R.; Määttänen, A.; Ihalainen, P.; Mäkelä, T.; Peltonen, J.; Toivakka, M.; Tenhu, H.; Österbacka, R. IR-Sintering of Ink-Jet Printed Metal-Nanoparticles on Paper. *Thin Solid Films.* **2012**, *520 (7)*, 2949–2955.

(129) Yaqoob, A. A.; Umar, K.; Ibrahim, M. N. M. Silver Nanoparticles: Various Methods of Synthesis, Size Affecting Factors and Their Potential Applications–a Review. *Appl. Nanosci.* **2020**, *10 (5)*, 1369–1378.

(130) Gu, X.; Yung, K. C. Ink-Jet Printed High Conductive Silver Traces on Polymer Substrates Sintered at Room Temperature by a Camera Flash Lamp. *16th Int. Conf. Electron. Packag. Technol. ICEPT.* **2015**, *978 (1)*, 642–644.

(131) Lee, D. J.; Oh, J. H.; Bae, H. S. Crack Formation and Substrate Effects on Electrical Resistivity of Inkjet-Printed Ag Lines. *Mater. Lett.* **2010**, *64 (9)*, 1069–1072.

(132) Kang, J. S.; Kim, H. S.; Ryu, J.; Thomas Hahn, H.; Jang, S.; Joung, J. W. Inkjet Printed Electronics Using Copper Nanoparticle Ink. *J. Mater. Sci. Mater. Electron.* **2010**, *21 (11)*, 1213–1220.

(133) Tobjörk, D.; Aarnio, H.; Pulkkinen, P.; Bollström, R.; Määttänen, A. IR-Sintering of Ink-Jet Printed Metal-Nanoparticles on Paper. *Thin Solid Films.* **2012**, *520 (7)*, 2949–2955.

Chapter 2: Experimental Methodology

2.1 Chemicals and materials

2.1.1 Inorganic salts and solvents:

All the following chemicals were used without any purification and purchased either from Alfa Asar, Fisher Scientific, Sigma Aldrich or Thermo Scientific companies. All the solutions were prepared with the use of analytical grade water.

Copper formate tetrahydrate (98%); nickel (II) acetate tetrahydrate; nickel acetyl-acetonate; nickel nitrate; silver nitrate (99.8%).

Absolute ethanol (≥ 99.9%); acetone; 1-amino-2-propanol (99.5%); ethylene glycol (99.5%); hexane; hydrazine(80%); oleic aci (99%);1-octadecene (90%); oleylamine (80%-90%);1-propanol (anhydrous, 99.7%); 2-Propanol (99.7%) was from VWR Chemical; paraffin liquid was bought from Acros Organics; sodium borohydride (98%); sodium hydroxide; 1,2-tetradecanediol (90%); triethanolamine (99.0%).

2.1.2 Polymers:

Poly acrylic acid (PAA) MW= 1800; polyvinyl alcohol (PVOH, 98-99%), MW= 85,000 - 124,000; polyvinyl alcohol (PVOH, 88%), MW= 78,000; polyvinyl alcohol (PVOH, 98%), MW= 25,000 and polyvinyl pyrrolidone (PVP, %), MW= 40,000.

2.1.3 Modifying plastic substrates materials :

An uncoated Poly(ethylene terephthalate) (PET) film was purchased from Office Depot (size A4 (210 mm x 297 mm) 100 microns – laser printer overhead projector slides) and used as a plastic substrate film., PI film was Kapton 300HN thermal insulating film (304 mm x 200 mm x 0.025 mm), obtained from RS Components Ltd. Microscope slides bought from Thermo scientific as rigid substrates were also used for coating.

A source of Cl^- in dilute solution was prepared by dissolving inorganic salts such as NaCl, KCl in water, though more organic soluble chloride salts (e.g. tetraalkyl ammonium chlorides) could be used in alternative solvents if needed.

In this work KCl bought from Riedel-deHaen (74.55 g/mol) was used. All the solutions were prepared in freshly prepared double-distilled water.

2.2 Synthesis of nano particles by aqueous method

2.2.1 Synthesis of silver nanoparticles (Ag NPs) by chemical reduction method in an aqueous solution

For synthesis of the Ag NPs, the route used by Mavuri A. *et al.* [1] was followed, but testing different capping agents. The PAA or PVOH or PVP were used as surface-capping molecules to control the particle size. Initially, Ag NPs were synthesised by the reduction of $AgNO_3$ with triethanolamine (TEA) in the presence of the capping agent. The following steps were followed to prepared Ag NPs. Firstly: in a round- bottom flask equipped with magnetic stirring bar were mixed TEA, capping agent (PAA or PVOH or PVP) and water with 10.3 mL, 0.15 g and 24 mL respectively and kept under stirring for a few minutes at room temperature till dissolved. Secondly, a stock of silver nitrate was prepared by dissolving 10 g of $AgNO_3$ in 10 mL of water under stirring to get a homogeneous solution. Then the $AgNO_3$ stock was added carefully dropwise to the above mixture and the reaction mixture left under continuous stirring for 60 min. Thereby, the Ag was completely dispersed, and the colour of the mixture altered in the sequence below: colourless, pale cream to brown colour. At this point, the temperature was adjusted to 70 °C under vigorous stirring for about 3 hours. After 3 h the hotplate was removed, and the solution left under continuous magnetic stirring overnight. The following day, the suspension was sonicated for 1 hour using sonics & material probe, vibra-cell by JENCONS scientific Ltd (Leighton Buzzard, UK) for ultrasonic processing under ambient temperature to achieve uniformity.

Finally, in order to remove the unreacted organic solvent and metal salts the mixture was centrifuged at 1000 rpm for 10 min. The supernatant containing impurities was removed by pouring it off the pellet into the waste container. The centrifugation was repeated 3-4 times until the supernatant became transparent. Each time, the mixture was resuspended with ethanol. The obtained product was dried in an oven at 70 °C to collect the nanoparticles and they were kept in a fridge until required.

2.2.2. Synthesis of silver nanoparticles by co-reduction of Ag and Ni metal precursors at room temperature

This method of synthesis was used by Srivastava C. *et al.* [2], so the same steps were followed while testing different polymers as capping agents, even using several ratios in some cases. In the synthesis, bimetallic Ag- Ni NPs were prepared with different ratios each time as follows (using the 50:50 ratio as an example): Initially, a mixture of 0.54 g of nickel nitrate and 0.5 g of silver nitrate were mixed. The salt mixture was added to 1.36 g PVP/ PVOH / PAA as a capping agent, dissolved with vigorous stirring in a beaker containing 100mL of water at room temperature. Once a clear solution was formed, a reduction solution was added, also at room temperature. In this second step, a reductant solution (0.52 g of sodium borohydride in 25 mL of water) was prepared separately under vigorously stirring. Once dissolved, the reductant solution was then added dropwise over a 10 min period to the salt/capping agent mixture. The moment that the mixture colour changed to black, which indicates the reduction of Ag ions, the stirring was stopped immediately. The whole synthesis was done under ambient atmosphere. Finally, to clean the obtained NPs, 100mL of ethanol was added to the mixture and left to cool about 3-4 hrs. As a result, a black dispersion precipitate was collected from the beaker bottom and centrifuged at 5000 rpm for 10 minutes. After that, the particles in the pellet from the centrifuge tube were dispersed in distilled water before measurement. A similar method was followed to prepare Ag-Ni alloy except the precursor amount each time was varied between 25:75, 75:25 or 40:60% of Ag and Ni respectively. The alloy nanoparticle synthesis was repeated and scaled up to ten times to confirm the reproducibility of the alloy results.

2.2.3. Synthesis of silver nanoparticles- polyvinyl alcohol (Ag/PVOH) composites

A method similar to Teerasong S. *et al.* [3] (with some modification) was used in preparing PVOH capped Ag NPs. An aqueous solution of PVOH in water was obtained by slowly adding 0.5 g of PVOH into 50mL of water while magnetic stirring on a hot plate. Next, 0.127 g of $AgNO_3$ was weighed and dissolved in 150 mL deionised water between 90-100 °C. The Ag^+ solution was added drop by drop to the PVOH mix under constant stirring and heating at about 90 °C for

90 minutes. Once the solution formed a yellowish colour (small silver nuclei), $NaBH_4$ solution (0.13 g with 10 mL water) was added, which caused the rapid reduction of silver salt, and the mixture was stirred for a further 30 minutes.

Lastly, the reaction mix was cooled to room temperature and ethanol added to let the particles precipitate. They were collected by centrifugation the following day. They were washed by centrifugation at 5000 rpm for 15 min and resuspended again in water ready for further measurements.

2.2.4. Synthesis of Ni-Ag /PAA core-shell NPs

This method has been reported by Pajor-swierzy A. *et al.* [4]. The procedure is briefly described as follows: The nickel acetate solution was prepared at concentration 0.1 M by dissolving 0.005g nickel acetate and 0.005 g of PAA in 30 mL distilled water (1:1 molar ratio Ni: PAA) while stirring and heating to 60 °C. After 10 minutes, 6 mL of as-prepared $NaBH_4$ solution (0.0949 g + 6 mL water) was injected into the solution at 60°C and the reaction kept for 1hr under nitrogen gas to prevent Ni oxidation. The obtained product was cooled at room temperature before silver nitrate solution was added. 0.05 g of $AgNO_3$ (1:0.1 molar ratio Ni : Ag) was dissolved in 1 mL of DI water and injected into the as-prepared mixture above to coordinate the Ag shell round the Ni core. The reaction mixture was stirred at room temperature for 1 h as before. Lastly, the mixture was centrifuged at 8000 rpm for 15 min to pellet the NPs. The reaction was repeated again using the molar ratio 1:1 of Ni : Ag to produce a thicker Ag shell.

2.3. Synthesis of nano particles by non-aqueous method

2.3.1. Synthesis of silver-polyvinyl pyrrolidone (Ag/PVP) by a modified polyol process

To synthesise silver-polyvinyl pyrrolidone (Ag/PVP) by a modified polyol process, the same approach as Wang Z. *et al*. [5] was used. In a 250 mL two necked round bottom flask, 60mL ethylene glycol and 2 g of PVP were dissolved and heated on an oil bath under magnetic stirring at 120 ºC for 1 h. The preheating was necessary to boost the EG reducibility and get better adsorption of PVP on the Ag NPs surface.

In another 100 mL flask, 40 mL of EG and 1.97 g of $AgNO_3$ were stirred until they formed a clear solution. After that, the $AgNO_3$ solution was added dropwise into the first flask then the mixture continuously stirred for 4 hours at 120 °C. At the end, the mixture colour turned to a grey black solution, indicating the formation of silver NPs. Then, about 20 mL of ethanol was added to help the particles to precipitate and the mixture centrifuged at 5000 rpm for 15 min. Finally, the obtained pellet was dried in an oven at 70 °C to remove solvents and achieve a grey black powder.

2.3.2. Synthesis of Ni-Ag /PAA core-shell NPs by polyol method

The synthesis of Ni-Ag /PAA core-shell NPs was performed according to the method reported by Anh T. *et al.* [6] with some changes. Hydrazine or sodium borohydride was used for reduction of nickel acetate and silver nitrate in ethylene glycol. PAA or PVP was used as the protective agent. The general process of synthesis was in two steps:

Firstly, 0.633 g (2.5 mmol) nickel acetate and 0.1 g PAA were dissolved in 50 mL ethylene glycol in sequence under mechanical stirring, until the solution turned to green. A solution of hydrazine (2.5 mmol) was prepared (0.08 g in 4 mL H_2O) and added to the above solution and 4 mL of NaOH (0.5 M) solution was added under continuous stirring till the resulting solution mixture became violet in color .

The solution mixture was then heated to 60 °C for 30 minutes, turning to black indicating the formation of Ni NPs. The synthesis reaction can be explained by the equation (2.1):

$$2Ni^{2+} + N_2H_4 + 4OH^- \rightarrow 2Ni + N_2 + 4H_2O \qquad (2.1)$$

Once the Ni NPs were formed, the colloidal dispersion was washed twice with ethanol and centrifuged at 8000 rpm for 20 min to separate the particles from suspension. The obtained Ni NPs were redispersed in 50 mL ethylene glycol.

A silver nitrate solution was separately prepared by dissolving 0.425 g Ag in 50mL ethylene glycol and this was added dropwise into the dispersed Ni solution as a reducing agent. The mixture was heated at 80 °C for 60 min, then centrifuged and washed by multiple resuspensions with ethanol, before finally

collecting the resulting NPs. The NPs were dried under vacuum overnight at room temperature.

2.4. Synthesis of nanoparticles by hot-injection method

2.4.1. Synthesis of core-shell silver / nickel nanoparticles by solvothermal hot injection method

Silver/nickel NPs were synthesised according to Vykoukal V. *et al.* [7]. The procedure for the synthesis of Ag Ni NPs was based on a two-stage process.

In the first stage, (1:1) molar ratio was applied to the precursors as follows: 51.38 mg $Ni(acac)_2$ and 34.82 mg $AgNO_3$ were weighed and placed in a three-necked round bottom flask, then the mixture was evacuated / refilled with dry N_2 several times. 4 mL oleylamine (OAM) (80%-90%) (dried over sodium, then stored in a round-bottomed flask until used) was added by a syringe under stirring. Following this, the mixture was heated up to about 85 °C or less until the solution changed from nearly transparent to a clear green colour, which confirms the precursors dissolved.

In the second stage, a mixture of 16 mL of OAM and 20 mL of 1- octadecene were decanted into a three neck Schlenk flask and kept under stirring while heating to 120 °C. After 20 mins, the mixture was evacuated / refilled with dry N_2 3-4 times. Then it was held under a flow of N_2, and the temperature increased to 230 °C. Immediately after reaching 230 °C the Ag/Ni precursor solution was rapidly injected to the hot mixture of solvents, accompanied by a colour change to black. Then the mixture was kept stirring for 10 min. Subsequently, the reaction mixture was cooled down to room temperature by setting it in a water bath. After cooling to room temperature, 20 mL of acetone was added. This allowed the particles to precipitate slowly from the solution.

The particles were then easily separated by centrifugation at 8000 rpm for 15 mins and were washed twice with a 1:3 acetone and hexane mixture and finally the pellet NPs were dispersed in hexane and characterized using appropriate methods. This experiment was repeating using different mass ratio of Ag: Ni at (50:50, 75:25, 25:75).

2.4.2 Synthesis of copper @ silver core-shell NPs by thermal decomposition and galvanic displacement

The experimental investigation of Cu@Ag NPs was carried out following a similar procedure to Dai X. *et al.* [8]. ICopper formate tetrahydrate (98%) was first dried at 90 °C under vacuum for 48 h to produce anhydrous copper formate. Then, the dried copper formate (1.2 g) and OAM (9.3 g) were dissolved together in 80 mL of paraffin liquid at 50 °C, and the air was removed from the solution by bubbling with N_2. The solution was heated at 170 °C for 30 min under N_2 and the colour of the solution changed from green to reddish brown due to the Cu reduction. The product was cooled down with a cold-water bath. In the second step, an additional OAM (35 mL) solution containing the desired amount of $AgNO_3$ (1.30 g) was then rapidly injected into the cooled reaction medium via a syringe. This led to Ag shell formation by galvanic displacement. Then, the mixture was heated to 80 °C for 2 h under N_2 bubbling while the colour changed from reddish brown to blackish brown, indicating the completion of the reaction.

After 2 h of reaction, the precipitates were centrifuged at 7000 rpm for 45 min to separate out the Cu@ Ag NPs and then washed twice with hexane: isopropyl alcohol 1:1 (v: v). Finally, the samples of NPs powder were dried under evacuation for 12 h before formulating the conductive ink.

2.4.3 Synthesis of nickel @ silver /PAA core-shell nanoparticles

To get better Ni@Ag core-shell NPs performance, Anh T. *et al.* [6] developed several modifications to the previous experiment (2.3.2. Synthesis of NiAg /PVP core-shell NPs by Polyol Method) to get more uniform particles. Details of the process are as follows. Firstly, nickel acetate tetrahydrate was dried at 90 °C under vacuum for 48 h to get anhydrous nickel acetate. In a flask of 250 mL 0.0622 g (0.25 mmol) of dried nickel acetate and 0.1 g PAA were dissolved in 50 mL ethylene glycol in sequence under mechanical stirring and the temperature set up at 60 °C for 30 min until the solution turned to green. Then, a solution of sodium borohydride (2.5 mmol) was prepared (0.095 g in 4 mL H_2O) and added to the above solution while stirring and 4 mL of NaOH (0.5 M) solution was added too, during which the colour changed to violet solution. Finally, the solution was heated up at 60 °C for another 30 min until a black colour appeared, indicating the formation of Ni NPs.

Once the Ni NPs were formed, the resulting solution was cooled in a water bath. Secondly, in another flask, a silver nitrate solution was separately prepared by dissolving 0.425 g (2.5 mmol) $AgNO_3$ in 50 mL ethylene glycol and was added dropwise into the above Ni solution as a reducing agent. The mixture was heated at 80 °C for 60 min then was centrifuged followed by multiple washing with ethanol before finally collecting the resulting NPs. The NPs were dried under vacuum overnight at room temperature.

2.5 Nanoparticle characterization

This section will briefly outline the major analytical techniques used for characterisation of the synthesised nanoparticles (NPs) materials. They have been used to characterise the composition and morphology of the obtained NPs.

2.5.1 Dynamic light scattering (DLS)

The particles size distribution was measured by DLS with a ZETASIZER Nano ZS from Malvern Instruments (Malvern, UK). To prepare the DLS sample, 0.0020 g was taken from the obtained nanoparticles and diluted by adding 1 mL of the solvent, filtered through a 0.45 µm syringe filter to confirm no dust or large aggregate contamination was present. After that, the mixture was dispersed by using an ultrasonic bath for 20 min to achieve a uniform mixture. The mixture was then taken by Gilson pipette (1000-100 µL) and transferred into a suitable cuvette, depending on the solvent type. Before the measurement was carried out, the instrument was initially set up with an SOP using the following DLS parameters- Ag NPs refractive index (RI = 0.207), Absorption (0.010), Temperature (25 °C), cell type was chosen depending on the solvent (glass, plastic or quartz) and dispersant. For better reliability, each result should be taken as an average of three measurements, and this approach was used routinely for standard material characterisation.

The same device was used for Zeta potential measurements, in order to confirm the protective efficiency of the nanoparticle's dispersion stabiliser and the stability of the ink formulation afterwards.

2.5.2 Transmission electron microscopy (TEM)

To determine the mean size and size distribution of nanoparticles, a JEOL (Welwyn Garden City, UK) 2010 200 kV Transmission Electron Microscope (TEM) was used.

TEM specimens were prepared by a drop infusion of a few µL of the colloidal solutions of Ag (or other) NP on to carbon-coated copper grids; and the sample allowed to dry by evaporation at ambient temperature.

2.5.3 Scanning electron microscopy (SEM)

The particle size, surface roughness and cross-sectional morphology of NPs and printed structures was investigated using field emission scanning electron microscopy (SEM) with EDS. A conductive carbon tape was stuck to an aluminium stub and the NPs powder/ printing track was placed on top of the tape. Then, the carbone tape along with the nano paericles/ printing track were coated with a fine layer (thin film of gold) using a typical SEM coater. Gold coating is necessary in case the nano particles are insulating in nature.

The SEM instrument used was a Zeiss Gemini 300 FE SEM fitted with an oxford instruments Ultim Max 170 EDS. This SEM offers great imaging flexibility for a wide range of samples and applications and has sufficient resolution for basic nanoparticle characterisation. However, extraction of nanoparticle sizes is not accurate from SEM imaging. In SEM, the electron beam excites a large volume of the substrate just under the nanoparticle layer, and SEM signal also comes from that volume, thus SEM results on nanoparticle sizes are not very accurate (below 20-30 nm). Therefore, for an accurate determination of nanoparticle sizes, TEM measurements are always superior.

2.5.4 Thermogravimetric analysis (TGA)

Thermogravimetric analysis (TGA) was performed to investigate the loss of capping groups from the surface of the inorganic NPs by using the instrument TA, Discovery, TGA5500 with a heating rate of 10 ºC/min from room temperature to 500 °C. The sample was prepared by filling dry NP powder in a clean glass sample holder.

2.6 Ink formulation

2.6.1 Typical ink formulation

Most printing technologies require stable and concentrated dispersions of Ag NPs in the conductive ink. The dispersion of Ag NPs was prepared by adding various amounts of silver NP powder 30, 20 or 10 wt% to the solvent mixture which involved solvents, dispersants and additives.

Itemized, the standard 30 wt% nano silver conductive ink was fabricated using a simple process in a typical reaction. The dry Ag NPs were ground gently in a mortar. Then 0.69 g ethylene glycol was mixed with 0.77 g water by weight in a glass container and stirred for 2-3 minutes. Ethylene glycol was used to achieve the desired viscosity and surface tension. Next, 0.9 g Ag NPs were dispersed in the mixing solution of both EG, and water followed by probe sonication for 20 minutes until Ag NPs and the mixture solution were well dispersed. After that, 0.63 g 1-propanol was added with continuous stirring for around 3 minutes.

The wt% was calculated by dividing the mass of the silver Np powder by the total weight of each ink. Thus, this wt% includes the masses of the capping agent and silver content.

A stock of 1 M solution of NaOH was prepared by mixing 0.4 g of NaOH with 10 mL of DI water and stirred until a homogenous solution was obtained. Finally, for pH adjustment, NaOH solution was dropped into the mixture above (3 drops, which is around 0.09 g) and stirring continued for around 10 minutes. The measured pH should be ≥ 6-8 to prevent any retardation of the drying reaction after printing. The ink was then transferred into a glass screw cap container wrapped by foil and stored in a fridge to be proteced from light. Table 2.1 shows the formulation of inks and their contents:

Table 2.1. Different ink contents ratios.

Chemicals	30 wt% Ag NPs ink	20 wt% Ag NPs ink	10 wt% Ag NPs ink
Ethylene glycol	33.30% (0.69 g)	33.30% (0.79 g)	33.30% (0.89 g)
DI Water	36.70% (0.77 g)	36.70% (0.88 g)	36.70% (0.99 g)
NPs Powder	30% (0.9 g)	20% (0.6 g)	10% (0.3 g)
1-Propanol	30% (0.63 g)	30% (0.72 g)	30% (0.81g)
NaOH	~ 0.09 g	~ 0.09 g	~ 0.09 g

The size distribution of the particles in the obtained ink was followed using DLS and the viscosity of the colloidal aqueous ink suspensions based on Ag NPs was measured using a Discovery Hybrid Rheometer (TA instruments) equipped with 40 mm parallel plate at 25 °C.

The obtained conductive ink was then ready to print by using a Jet lab 4 inkjet printer with different nozzles size 80 or 50 µm on a suitable substrate (see section 2.8.2 for a detailed description). The printed conductive ink will form a conductive track after drying through solvent evaporation. This is achieved through a desired sintering process e.g., by heating and decomposing the organic insulating material until the residual silver layer possesses enough interconnected conductive pathways and has fused sufficiently to form the dense structure required to produce electrically conductive properties.

2.6.2 Ink formulation of the Cu@ Ag NPs for conductive inks

As oleylamine is a hydrophobic ligand, to get a very dispersed ink with low resistance a solvent must be chosen non-polar enough to disperse the hydrophobic surface ligand. For this purpose, a variety of solvents were chosen (octane, toluene, butanol, 1-propanol, dimethyl formide, butyl acetate and butyl ether). In the beginning, 10 wt% inks were formulated for the synthesized copper–silver core-shell nanoparticles by dispersing these in the different solvents using probe sonication for 30 minutes to accomplish the formulation of the conductive ink.

2.6.3 Rheological properties of silver inks

Herein, the viscosity of the colloidal aqueous suspensions of ink based on Ag NPs was measured using a Discovery Hybrid Rheometer (TA instruments) equipped with 40mm parallel plate. All of the testing was performed by using the rheometer at constant shear rate (25000.0 1/s) and the velocity (150 rad/s), stress (6.3662 x10^6 µPa) and Torque (10.0 µN·m) at room temperature. The viscosity should be within the viscosity range recommended for stable printing by Jetlab 4 inkjet printers, which is 8-15 cps [8].

2.7 Substrate materials

For most of the development work in this thesis, the selected substrate was photo paper (Epson Glossy (200 g/m^2)). This was known to allow spontaneous room temperature sintering of silver inks from previous work in the group and other published work [1,9,10,11,12]. This is believed to be due to mobilisation/diffusion of chloride ions in the paper/coating when the aqueous-based ink droplets make contact with the surface.

For transfer of printing to flexible polymer substrates, PVOH solution containing “doped” chloride ions was prepared and coated over polyethylene terephthalate (PET) or polyimide (PI) to form a thin film which was used as a flexible substrate. These polymers are widely chosen as a substrate material due to their flexibility and high thermal stability.

2.8 Ink jet printer

The inkjet printing for the formulated ink was completed by using a Microfab (Plano, TX, USA) Jet lab 4 inkjet printer equipped with 80 or 50 µm nozzle diameters in ambient atmosphere. The silver ink was printed typically into a pattern of 5 replica lines with a length of 5 mm, printed in a single pass for each print pitch.

2.8.1 Principles of operation of a drop on demand (DOD) printer

DOD inkjet printers generate individual drops when required and are thus more economical with ink delivery than continuous inkjet printing (CIJ) systems.

For the drop generation process, drop positioning is achieved by manually locating the printhead above the substrate before drop ejection. Drops are formed by propagating a pressure pulse in the fluid held in a chamber behind the printing nozzle. If the pulse exceeds some threshold at the nozzle, a drop is ejected. However, in the absence of a pressure pulse, ink is held in place by its surface tension. Typically, the pressure pulse is generated by direct mechanical actuation using a piezoelectric transducer (Figure 2.1).

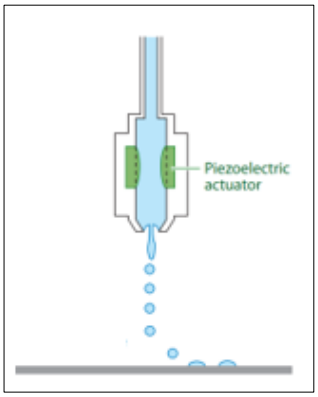

Figure 2.1. Schematic diagram showing the principle of a piezoelectric inkjet printer [13].

The frequencies have a main effect on drop generating and typically should be 1-20 kHz. As a result, resonances are generated within the chamber behind the nozzle and influence pressure pulse propagation, drop volume and velocity. DOD printers are able to generate drops with a small diameter, typically (20-50 μm) and that can be controlled by management of the pressure pulse [14].

For all work in this thesis, the piezoelectric inkjet printing approach was used. Figure 2.2 below shows the overall image of the actual printer used, with parts labelled.

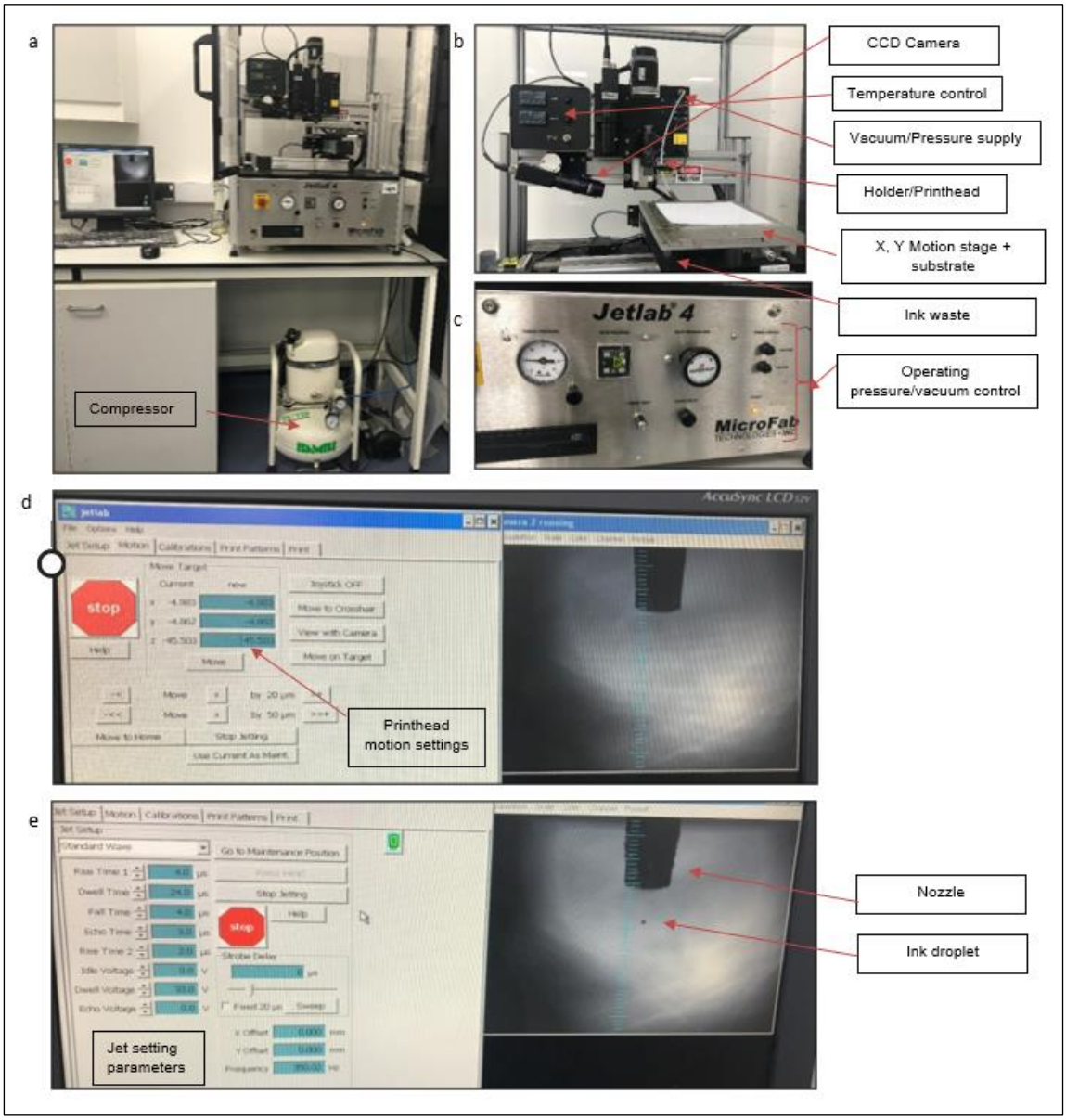

Figure 2.2. (a &b) Inkjet printer image, (c) panel control, (d) stage & nozzle control, (e) parameter control & ink droplet.

2.8.2 Inkjet printing setup

Initially, the nano ink was well sonicated for 30 min using sonics and material vibra cell by JENCONS scientific Ltd (Leighton Buzzard, UK) with an amplitude of 56%, full mode at room temperature to avoid agglomeration and remove any large particles that may clog the nozzle. Then, it was filled in the syringe and mounted on the holder and an appropriate substrate was selected. The printing jetting parameters, such as, time, voltages, back pressure and frequency, were tailored in order to examine their influence on drop dispensing and the print quality. The drop spacing (print pitch) was varied between 95 and

15 μm. A printed pattern was composed of a square of 10x10 pixels and 5 mm long line varied in width / thickness depend on print pitch setting.

The piezoelectric inkjet printhead's actuating waveform strongly influences the droplet jetting behaviour, controlling the jetting process and quality of droplets. In order to achieve jetting and suppress satellite droplet formation, the actuating waveform of the print head must be properly designed.

It was defined using the software on the PC (Figure 2.2 (e)), with either unipolar or bipolar signals possible (Figure 2.3) for good quality jetting.

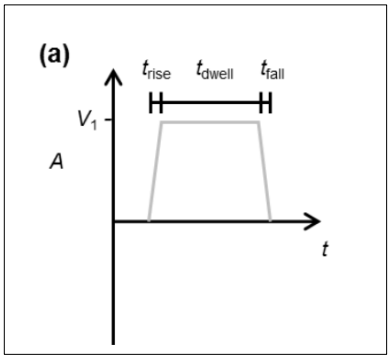

Figure 2.3. Typical unipolar waveforms for piezoelectric inkjet print-head [14,15].

Once a stable jetting had been achieved, the print pitch between droplets was modified to separate the printed features in order to define dot size and tune deposition to overlap the features to make lines and 2D patterned features of controlled geometry.

Some relevant parameters mentioned earlier affect the ink jetting quality. It was noticed that driving voltages less than 18 or more than 80 V respectively, resulted in poor deposition of the Ag ink regardless of the values of other parameters. It was observed that tiny droplets are undesirably formed through the ejection of the ink (satellite droplets) (Figure 2.4). In time, stable droplet ejection is achieved by adjusting voltage and pressure parameters to achieve an appropriate balance (Figure 2.5 (a,b)). This sometimes takes a little trial and error.

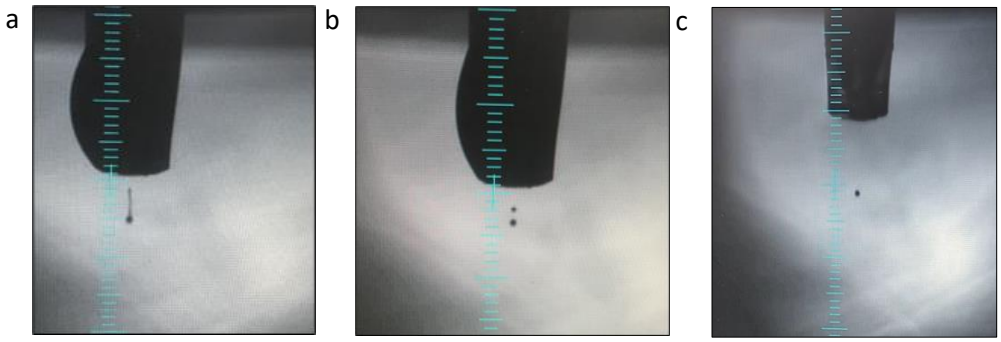

Figure 2.4. Drop generation from inkjet printer (a) with satellite, (b) mist and (c) stable ejection.

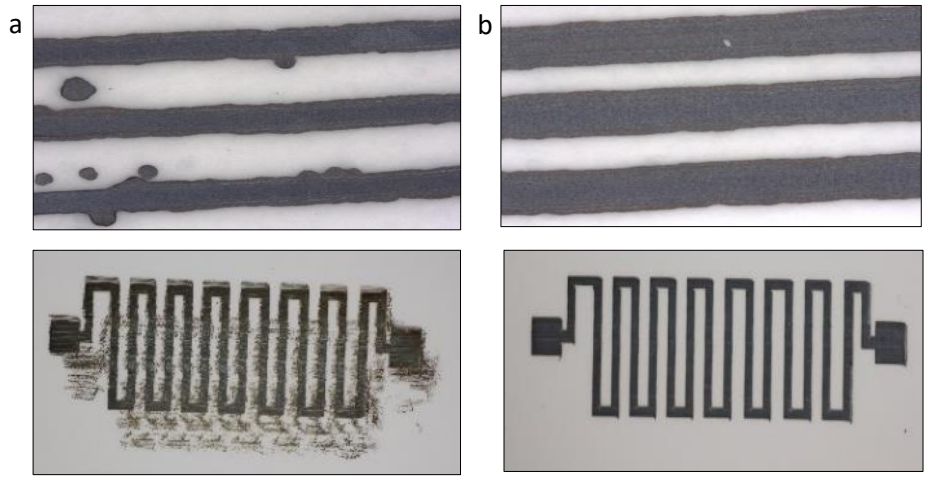

Figure 2.5. Microscope images of (a) poor-quality printing on photo paper, (b) good quality printing on photo paper.

2.8.3 Ink deposition

The silver nanoparticle-based ink was ultrasonically dispersed for 30 min, then loaded into the nozzle syringe (Figure 2.6) which connected to the piezo nozzle via a cut off hypodermic needle and a small piece of soft silicone tubing. This was held in a custom-machined PVC holder . Then, once stable droplet formation had been tuned (see section 2.8.2), ink was deposited on the substrate by an ink jet printing program, using either standard commands to print simple lines, or using a bitmap image to control printing. The printed patterns sintered at room temperature on photo paper. The film thickness was controlled by the pitch size of ink droplets deposited onto the substrate, and the number of layers overprinted.

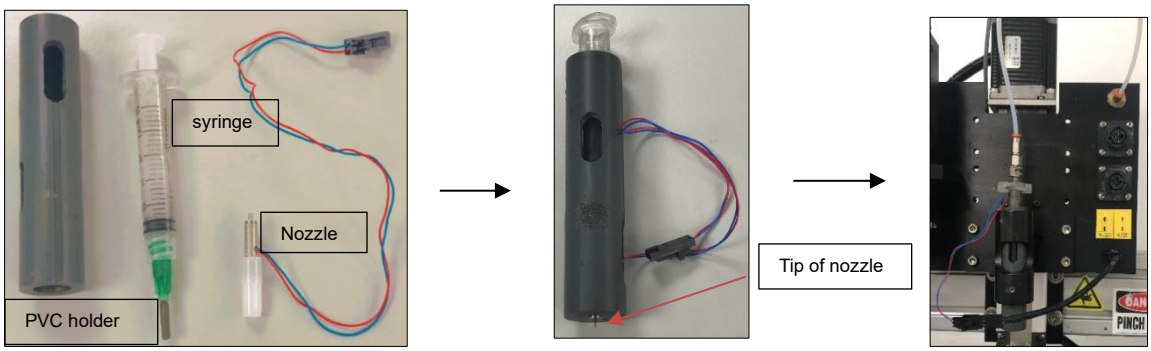

Figure 2.6. Nozzle, syringe, holder image and assembly.

2.9 Characterization of deposited films

After production, the printed samples were investigated via optical microscopy. Images were obtained using a Nikon Eclipse LV150N microscope with CCD camera (Minato, Tokyo, Japan) to visualize the inkjet-printed droplets.

SEM/EDS for surface morphology and a Bruker DektakXT Stylus Profiler (Coventry, UK) was used for physical size measurements (width/thickness), where the average of four or more measurements were used.

The profilometer based on a diamond stylus tip was used to measure the physical dimension of the silver track on different substrates. Data was evaluated by Vision 64 (Bruker) analysis software. The principle is illustrated with the help of the visual images (Figure 2.7).

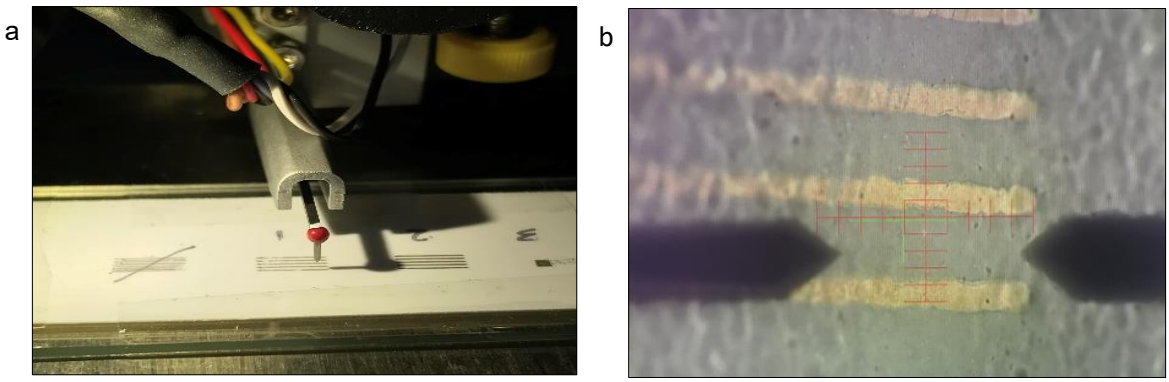

Figure 2.7. (a) Diamond stylus profilometer in contact with the printed track; (b) area markers showing the region to be scanned.

Profilometry is a process that is used to detect the surface of the printed pattern by using a sharp probe with radius 2 μm to scan across the feature surface. As a result, the overall thickness and width of the film, and the pattern roughness can be evaluated [7].

This kind of profilometer takes measurements electromechanically, by moving the diamond stylus vertically over the printed pattern surface (Figure 2.7) according to user programmed scan length, speed and stylus force. The radius of the diamond stylus can measure small surface variation /vertical features ranging from 10 nm- 1 mm height. The height position of the stylus generates an analog signal which is transformed into a digital signal, stored, analysed and displayed (Figure 2.8). More examples of "cross- sectional" scans can be found in Appendix A (Chapter 9).

Figure 2.8. Stylus profilometer trace across a printed track.

The profilometer measurements were set up as follows, stylus type (radius: 2 μm) was used , profile (Hills and valleys), the scan range was set (6.5-100 μm) to sufficiently cover each experiment sample. The length varied depending on the line thickness/width (250-600 μm). To improve the accuracy of the profile area measurements, the scan duration and stylus force were set to 10 sec and 1 mg, respectively.

2.9.1 Conductivity measurement

Conductivity measurements of printed tracks on substrates were performed by measuring the resistance of printed patterns using a Beha-

Amprobe (Glottertal, Germany) digital multimeter (True RMS Data logging Multimeter 72-3540, Max. voltage (1000 V), Input resistance: about 10 MΩ). When measuring low resistance for highly conductive samples, the test lead will bring about measurement errors of resistance between 0.10 and 0.20 Ω.

Additional electrical measurement techniques for resistivity could be used for more accurate measurements such as a 4-point-probe (4PP). However, for the reported experiments, only a Digital Multimeter was available at the time of conducting the experiments. As the contact resistance plays an important role in the accuracy of measurements, especially for samples with short track lengths (5 mm), the resistance measurement was repeated multiple times for the same track and the average was taken at the end. Then, key values were calculated using the expression relating resistance to resistivity and conductivity, $\rho = R \cdot A/L$, $A = h \cdot W$, $\sigma = 1/\rho$, according to equations (1.1, 1.2, 1.3) in Chapter 1.

2.9.2 Sintering

In this work, a more desirable strategy was used which employs a surface coating or post-printing coating that facilitates spontaneous chemical sintering of NPs at room temperature. It had mostly used chloride-based room-temperature sintering on different types of substrates, both those that have a chloride content already (photo paper) and others that do not naturally contain chloride ions. The halide can detach the anchoring groups of stabilisers, which are attached to the NPs, to enable the particles to accumulate and eventually become connected, allowing them to be sintered(Figure 2.9).

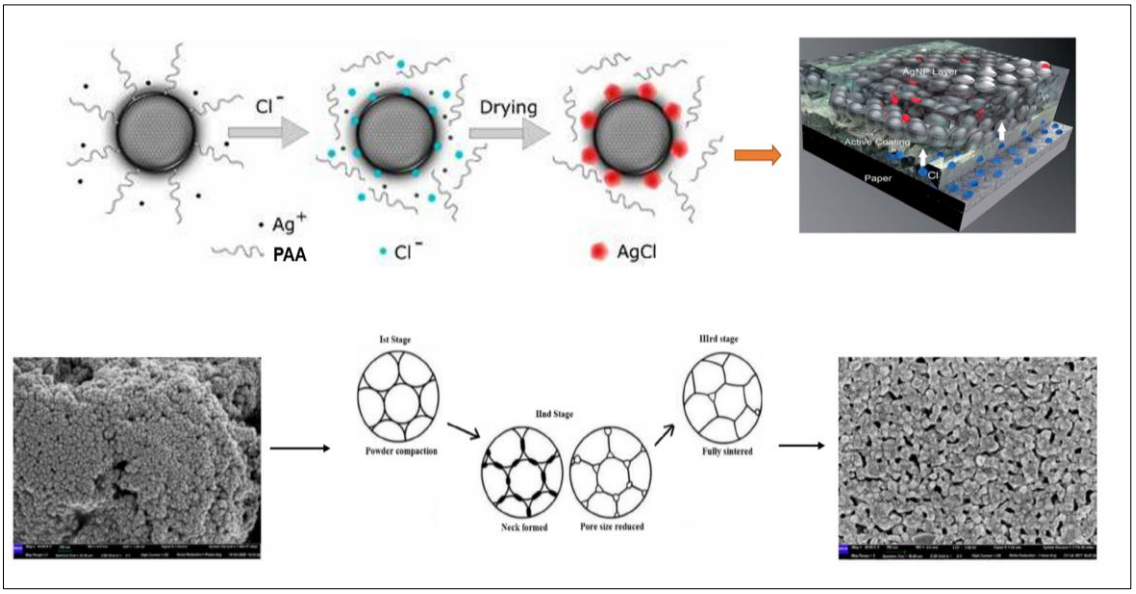

Figure 2.9. Schematic diagram showing the chemical sintering process [16,17].

In order to produce conductive tracks from the printed core-shell inks, it is necessary to remove the strong stabilizer that is adsorbed on the surface of the nanoparticles, required to give the particles stability during synthesis and in the ink formulation. Other previous studies have used a high temperature to achieve sintering and allow particles to merge. However, this could damage the Ag shell [8] and/or the substrate. In this work, sintering at room temperature was achieved by trying to destabilise the OAM through chemical processes, similar to the chloride displacement of PAA/or PVP/or PVOH discussed above. For this dip chemical sintering two simple steps were followed: ligand exchange and electrolyte immersion, as described by [8]. Firstly, a solution (10 v%) of the hydrophilic amine 1-amino-2-propanol (MIPA) in methanol was prepared. To get the ligand exchange, the coated film should be immersed in this solution for 1 minute and rinsed with methanol. That way hydrophobic-to hydrophilic transition was obtained, thus improving the wetting capability of electrolyte solution on the surface of the metal film [10]. Secondly, a 2 wt% reducing electrolyte solution was prepared by dissolving $NaBH_4$ in pH=12 (10 mM) NaOH and the film was then immersed again into the electrolyte solution for 1-5 min and finally washed with de-ionized water. In this step, the solution allows particles to coalesce together by destabilizing the ligand to achieve effective sintering at room temperature [8].

2.10 Preparation of coating solution

The concentrated PVOH solution (10% w/w) was prepared by dissolving the required amount of solid polymer (20 g) into pre-heated double-distilled water over a hotplate at a temperature ~100 °C followed by continuous stirring for 1-2 hours, until a uniform solution was produced. The polymer powder was sprinkled into the vortex of the stirring water to avoid clumping.

A primary stock solution of KCl having a concentration of 1 M was prepared in a 100 mL volumetric flask by dissolving 7.45 g of KCl into double-distilled water. The different solutions of KCl in the concentration range 1 M,0.1 M,0.01 M and 0.001 M were prepared from this primary stock solution by serial dilution.

Finally, 20 mL disposable scintillation vials were used to prepare five different aqueous PVOH/KCl solutions with different compositions (9:1). The solutions were homogenized by shaking the vials for a while to get a final solution with a PVOH content of 9% and varying Cl^- concentration.

The behaviours of these solutions were tested immediately by wire wrapped coating bar from RK printcoat Instrumenta (https://www.rkprint.com/products/k-hand-coater/) on the substrate to see if they produced sintered films and low resistance in order to improve the printability of silver ink.

References

(1) Mavuri, A.; Mayes, A. G.; Alexander, M. S. Inkjet Printing of Polyacrylic Acid-Coated Silver Nanoparticle Ink onto Paper with Sub-100 Micron Pixel Size. *Materials*. **2019**, *12 (2277)*, 1-10

(2) Srivastava, C.; Chithra, S.; Malviya, K. D.; Sinha, S. K.; Chattopadhyay, K. Size Dependent Microstructure for Ag-Ni Nanoparticles. *Acta Mater*. **2011**, *59 (16)*, 6501–6509.

(3) Teerasong, S.; Jinnarak, A.; Chaneam, S.; Wilairat, P.; Nacapricha, D. Poly(Vinyl Alcohol) Capped Silver Nanoparticles for Antioxidant Assay Based on Seed-Mediated Nanoparticle Growth. *Talanta*. **2017**, *170 (4)*, 193–198.

(4) Pajor-Świerzy, A.; Socha, R.; Pawłowski, R.; Warszyński, P.; Szczepanowicz, K. Application of Metallic Inks Based on Nickel-Silver Core-Shell Nanoparticles for Fabrication of Conductive Films. *Nanotechnology*. **2019**, *30 (2)*, 1-8.

(5) Wang, Z.; Liang, X.; Zhao, T.; Hu, Y.; Zhu, P.; Sun, R. Facile Synthesis of Monodisperse Silver Nanoparticles for Screen Printing Conductive Inks. Journal of Materials Science: *Materials in Electronics*. **2017**, *28 (22)*, 16939–16947.

(6) Thu, N. N. A.; Park, J. G.; Kim, S. H. Synthesis of Ni-Ag Core-Shell Nanoparticles by Polyol Process and Microemulsion Process. *Bull Korean Chem Soc*. **2013**, *34 (10)*, 2865–2870.

(7) Vykoukal, V.; Bursik, J.; Roupcova, P.; Cullen, D. A.; Pinkas, J. Solvothermal Hot Injection Synthesis of Core-Shell AgNi Nanoparticles. *J Alloys Compd*. **2019**, *770 (8)*, 377–385.

(8) Dai, X.; Xu, W.; Zhang, T.; Shi, H.; Wang, T. Room Temperature Sintering of Cu-Ag Core-Shell Nanoparticles Conductive Inks for Printed Electronics. *Chemical Engineering Journal*. **2019**, *364 (1)*, 310–319.

(9) Shen, W.; Zhang, X.; Huang, Q.; Xu, Q.; Song, W. Preparation of Solid Silver Nanoparticles for Inkjet Printed Flexible Electronics with High Conductivity. *Nanoscale*. **2014**, *6 (3)*, 1622–1628.

(10) Lee, J.; Kim, J.; Park, J.; Lee, C. Characterization of in Situ Sintering of Silver Nanoparticles on Commercial Photo Papers in Inkjet Printing. *Flexible and Printed Electronics*. **2018**, *3 (10)*, 1-10

(11) Tobjörk, D.; Aarnio, H.; Pulkkinen, P.; Bollström, R.; Määttänen, A.; Ihalainen, P.; Mäkelä, T.; Peltonen, J.; Toivakka, M.; Tenhu, H.; Österbacka, R. IR-Sintering of Ink-Jet Printed Metal-Nanoparticles on Paper. *Thin Solid Films*. **2012**, 520 (7), 2949–2955.

(12) Lee, J.; Kim, J.; Park, J.; Lee, C. Characterization of in Situ Sintering of Silver Nanoparticles on Commercial Photo Papers in Inkjet Printing. *Flex. Print. Electron*. **2018**, *3 (10)*, 1-10

(13) Derby, B. Inkjet Printing of Functional and Structural Materials: Fluid Property Requirements, Feature Stability, and Resolution. *Annu Rev Mater Res.* **2010**. *40 (6)*, 395–414.

(14) JOHNS, ASHILEY, STEPHEN. Ink-jet Printing of Multi- Phase Formulation. Durham Theses, *Durham University*, **2017**. 1-206.

(15) Cummins, G.; Desmulliez, M. P. Y. Inkjet Printing of Conductive Materials: A Review. *Circuit World*. **2012**, *38 (4)*, 193–213.

(16) Öhlund, T.; Hummelgård, M.; Olin, H. Sintering Inhibition of Silver Nanoparticle Films via AgCl Nanocrystal Formation. *Nanomaterials*. **2017**, *7 (8)*, 1-13.

(17) Prakasam, M.; Locs, J.; Salma-Ancane, K.; Loca, D.; Largeteau, A.; Berzina-Cimdina, L. Fabrication, Properties and Applications of Dense Hydroxyapatite: A Review. *J. Funct. Biomater*. **2015**, 6 (4), 1099–1140.

Chapter 3. Pure silver nanoparticles results and discussion

3.1 Characterisation of Ag-PAA NPs formed by chemical reduction method in an aqueous solution.

Ag NPs play a crucial role as the most common conductive ink material, when high conductivity is required, due to the excellent oxidation resistance and high conductivity of silver, and due to the existence of suitable capping agents for the sake of grain size stabilization and homogeneous particle production. In addition, the use of aqueous solvent will be a substantial benefit to achieve the easier process of synthesis during the chemical reduction method, which is the most frequently used method for the production of Ag NPs as stable colloidal dispersions, in water or organic solvents. Additionally, Ag can be conveniently integrated into inks that adhere better to substrates than other metals [1].

In this presented study, it was attempted to produce Ag nano ink for inkjet printing using a concentrated solution based on Ag NPs, which makes this aqueous synthesis practical for large scale production. In fact, analogous results obtained by other methods of synthesis of the AgNP can be found in the literature. For example, a similar route was used in a previous study by Mau Dang C. *et al.* [2], who successfully synthesised stable silver/poly (acrylic acid) NPs by reducing silver nitrate in aqueous solution with the presence of ethanolamine (mEA) as the reducing agent. The acquired Ag NPs showed an average size about 22 nm in water. Their suspension ink, which contained 10%wt. of Ag NPS was stored for three months, showing a great stability with no aggregation.

Similarly, Shen W. *et al.* [3] synthesized a highly stable PAA-coated silver NP by a simple and environmentally friendly wet chemistry method in an aqueous medium. The fully aqueous phase contained silver nitrate, PAA as the capping agent and monoethanolamine (MEA) as the reducing agent. The main major particle size distribution of the Ag NPs was in the range of 30-50 nm with a narrow size distribution. That is relatively bigger compared with the nanoparticle that we have achieved with similar chemicals and slight differences in the synthesis process. The Ag NP ink was prepared simply by dispersing the as-synthesised silver NP powder in water and showed a highly stable /homogenous dispersion

of silver NP ink. The inks were printed on paper and PET substrate using a common colour printer. The printed pattern showed a resistivity about $3.7x10^{-8}$ Ω.m, which is close to twice that of bulk silver, when heat-treated at 180 °C. In the study reported in this thesis, the electric resistivity reached around 2 times RBS ($2.918x10^{-8}$ Ω.m) with room temperature sintering (see results below).

In our approach, for synthesis of the Ag NPs we have followed Mavuri A. *et al.* [4] routes, which involved silver nitrate, triethanolamine (TEA) serving as reducing agent (the hydroxy groups are the key to reduce silver ion), and PAA as the capping agent, in order to produce particles with a nano range size, which helps in achieving our goal to formulate a silver conductive ink for inkjet printing. Also, it implies that Ag NPs with a reasonably narrow size dispersity can be typically obtained by this reduction method. Figure 3.1 shows the mechanism of polymer protection and the synthesis of silver nanoparticles from silver nitrate.

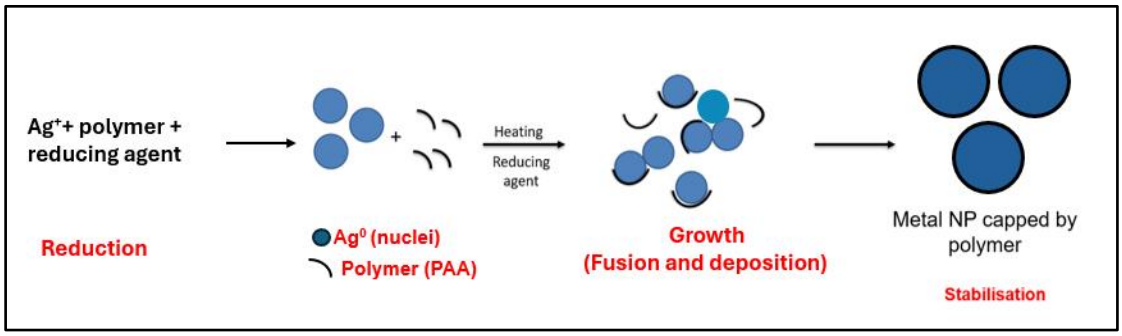

Figure 3.1. Schematic sketch of the mechanism of polymer protection.

After adding TEA to a silver nitrate solution and PAA solution, the mixture goes through a gradual change in colour from colourless to dark black solution, which concurs with the nucleation and growth of silver nanoparticles. At the time of nucleation, some Ag° species convert to nuclei and some Ag^{+} are reduced continuously to Ag° leading to both deposition on existing nuclei and creation of new ones. The nucleation stage extends for a while, after which growth predominates. Generally, a short nucleation phase leads to more monodisperse particles, but unlike in hot injection methods (where sudden injection of a component initiates a large number of nuclei in a very short time), this temporal aspect is not well controlled in these aqueous syntheses. Finally, the mixture colour gradually becomes dark as the Ag NPs grow in size. After a 24 h period, the colour changing stops, which clearly marks the termination of nanoparticle

growth. After the reaction, EtOH is added to induce rapid particle coagulation, which then precipitates the NPs more easily.

The prepared AgPAA NPs were dispersed in water at 25 °C to measure the particle size distribution with DLS. The determined size was obtained from the average of three sequential runs to be about 4 nm without any filtration as illustrated in Figure 3.2 (number averaged data). The value of the polydispersity index (PDI) indicated a good range of particle size distribution about 0.4.

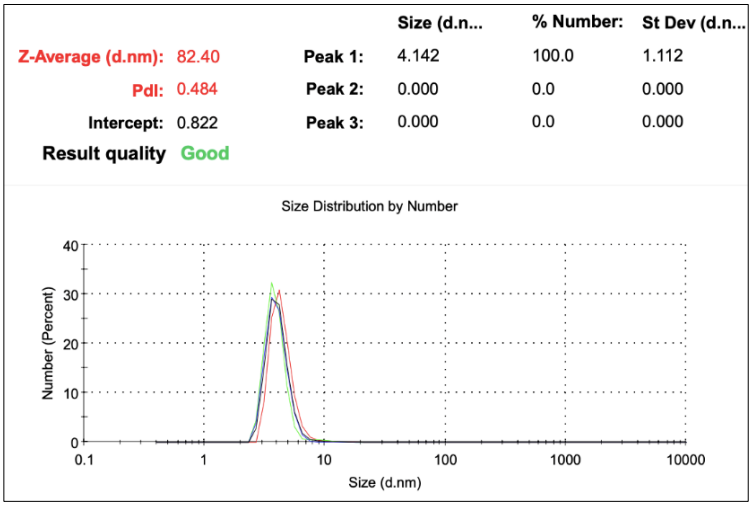

Figure 3.2. The DLS graphs of as-synthesised Ag-PAA NPs.

As shown, there was some variability of the replicate measurements and this is most likely due to the presence of a small amount of aggregated material in the (unfiltered) sample (hinted at by the Z-average size, compared with the number averaged size), coupled with the size distribution making the data a bit unstable. Lots of different size distributions give almost identically good fits to the function within the DLS software under these conditions, which makes accurate and reproducible measurements difficult by this technique. Despite this slight uncertainty, the mean particle size distribution of about 4 nm means most of the particles are within the appropriate size range, and not 100s of nm, which might cause problems with nozzle clogging during printing.

It is useful to compare these results with the study by Milardovic S. *et al.* [5], who have synthesised silver nanoparticles by a similar chemical reduction method using hydrazine monohydrate as the reducing agent and PAA as the protecting agent in an aqueous solution. The obtained silver NPs were approximately between 1.6-3.2 nm, which is much smaller than the Ag NPs

intended for inkjet printing found in other literature. In contrast, our approach to reducing silver nitrate was carried out with a nontoxic reducing agent (triethanolamine) and we have produced a similar particle size (4 nm). In their study, hydrazine is a highly toxic and explosive chemical that needs much care in a large scale. These results confirmed that such small particle sizes do not seem to compromise the quality of printed patterns.

The stability of the PAA-Ag NPs conductive ink has been confirmed by a measurement of the electrokinetic potential. The zeta potential measured value was -38 ± 8.2 mV, and this suggests ink stability. Typically, particles with zeta potentials more positive than +30 mV or more negative than -30 mV are normally considered stable. This result also confirmed that it has a negative charge, which by assumption must come from carboxylate ionisation (that would be the COO^- facing outwards into solution most likely).

In this study, the pH was ca. 7 and this caused the electrolytic dissociation of the carboxylic groups to form carboxylate anions and hence a negative electric charge on the Ag NPs surface. Thus, the Ag NPs become highly dispersed without aggregation due to the electrostatic repulsion between the Ag NPs [6] which will be enhanced by the steric (wrapped polymer backbones) stabilisation of the polymer.

Some evidence to support these results is provided by a study done by Huang Q. *et al.* [6]. They investigated the effect of pH on the zeta potential of the silver ink and its effect on the stability of silver nanoparticle-based ink. At a pH above 5, the layer of polymeric dispersant molecules absorbed on the surface of the particles acted as an effective layer for steric stabilization to prevent them from agglomerating. In contrast, at a pH below 5, the silver nanoparticles undergo aggregation, due to the surface being electrostatically neutral and the repulsive force for dispersion of particles being lost [6].

For comprehensive study, the particle size distribution was measured by TEM, as shown in Figure 3.3, indicating the formation of nonuniform Ag NPs with the size distribution mainly between 5 nm and 27 nm. It is clear that the variability of measurements is most likely due to the presence of clustering NPs in the sample and that is caused by the tendency of the small size particles in the solution to agglomerate, especially as the particles dry and concentrate on the

grids during the TEM sample preparation. The DLS data suggest that the particles are much better dispersed in dilute solution.

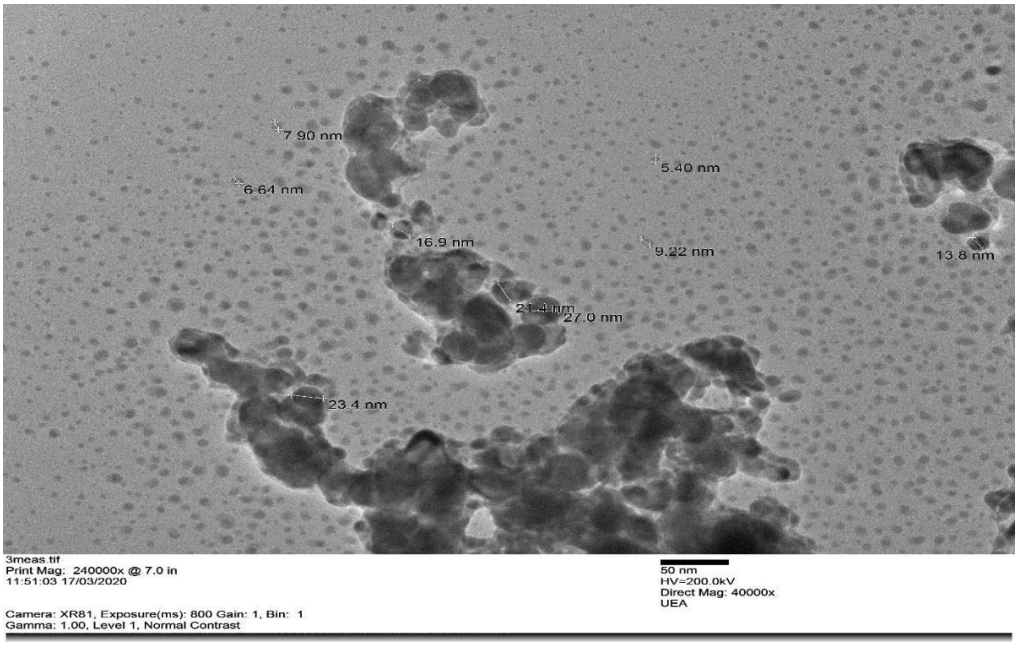

Figure 3.3. TEM image of an Ag-PAA NPs.

It is important to be mindful of the fact that the DLS size distribution tends to present as an overestimate of size comparing with TEM results. This is for the reason that the DLS measurements were done in a fully solvated liquid environment, and thus give a measurement for the hydrodynamic radius and not the physical radius of the core particles, as given by the TEM images. The TEM tends to show the inorganic core crystal size only, since this is the electron- dense material. The organic ligands usually show up only faintly, unless specifically stained.

The SEM image (Figure 3.4) shows a near complete monolayer of Ag NPs and the majority were approximately spherical in shape with a relatively narrow size distribution. The image shows some areas of rather smaller particles, as well as the (mostly larger) particles that have been measured, which highlights the difficulty of obtaining objective size measurements from limited numbers of particles in single (or maybe a few) images. These results were in reasonable agreement with the size distribution estimated by DLS, however.

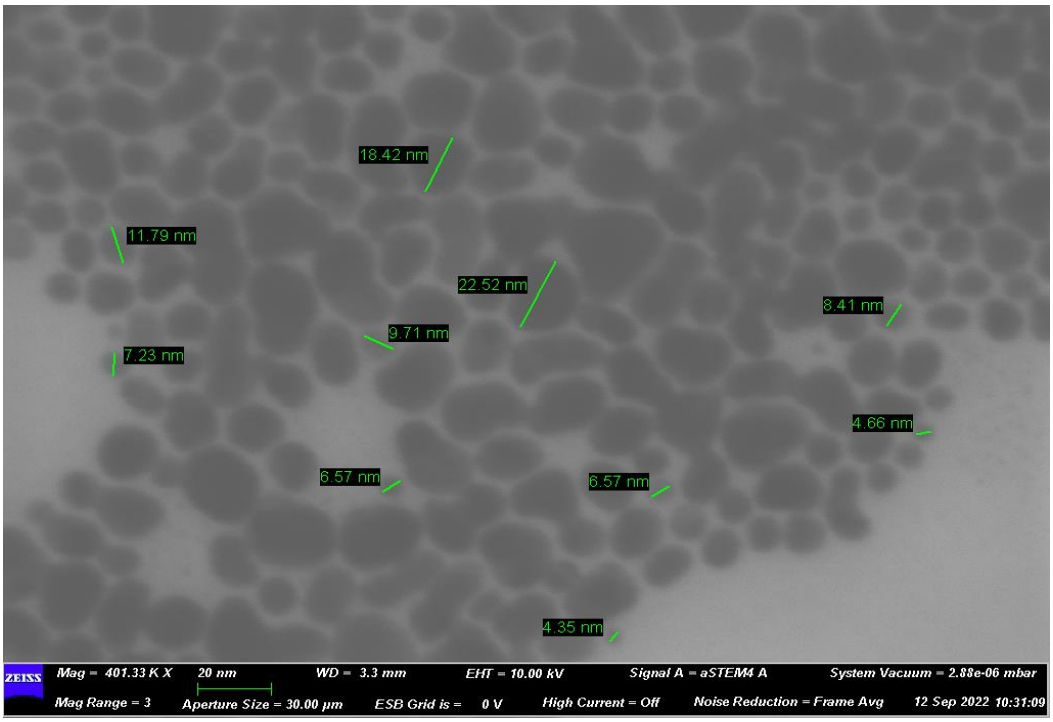

Figure 3.4. SEM image of the Ag-PAA NPs powder.

The prepared Ag-PAA NPs have been dried in the oven at 80 °C in order to get the dry powder sample, prior to measuring by TGA. Then about 10 mg of the powder was analysed with TGA at a heating rate of 10 °C/min from room temperature to 500 °C. The result is presented in Figure 3.5. The thermal decomposition of the Ag-PAA NPs begun at about 100 °C, shown by a rapid decrease in mass, and stabilized at 450 °C, decomposing in two steps. Firstly, the sharp mass loss gradient curves observed was interpreted as describing the reaction of the nearby -COOH groups on the stabilising polymer to generate anhydride rings with loss of water. At the higher temperature, complete decomposition of the organic material occurs to volatile fragments that are lost. The overall weight loss up to 500 °C was very small, about 2.15%. That confirmed almost all the material is inorganic core and very little organic stabilising ligand.

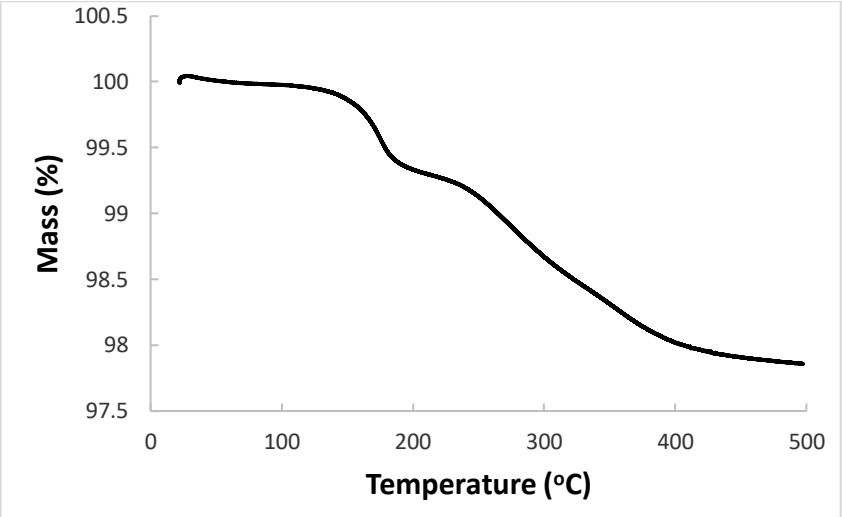

Figure 3.5. TGA of the Ag-PAA NPs powder.

PAA is a highly hydrophilic polymer and initial weight reduction in the TGA curve (up to about 120 °C) is due to physical moisture loss (evaporation). The weight loss of 1.25% in TGA curve (around 120-180 °C) is due to dehydration – chemical loss of water by two OH groups on adjacent COOH groups from parts of the chain coming together with elimination of water and formation of an anhydride, which is in agreement with the work of Lu and Hsieh [7] and Shen W. *et al.* [3]. The weight loss from 200 to 500 °C represents organic material oxidation and removal as small volatiles (e.g., CO_2 or small organic fragments).

3.1.1. Characterisation of 30%, 20% and 10% AgPAA standard ink

The inkjet printing for the formulated inks was completed by using a Microfab (Plano, TX, USA) Jetlab 4 inkjet printer equipped with 80 or 50 μm nozzle diameters in ambient atmosphere. The silver conductive ink was formulated by dispersion of dried as-synthesised Ag NPs capped by PAA in a water-EG mixture with no surfactants or other additives and that was obtained by ultrasonic treatment. The conductive standard ink with 33% EG in the presence of NaOH (pH ca.7.31) was stored about 9 months without any sedimentation stored in a fridge and shows an optimal size distribution while storing as shown in Table 3.1.

Table 3.1. The DLS data of prepared 30% standard silver ink.

Period	Size (d. nm)	PDI	Z-Average
June 2020	3.7	0.48	75.9
July2020	4.5	0.46	72.9
August 2020	4.1	0.55	77.6
September 2020	3.9	0.55	60.6
October2020	3.8	0.48	63.1
November2020	3.1	0.48	91.1
December2020	3.4	0.55	85.8
January2021	8.6	0.57	52.9
Februrury2021	8.8	0.58	53

Table 3.2 and 3.3 show the DLS data of prepared 20% and 10% standard silver inks respectively. The size of particles in ink formulations did not show any large changes, which is very useful if they were to be used commercially. There was a small trend towards larger size and increased PDI (slight aggregation), although interestingly, the Z-average value tended to decrease slightly, suggesting that maybe the small number of larger aggregates tended to disperse over time. This was less evident for the 10% formulation, however.

Table 3.2. The DLS data of prepared 20% standard silver ink.

Period	Size (d. nm)	PDI	Z-Average
August 2020	5.5	0.53	99.6
September 2020	2.7	0.57	32.5
October2020	2.4	0.42	34.5
November2020	4.1	0.43	40.4
December2020	4.2	0.43	58.2
January2021	6	0.56	58.2
Februrury2021	6.9	0.56	58.6

Table 3.3. The DLS data of prepared 10% standard silver ink.

Period	Size (d. nm)	PDI	Z-Average
June 2020	4.4	0.46	85.5
July2020	3.6	0.57	48.2
August 2020	4.4	0.46	85.5
September 2020	3.6	0.57	48.2
October2020	5.9	0.49	114.4
November2020	3.1	0.52	88
December2020	4.1	0.55	72.6
January2021	7.4	0.52	73.6
Februrury2021	10.9	0.52	79.7

The obtained conductive silver ink in 30% w/w AgPAA showed an electrical resistance about 5.4 Ω for a single layer which was produced by a simple manual 'smear test 'on glossy photo paper with smooth surface and the smeared layer had a shiny metal-like appearance. This simple qualitative "spot-test" demonstrates that the ink has a good stability and can likely be printed to form films of good quality.

3.1.2 Ink viscosity measurement

The viscosity measurement was performed by using the rheometer at constant shear rate (25000.01/s) and velocity (150 rad/s), stress($6.366x10^{-6}$μPa) and Torque (10.0 μN·m) at room temperature. Figure 3.6 shows the viscosity over time which is about $0.5×10^{-2}$ Pa·s and it is almost constant over time.

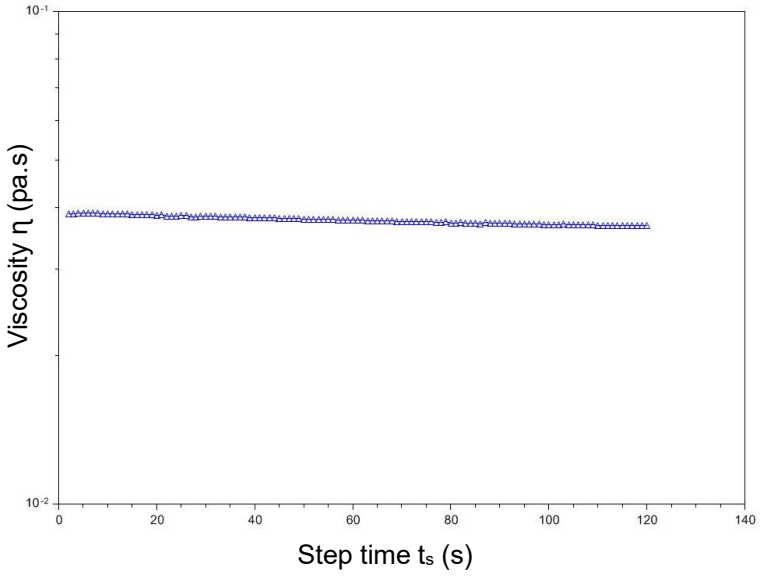

Figure 3.6. Viscosity of Ag NPs formulated ink.

3.1.3 The Effect of printing AgPAA patterns on photo paper with different parameters

The inkjet printer was used to form silver tracks with different printing passes. Figure 3.7 shows optical microscope images of tracks with different width dimensions as it is controlled by pitch size. When the size between droplets is set at 95 μm the line width was about 82 μm and gradually increased to 180 μm as the pitch size dropped down to15 μm (Figure 3.7 (d)).

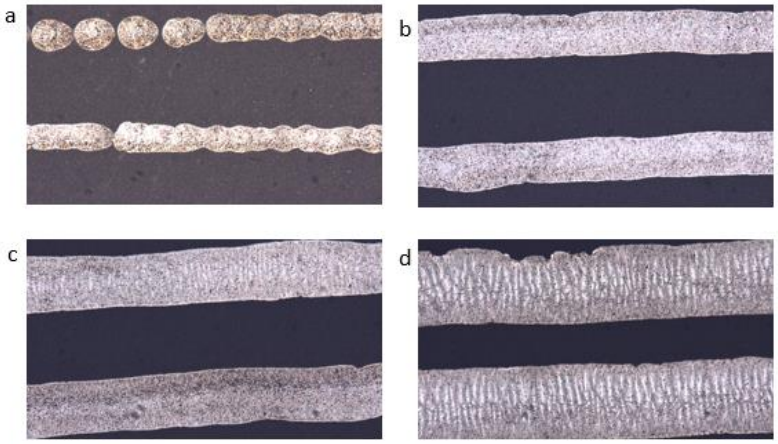

Figure 3.7. Optical microscope images comparing different line widths produced at different print pitch size settings for the inkjet printer (a) 95 μm, (b) 55 μm, (c) 35 μm, and (d) 15 μm.

As shown in these images, there was some single silver dot pattern and breaking of the line on the pitch size 95 μm. The silver track in this state cannot be conductive. However, when the distance between dots decreased, the droplets have more overlap and formed a continuous line. Meanwhile, the silver printing track thickness increased from 6.58 μm to 32.5 μm with decreasing the pitch size and the line becomes denser because more inks was applied during printing.

3.1.4 Morphology of AgPAA ink and printed track film

On the sintered conductive silver patterns, neck-like junctions between nanoparticles were observed using SEM as shown below. Once the ink is confirmed jetting, an important aspect is the interaction of the droplet with the substrate, such as spreading and solvent evaporation. The surface quality and smoothness of the selected substrates are important in order to define their

surface characteristics. Paper substrates have been used with printable ink because of their advantages such as: low cost, electrical and chemical reliability.

Figure 3.8 shows the SEM images of the surface of printing paper used in these experiments at different magnification (10,000 – 20,000 – 40,000 – 80.000 kx) respectively. This may be used as a baseline to distinguish the particles and the paper surface on SEM images more clearly.

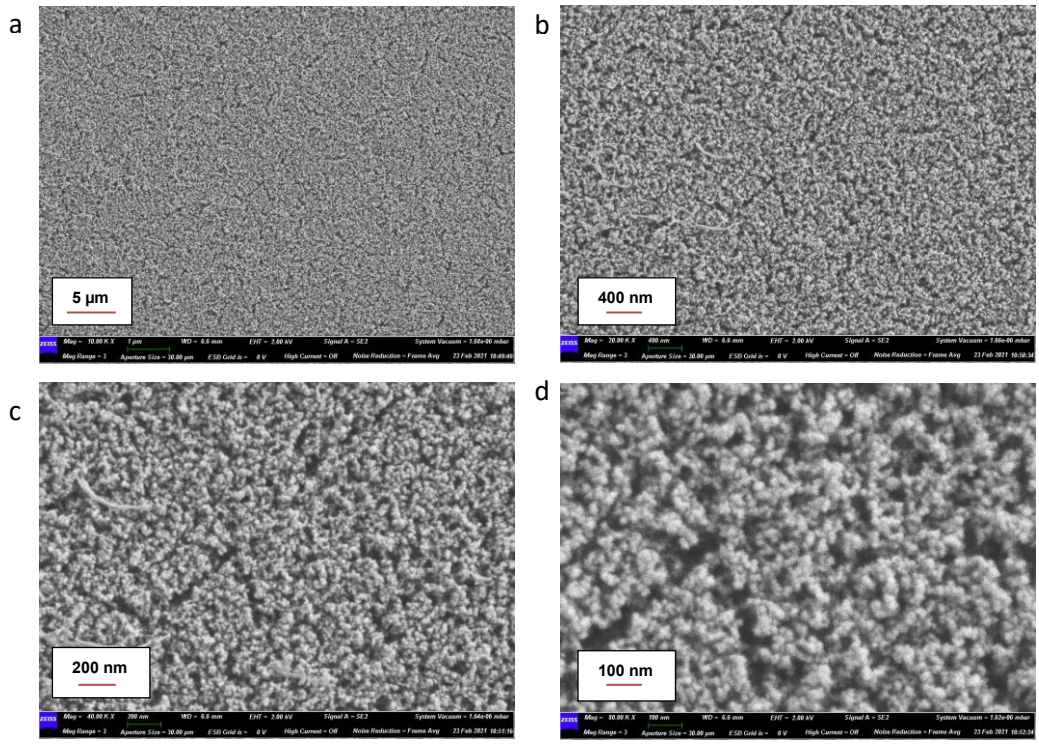

Figure 3.8. SEM images of printing paper surface at different magnifications. (a) 10,000 kx, (b) 20,000 kx, (c) 40,000 kx, (d) 80,000 kx.

To compare the physical appearance of deposited ink before and after sintering, samples of inks were deposited directly on SEM stubs, where no chloride is available and hence no sintering mechanism should be possible. Figure 3.9. shows comparative SEM images of un-sintered AgPAA ink samples. It can be seen that no physical change in the nanoparticle layer is apparent. In 10wt.% standard ink image (Figure 3.9 (a)) there are some uniform parts as well as some holes between particle groups. On increasing the concentration of the nanoparticles to 20wt.% (Figure 3.9 (b)) the layer appears to be more tightly packed compared with 10wt.%.

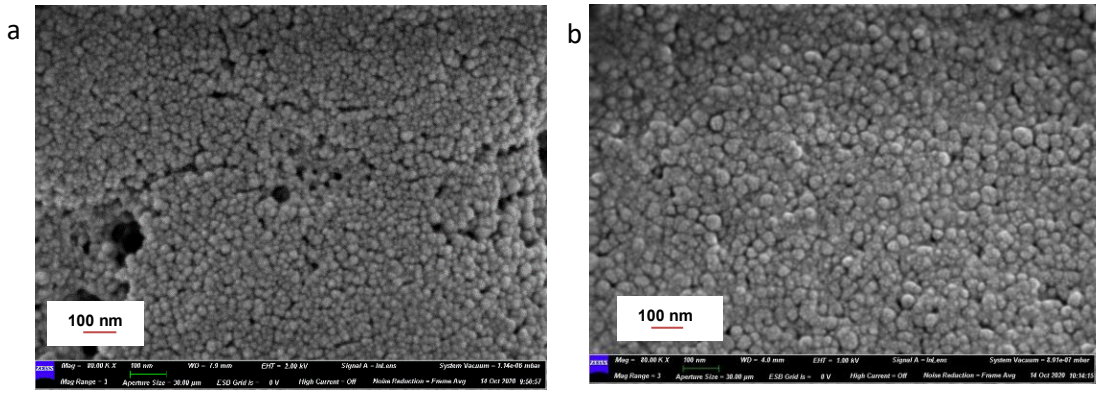

Figure 3.9. SEM images of un-sintered AgPAA standard ink before printing (a) 10 wt.%; (b) 20 wt.% AgPAA ink.

Figures 3.10-3.11 show the SEM images of a 10 wt.% AgPAA layer printed at temperature 25, 42 and 60 °C on paper substrate. It can be seen that crystals form in the films with (95 -15 μm) pitch size and the silver nanoparticles began to agglomerate, but the low-density packing of the nanoparticles and the sizes of agglomerated particles were not large enough to form a conductive path and look quite isolated and result in a non-conductive film, which can be due to low content of nanoparticles.

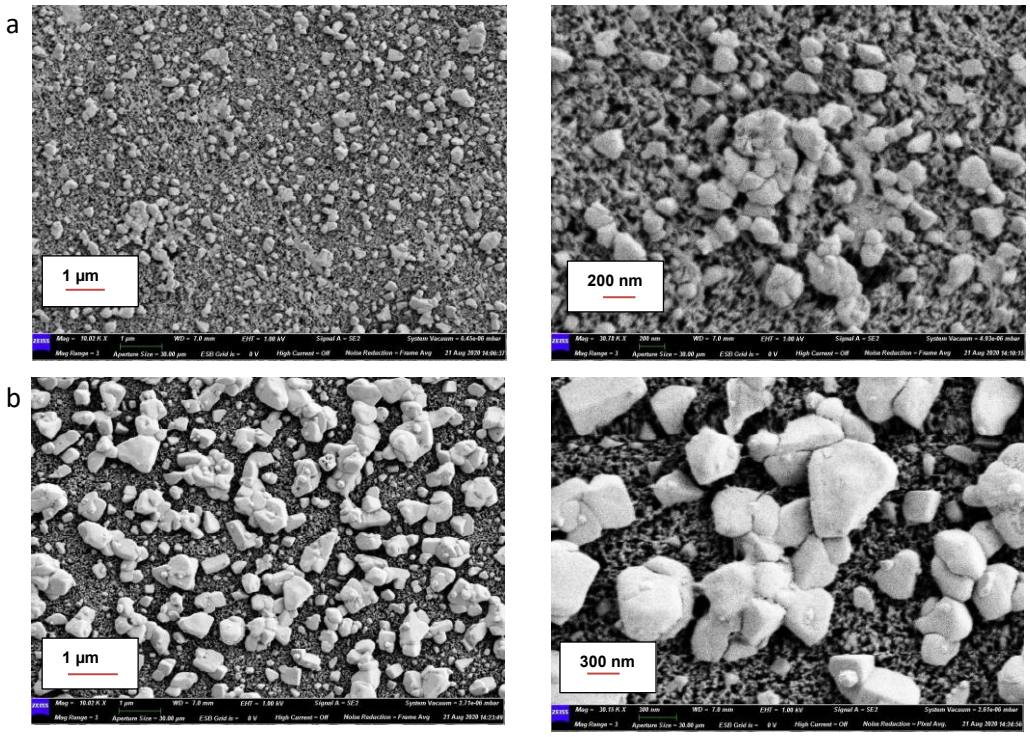

Figure 3.10. SEM images of 10 wt.% AgPAA printed tracks with (a) 95 μm and (b) 15 μm pitch size at 25 °C.

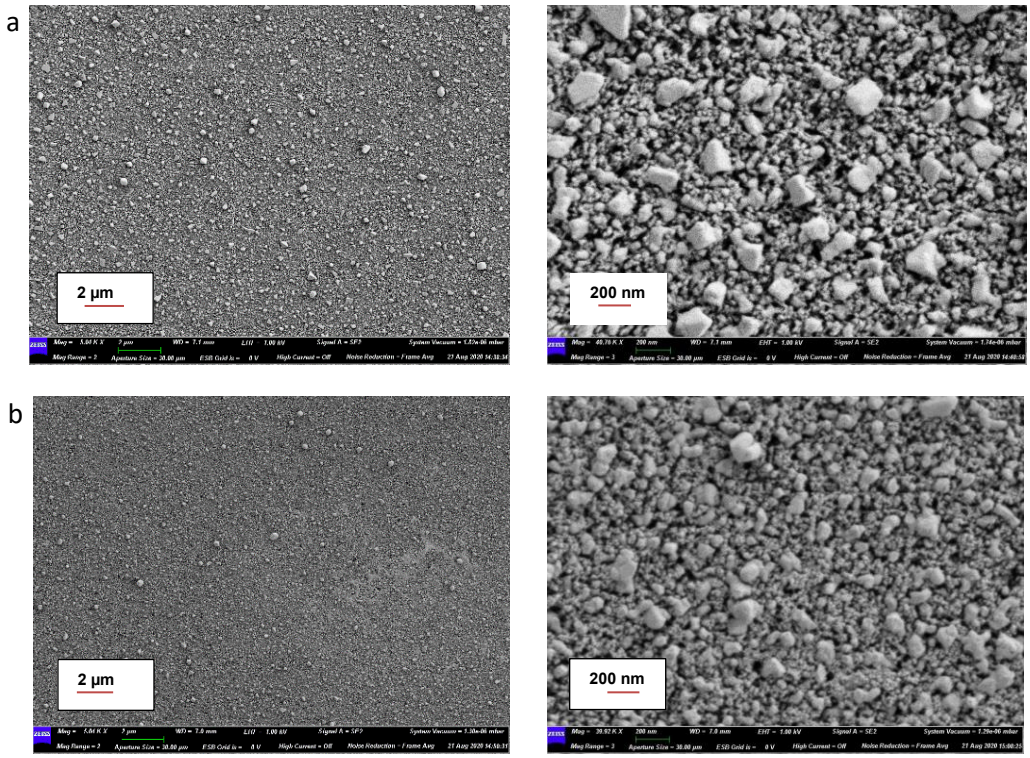

Figure 3.11. SEM images of 10 wt.% AgPAA printed tracks with (95 µm) pitch size (a) at 42 °C and (b) 60 °C.

The SEM images in Figure 3.12 display the nanostructures of 20 wt.% Ag PAA films with 95 µm and 15 µm pitch size at 25 °C. Significant differences in the morphologies of Ag PAA ink can be observed. With the increase of the nanoparticle ratio, the surface becomes more uniform with no significant holes as the NPs are allowed to come close enough on close contact which is sufficient to trigger their coalescence. The difference in the morphology observed on the substrate may result from the restricted mobility of the particles on the substrate once they are closely packed. Since the particles are already closely packed, contact between the metallic particles' surfaces may be formed, which leads to their coalescence and forming a conductive path.

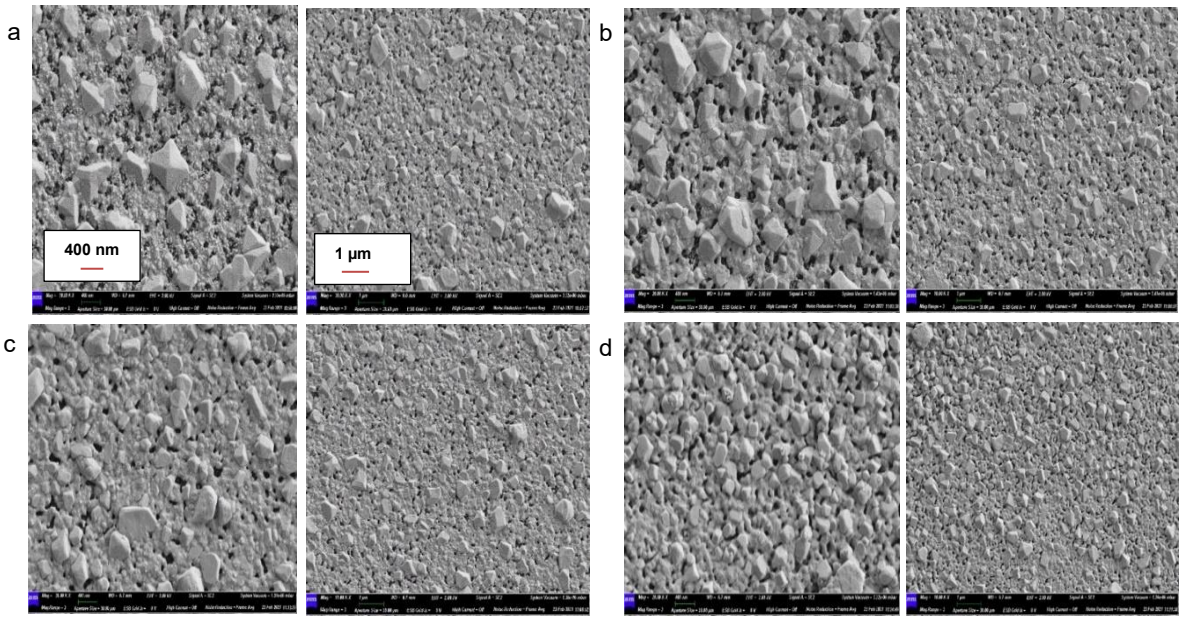

Figure 3.12. SEM images of 20 wt.% AgPAA printed tracks with (a) 95 µm; (b) 65 µm; (c) 45 µm; and (d) 15 µm pitch size at 25 °C.

The SEM images in Figure 3.13 show the nanostructures of 30% Ag PAA printing tracks at room temperature. At higher Ag weight ratios, the particle size increases as the pitch size decreased, and multiple percolation paths between particles are clearly observed as most of the particles are sintered. For more images see Appendix B (Chapter 9).

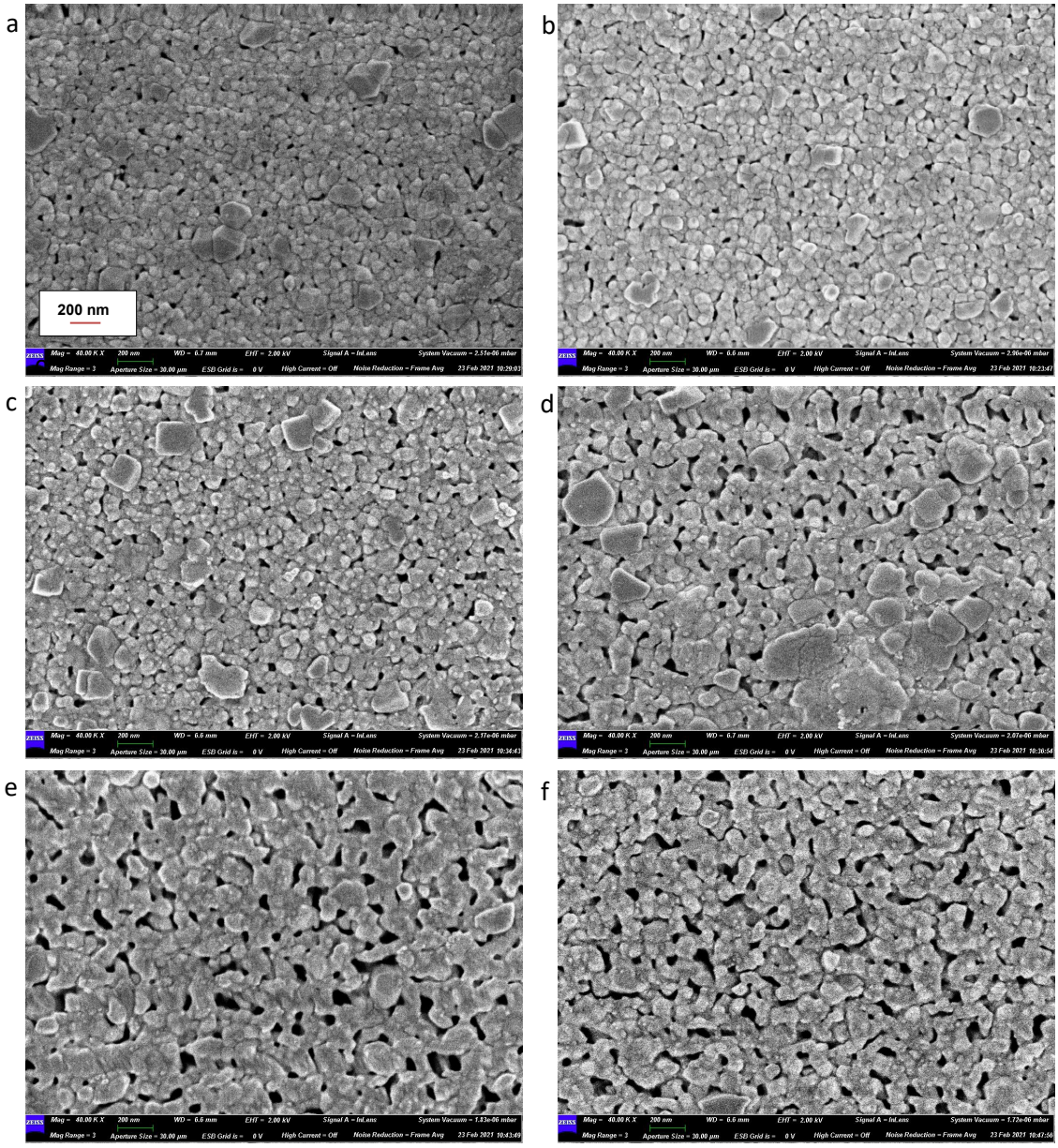

Figure 3.13. SEM images of the surface of the 30 wt. % AgPAA printed tracks at different pitch size (a)75 μm; (b) 55 μm; (c) 35 μm; (d) 15 μm; (e) overprinting x2 (65 μm); and (f) overprinting x4 (65 μm) at room temperature. Further relevant SEM images can be found in Appendix B).

The sintered pattern became conductive after sintering at room temperature; the particles agglomerated to create a conductive path, as shown in Figure 3.13 and the resistivity decreased to about two times higher than that of bulk silver (1.57 x10^{-8} Ωm). The most notable feature in these images is that smaller particle spacing will increase the number of contact points that allow electrons to pass, and therefore increase electrical conductivity of the NP.

Therefore, it can be concluded that with higher solid content inks, the sintering at room temperature for obtaining conductive patterns was successful.

3.1.5 Effect of print pitch on geometry, electrical and mechanical properties of Ag patterns printed on photo paper with room temperature sintering

For comparison of the electrical performance of films with 30wt.%, 20wt.% and 10 wt.% Ag/PAA, films were obtained using the same ink formulation, deposition, and sintering processes. The resistivities of the 30 and 20 wt.% Ag /PAA ink films were excellent and reached a resistivity of only x2 bulk silver (1.59×10^{-8} Ωm). This was calculated from the measured resistance and film thickness using the equation (1.1 in Chapter 1).

L is the printed line length, as described in Table 3.4. **L** was defined by the total printed track length (5 mm). The error on this was estimated from the likely reproducibility of placing the pointed resistance probes consistently at the two ends of this track (estimated to be ±0.2 mm), giving an error estimate of 4%. However, although the deposition of the ink for 10% AgPAA ink was good, there was no resistance from the printed track, unlike the other ink ratios.

To estimate errors for measurement from the tables below (Tables 3.4) (width, thickness and resistance) from the printed silver tracks, five measurements were performed for each track and then averaged. The uncertainty in the average was calculated using the standard deviation of the measured values for more accurate results. A potential error in estimating the resistivity/ conductivity of printed tracks is possible. The reason behind that is for highly conductive samples that are also short in length, overall resistance is very small, and electrical equipment can be at the limit of its measurement resolution. Therefore, longer printed tracks may provide more reliable data.

Table 3.4. Effect of pitch size on line width, thickness and resistivity for printed lines of 30% AgPAA ink on glossy paper with a 50 μm nozzle diameter, printed at room temperature.

Pitch size (mm)	Width (m)	Relative error in width	Thickness (m)	Relative error in thickness	Length (m)	Relative error in length	Resistance (Ω)	Relative error in resistance
0.095	80.9×10^{-6}	0.027	6.58×10^{-8}	0.287	0.005	0.004	-	-
0.085	81.9×10^{-6}	0.074	7.47×10^{-8}	0.557	0.005	0.004	-	-
0.075	89.1×10^{-6}	0.025	8.13×10^{-8}	0.141	0.005	0.004	30	0.027
0.065	89.5×10^{-6}	0.060	10.3×10^{-8}	0.311	0.005	0.004	22	0.090
0.055	96.6×10^{-6}	0.024	13.7×10^{-8}	0.338	0.005	0.004	15	0.066
0.045	102×10^{-6}	0.016	13.8×10^{-8}	0.151	0.005	0.004	14	0.046
0.035	126×10^{-6}	0.026	14.8×10^{-8}	0.172	0.005	0.004	10	0.041
0.025	128×10^{-6}	0.028	17.7×10^{-8}	0.170	0.005	0.004	9	0.044
0.015	180×10^{-6}	0.039	32.5×10^{-8}	0.158	0.005	0.004	5	0.043

Pitch size (mm)	Resistivity (Ω.m)	Relative error in resistivity	Resistivity ± error (Ω.m)	Conductivity (s/m)	Conductivity ± error (s/m)
0.095	-	-	-	-	-
0.085	-	-	-	-	-
0.075	4.34×10^{-8}	0.145	$(4.3 \pm 0.62) \times 10^{-8}$	2.30×10^{7}	$(2.3 \pm 0.33) \times 10^{7}$
0.065	4.05×10^{-8}	0.329	$(4 \pm 1.3) \times 10^{-8}$	2.46×10^{7}	$(2.5 \pm 0.81) \times 10^{7}$
0.055	3.97×10^{-8}	0.345	$(4 \pm 1.4) \times 10^{-8}$	2.51×10^{7}	$(2.5 \pm 0.87) \times 10^{7}$
0.045	3.96×10^{-8}	0.158	$(4.0 \pm 0.63) \times 10^{-8}$	2.52×10^{7}	$(2.5 \pm 0.40) \times 10^{7}$
0.035	3.72×10^{-8}	0.178	$(3.7 \pm 0.66) \times 10^{-8}$	2.68×10^{7}	$(2.7 \pm 0.48) \times 10^{7}$
0.025	4.08×10^{-8}	0.177	$(4.1 \pm 0.72) \times 10^{-8}$	2.45×10^{7}	$(2.5 \pm 0.43) \times 10^{7}$
0.015	5.85×10^{-8}	0.168	$(5.9 \pm 0.98) \times 10^{-8}$	1.70×10^{7}	$(1.7 \pm 0.29) \times 10^{7}$

Let's illustrate an example of an error calculation done attempting to obtain the absolute resistivity of the printed tracks. To determine the error on the calculated resistivity, the compounded errors from the measurement of each quantity needs to be calculated.

$$\text{Resistivity} = \text{resistance} \,.\, \text{area}/\ \text{length}$$

$$\text{Error on resistivity} = \sqrt{\left(\frac{\Delta\text{resistance}}{\text{resistance}}\right)^2 + \left(\frac{\Delta\text{width}}{\text{width}}\right)^2 + \left(\frac{\Delta\text{thickness}}{\text{thickness}}\right)^2 + \left(\frac{\Delta\text{length}}{\text{length}}\right)^2}$$

$$\text{Error on resistivity} = \sqrt{(0.027)^2 + (0.025)^2 + (0.141)^2 + (0.04)^2}$$

$$= 0.145$$

Thus, the vast majority of the error comes from the uncertainty of measuring the very thin and somewhat variable thickness with the profilometer. The errors on the other quantities are much smaller in comparison.

In order to examine the effect of print pitch on the geometry and electrical properties of the printed features, the print pitch between droplets was varied over the range 95 μm to 15 μm and 5 replica lines were printed in a single pass for each print pitch. In the beginning, a 50 μm nozzle was used with photo paper substrate at room temperature. Figure 3.14 illustrates the effect of print pitch on the line width, thickness and resistivity, respectively. Clearly, line width was found to increase as the print pitch was decreased from 81 μm at print pitch 95 μm to about 180 μm at 15 μm pitch, because of the increased amount of lateral spreading prior to drying. In contrast, the resistance of the lines decreased with decreasing pitch size from 30 Ω at 75μm pitch to 5 Ω at 15 μm pitch size. Also, the thickness was corresponding with the width increase as the pitch decreased. The resistivity at the lower pitch range 15 μm was found to be 5.85×10^{-8} Ω.m, which is around 4 times RBS. With increasing the pitch size to 35 μm, the resistivity was reaching about 2 times RBS(3.72×10^{-8} Ω.m).

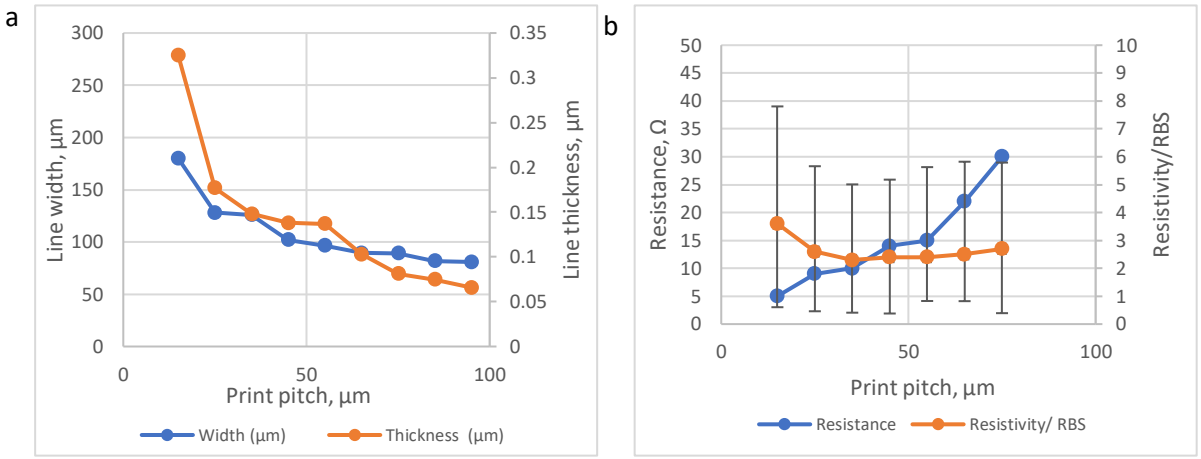

Figure 3.14. Results for lines printed of 30% AgPAA on glossy paper with a 50 µm nozzle diameter at room temperature (a) effect of print pitch on the line width/thickness, (b) effect of print pitch on resistance/RBS. Error bars show the resistivity/ RBS ± error.

After sintering at room temperature, most boundaries between particles disappeared as particles have fused together to form a network throughout the entire silver film because of the sintering. As a result, the electrical resistivity reached very low values at 55, 45 and 35 µm pitch size, corresponding to about x2 RBS. For spontaneous room temperature sintering, this is a notable result and compares very favourably with other values for sintered silver tracks reported in the literature [9,10,11,12].

The effect of print pitch on the line width, thickness and resistivity of 20 wt.% AgPAA ink is summarised in Table 3.5 and Figure 3.15. The data followed the same trend as that with 30 wt.% AgPAA ink. It is easy to perceive that the width and thickness have increased from 97 µm to 241 µm and 0.17 µm to 0.25 µm, respectively when decreasing the pitch size between droplets. The films width and thickness increased corresponding with decreasing the print pitch of droplets as expected, and the Ag films exhibited a great decrease in resistance to 4 Ω at 15 µm. The resistivity at the lower pitch range was found to be 0.491×10^{-7} Ω·m, which is about 3 times bulk silver. With increasing the pitch size up to 25 µm, the resistivity was reaching the lowest value 0.461×10^{-7} Ω.m, around 2.8 times RBS. From this work, it was found that the 30 and 20 wt.% AgPAA sintered pattern had a low resistivity of 2.67×10^{-8} Ω.m, which is low enough to be used for printed electronics.

Table 3.5. Effect of pitch size on line width, thickness and resistivity for printed lines of 20% AgPAA ink on glossy paper with a 50 μm nozzle diameter, printed at room temperature.

Pitch size (mm)	Width (m)	Thickness (m)	Resistance (Ω)	Length (m)
0.095	0.97×10^{-4}	1.65×10^{-7}	44	0.005
0.085	0.99×10^{-4}	1.73×10^{-7}	40	0.005
0.075	1.01×10^{-4}	1.78×10^{-7}	34	0.005
0.065	1.03×10^{-4}	1.79×10^{-7}	25	0.005
0.055	1.13×10^{-4}	1.85×10^{-7}	17	0.005
0.045	1.34×10^{-4}	1.95×10^{-7}	13	0.005
0.035	1.49×10^{-4}	2.34×10^{-7}	8	0.005
0.025	1.93×10^{-4}	2.39×10^{-7}	5	0.005
0.015	2.41×10^{-4}	2.55×10^{-7}	4	0.005

Pitch size (mm)	Resistivity (Ω.m)	Relative error in resistivity	Resistivity ± error (Ω.m)	Conductivity (s/m)	Conductivity ± error (s/m)
0.095	1.41×10^{-7}	0.028	$(1.41 \pm 0.04) \times 10^{-7}$	0.712×10^{7}	$(0.71 \pm 0.02) \times 10^{7}$
0.085	1.37×10^{-7}	0.042	$(1.37 \pm 0.06) \times 10^{-7}$	0.645×10^{7}	$(0.65 \pm 0.03) \times 10^{7}$
0.075	1.22×10^{-7}	0.145	$(1.2 \pm 0.18) \times 10^{-7}$	0.847×10^{7}	$(0.85 \pm 0.12) \times 10^{7}$
0.065	0.921×10^{-7}	0.329	$(0.9 \pm 0.30) \times 10^{-7}$	1.09×10^{7}	$(1.1 \pm 0.36) \times 10^{7}$
0.055	0.711×10^{-7}	0.345	$(0.7 \pm 0.25) \times 10^{-7}$	1.49×10^{7}	$(1.5 \pm 0.51) \times 10^{7}$
0.045	0.679×10^{-7}	0.158	$(0.7 \pm 0.11) \times 10^{-7}$	1.23×10^{7}	$(1.2 \pm 0.19) \times 10^{7}$
0.035	0.558×10^{-7}	0.178	$(0.2 \pm 0.10) \times 10^{-7}$	3.13×10^{7}	$(3.1 \pm 0.56) \times 10^{7}$
0.025	0.461×10^{-7}	0.177	$(0.18 \pm 0.08) \times 10^{-7}$	2.04×10^{7}	$(2.0 \pm 0.36) \times 10^{7}$
0.015	0.491×10^{-7}	0.168	$(0.17 \pm 0.08) \times 10^{-7}$	2.89×10^{7}	$(2.9 \pm 0.49) \times 10^{7}$

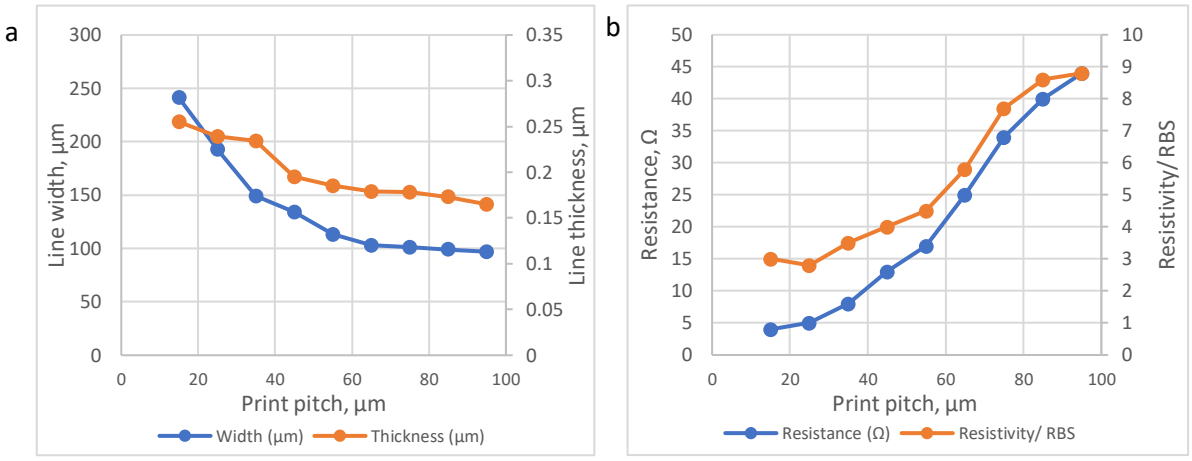

Figure 3.15. Results of printed lines of 20% AgPAA on glossy paper with a 50 µm nozzle diameter at room temperature (a) effect of print pitch on the line width /thickness (b) effect of print pitch on resistance / RBS.

In a published report by Huang Q. *et al.* [6], Ag NPs were synthesised similarly by using triethanolamine as a reducing agent and PAA as the protective agent in an aqueous solution and printed with inkjet printing with a common colour printer (Epson Stylus Photo R230), on Kodak premium photo paper as the substrate. The inkjet-printed silver patterns were printed then sintered at various temperatures between 25 °C and 150 °C for 10 min. After sintering at room temperature (25 °C), the resistivity of the silver films was 12.6 µΩ.cm. This self-sintering phenomenon of the Ag nanoparticles was due to the polymer coating on the paper substrate. While sintering at 150 °C, the resistivity of the printed silver patterns decreased to 4.7 µΩ.cm, which is close to triple that of bulk silver. Their printed silver tracks showed some voids and cracks formed on the surface of the track after sintering at 150 °C. Comparing with our results, the nanoparticles were made with a similar method, they used different substrates and inkjet printer. We successfully printed AgPAA ink on photo paper with room temperature sintering and the measured resistivity was 2 times bulk silver. It is possible that the Kodak paper does not contain (much) chloride ion, but since we have not investigated it, this is unknown.

Going back to the study mentioned above by Milardovic S. *et al*. [5], silver NP-based ink was prepared in their study by dispersing dried NPs with a solid loading of 25 wt% into a mixture of water and ethylene glycol and was stable for over seven months, which was similar to our results. The printed line was produced with an Epson stylus D92 inkjet printer and exhibited a resistivity of $8x10^{-8}$ Ω.m, which was 4.7 times greater than RBS. For comparison, in our results

the resistivity was about 2 times RBS. Although their conductivity was somewhat lower than ours, it is interesting because it demonstrates that these inks can be used successfully with inexpensive office-type inkjet printers, which makes the concept accessible to a much wider community and simplifies manufacturing.

3.1.6 Comparison of layer overprinting and print pitch variation on electrical and mechanical properties

To decide whether the geometry and electrical performance of printed lines were affected by an overprinting path instead of a single pass printing method, the pitch size was selected at 65 μm, and the lines were overprinting up to five times on photo paper substrate. In particular, the thickness of the tracks could be controlled by changing the solid content of the ink or the number of printing cycles. In this experiment, all printed patterns were prepared by printing 30 wt% silver ink, so their thickness could be controlled simply by changing the number of printing cycles [2].

By looking at Table 3.6 and Figure 3.16 below, the thickness and width of the printed lines both increase with overprinting from a thickness of about 0.103 μm and width 90 μm with a single layer at 65μm pitch to a thickness of 0.28 μm and width 165 μm after overprinting to obtain five layers. The resistivity of the overprinted layers slightly decreased up to 4 printed layer from $4.7x10^{-8}$ Ω·m to $3.37x10^{-8}$ Ω·m. However, the resistivity increased with the 5 layers, and this may indicate a reduction in chloride diffusion/ penetration, hence less efficient sintering in the upper layers.

Table 3.4. Summary of properties of room-temperature overprinted features of 30% AgPAA ink on photo paper from a 50 µm nozzle at 65 µm print pitch.

No. of printed Layers	Width (m)	Relative error in Width	Thickness (m)	Relative error in thickness	Resistance (Ω)	Relative error in resistance	Length (m)	Relative error in length
1	89.5×10^{-6}	0.060	10.3×10^{-8}	0.311	22	0.090	0.005	0.004
2	109×10^{-6}	0.0023	21.3×10^{-8}	0.0072	10	0.007	0.005	0.004
3	125×10^{-6}	0.0016	24.7×10^{-8}	0.0084	6	0.02	0.005	0.004
4	131×10^{-6}	0.012	25.8×10^{-8}	0.0059	5	0.04	0.005	0.004
5	165×10^{-6}	0.00093	27.7×10^{-8}	0.0075	4	0.05	0.005	0.004

No. of printed layers	Resistivity (Ω.m)	Relative error in resistivity	Resistivity ± error (Ω.m)	Conductivity (s/m)	Conductivity ± error (s/m)
1	4.05×10^{-8}	0.329	$(4 \pm 1.3) \times 10^{-8}$	2.46×10^{7}	$(2.5 \pm 0.81) \times 10^{7}$
2	4.64×10^{-8}	0.011	$(4.6 \pm 0.05) \times 10^{-8}$	2.15×10^{7}	$(2.1 \pm 0.02) \times 10^{7}$
3	3.70×10^{-8}	0.023	$(3.7 \pm 0.09) \times 10^{-8}$	2.70×10^{7}	$(2.7 \pm 0.06) \times 10^{7}$
4	3.37×10^{-8}	0.042	$(3.4 \pm 0.14) \times 10^{-8}$	2.96×10^{7}	$(3.0 \pm 0.12) \times 10^{7}$
5	3.66×10^{-8}	0.051	$(3.7 \pm 0.19) \times 10^{-8}$	2.73×10^{7}	$(2.7 \pm 0.14) \times 10^{7}$

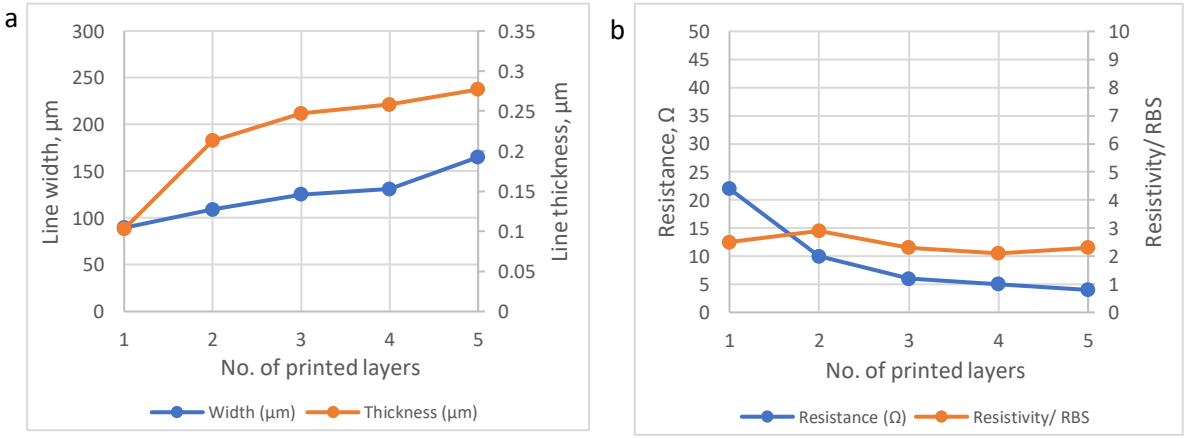

Figure 3.16. Properties of room-temperature overprinted features on photo paper from a 50 µm nozzle at 65 µm print pitch, (a) effect of layers printed on line width /thickness, (b) effect of layers printed on resistance /RBS.

In a similar way, a steady decrease in resistance was observed as shown in Figure 3.16. In a study by Shen W. *et al.* [3], the silver NP ink patterns were printed 10 times on photo paper. The thickness of the Ag track was approximately 5.30×10^{-7} µm. That is relatively similar to these results where printing the Ag track 5 times gave a thickness about 2.77×10^{-7} µm, which was half the thickness Shen

obtained with 10 times. This confirmed that the printed patterns' thickness increased with the number of printed layers. Thus, this led to a decrease in the electrical resistance as the silver NPs coalesced throughout the entire thickness of the printed track.

In support of the results above, the visual demonstration by the microscope images in Figure 3.17 shows the increased amount of lateral spreading prior to drying for five layers (b) compared with a single layer (a) (photos shown at the same scale).

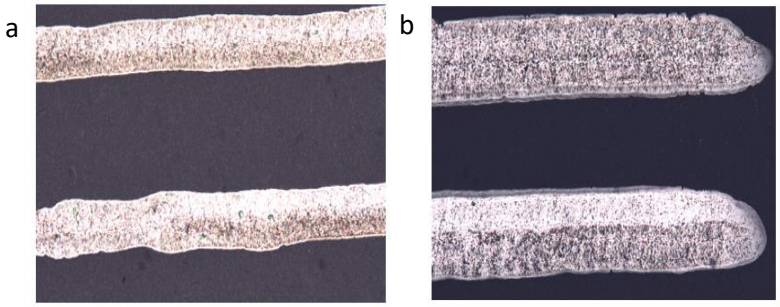

Figure 3.17. Microscope images of printing passes for 30% AgPAA at the same pitch size (65 μm) with different numbers of printed layers (a) single layer, (b) five layers.

3.2 Characterisation of Ag-PVOH NPs

As reported by Mavuri A. *et al.* [4], in her experiment, she successfully produced Ag-PAA NPs by using silver nitrate dissolved in a mixture of water and triethanolamine (TEA) as a metal precursor. In this work we followed the same route with a different capping agent. We tried to use polyvinyl alcohol (PVOH) with a variety of molecular weights, (i.e., different chain lengths) and also different degree of hydrolysis, to produce polymer embedded silver nanoparticles. PVOH would be attractive for this purpose for two reasons. Firstly, it is a biodegradable polymer, readily available compound and is not hazardous to the environment [13]. Secondly, sterically stabilized aqueous particles with low surface charge would be desirable since the particles would not be pH sensitive in the way that the PAA-capped ones are.

Interpreting the data, the 85,000 – 124,000 MW acts much better as a stabilizer by enveloping the particles, protecting them from aggregation, thereby we got a smaller size according to Table 3.7. The overall size range was much larger than with PAA as stabiliser, however.

Table 3.7. DLS data of Ag-PVOH NPs with the different PVOH molecular weight.

PVOH Molecular weight	PVOH Hydrolyzed degree	Size (d. nm)	%Number	PDI	Z-Average
85,000-124,000	98-99%	87.17	100.0	0.337	357.7
78,000	88%	296.0 970.6	20.2 79.4	0.343	1522
25,000	98%	1737 448.8	27.9 72.1	0.303	1808

While we were using PVOH as a capping agent, we noticed that there was a high degree of polydispersity, and larger particles settled down within 10 min. Moreover, Figure 3.18 displays TEM images of a very dilute suspension of the prepared Ag-PVOH NPs (78,000 MW), which show anisotropy in particles shape (spherical and nanorod) with an obvious agglomeration also apparent, although this could be an artefact of sample preparation.

Figure 3.18. TEM images of Ag-PVOH NPs (78,000 MW).

3.3 Characterization of silver nanoparticles – polyvinyl alcohol (Ag/PVOH) composition

In the current study, we have used the method from Teerasong S. *et al.* [8] to prepare monodisperse nanoparticles, with some modification. This was a simple, fast synthesis method using PVOH (85,000 – 124,000 MW) as a reducer and stabilizer, which is dispersed in hot deionized water, then a solution of $AgNO_3$ added dropwise to the above solution. Next, we used $NaBH_4$ to rapidly reduce the Ag^+ and deposit it onto the pre-formed nuclei in order to control the size.

The size distribution of Ag-PVOH particles (Figure 3.19), analysed by DLS, showed a very clear polydisperse sample and large particles compared to other capping agents we have used in previous experiments. Successive

measurements showed a progressive drift in size as the very large particles sedimented. No other characterization was done following these obtained results (3.2) & (3.3), since the material is clearly not suitable for printing.

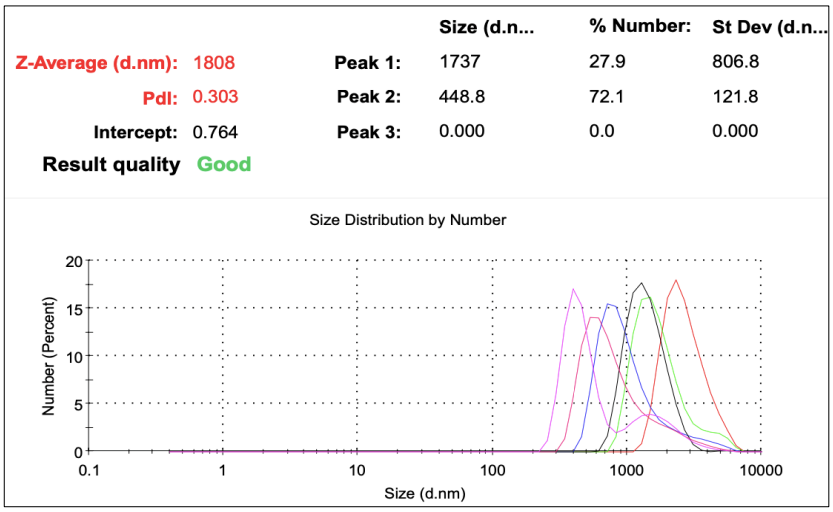

Figure 3.19. The DLS graph of Ag-PVOH NPs.

The effect of PVOH on stabilization of silver colloids was also reported by Zielinska A. *et al*. [14]. They also obtained aggregated nanoparticles after one day of preparation and this confirms that the protecting agent has an important role in stability and optical properties of silver nanoparticles, and PVOH does not appear to coordinate strongly enough to the surface to provide the necessary stabilisation, hence the potential benefits of using this polymer cannot be realised in practice.

The decision was thus made to end investigations of PVOH for this application. This decision was due to the fact that particles always settled down so quickly, causing clustered particles and serious aggregation of the solution. This would make them difficult to handle in the printing stage since formulated inks would not be stable. Also, although its suspension produced spontaneously sintered films that had some electrical resistance when crudely tested using the ‘smear test’, it wasn’t very shiny/metallic looking and peeled very easily when it was applied on Epson photo paper to measure electrical resistance.

Despite these unsuccessful results, PVOH has still been widely reported in other studies in bio-related applications. Among all capping agents, PVOH has drawn a great deal of attention due to its convenient and user-friendly properties.

3.4 Characterisation of Ag-PVP NPs

It was reported in many previous studies [8,13] that using polyvinylpyrrolidone (PVP) during the Ag NPs synthesis as a protection agent (surfactant) could chemically control the size or stop the growth of metal colloids through absorption and desorption onto the surface of silver NPs. This behaviour of the capping agent suggests that it is absorbed on the surface of the Ag NPs by organized bonding, by donating loan pair electrons of O and N atoms to silver ions, and thus forms the Ag ions and PVP complex structure to control the size and block the agglomeration under high concentration [14,15].

Following the method mentioned above by Mavuri A. *et al.* [4], but using PVP as a capping agent was initially tested but it was not worth further investigation due to the fact that the particle size was barely in the nano range, having a size of about 570 nm. To avoid this either a longer time sonication (about 2 h) was done or filtration to eliminate the large particles. After this treatment the particle size was in the range about 179-118 nm with a PDI 0.233 – 0.18 respectively, indicating a relatively low-dispersity distribution with a very consistent measurement (Table 3.8). This process was not favourable, because it removed much of the clustered nanoparticles and a lot of material was lost. It also takes a lot of time and effort, which is undesirable when thinking about future larger-scale production.

Table 3.8. DLS data for Ag-PVP NPs with different PVP treatments.

PVP	Size (d. nm)	% Number	PDI	Z-Average
Before filtration /or Sonication	570 5108	99.9 0.1	0.323	711.5
After Filtration	118.1	100	0.187	180.8
After 2 h Sonication	179	100	0.233	211.2

Finally, we found that, by using PAA as a capping agent, we obtained better control of particle size, whereas using PVOH and PVP following the same methodology would need huge effort to be invested in developing size-controlled syntheses more suitable for use in conductive materials. It may be that the polymer properties would make this impossible.

3.5 Characterization of silver- polyvinyl pyrrolidone (Ag/PVP) by a modified polyol process

An attempt has been made towards the development of silver ink with improved physical properties by using PVP as a capping agent again regarding its reducing properties. As a stabilizer, it has a polyvinyl skeleton with polar groups (amide) of the pyrrolidone rings, which can act as a capping agent for dissolved metallic salts. This is a very polarised functional group, though, which does give charge redistribution and would allow some electrostatic interaction with the particle surface. PVP donates loan pair electrons of oxygen and nitrogen atoms to silver ions and thus forms the Ag ions and PVP complex structure. The result from other literature indicates that PVP has a major contributing factor in stabilising the particles, stopping their growth and forming highly stable ink [15].

This time, we followed the same approach as Wang Z. *et al.* [16]. A high concentration of $AgNO_3$ was used with PVP as a capping agent by a modified polyol process using ethylene glycol as solvent and reducing agent, which promotes lower cost production and promoting the electrical conductivity.

The phenomena suggested that as a small amount of PVP was used, so only a small amount of PVP is adsorbed on Ag NPs surface by coordination bonding with N and O atoms and that results in forming Ag-ions-PVP complexes. As a result, that leads to prevent the formation of large Ag accumulation under high concentration of $AgNO_3$. The potential mechanism for that prevention is as follows: Firstly, when the $AgNO_3$ solution was added to the flask, the Ag^+ ion is rapidly distributed to all the solution and is reduced by a reductive aldehyde ligand that is generated as a result of the ethylene glycoloxidation under heating as shown below:

$$2\ HOCH_2CH_2OH \longrightarrow 2\ CH_3CHO + 2\ H_2O$$

$$2\ Ag^+ + 2\ CH_3CHO \longrightarrow CH_3CHO\text{-}OHCH_3 + 2\ Ag + 2\ H^+$$

Secondly, the PVP adsorbs to the Ag NPs and prevents the particles from aggregating by providing steric stabilisation. The interpretation of data had been demonstrated as a very promising potential method for further work, but this has not yet been done.

In order to monitor the size distribution of Ag NPs, DLS measurements were done. According to the Figure 3.20, the size distribution of the Ag NPs is

about 105 nm with a very consistent measurement, which reveals that high purity low dispersity silver NPs are synthesised. According to the zeta potential result, it was equal to zero in a solution adjusted at pH ca. 7 with a very sharp peak which is expected with PVP and in good agreement with the literature [17].

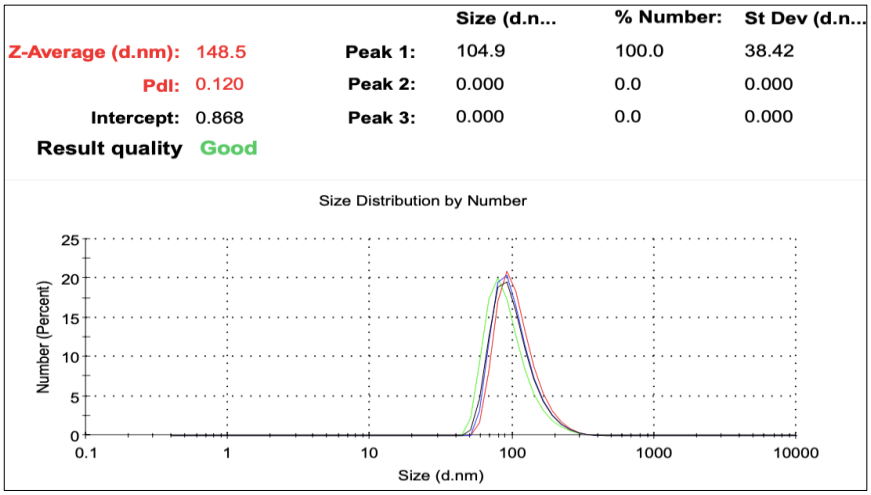

Figure 3.20. The DLS graph of Ag- PVP NPs made by a modified polyol process.

Kosmala A. [18] synthesised Ag nanowires using a seed-assisted, polyol process. The formation of the Ag nanostructures involved reducing the $AgNO_3$ with ethylene glycol using PVP as a capping agent. This resulted in wires with a diameter of 20-30 nm. They are very well dispersed due to the presence of PVP which kinetically controls the growth rates of Ag by chemically adsorbing onto the surface of Ag through O-Ag bonding.

The development of such a method has been reported by Leng Z. *et al.* [19]. The authors used a liquid phase of EG as a reduction agent in the presence of PVP to synthesis uniform and monodispersed Ag NPs. The results showed a stable and good size distribution of Ag NPs within the range of 20-30 nm. They studied the effect of the Ag: PVP molar ratio on the size distribution of Ag NPs. Generally, higher mass ratio led to reduction of the silver NPs size. Compared with our results, clearly, we have produced a larger size of particles as the reaction temperature was different in the initial reaction. 160 °C was enough to increase the speed of nucleation of silver atoms faster than the growth rate, besides intensifying the Brownian motion that increase the possibility of collision between particles [15]. Another possible cause is that the high concentration of PVP might control the growth rates kinetically with adsorbing mechanism and

increasing the coverage layers on some particles could significantly decrease their growth rates [20].

Figure 3.21 shows the TGA graph of Ag-PVP NPs. There are many decomposition steps. The first decomposition step before 100 °C is due to eliminating residual water and ethylene glycol by evaporation. Thermal decompositions between 150-350 °C are due to degradation of polymer side and main chain. The total weight loss at 500 °C is about 1.3%, which demonstrates total mass loss less than with PAA particles, but the particles size is also bigger. Thus, the surface-to-volume (mass) ratio will be less and there is less surface for the polymer to adsorb to, so we would expect less, even if it had the same binding properties and chain lengths as PAA.

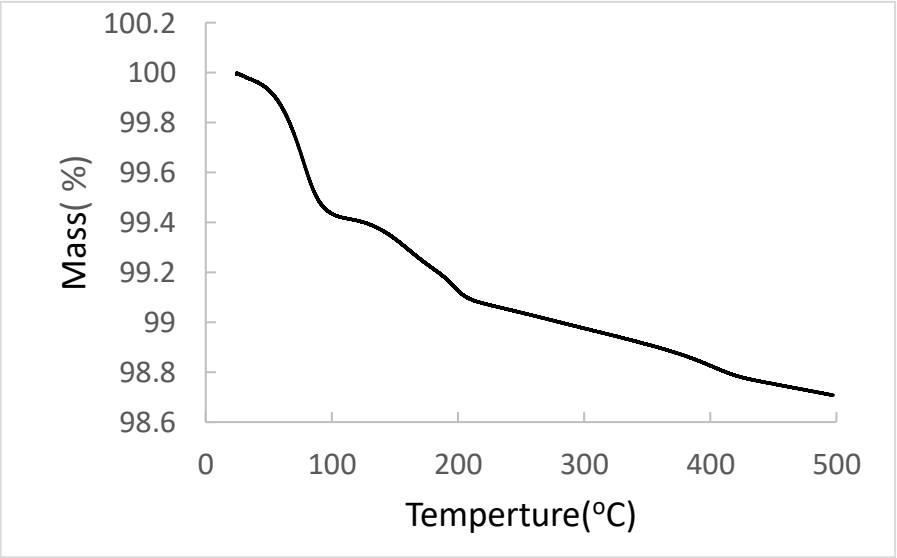

Figure 3.21. TGA of the Ag-PVP NPs powder.

3.5.1 Characterisation of 30%, 20% and 10% AgPVP standard ink

AgNPs ink synthesis targeting conductive patterns for microfabricated devices by inkjet printing technology is presented. The well-dispersed nanoparticles ink was composed of silver colloid protected by PVP as a capping layer at varying silver concentration of 30, 20 and 10 wt.%. Stable aqueous inks were formulated in a similar way as Ag-PAA ink by using a combination of solvent (ethylene glycol, water, and 1-propanol) under vigorous stirring.

After the formulation, the size distribution was measured by DLS at different times, as shown in Table 3.9, to ensure the silver ink stability. Samples for DLS measurements were prepared by redispersal using a small sample from the ink in 1 mL of deionized water, to obtain a solution with a high concentration of nanoparticles. Table 3.9 shows a size distribution of AgPVP ink over the period of storage. The mean diameter of nanoparticles is 61 nm to 104 nm , with a narrow distribution, which is suitable for printing. They present little change with different nanoparticles loading up to 30 wt.%.

Table 3.9. DLS size distributed during period of time.

Size distribution during period of storage	Ink ratio (wt.%)		
	30% AgPVP	20% AgPVP	10% AgPVP
Size (d. nm) after formulation	104	61	74
Size (d. nm) in one month	106	64	76
Size (d. nm) in two months	108	65	78
Size (d. nm) in three months	110	67	77
Size (d. nm) in four months	112	67	78
Size (d. nm) in five months	113	68	79

The ink was stored in the fridge for five months. It showed some aggregation from the first week of storage, However, it has been successfully printed on photo paper substrate with good resistivity. It was sonicated then filtered through a 0.2 μm syringe filter to eliminate large particles before the printing process to avoid nozzle clogging.

To obtain a good jetting through the printhead nozzles, the ink should have an appropriate viscosity. The viscosity measurements were made with a rheometer at 25 °C and a constant shear rate of (25000.01/s). The ink containing 30 wt.% silver has a viscosity about 0.3- 0.4×10^{-2} Pa.s at room temperature that

met inkjet printer requirements (Figure 3.22), indicating that an appropriate ink composed of silver nanoparticles has been successfully prepared.

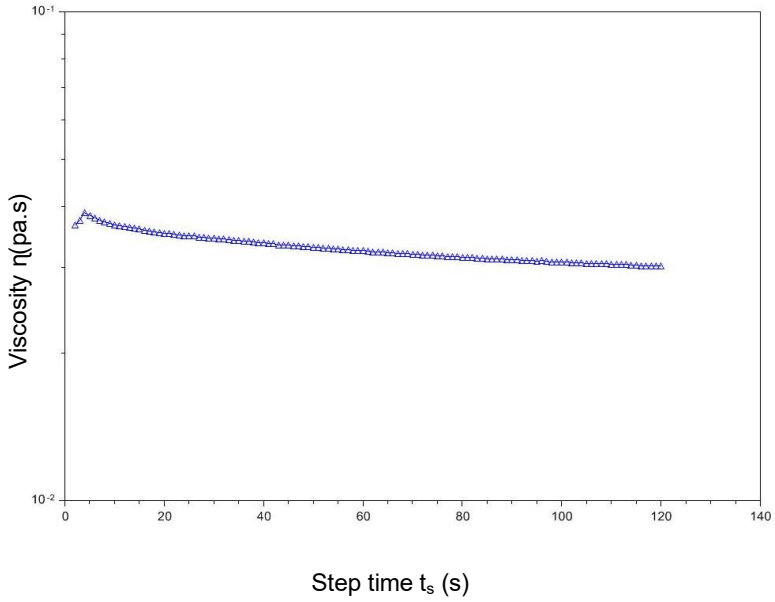

Figure 3.22. Viscosity measurement of 30% AgPVP ink.

The basic requirements for the ink should provide good printability with good electrical conductivity of printed patterns. Optimization of AgPVP ink quality is one of the crucial factors to obtain a good printing pattern with high electric conductivity and avoiding nozzle clogging. Also, it requires highly concentrated dispersions of silver nanoparticles loading (usually 30 wt.%) for high conductivity.

3.5.2 The effect of printing AgPVP patterns on photo paper with different parameters

In order to produce high quality conductive tracks after printing, it is necessary to control the track physical dimensions (width, thickness) by controlling the pitch size.

Figure 3.23 displays optical microscope images with different width controlled by pitch size. When the size between droplets was set at 85 μm the line width became 99 μm and gradually increased to 229 μm as the pitch size dropped down to 15 μm. Meanwhile, there was some single silver dot pattern and breaking line on the pitch size 85 μm as shown in Figure 3.23 (a). The silver track at this stage cannot be conductive. However, when the distance between dots decreased, it created conductive necks between the particles and increased their packing density.

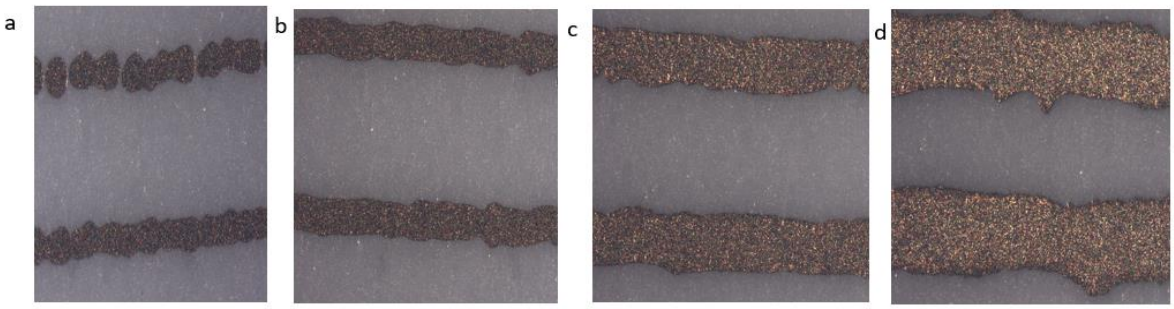

Figure 3.23. Optical microscope images showing different line widths at different pitch size (a) 85 μm; (b) 65 μm; (c) 35 μm; and (d) 15 μm.

Coalescence and neck-forming of individual particles imply that the larger voids increase in size and Ag is redistributed to bridge smaller voids during sintering and thus increases the conductivity of the pattern. Moreover, the silver printing track thickness increased from 55 μm to 95 μm with decreasing the pitch size and the line becomes denser because more ink was applied during printing.

3.5.3 Morphology of AgPVP ink printed patterns on photo paper

SEM was used to analyse the surface morphology of sintered and also non-sintered nanoparticles, which will be discussed in more detail later. On the sintered conductive silver patterns, neck-like junctions between nanoparticles were observed using SEM. During the printing process, the value of droplet spacing was varied for all the experiments. In order to ensure the best conditions for comparing printed lines, only one nozzle size (50 μm) was used for all experiments.

Figures 3.24 and 3.25 show SEM images for 10% and 20% AgPVP printing tracks at room temperature respectively. As is shown in these images, these tracks have no resistance and no conductivity which indicates these amounts of NPs couldn’t provide enough connectivity for sintering. The surface of the substrate is visibly seen in the gaps between particles. This improved later with increasing the Ag contents.

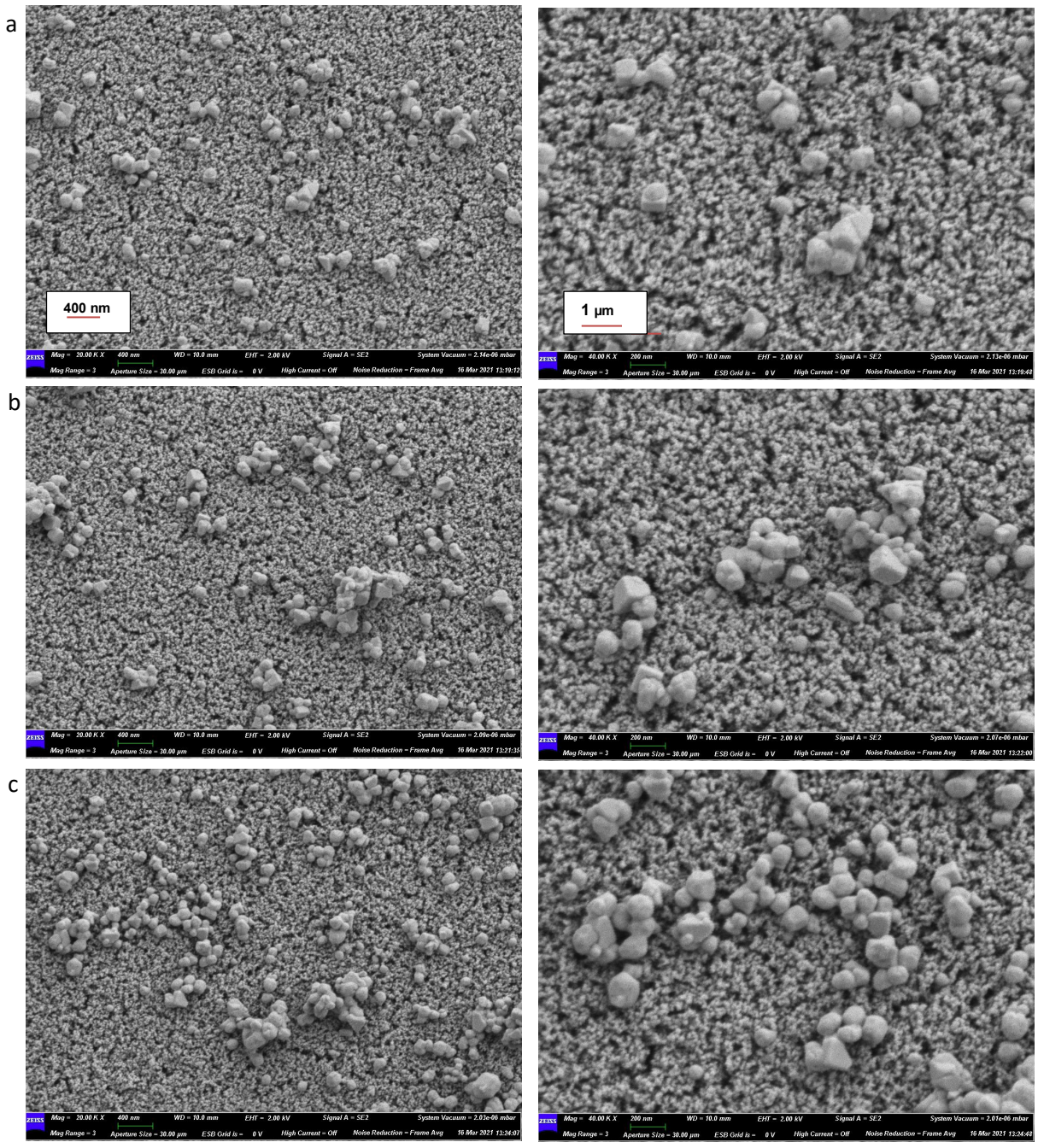

Figure 3.24. SEM images of the surface of the 10 wt.% AgPVP patterns at different pitch size (a) 85 µm, (b) 45 µm, and (c) 15 µm.

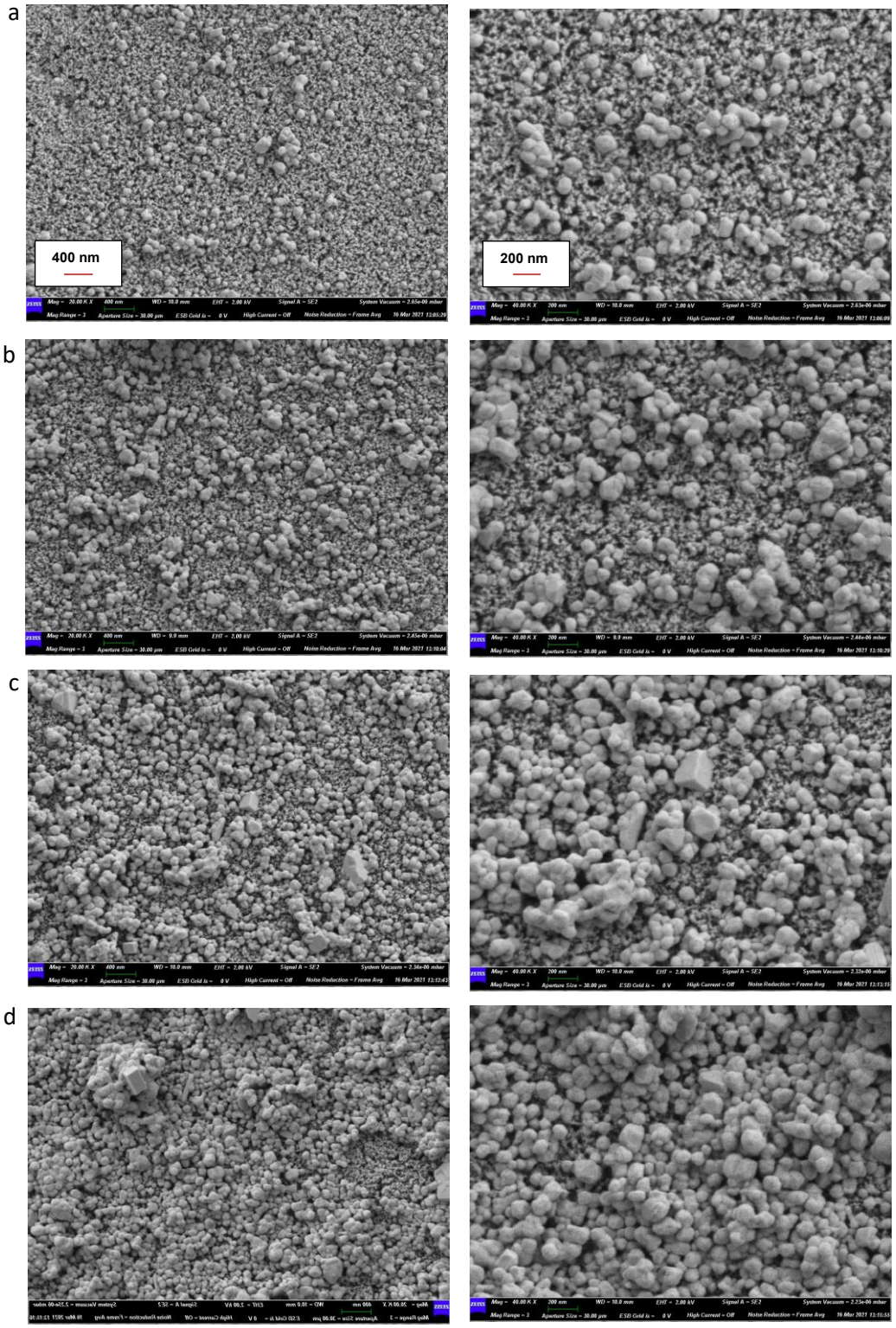

Figure 3.25. SEM images of the surface of the 20 wt. % AgPVP patterns at different pitch size (a) 85 μm, (b) 45 μm, (c) 15 μm, and (d) 45 μm (overprinting x5).

Figure 3.26 shows SEM images of 30% AgPVP ink before sintering. The figure clearly shows that the particles are well separated, very well packed in spherical and some stick shape (nanorods). Since they have not been exposed to chloride, or other sintering agents/processes, it is clear that the particles have not coalesced and fused.

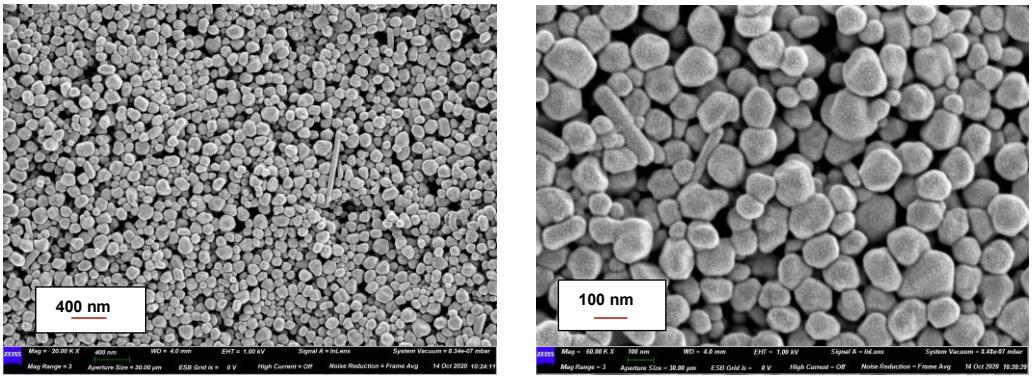

Figure 3.26. SEM of un-sintered 30% AgPVP ink.

The pictures in Figures 3.27 & 3.28 present film of 30 wt.% AgPVP ink on the photo paper substrate. The droplets coalesce into a continuous pattern on Figure 3.27 (b, c, and d) & Figure 3.28 (e and f) as the pitch size was varied between 85, 65, 45 μm and 45 μm with overprinting (x5 and x3) while they no longer form a continuous track on pattern (a) when the pitch size was 95 μm. This shows that AgPVP NPs ink presents a proper conductivity when particles start to coalesce, which is visible through the necking between adjacent particles as the size and homogeneity of nanoparticles interferes directly in the quality of the formed conductive layers, but a poor conductivity when the particles do not look connected as shown in the Figure 3.27 (a).

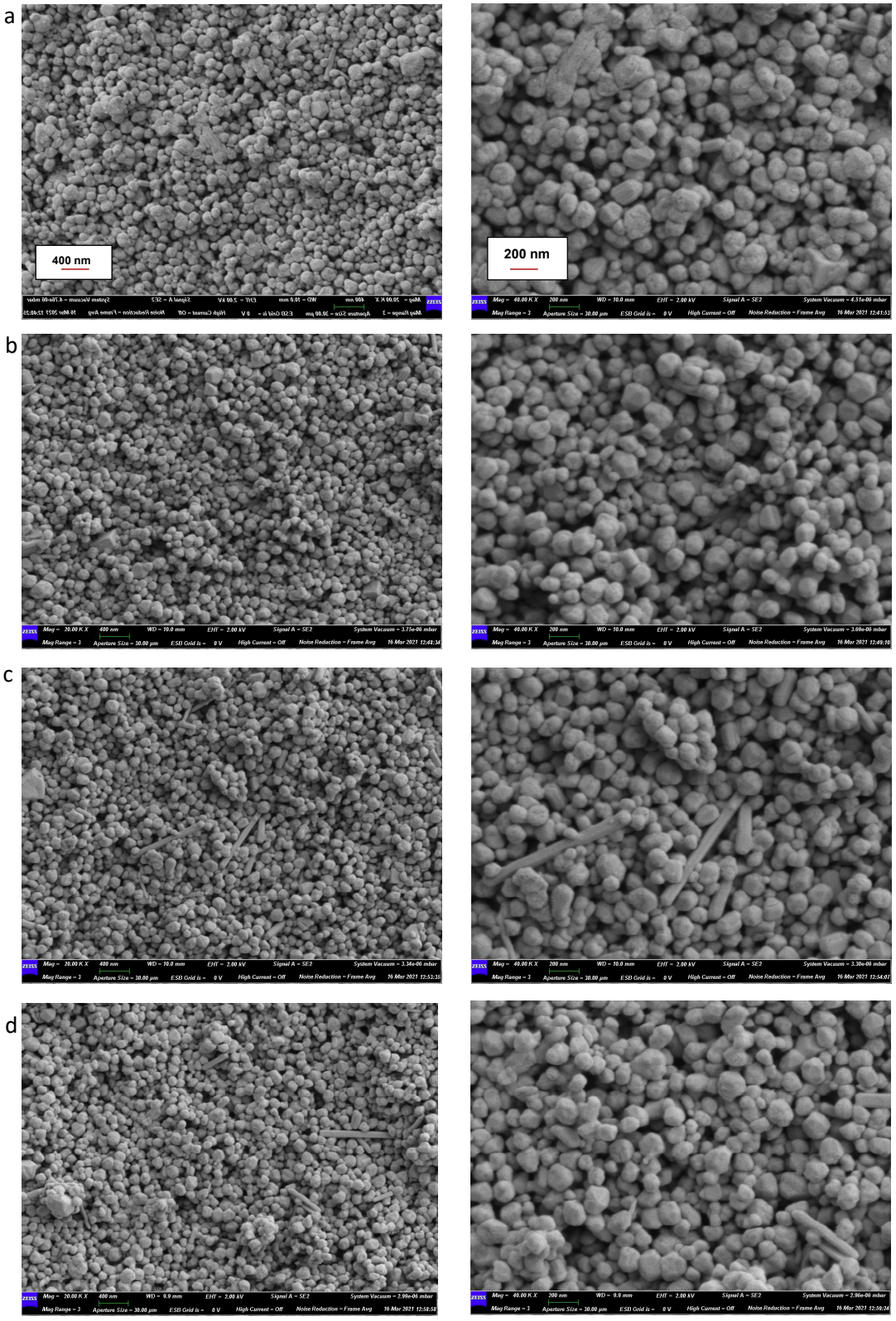

Figure 3.27. SEM images of the surface of the 30 wt.% Ag PVP patterns at different pitch size (a) 95 μm, (b) 85 μm, (c) 65 μm and (d) 45 μm at room temperature.

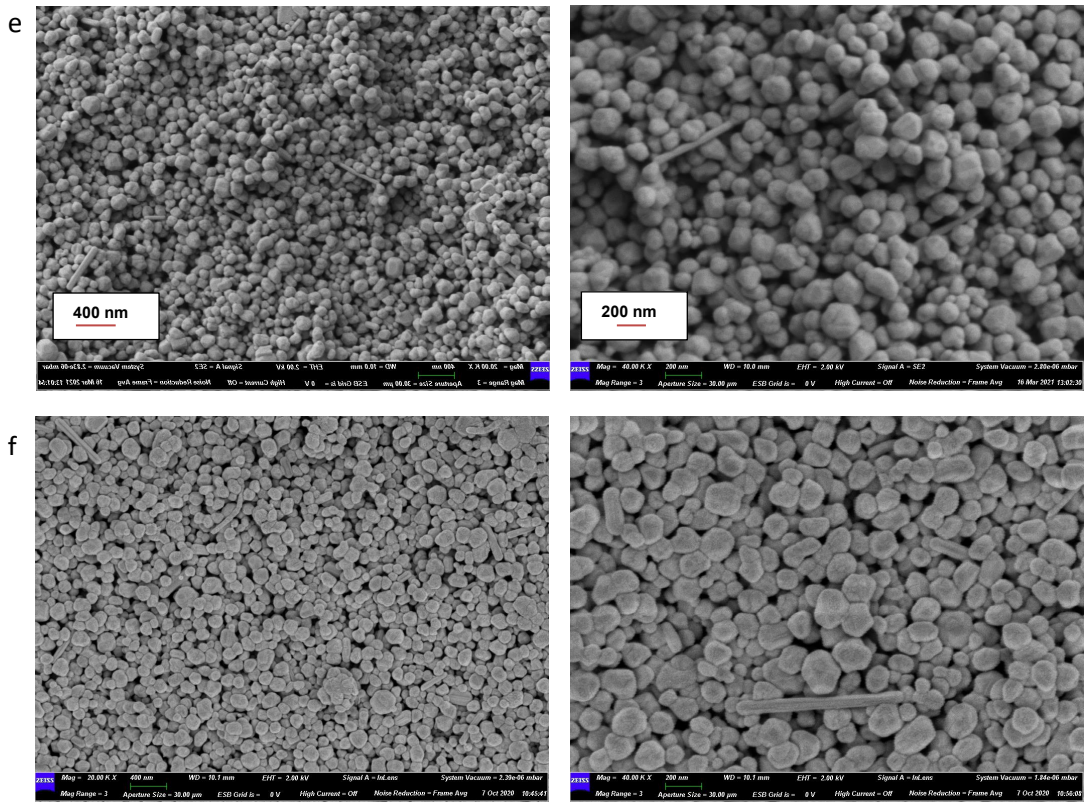

Figure 3.28. SEM images of the surface of the 30 wt.% AgPVP patterns at 45 μm pitch size (e) overprinting (x3), (f) (overprinting x5) at room temperature.

Figure 3.29 demonstrates how particles look after sintering at room temperature. Mostly particles are fused together and show very large crystals sticking together to form a tight compact mass of particles. In the presence of PVP, the growth of silver could be directed into a highly anisotropic mode. Significantly, these silver nanoparticles were well-dispersed because of the presence of PVP, a polymeric surfactant that could chemically adsorb onto the surfaces of silver solids through O-Ag bonding. As the reaction continued and the temperature increased the small silver particles were no longer stable in solution, and they started to dissolve and contribute to the growth of larger ones via a process known as Ostwald ripening. With the assistance of PVP, some of the large nanoparticles were able to grow into rod-shaped structures, with quite extended axial ratios in some cases. These can be seen in the SEM images (e.g., Figure 3.29). This process usually takes place at a temperature as low as ~85°C [20].

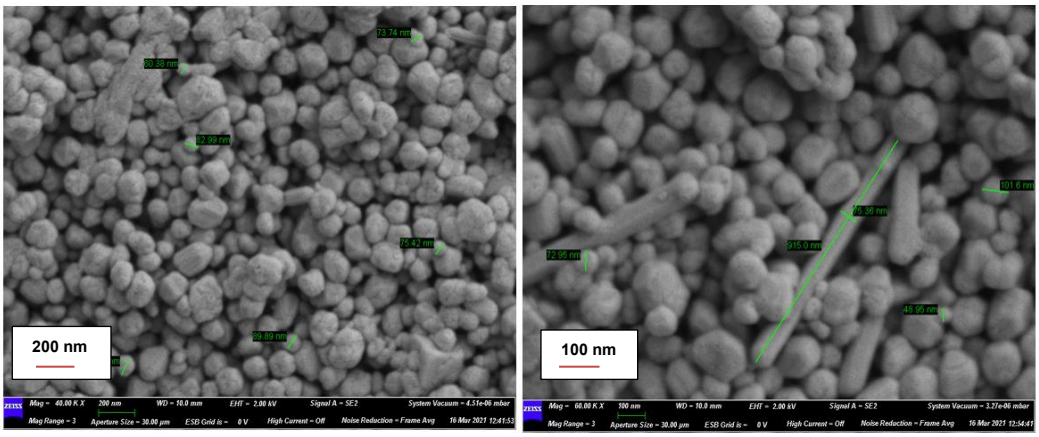

Figure 3.29. SEM images of the surface of the 30 wt.% AgPVP printing film with size measurements.

The SEM results confirm that the size distribution is comparable with DLS sizes, which show an average size between 48.95 nm - 102.5 nm, although the presence of rod-shaped particles will slightly skew the distribution, since the measurement process reports an “equivalent sphere” size.

3.5.4 Effect of print pitch on geometry, electrical and mechanical properties with room temperature sintering of AgPVP ink

Understanding the electrical and mechanical properties of printed patterns is important to predict and improve the performance of the ink. To highlight the difference in the electrical properties, the print pitch between droplets was varied over the range of 95 µm to 15 µm and 5 replica lines were printed in a single pass for each print pitch. All the printed patterns were done via a 50 µm nozzle on photo paper at room temperature.

For the resistivity measurement on the photo paper, only 30% AgPVP ink was used in the characterization, and the other two inks show no resistance. The profilometer was used to determine the physical dimensions of the ink samples deposited on the substrate. Table 3.10 and Figure 3.30 below show the effect of varying print pitch on the line width, thickness and resistivity, respectively.

Table 3.10. Effect of pitch on width, thickness and resistivity of printed lines. 30% AgPVP ink was printed with a 50 µm nozzle diameter on glossy photo paper at room temperature.

Pitch size (mm)	Width (m)	Thickness (m)	Resistance (Ω)	Length (m)
0.095	0.97×10^{-4}	5.51×10^{-7}	-	0.005
0.085	0.97×10^{-4}	5.56×10^{-7}	3.3	0.005
0.075	0.99×10^{-4}	5.57×10^{-7}	2.4	0.005
0.065	1.09×10^{-4}	5.59×10^{-7}	2	0.005
0.055	1.13×10^{-4}	5.67×10^{-7}	1.9	0.005
0.045	1.36×10^{-4}	6.40×10^{-7}	1.2	0.005
0.035	1.56×10^{-4}	8.16×10^{-7}	0.8	0.005
0.025	2.07×10^{-4}	8.22×10^{-7}	0.7	0.005
0.015	2.29×10^{-4}	9.96×10^{-7}	0.7	0.005

Pitch size (mm)	Resistivity (Ω.m)	Relative error in resistivity	Resistivity ± error (Ω.m)	Conductivity (s/m)	Conductivity ± error (s/m)
0.095	-	-	-	-	-
0.085	3.55×10^{-8}	0.042	$(3.6 \pm 0.15) \times 10^{-8}$	2.81×10^{7}	$(2.8 \pm 0.12) \times 10^{7}$
0.075	2.64×10^{-8}	0.145	$(3.6 \pm 0.38) \times 10^{-8}$	3.78×10^{7}	$(3.8 \pm 0.55) \times 10^{7}$
0.065	2.55×10^{-8}	0.329	$(2.6 \pm 0.84) \times 10^{-8}$	3.92×10^{7}	$(4 \pm 1.3) \times 10^{7}$
0.055	2.43×10^{-8}	0.345	$(2.4 \pm 0.84) \times 10^{-8}$	4.11×10^{7}	$(4 \pm 1.4) \times 10^{7}$
0.045	2.08×10^{-8}	0.158	$(2.1 \pm 0.33) \times 10^{-8}$	4.80×10^{7}	$(4.8 \pm 0.76) \times 10^{7}$
0.035	2.03×10^{-8}	0.178	$(2.0 \pm 0.36) \times 10^{-8}$	4.92×10^{7}	$(5.0 \pm 0.88) \times 10^{7}$
0.025	2.38×10^{-8}	0.177	$(2.4 \pm 0.42) \times 10^{-8}$	4.20×10^{7}	$(4.2 \pm 0.74) \times 10^{7}$
0.015	2.87×10^{-8}	0.168	$(2.9 \pm 0.48) \times 10^{-8}$	3.48×10^{7}	$(3.5 \pm 0.58) \times 10^{7}$

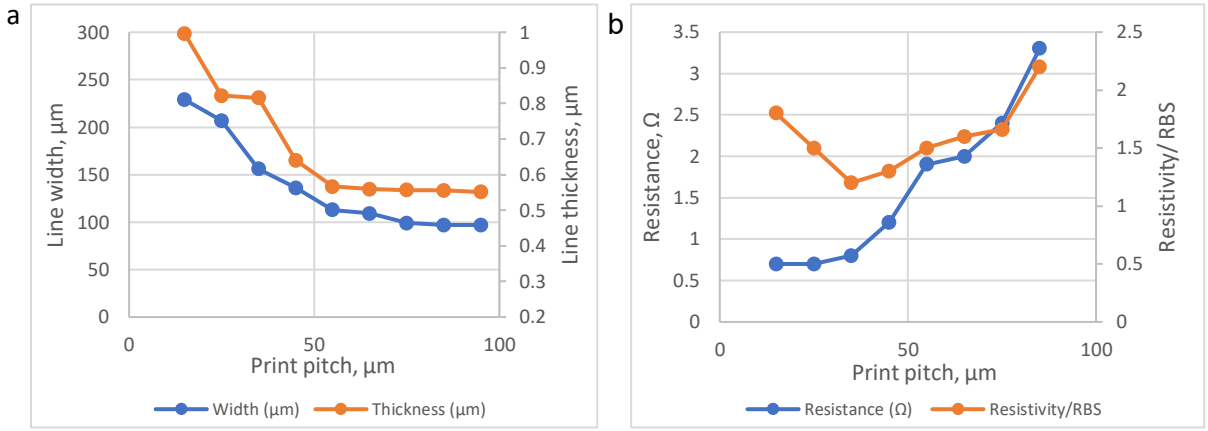

Figure 3.30. Characteristics of printed lines on glossy photo paper with a 50 µm nozzle diameter at room temperature (a) effect of print pitch on the line width/ thickness (b) effect of print pitch on resistance /RBS.

Clearly, line width was found to increase as the print pitch was decreased from 97 µm at print pitch 95 µm to about 229 µm at 15 µm pitch, because of the increased amount of lateral spreading prior to drying. In contrast, the resistance of the lines decreased with decreasing pitch size from 2.2 Ω against 85 µm to 0.7 Ω at 15 µm pitch size. Also, the thickness was corresponding with the width increase as the pitch decreased. The resistivity at the lower pitch range 15 µm was found to be (2.87×10^{-8} Ω.m), which is around 2 times RBS. With increasing the pitch size to around 35 µm, the resistivity reached around 1.3 times RBS (2.03×10^{-8} Ω.m), the lowest value achieved in any of this work.

3.5.5 Comparison of layer overprinting and print pitch variation on properties of AgPVP ink

To decide whether the geometry and electrical performance of printed lines were affected by an overprinting path instead of a single pass printing method, the pitch size was selected at 45 µm and the lines were overprinted up to five times on photo paper substrate.

Table 3.11. Summary of properties for room-temperature overprinted line features of 30% AgPVP on photo paper from a 50 μm nozzle at 45 μm print pitch.

No. of printed Layers	Width (m)	Thickness (m)	Resistance (Ω)	Length (m)
1	1.36×10^{-4}	0.64×10^{-6}	1.66	0.005
2	2.03×10^{-4}	0.90×10^{-6}	0.76	0.005
3	2.45×10^{-4}	1.19×10^{-6}	0.76	0.005
4	2.98×10^{-4}	1.35×10^{-6}	0.70	0.005
5	3.35×10^{-4}	1.54×10^{-6}	0.62	0.005

No. of printed layers	Resistivity (Ω.m)	Relative error in resistivity	Resistivity ± error (Ω.m)	Conductivity (s/m)	Conductivity ± error (s/m)
1	2.08×10^{-8}	0.158	$(2.1 \pm 0.33) \times 10^{-8}$	4.80×10^{7}	$(4.8 \pm 0.76) \times 10^{7}$
2	2.77×10^{-8}	0.011	$(2.8 \pm 0.03) \times 10^{-8}$	3.61×10^{7}	$(3.6 \pm 0.04) \times 10^{7}$
3	4.43×10^{-8}	0.023	$(4.4 \pm 0.10) \times 10^{-8}$	2.25×10^{7}	$(2.3 \pm 0.05) \times 10^{7}$
4	5.63×10^{-8}	0.042	$(5.6 \pm 0.24) \times 10^{-8}$	1.77×10^{7}	$(1.8 \pm 0.07) \times 10^{7}$
5	6.39×10^{-8}	0.051	$(6.4 \pm 0.33) \times 10^{-8}$	1.56×10^{7}	$(1.6 \pm 0.08) \times 10^{7}$

a

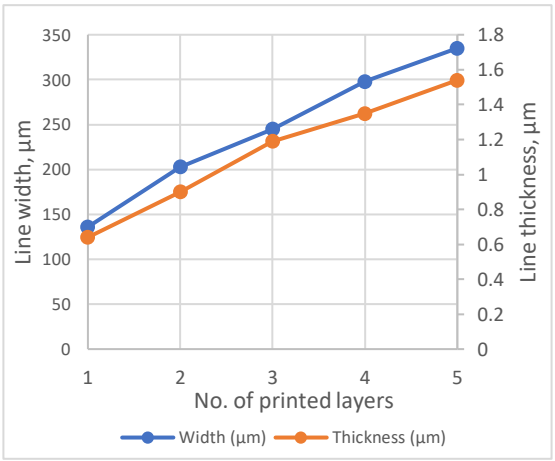

b

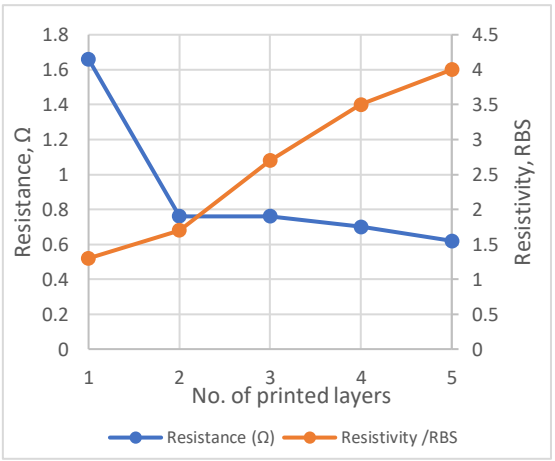

Figure 3.31. Properties of room-temperature overprinted features on photo paper from a 50 μm nozzle at 45 μm print pitch. (a) Effect of number of printed layers on line width/thickness, (b) effect of number of printed layers on resistance /RBS.

By looking at Table 3.11 and Figure 3.31 above, it can be seen the thickness and width of the printed lines both increase with overprinting from a thickness of about 0.64 μm and width 136 μm with a single layer at 45 μm pitch to a thickness of 1.54 μm and width 335 μm after overprinting to obtain five layers. The resistivity of the overprinted layers was increased by increasing the printed layers up to 5. In contrast, to the previous work by using AgPAA overprinted layers the resistivity showed a slight decrease, and this could be explained by the AgPVP thicker film (1.54 μm) compared with AgPAA film thickness (0.258 μm) with 5 printed layers.

In a similar way a steady decrease in resistance is observed as shown in Figure 3.32. From the microscope images, it can be significantly noticed that the increase in width and thickness corresponds with increasing the printed layers.

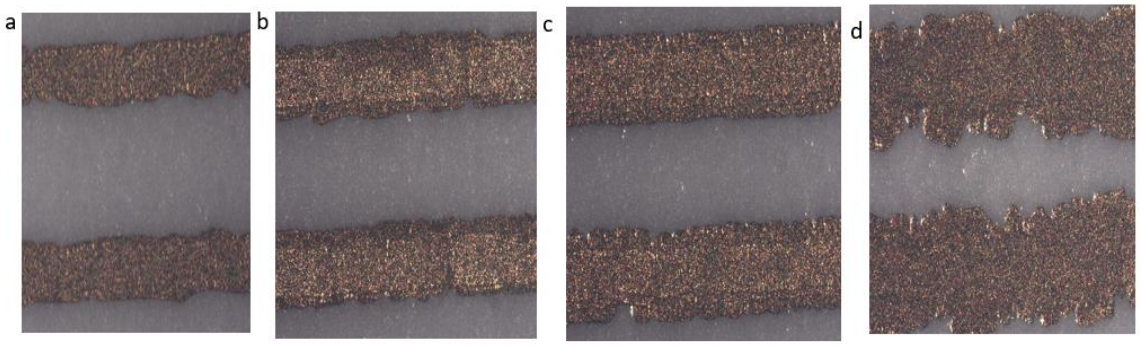

Figure 3.32. Microscope images of printing passes for 30%AgPVP at same pitch size (45 μm) with different numbers of printing layers (a) 1 layer, (b) 2 layers, (c) 3 layers and (d) 5 layers.

3.6 Conclusion

In summary, we have prepared highly concentrated and stable suspensions of silver nanoparticles by chemical reduction of silver nitrate by EG or $NaBH_4$ with PAA /or PVP/or PVOH as a stabilizer and protective agent. Our result confirmed that PAA /PVP were found to be very effective stabilizers for the dispersion of silver NPs.

The average size of the Ag particles in this method is in the nanoscale range, but sizes varied depending on synthesis methods and conditions. On the basis of these findings, some of the obtained Ag NPs can be utilized in conductive ink fabrication.

A stable Ag ink was formulated by dispersing as-prepared Ag NPs in water, with the presence of tri-solvent inkjet mixture, and then being treated with ultrasound to ensure it is well dispersed and achieving continuous ink flow without nozzle clogging.

This chapter also described progress in printing films of silver NPs with particular emphasis on their synthesis, physical characterisation, and electrical properties.

As already discussed, a remarkable resistivity for a printed film was obtained from Ag / PAA or Ag / PVP films on photo paper substrate after spontaneous sintering at room temperature. The final value, about 2 times RBS ($1.59 \times 10^{-8} \Omega.m$), is a substantial improvement on other values reported in the published literature [9, 10].

DLS, TGA, TEM and SEM/EDS were employed to confirm the ink stability, chemical composition, morphologies and thermal decomposition temperature and finally to demonstrate the effect of sintering at room temperature on the microstructure of printing films.

References

(1) Ibrahim, N.; Akindoyo, J. O.; Mariatti, M. Recent Development in Silver-Based Ink for Flexible Electronics. *J. Sci. Adv. Mater. Devices* **2022**, *7 (1)*, 100395.

(2) Mau Dang, C.; Kim Huynh, K.; My Thi Dang, D. Synthesis of Silver Nanoparticles Using Poly(Acrylic Acid) as a Capping Agent for Conductive Ink in Inkjet Printing Application. *Sci. Stay. True Here" Biol. Chem. Res.* **2019**, *6 (5)*, 111-119

(3) Shen, W.; Zhang, X.; Huang, Q.; Xu, Q.; Song, W. Preparation of Solid Silver Nanoparticles for Inkjet Printed Flexible Electronics with High Conductivity. *Nanoscale.* **2014**, *6 (3)*, 1622–1628.

(4) Mavuri, A.; Mayes, A. G.; Alexander, M. S. Inkjet Printing of Polyacrylic Acid-Coated Silver Nanoparticle Ink onto Paper with Sub-100 Micron Pixel Size. *Materials* **2019**, *12 (14)*, 1-10.

(5) Milardović, S.; Ivaniševic, I.; Rogina, A.; Kassal, P. Synthesis and Electrochemical Characterization of AgNP Ink Suitable for Inkjet Printing. *Int. J. Electrochem. Sci.* **2018**, *13 (11)*, 11136–11149.

(6) Huang, Q.; Shen, W.; Xu, Q.; Tan, R.; Song, W. Properties of Polyacrylic Acid-Coated Silver Nanoparticle Ink for Inkjet Printing Conductive Tracks on Paper with High Conductivity. *Mater. Chem. Phys.* **2014**, *147 (3)*, 550–556.

(7) Lu, P.; Hsieh, Y. Lo. Cellulose Nanocrystal-Filled Poly(Acrylic Acid) Nanocomposite Fibrous Membranes. *Nanotechnology.* **2009**, *20 (41)*, 1-9.

(8) Teerasong, S.; Jinnarak, A.; Chaneam, S.; Wilairat, P.; Nacapricha, D. Poly(Vinyl Alcohol) Capped Silver Nanoparticles for Antioxidant Assay Based on Seed-Mediated Nanoparticle Growth. *Talanta* **2017**, *170 (1)*, 193–198.

(9) Magdassi, S.; Grouchko, M.; Berezin, O.; Kamyshny, A. Triggering the Sintering of Silver Nanoparticles at Room Temperature. *ACS Nano.* **2010**, *4 (4)*, 1943–1948.

(10) Tang, Y.; He, W.; Zhou, G.; Wang, S.; Yang, X.; Tao, Z.; Zhou, J. A New Approach Causing the Patterns Fabricated by Silver Nanoparticles to Be Conductive without Sintering. *Nanotechnology.* **2012**, *23 (35)*, 1-7.

(11) Zhang, Z.; Zhu, W. Controllable Synthesis and Sintering of Silver Nanoparticles for Inkjet-Printed Flexible Electronics. *J. Alloys Compd.* **2015**, *649 (7)*, 687–693.

(12) Tang, Y.; He, W.; Wang, S.; Tao, Z.; Cheng, L. New Insight into the Size-Controlled Synthesis of Silver Nanoparticles and Its Superiority in Room Temperature Sintering. *CrystEngComm* **2014**, *16 (21)*, 4431–4440.

(13) Tolaymat, T. M.; El Badawy, A. M.; Genaidy, A.; Scheckel, K. G.; Luxton, T. P.; Suidan, M. An Evidence-Based Environmental Perspective of Manufactured Silver Nanoparticle in Syntheses and Applications: A Systematic Review and Critical Appraisal of Peer-Reviewed Scientific Papers. *Sci. Total Environ.* **2010**, *408 (5)*, 999–1006.

(14) Zielińska, A.; Skwarek, E.; Zaleska, A.; Gazda, M.; Hupka, J. Preparation of Silver Nanoparticles with Controlled Particle Size. *Procedia Chem.* **2009**, *1 (2)*, 1560–1566.

(15) Ajitha, B.; Kumar Reddy, Y. A.; Reddy, P. S.; Jeon, H. J.; Ahn, C. W. Role of Capping Agents in Controlling Silver Nanoparticles Size, Antibacterial Activity and Potential Application as Optical Hydrogen Peroxide Sensor. *RSC Adv.* **2016**, *6 (42)*, 36171–36179.

(16) Wang, Z.; Liang, X.; Zhao, T.; Hu, Y.; Zhu, P.; Sun, R. Facile Synthesis of Monodisperse Silver Nanoparticles for Screen Printing Conductive Inks. *J. Mater. Sci. Mater. Electron.* **2017**, *28*

(22), 16939–16947.

(17) Rónavári, A.; Bélteky, P.; Boka, E.; Zakupszky, D.; Igaz, N.; Szerencsés, B.; Pfeiffer, I.; Kónya, Z.; Kiricsi, M. Polyvinyl-Pyrrolidone-Coated Silver Nanoparticles—The Colloidal, Chemical and Biological Consequences of Steric Stabilization under Biorelevant Conditions. *Int. J. Mol. Sci.* **2021**, *22 (16)*, 8673.

(18) Kosmala A .Development of high loading Ag nanoparticle inks for inkjet printing and Ag nanowire dispersions for conducting and transparent coatings (PhD thesis) .*Cranfield university. School of applied science.* **2012**, 1-219.

(19) Leng, Z.; Wu, D.; Yang, Q.; Zeng, S.; Xia, W. Facile and One-Step Liquid Phase Synthesis of Uniform Silver Nanoparticles Reduction by Ethylene Glycol. *Optik (Stuttg).* **2018**, *154 (10)*, 33–40.

(20) Sun, Y.; Yin, Y.; Mayers, B. T.; Herricks, T.; Xia, Y. Uniform Silver Nanowires Synthesis by Reducing $AgNO_3$ with Ethylene Glycol in the Presence of Seeds and Poly(Vinyl Pyrrolidone). *Chem. Mater.* **2002**, *14 (11)*, 4736–4745.

Chapter 4. Alloy silver – nickel nanoparticle results and discussion

4.1 Synthesis and characterization of silver nanoparticles by co-reduction of Ag and Ni metal precursors at room temperature

Synthesis and characterization of mono-, and bi-metallic nanomaterials have been the subject of varied research work from the last two decades due to the enormous applications in all areas of industry. Bimetallic materials exhibit unique catalytic and sensing properties compared to their mono-metallic counterparts, due to new bifunctional or synergistic effects.

Among the various bimetallic materials, Ag@Ni, Ni@Ag and Ag-Ni alloys have been studied a lot due to their potentially valuable properties, despite pronounced lattice mismatch between the Ag and Ni metals, the lower surface energy of Ag, and the considerable difference between their reduction potentials [1]. Consequently, nickel-based inks are developed as an attractive alternative material to silver-based ink since they are cost-effective and have adequate conductivity [2,3,4], as well as good solderability [5].

However, nickel nano inks are not stable and are prone to oxidizing during the synthesis process. They usually require a reductive atmosphere or a special sintering method to ensure good conductivity. This contrasts with silver ink, where Ag does not require additional care during its formulation as it is chemically relatively stable, which is an advantage. In this work, nickel-silver alloy ink was synthesised and formulated, to take full advantage of these two materials to reduce the cost of metal ink while maintaining its conductivity and printability.

In this study, the synthesis of Ag-Ni alloy nanoparticles was carried out in a one-step process by co-reduction of mixed metal salts ($AgNO_3$ + $Ni(NO_3)_2$) solutions using sodium borohydride as a reducing agent and it is discussed in detail in section (2.2.2). This methodology is quite unsophisticated, but if a primary driver is cost reduction, it is essential to use simple and scalable processes if the work is to have real-world application.

We have successfully demonstrated the use of a co-reduction method, to synthesis the Ag-Ni NPs in water medium at room temperature with different stabilizing agents (PVOH or PVP or PAA) (Table 4.1). Four ratios of Ag^{+}/Ni^{2+}

suspension was prepared in the corresponding precursors in order to achieve the desired shape and size distribution of the synthesised Ag/Ni NPs.

As a final remark, the Ag-Ni alloy nanoparticles with different ratio 50:50, 75:25, 25:75 and 40:60 w/w % clearly shows reasonable results with a good size distribution (for printing) between 88 to 21 nm depend on metal composition.

Table 4.1. Summary of metal composition and the size distribution results.

Metal ratios w/w %	Stabilizing polymer	DLS size (d. nm)	PdI
Ag-Ni (50:50)	PVOH	194.9	0.23
Ag-Ni (50:50)	PVP	388.8	0.14
Ag-Ni (50:50)	PAA	79.12	0.22
Ag-Ni (75:25)	PAA	75.48	0.34
Ag-Ni (40:60)	PAA	88.06	0.29
Ag-Ni (25:75)	PAA	21.12	0.19

We can notice that the average particle size was considerably larger in the case of using the PVP and PVOH as a polymer compared with PAA. This can be explained by the decrease in surface charge when using these neutral polymers, hence there was less electrostatic force to prevent nanoparticle aggregation. Without the electrostatic barrier between particles, dramatic aggregation occurs and the average particle size increases. However, in the presence of PAA, the surface charge was negative, and the electrostatic force prevented the nanoparticles from aggregation.

PAA adsorbed on AgNP surface behaves as a weak acid and was completely deprotonated in the alkaline medium. Fully deprotonated PAA adsorbed on AgNP surface produces a negative surface charge, which impacts the coulombic repulsion force between nanoparticles. The strength of the repulsion between the nanoparticles in this type of stabilization is defined by the magnitude of the surface charge. The particles in a dispersion medium are stabilized with the forces of an electrical double layer: they obtain surface charge by the dissociation of surface groups. The growth of this charge at the surface influences the distribution of ions in the surrounding interfacial region. The formation of an electrical double layer is an effect of an increase in the concentration of counter ions close to the surface of the particle. The electrical

double layer is made up of two parts, an inner and outer region. The inner region is where the ions are strongly bound, and the outer region is where they are less strongly associated. Inside the diffuse layer, there is a boundary in which the ions and particles create a stable entity. Ions within the boundary move when a particle moves and these beyond the boundary stay with the bulk dispersant [6,7].

PVOH and PVP stabilize AgNPs through steric interactions. Polymeric molecules are either covalently attached or adsorbed onto the surface of the nanoparticles. Such polymeric molecules prevent the particles from getting close enough to each other to form aggregates due to their motion. The metal centre is surrounded by sterically bulky layers of material, banning the particles from coming close enough for Van der Waals forces to cause irreversible attraction.

On the other hand, the presence of polymers added to the dispersion medium can cause flocculation when polymers do not completely coat the particles. Adsorbed polymer can also be displaced from the area between two surfaces, creating a gradient of concentration. These processes are important in particle sintering, since during this process the stabilising ligand needs to be displaced off the surface to allow metal redistribution[7].

From the data in Table 4.1 it appears that electrostatic stabilisation is much more effective than steric stabilisation alone, leading to much smaller NP. The uncharged polymers achieved sufficient steric stabilisation to produce larger but still relatively stable NP, however, and these particles were still sufficiently stable and small enough to be used in printing. Uncharged particles should be stable at a wide range of pH values, which might have advantages in formulating more complex inks with multiple components.

The average size for the alloy was plotted against silver ratio in the alloy composition. As shown in Figure 4.1 there is not any obvious relationship between the size of particles and the percentage of Ag and Ni in alloy formulation, suggesting that the composition of the particle does not have a big effect on the nature and effectiveness of the polymer binding to the nanocrystal surface to provide stabilisation of the nanoparticles.

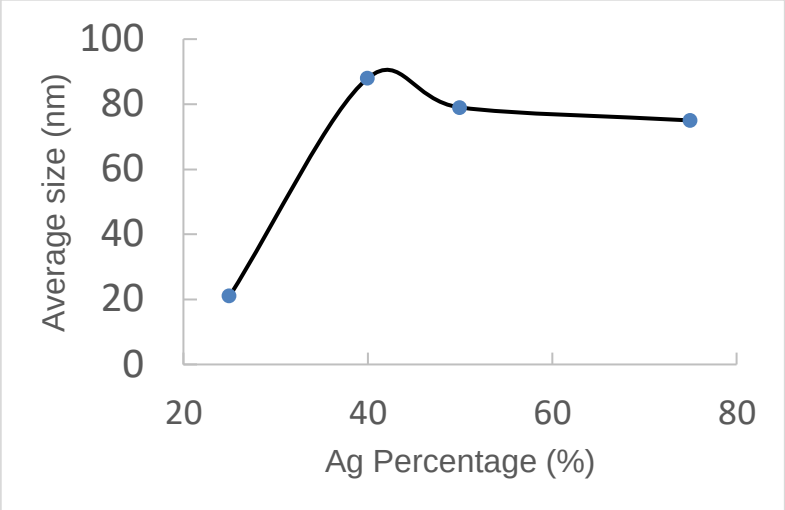

Figure 4.1. Average alloy nanoparticle size for Ag/Ni particles, plotted against the ratio used in particle synthesis.

In order to determine the morphological features of silver-nickel alloy NPs, SEM and TEM were used. SEM pictures of the samples with different Ag: Ni ratios (50:50, 75:25, 40:60 and 25:75 w/w%) are given in Figure 4.2. According to these results, it can be deduced that particles in all the samples are quasi-spherical. Size distributions for samples with different Ag/Ni ratios are nearly similar, with narrow distributions, which confirms that changing the metal composition ratios doesn't affect the particle sizes. The SEM results are not in line with DLS sizes. The SEM images show that these differences are likely due to the aggregation of particles, which makes a bigger hydrodynamic radius of particles in DLS measurements, although aggregation can be caused by the sample drying for SEM.

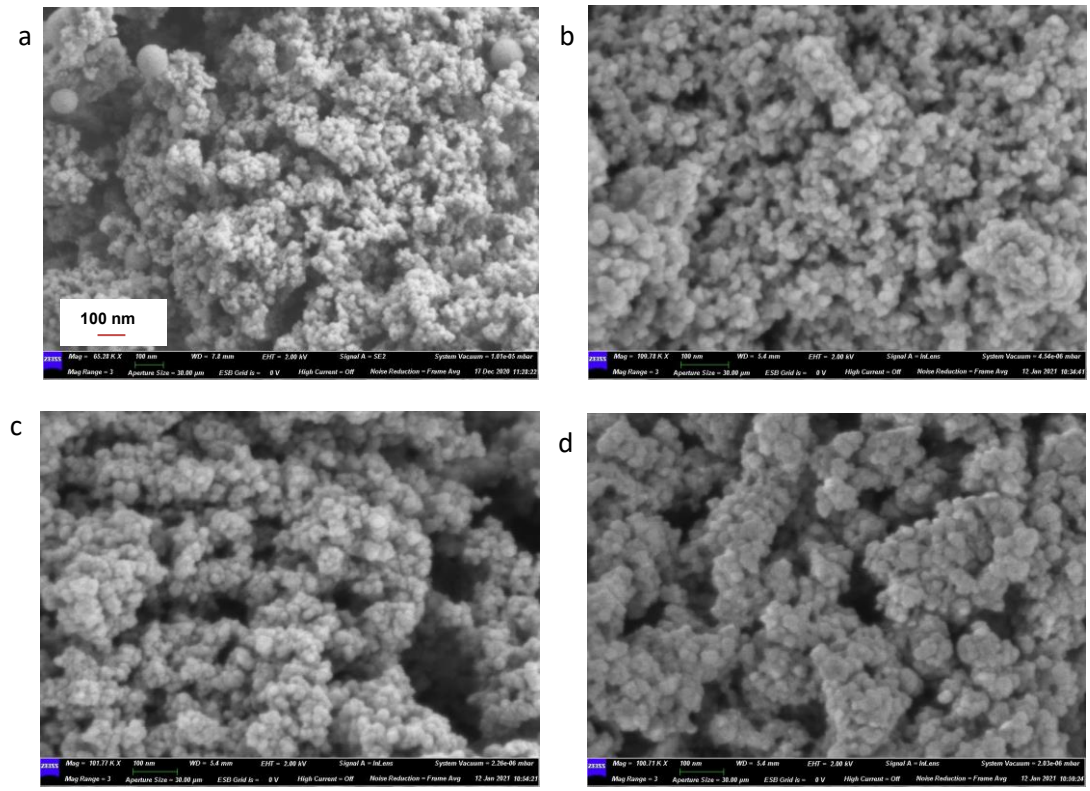

Figure 4.2. SEM of Ag/Ni alloy NP (a) 50:50, (b) 75:25, (c) 40:60 and (d) 25:75 w/w%.

The sample for TEM analysis was obtained by placing a drop of the colloidal solution onto a carbon-copper grid and evaporating it in air at room temperature. A typical TEM image for the Ag-Ni (50:50 w/w%)-PAA alloy is presented in Figure 4.3 (a). There exists large amount of hetero structures and their aggregation is observed with some formation of nanorod like morphology with size distributed between 25 nm and 74 nm. In Contrast, when a lower Ag content was used, a large number of irregular tiny NPs were seen, with a narrow size dispersity between 12-27 nm (Figure.4.3 (b)). The Ag NPs appear black, since Ag has a higher electron density and allows fewer electrons to transit, and Ni NPs are lighter coloured as shown clearly in the image [8]. The sizes observed are more consistent with the DLS size distribution results, suggesting that the PAA-stabilised particles are well dispersed in this sample.

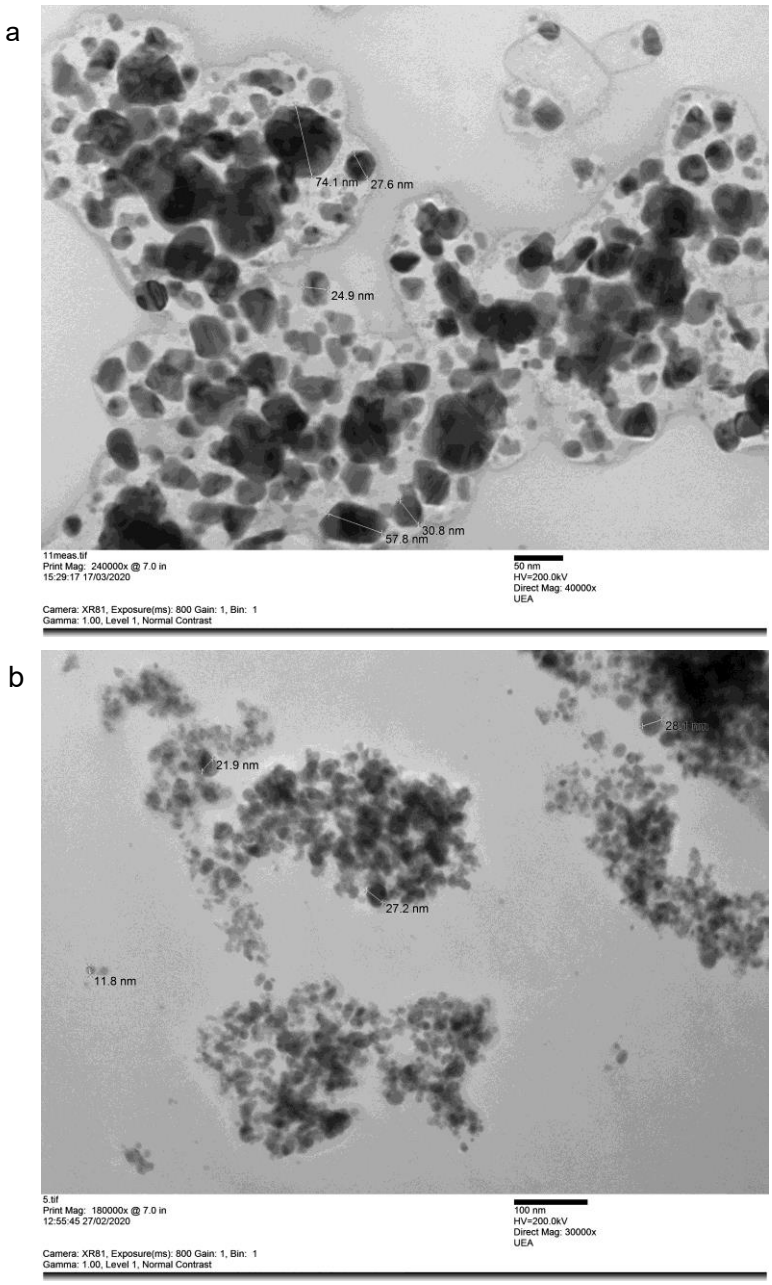

Figure 4.3. (a) TEM image of Ag-Ni (50-50 w/w%)-PAA, (b) Ag-Ni (25-75 w/w %)-PAA.

Thermogravimetric Analysis was conducted to confirm the presence and approximate amount of ligand on the surface of the metal nanoparticles (Figure 4.4). Sample was heated in a nitrogen environment to 500 °C at a heating rate of 10 °C min^{-1}.The thermal decomposition of the (Ag-Ni)-PAA (50:50 w/w%) Alloy NPs was began before 100 °C, about 4%, with a second major degradation before 300 °C, about 6%, and finally about 1% relatively sharp degradation at 450 °C .

The sharp mass loss from room temperature to 100 °C is attributed to the loss of hydroxyl groups on the surface as well as adsorbed water and contaminations from the atmosphere. At the higher temperature, complete

decomposition of the organic material occurs to volatile fragments that are lost. However, in comparison to Ag-PAA NPs, the alloy material had a higher weight loss about 11%. This must be due to more polymer bonding to the Ag -Ni alloy nanoparticle surface rather than Ag nanoparticles. Since the average particle size was also larger (lower surface to volume ratio), this suggests that the polymer may be binding more loosely to the surface with more/bigger loops. Investigating this in detail is a complex study however, and it was not investigated further.

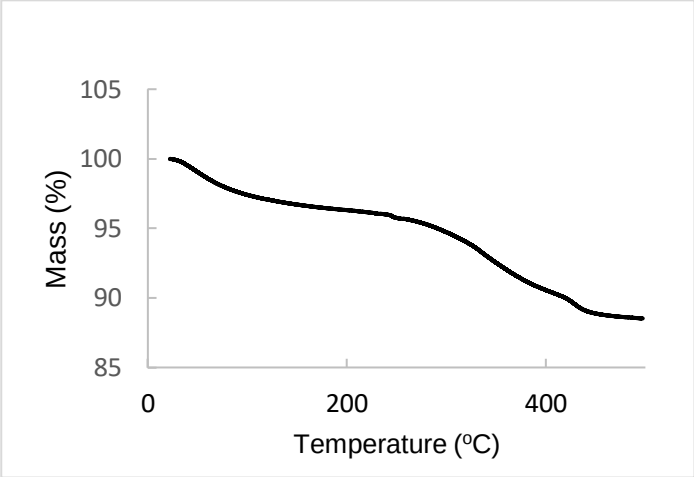

Figure 4.4. TGA of the Ag-Ni/PAA (50:50) w/w% alloy NPs powder.

4.2 Characterisation of 10% Ag-Ni/PAA (50:50 w/w%) standard ink

In terms of Ag conductive ink, small silver NPs size with functioning stability (to prevent sedimentation) were required to get a high-quality ink with a low sintering temperature. In this work, Ag-Ni stabilised with PVA and PVP gave a negative electrical resistance result as it appeared in a ‘smear test’ with lots of particle’s aggregation which make them unsuitable for ink formulation. In contrast, matched samples were prepared in the same manner with different metal ratio using PAA as capping ligand.

The size distribution was measured by DLS at different times, as illustrated in Table 4.2, to evaluate the silver-nickel alloy ink stability. The mean diameter of the particles is in nanoparticle size range, which ensures its jetting through the printhead nozzles.

Table 4.2. DLS size distribution of 10% Ag-Ni/PAA Alloy ink after different periods of storage time and the resistance from manual “smear test” .

Ink ratio (w/w%)	Ag: Ni (75:25)	Ag: Ni (50:50)	Ag: Ni (40:60)	Ag: Ni (25:75)
Resistance (Ω)	1-20	15-30	4-18	75-250
Size (d. nm) after formulation	7.65	44.49	56.84	71.68
Size (d. nm) in one month	9.712	45.60	60.99	87.07
Size (d. nm) in two months	12.29	46	61.84	94.03
Size (d. nm) in three months	12.92	50.03	62.67	94.90
Size (d. nm) in four months	15.36	56.5	65.69	95.67

The basic requirements for the ink should provide good printability with good electrical conductivity of printed patterns. Therefore, the fluid properties of the conductive ink are important because these must be compatible with various patterning technologies. For instance, a fluid with a high viscosity moves along slowly due to its molecular interactions causing high internal friction and this helps to restrain the formation of coffee ring structures when droplets dry. Conversely, a fluid with low viscosity flows readily as there is little friction in the liquid when it is in movement. The viscosity of the ink not only controls the velocity, size, and stability of the ejected droplet but also influences the shape of the droplets impinging on the substrate. These impingement shapes establish the pattern resolution and thickness and further affects its mechanical and electronic properties [9].

As shown in Figure 4.5, the ink containing 10% Ag-Ni/PAA (50:50 Ag:Ni) had a viscosity value about 0.5×10^{-2} pa. s at room temperature, which meets the inkjet printer requirements. Other alloy compositions had almost the same viscosity, so formulations did not need to be adjusted for printing. The viscosity results show that the changes in ratios of metal compositions don’t affect the value of viscosity of the final inks. It indicates that the inks composed of Ag-Ni/PAA nanoparticles have been successfully prepared.

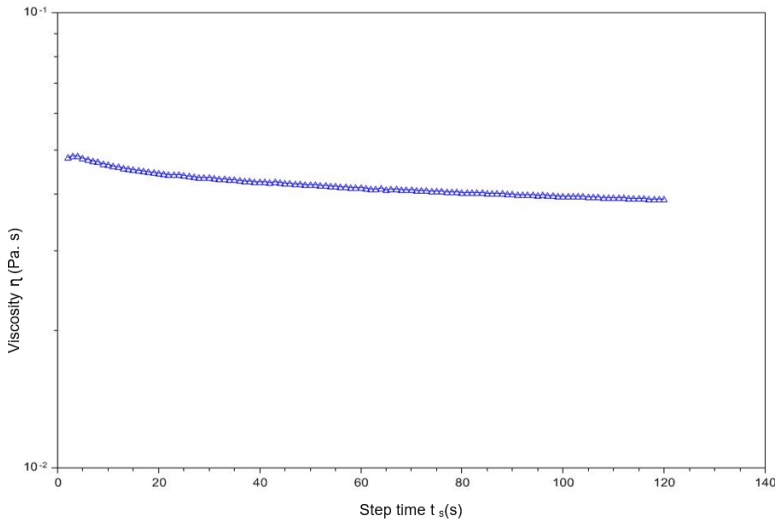

Figure 4.5. 10% Ag-Ni/PAA Alloy (50:50 Ag:Ni) ink viscosity.

4.2.1 Morphology of printed patterns

An inkjet printer was used to form nickel-silver tracks with different printing passes. Figure 4.6 displays optical microscope images with different width size as controlled by print pitch size. When the size between droplets was set at 95 µm, the line width was too thin and gradually increased to 1.74×10^{-4} m as the pitch size dropped down to 15 µm. As shown in Figure 4.6 (a), single dot pattern and breaking lines were produced on the pitch size 95 µm, hence the silver track cannot be conductive. However, when the distance between dots decreased starting from 65 µm, the droplets have more overlap and formed a continuous line. Coalescence and neck-forming of individual particles imply that the larger voids increase in size and Ag is redistributed to bridge smaller voids during sintering and thus increases the conductivity of the pattern. Moreover, the nickel-silver printing track thickness increased from 2.8×10^{-7} m to about 3.7×10^{-7} m with decreasing the pitch size and the line becomes denser because more inks was applied during printing. That was measured by profilometry and verified by the optical images too.

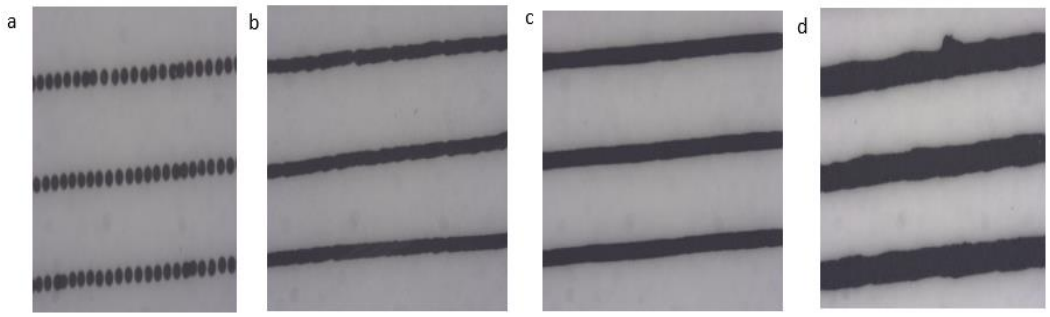

Figure 4.6. Optical microscope images of 10% Alloy Ag: Ni (50:50) w/w% ink showing the different line widths at different pitch size (a) 0.095 m, (b) 0.065 m, (c) 0.045 m, (d) 0.015 m.

The morphology of un-sintered ink and printed patterns were studied with SEM. The SEM images of 10% Ag-Ni/PAA (50:50), (75:25), (40:60) and (25:75) w/w% alloy inks before sintering respectively are shown in Figure 4.7. All these alloy inks look quite similar by SEM, although some slightly differences in the morphologies can be observed with change in metal ratio. They packed well together with some holes between particles either because they aren't sintered yet to fuse more closely or probably due to air trapped during drying. Besides, there are some cracks on the surface possibly attributed to the rapid drying of the solvent at room temperature.

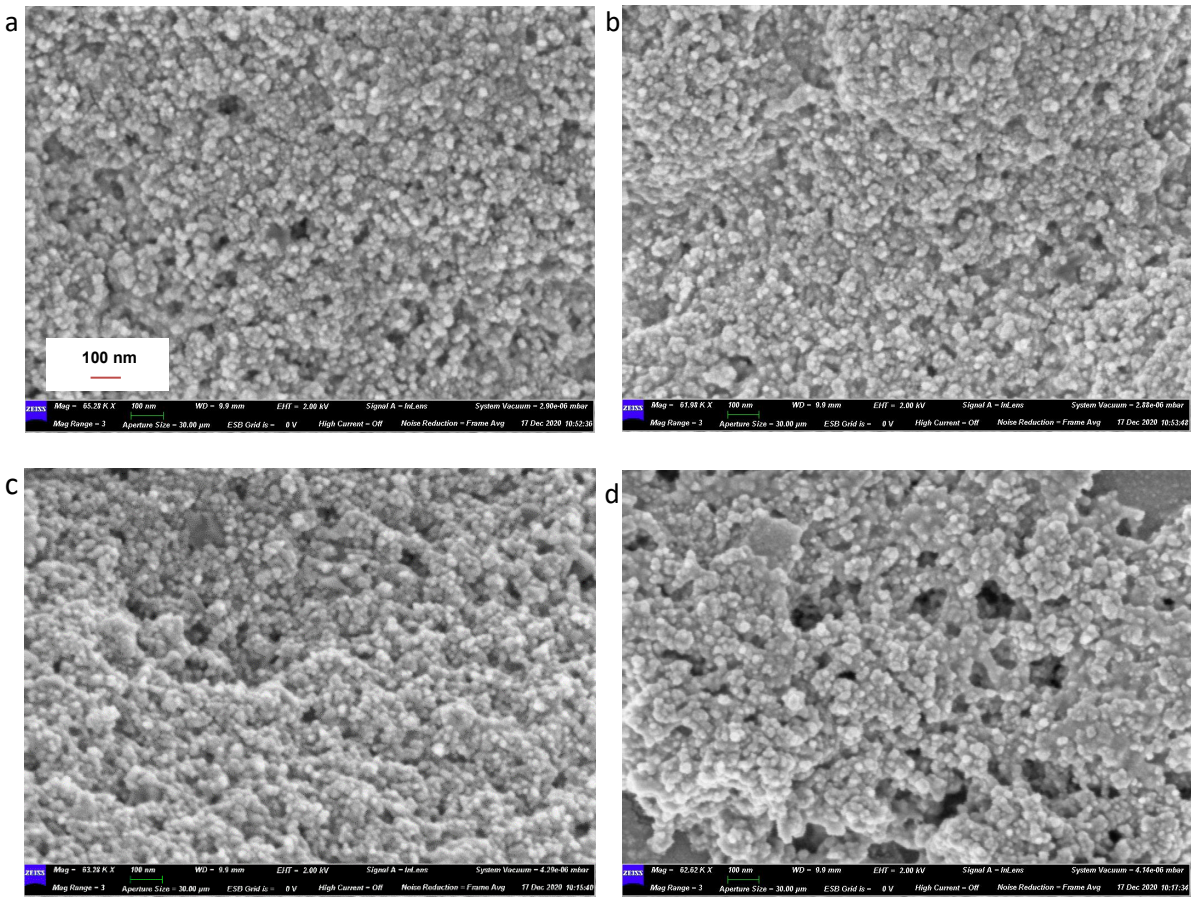

Figure 4.7. SEM of 10% Ag-Ni/PAA alloy ink without sintering (a) (50:50), (b) (75:25), (c) (40:60), (d) (25:75) w/w%.

The SEM images of the 10% (50:50 w/w%) alloy films sintered at room temperature are shown in Figure 4.8. It can be seen that the morphologies of the films change depending on the print pitch size. Printing at a lower pitch size made the silver nanoparticles grow forming larger particles through neck connection and improving the stacking density of the film. It should be noted that pores and voids among the NPs became fewer and smaller too at this stage and produced a relatively complete film. However, the film conductivity was low when printing at a large pitch size of 75 μm indicating insufficient formation of Ag particles from the complex as shown in Figure 4.8 (a).

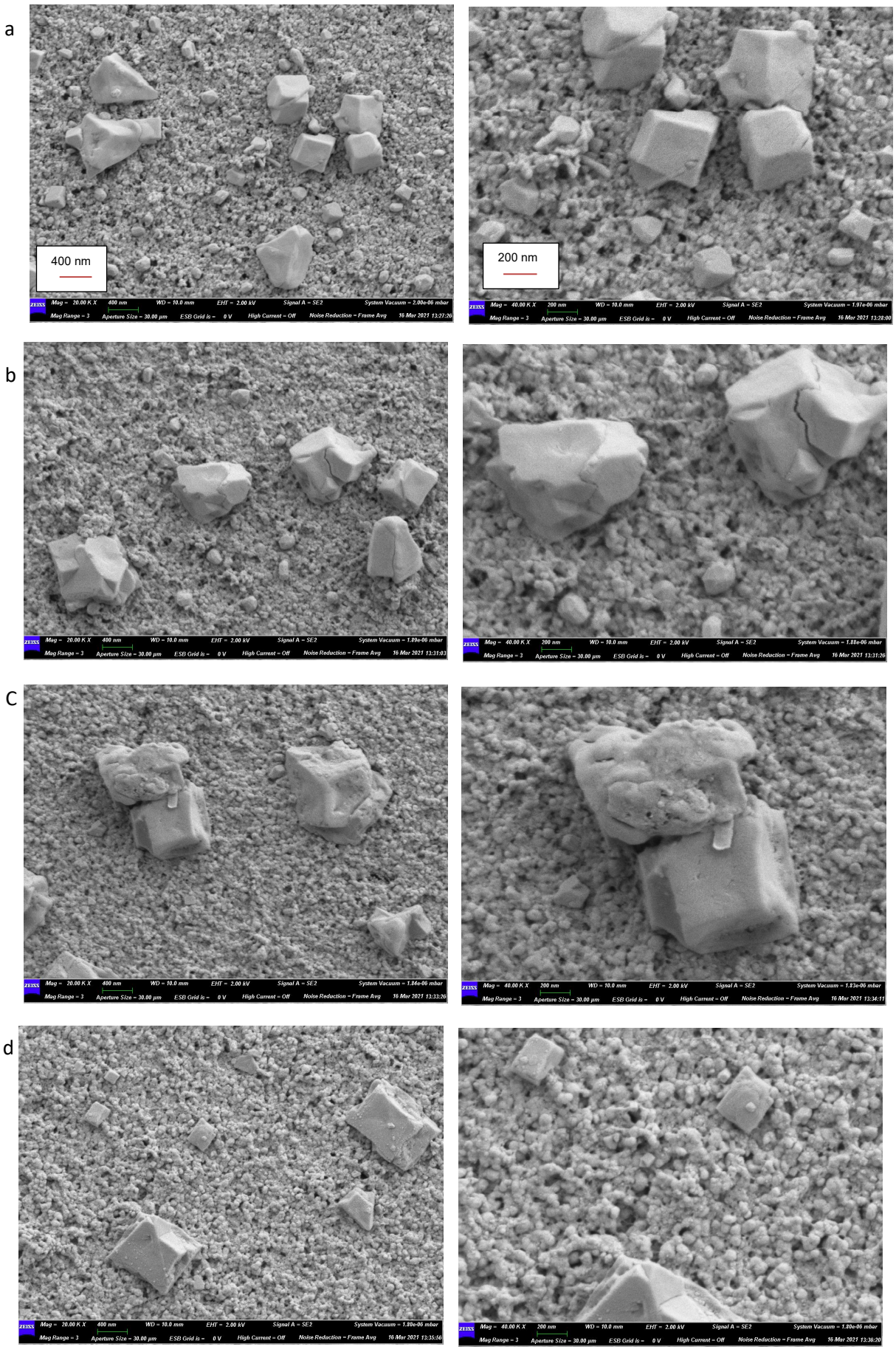

Figure 4.8. SEM images of the surface of the 10 % Ag-Ni/PAA (50:50 wt.%) alloy printed patterns at different pitch size (a) 75 µm, (b) 45 µm, (c) 25 µm and (d) 15 µm at room temperature.

Figure 4.9 shows the SEM images of the surface of the 10% Ag-Ni/PAA alloy overprinting patterns at 45μm print pitch sizes. The film seems to be made up of many layers where lines are overprinted 3 or 5 times. That leads consequently to the conductivity getting worse as the Cl^- ions don't efficiently get to the top layers and sinter the particles properly as they did on one layer of printing.

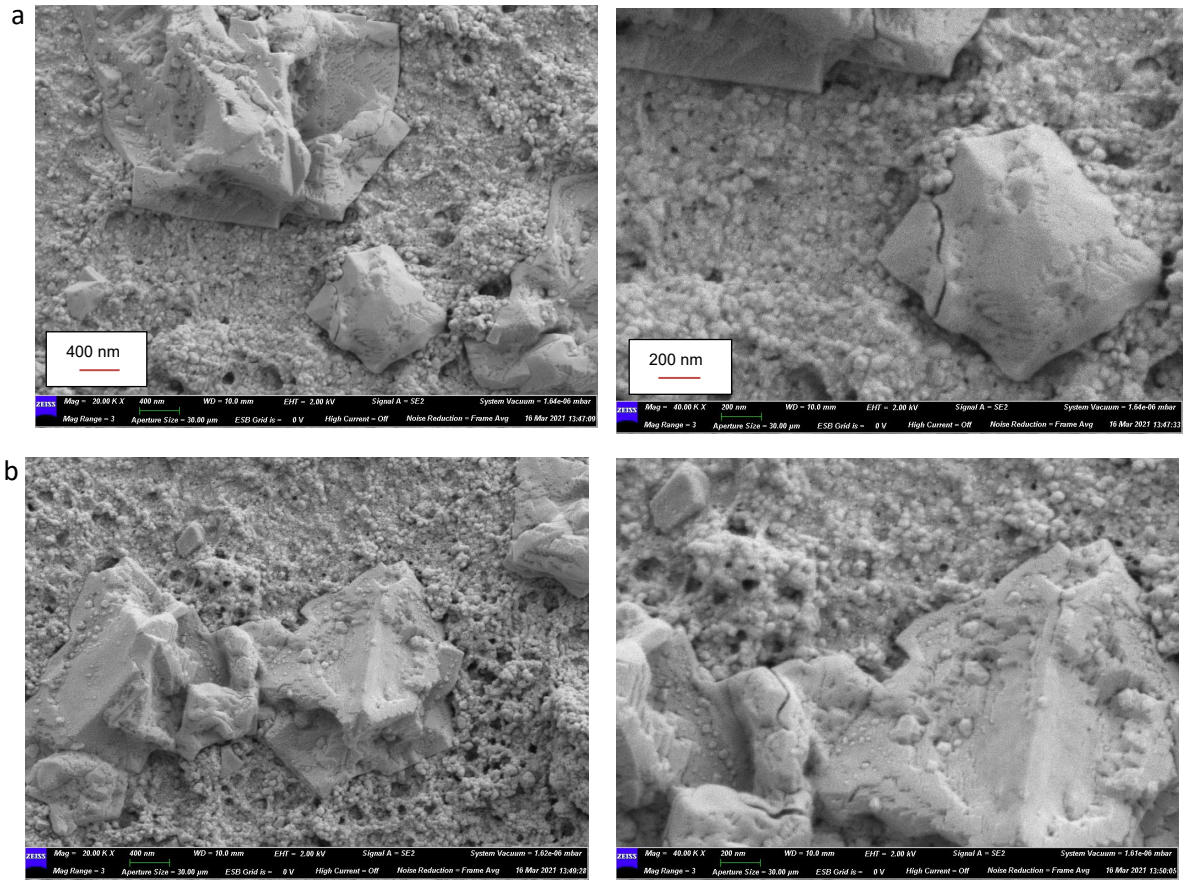

Figure 4.9. SEM images of the surface of the 10 % Ag-Ni/PAA (50:50 w/w%) alloy overprinting patterns at pitch size (45 μm) (a) 3 layers, (b) 5 layers.

Figure 4.10 demonstrates how are particles fused together and show a tightly compact mass of large particles after printing. Consequently, the SEM results in size distribution do not correspond with DLS sizes. The average size after sintering gets bigger about 174 nm – 519 nm.

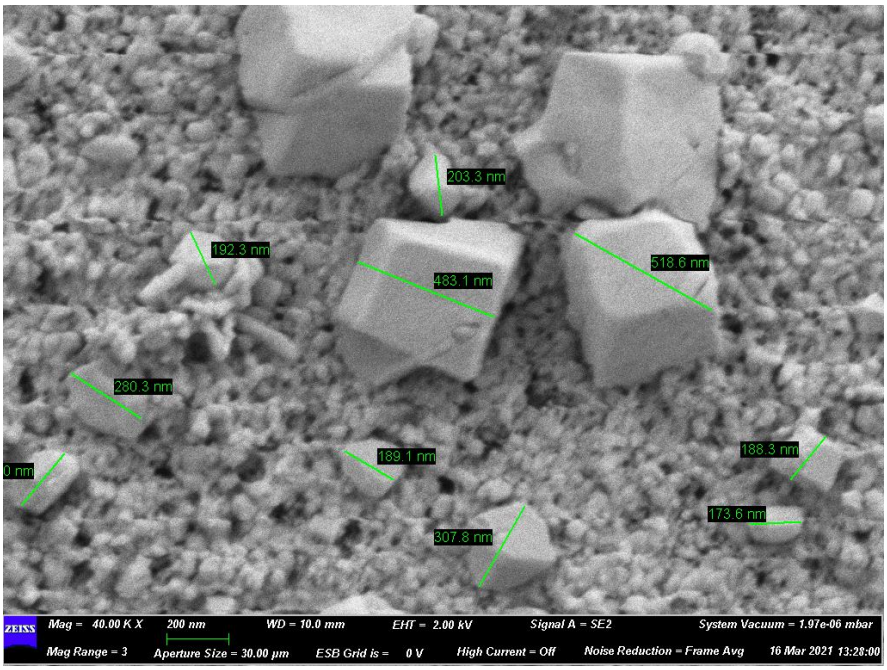

Figure 4.10. SEM images for 10 wt% Ag-Ni/PAA printing alloy after sintering with size measurements at room temperature.

4.2.2 Effect of Print Pitch on Geometry and Electrical Properties with Room Temperature Sintering

In order to discover and examine the effect of print pitch on the geometry and electrical properties of the printed features, the print pitch between droplets was varied over the range 95 µm to 15 µm and 5 replica lines were printed in a single pass for each print pitch. Printing by a 50 µm nozzle on photo paper substrate was done at room temperature. In Table 4.3 and Figure 4.11 the effect of varying print pitch on the line width, thickness and resistivity are shown respectively.

Table 4.3. Effect of pitch on width, thickness and resistivity of printed lines. 10% AgNi/PAA (50:50) w/w% alloy ink was printed with a 50 µm nozzle diameter on glossy photo paper at room temperature. The first five print pitches showed no conductivity, so their other parameters were not measured.

Pitch size (mm)	Width (m)	Thickness (m)	Resistance (Ω)	Length (m)
0.095	-	-	-	0.005
0.085	-	-	-	0.005
0.075	-	-	-	0.005
0.065	-	-	-	0.005
0.055	-	-	-	0.005
0.045	0.97×10^{-4}	2.81×10^{-7}	853	0.005
0.035	1.11×10^{-4}	2.83×10^{-7}	307	0.005
0.025	1.34×10^{-4}	3.39×10^{-7}	209	0.005
0.015	1.74×10^{-4}	3.73×10^{-7}	80	0.005

Pitch size (mm)	Resistivity (Ω.m)	Relative error in resistivity	Resistivity ± error (Ω.m)	Conductivity (s/m)	Conductivity ± error (s/m)
0.045	46.5×10^{-7}	0.158	$(46 \pm 7.3) \times 10^{-7}$	2.15×10^{5}	$(2.1 \pm 0.33) \times 10^{5}$
0.035	19.2×10^{-7}	0.178	$(19 \pm 3.4) \times 10^{-7}$	5.20×10^{5}	$(5.2 \pm 0.93) \times 10^{5}$
0.025	18.9×10^{-7}	0.177	$(18 \pm 3.4) \times 10^{-7}$	5.29×10^{5}	$(5.3 \pm 0.93) \times 10^{5}$
0.015	10.3×10^{-7}	0.168	$(10 \pm 1.7) \times 10^{-7}$	9.70×10^{5}	$(10 \pm 1.6) \times 10^{5}$

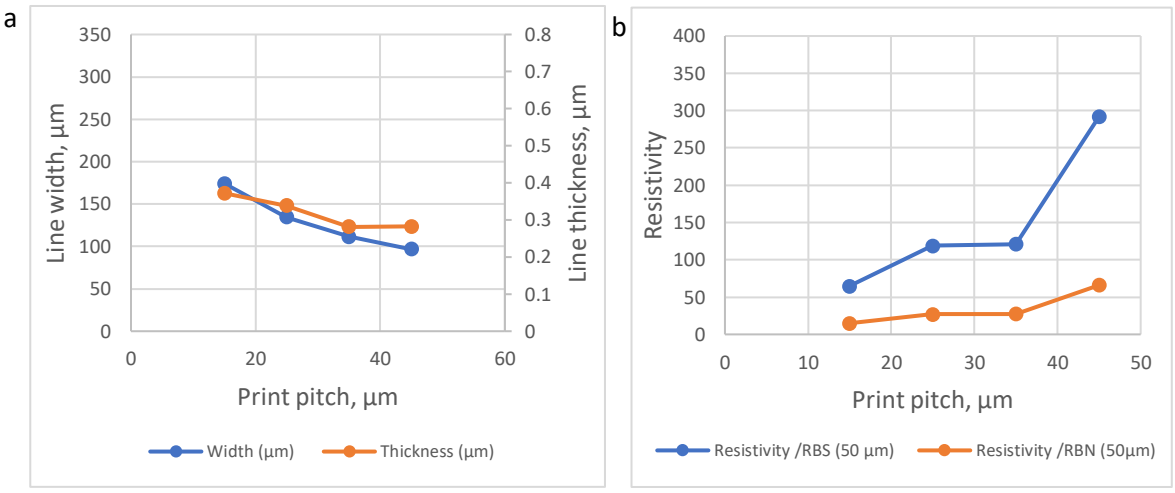

Figure 4.11. Characteristics of printed lines of 10% AgNi/PAA (50:50) w/w% alloy ink on glossy photo paper with a 50 µm nozzle diameter at room temperature (a) effect of print pitch on the line width/ thickness, (b) effect of print pitch on resistivity.

Clearly, line width was found to increase as the print pitch was decreased from $0.97x10^{-4}$ m at print pitch 45 µm to about $1.74x10^{-4}$ m at 15µm pitch, because of the increased amount of lateral spreading prior to drying. In contrast, the resistance of the lines decreased with decreasing pitch size from 853 Ω at 45 µm to 80 Ω at 15 µm pitch size. Also, the thickness was corresponding with the width increase as the pitch decreased too. The resistivity at the lower pitch range 15 µm was found to be ($10.3x10^{-7}$ Ωm), which is around 65 times RBS ($1.59x10^{-8}$ Ωm) and 15 times bulk nickel ($6.99x10^{-8}$ Ωm). With increasing the pitch size around 45 µm the resistivity was reaching around 66 times bulk nickel. On the other hand, the electrical resistivity reached very low values at 55, 45 and 35 µm pitch size, corresponding to about 2 times RBS while using AgPAA based ink (see section 3.1.5).

4.2.3 Comparison of layer overprinting and print pitch variation on properties

To decide whether the geometry and electrical performance of printed lines were affected by an overprinting path rather instead of a single pass printing method, the pitch size was selected at 45 µm and the lines were overprinting up to five times on photo paper substrate.

By looking at the Table 4.4 and Figure 4.12, it can be seen that the thickness and width of the printed lines both increase with overprinting from a

thickness of about $2.81x10^{-7}$ m and width $0.97x10^{-4}$ m with a single layer at 45 µm pitch to a thickness of $7.02x10^{-7}$ m and width $3.11x10^{-4}$ m after overprinting to obtain five layers. The resistivity of the overprinted layers showed a great decrease with increasing the printed layers, however. By reaching 5 layers, the resistivity increased and became 84 times worse than bulk nickel and 370 times worse compared with bulk silver. That clearly confirmed the Cl^- sintering on the paper wasn't enough to reach the top layer and exchange the polymer to make a sinter film compared with layer underneath. It is also indirect evidence that the polymer stabiliser may be binding differently to these alloy particles, inhibiting the chloride diffusion and polymer displacement and, hence preventing effective sintering. It is also possible that chloride induced mobilisation and redeposition of Ni ions may be harder than for Ag ions . No literature reports were found for room temperature Ni sintering, so it is likely that the conductivity achieved here is due to Ag redeposition, but it is clear that the presence of Ni is disrupting this process.

Table 4.4. Summary of properties of room-temperature overprinted features on photo paper from a 50 µm nozzle at 45 µm print pitch.

No. of printed Layers	Width (m)	Thickness (m)	Resistance (Ω)	Length (m)
1	$0.97x10^{-4}$	$2.81x10^{-7}$	854	0.005
2	$1.25x10^{-4}$	$3.44x10^{-7}$	522	0.005
3	$1.78x10^{-4}$	$4.32x10^{-7}$	245	0.005
4	$2.55x10^{-4}$	$6.02x10^{-7}$	115	0.005
5	$3.11x10^{-4}$	$7.02x10^{-7}$	134	0.005

No. of printed layers	Resistivity (Ω.m)	Relative error in resistivity	Resistivity ± error (Ω.m)	Conductivity (s/m)	Conductivity ± error (s/m)
1	$46.5\ x10^{-7}$	0.158	$(47 \pm 7.3)\ x10^{-7}$	$2.15\ x10^{5}$	$(2.1 \pm 0.34)\ x10^{5}$
2	$44.9\ x10^{-7}$	0.011	$(44.9 \pm 0.49)\ x10^{-7}$	$2.22\ x10^{5}$	$(2.22 \pm 0.02)\ x10^{5}$
3	$37.7\ x10^{-7}$	0.023	$(37.7 \pm 0.87)\ x10^{-7}$	$2.65\ x10^{5}$	$(2.65 \pm 0.06)\ x10^{5}$
4	$35.2\ x10^{-7}$	0.042	$(35 \pm 1.5)\ x10^{-7}$	$2.84\ x10^{5}$	$(2.8 \pm 0.12)\ x10^{5}$
5	$58.5\ x10^{-7}$	0.051	$(59 \pm 3)\ x10^{-7}$	$1.70\ x10^{5}$	$(1.70 \pm 0.09)\ x10^{5}$

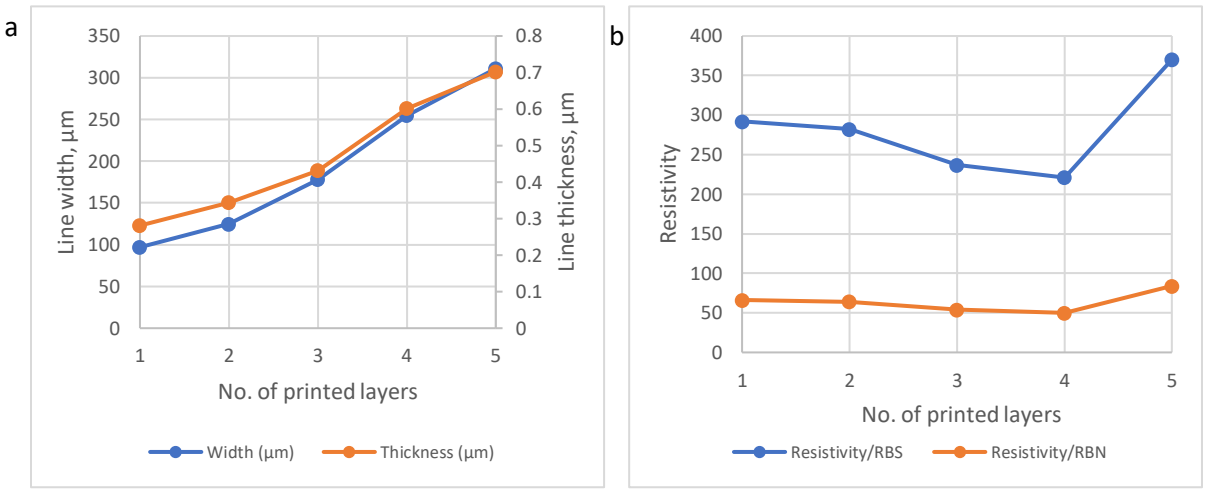

Figure 4.12. Properties of room-temperature overprinted features of 10% AgNi/PAA (50:50) w/w% alloy ink on photo paper from a 50 µm nozzle at 45 µm print pitch (a) effect of number of printed layers on line width/thickness, (b) effect of number of printed layers on resistivity.

From the microscope images of Figure 4.13, the increase in width and thickness can be easily seen, corresponding with the decrease in the pitch size between droplets and eventually the resistivity of the film.

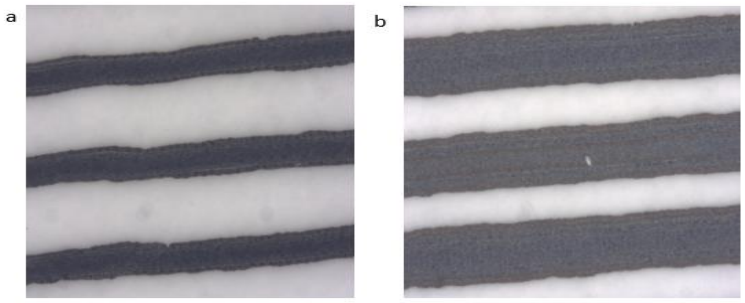

Figure 4.13. Optical microscope images of over printing pattern of 10% alloy Ag:Ni (50:50 w/w %) at pitch size 45 µm (a) 3 layers, (b) 5 layers.

4.2.4 Analysis of the elemental composition of printing film surface and dried formulated alloy ink

To analyze the ratio of Ag/Ni in printed film on photo paper, EDS characterization was performed, and the results are given in Figure 4.14. Clearly, the Ag, Ni, C and Cl^- elements were detected in each film as shown in the figures below, which is in accordance with the original chemical composition of the compounds in the alloy ink.

EDS results confirmed the presence of Ag and Ni elements in selected samples. The content of Ag was quite high between (90.08- 44.51 wt%), while Ni

existed in a low percentage and that could be explained either because it experiences some oxidation during processing and is not effectively incorporated into the NP or cannot be seen in the EDS data (e.g., because it is buried under Ag and AgCl).

It was very interesting to see that the Cl^- peak is quite prominent since we believe that this plays a major part in the mobilisation and redistribution of the metals to sinter the particles together and create conductivity.

In order to study the distribution of the Ag and Ni in analysed samples, the 2D distribution maps of the Ag, Ni as well as Cl^- were produced from the SEM images (Figure 4.14). The key elements are clearly associated with the crystals visible in the images, but very little Ni is evident (Table 4.5). Moreover, the EDS results show a reasonable amount of C, which could be attributed to the ligand PAA, (and possibly residual solvents that have been used, though the SEM is measured under high vacuum, so these might be expected to evaporate).

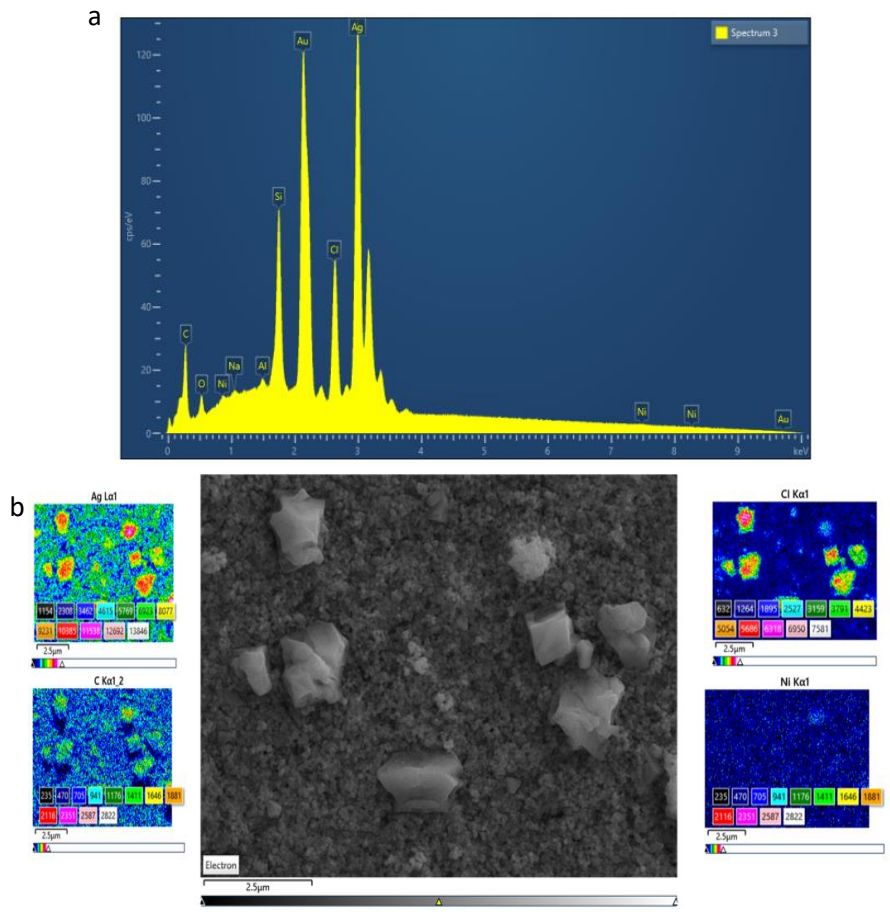

Figure 4.14. (a) EDS analysis results of printed Ag: Ni/PAA alloy film, (b) element distribution map.

Table 4.5. EDS elemental analysis results from printed film on photo paper.

Print pitch size (mm)	Metal ratio %	Silver weight %	Nickel weight %
0.075	50: 50	80.15	2.28
0.045	50: 50	65	2
0.025	50: 50	65.04	2.13
0.015	50: 50	57.68	1.55

The Ag, Ni, Cl^- and C individual element maps were quite informative, to see where the individual components within the ink go. However, only about 3% by weight of the NP is polymer, so there is not a large signal from C and it appears to follow the metal elements (i.e. still associated with the metal NP) as it appears on the Figure 4.14 (b). In this case, Ni shows in low concentration except in one particle, which also contained Ag, but very little Cl^-. However, Ag was clearly concentrated in discrete particles on the surface of the paper. The inhomogeneous distribution of Ag and Ni atoms might be affected by the differences in the reduction, nucleation, and growth rates of silver and nickel ions [7].

Furthermore, it could be seen that there were many large crystals formed up of AgCl as a result of Cl^- in the paper mobilising the Ag as part of the sintering process.

In consideration of the print pitch size, as the pitch size was decreased from 75 μm to 15 μm, an obvious change in Ag content was observed. However, the change was not much in Ni, Cl^- and C. This is also a reason why Ag-Ni alloy ink cannot achieve the same electrical properties as bulk silver. The results indicate that PAA was probably redistributed, but not fully removed from the particles, and the reduction of silver and nickel alloy was continued to a large extent. Many (more than 10) such element distribution maps were measured, but they all showed similar behaviour.

There were some contaminations present such as Si / Al / Na / O on the printing films, maybe arising from the glassware from synthesis or (more likely) mineral fillers used in the paper to make a smooth surface, or other sources during synthesis. They are clearly shown in Figure 4.15.

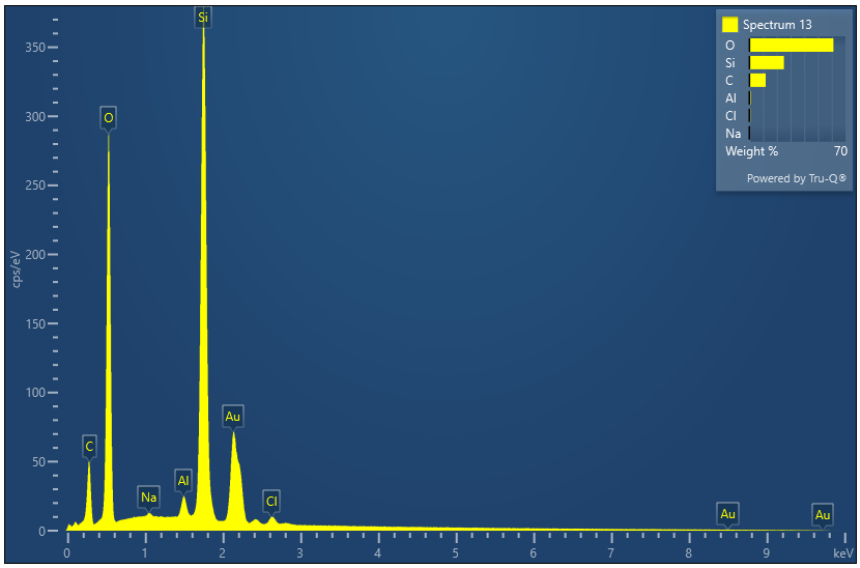

Figure 4.15. EDS results of the substrate (photo paper) prior to printing.

By looking at these spectra from the photo paper substrate under SEM without any printing film (Figure 4.15), the elements are clearly arising from the substrate itself and not from the printing ink. Au is present from the coating element within the EDS pre-analysis process. Si and O were existing in high level about 34.99% and 61.39% respectively. However, Cl^- exists at a low level of about 1.05% alongside Na 0.26%.

Interestingly, the Cl^- seems not completely uniformly distributed across the surface of the paper at the start as it appears faintly across the paper.

From the results based on the SEM and EDS, it can be concluded that, during the sintering process, the films experienced a sequence of processes including solvent evaporation, reduction of silver ions and neck connection of the silver and nickel nanoparticles.

Doing more studies by EDS for ink formulations dried directly onto SEM metal stubs (where there will definitely be no Cl^- present as on the photo paper substrate) size distributions and elemental spectra present in the ink itself could be checked. It can be seen from Figure 4.16 that the Cl^- peak was not observed in the EDS spectrum either on the ink or SEM stub, so the AgCl crystals seen on the printed paper definitely formed in-situ as a result of Cl^- in the paper mobilising the Ag as part of the sintering process. Elements found using EDS were C, O, Na, Al, Si, Ni and Ag. This would suggest the presence of metals and other elements that were likely to be found in the ink. This analysis also acted as confirmation of the likelihood that the some of the “contamination” contained within the printed film was present in the ink formulation as well with different

percentages depending on metals ratios, so it may have arisen in part from lab glassware.

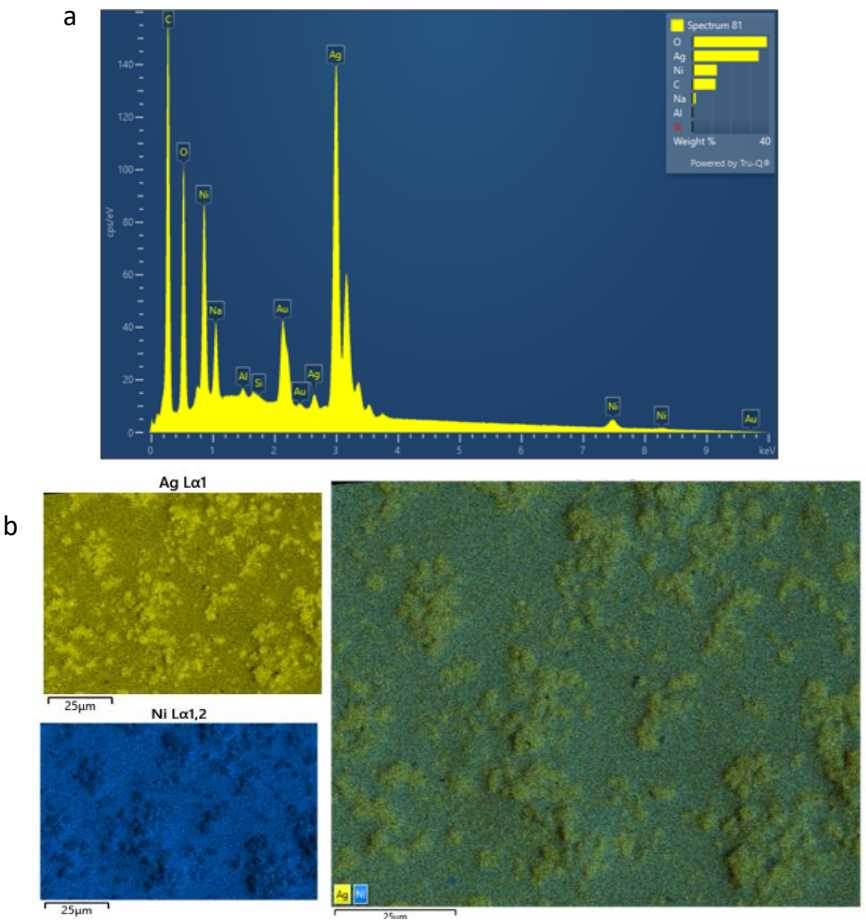

Figure 4.16. (a) EDS results of 10% Ag-Ni/PAA dried ink on SEM metal stub, (b) element distribution map.

It can be concluded that from figures seen above, there is little or no difference between the elements present on printing film and dried ink, other than Cl^-. Based on the ink formulation, the ratio of the metal is varied from one sample to another.

EDS mapping of Ag-Ni distribution in dried formulated ink is shown in Figure 4.16. The 2D distribution maps were employed to confirm the presence of chosen elements silver and nickel among other elements present on the sintered film. It was observed that silver has a higher content in both ink and sintered film. However, the Ni in printed film was quite uniformly distributed around the surface, while it was clearly shown in the ink compared to the printed film and that could be explained by whether the Ni is present in higher content in the samples but cannot be seen in the EDS data (e.g., because it is buried under Ag and AgCl) in the sintered film (Table 4.6).

Table 4.6. EDS elemental analysis results from dried ink.

Metal ratios %	Silver weight%	Nickle weight %
75: 25	48	3.4
50: 50	64	4.8
40: 60	34	3.3
25: 75	33	13.4

In order to better understand the Ni results from EDS, more elemental analysis was done of the dried nanoparticles by ICP- MS, since the EDS from SEM suggests that there is very little Ni in the alloy samples alongside other elements. Also, this would provide a definitive quantitation of the element ratio in the final materials, what elemental purity is like and whether there is significant contamination from other elements coming through from starting material to product. Consequently, after evaluating all the digested samples with the ICP-MS, we have seen only silver and nickel isotopes and other elements from the background (e.g., water and acid). The Ni percentage was still quite low, but it shows some consistent increase with increasing the percentages of Ni in the sample (Table 4.7). These results were confirmed by repeating alloy nanoparticle synthesis, scaling them up to 10 times, and new ink formulations, which were all reproducible each time.

Table 4. 7. ICP-MS elements analysis results from Ag: Ni /PAA nanoparticles.

Metal ratios	Silver content %	Nickel content %
Silver nitrate	99.98	0.02
Nickel Nitrate	0.49	99.51
Ag/PAA nanoparticle	99.96	0.04
Ag-Ni/PAA Alloy 75:25	97.22	2.78
Ag-Ni/PAA Alloy 50:50	96.48	5.52
Ag-Ni/PAA Alloy 40:60	92.29	7.71
Ag-Ni/PAA Alloy 25:75	80.55	19.45

The weight ratios of the constituent metals Ag and Ni in the samples prepared from precursors containing $AgNO_3$ and $Ni(NO_3)_2$ in ratios 75:25, 50:50, 40:60 and 25:75 is shown in Table 4.8, along with the EDS and ICP-Ms results. Comparison between these ratios indicates that the metal compositions of the synthesized alloys are not in very good agreement with the precursor compositions. As stated above, this might be slightly affected by the composition of the reaction solution which causes the differences in the reduction, nucleation,

and growth rates of nickel and silver ions and the alloy composition ratio at the end [10]. The EDS analyses present in the table are averages from more than one area selected over the sample (small and big particles). There are more elements detected in these samples (Cl^-, Si, Al, Na, O, C) for more details see section 4.2.4.

Table 4.8. Composition of metals in Ag–Ni alloy samples as obtained by ICP-MS and from EDS analyses.

Sample	$AgNO_3$: $Ni(NO_3)_2$ ratio by weight in precursor	Ag: Ni ratio in alloy by EDS analysis (on average)	Ag: Ni ratio in alloy by ICP-MS analysis
Ag75: Ni25	3:1	14:1	247:1
Ag50: Ni50	1:1	13:1	35:1
Ag40: Ni60	0.6:1	10:1	12:1
Ag25: Ni75	0.3:1	2:1	4:1

While my results indicated that there was very little nickel incorporation into the alloy, it is interesting to compare with the data published by Yan S [11]. In their work, XRD data suggested low nickel incorporation into the silver crystal structure, which caused slight distortion of the key Ag diffraction peaks, but no nickel-specific diffraction pattern was observed, suggesting nickel was only a minor component. This is similar to that reported here. In contrast, they reported EDS data that broadly matched the stoiciometric ratios expected. This seems contradictory. In my work, the ratios were checked using ICP-MS an analytically robust and accurate bulk technique, which confirmed my averaged EDS data (i.e. low nickel incorporation). Since EDS is a localised surface technique, it is possible that Yan's data came from individual areas of samples that had the expected ratios, rather than accurately reflecting the whole sample, but they did not comment on this, so it can only be speculation. Yan's XRD data is very consistent with results obtained by Kumar M. *et al.* [12] using a different synthesis method. Cheng Y. *et al.* [13], pointed out that the synthesis of alloy NPs was relatively easier than the core-shell NPs synthesis (see chapter 5) and their properties can be tailored by altering the metal ions composition.

4.3 Effect of using different nozzle size (80 μm) on the physical diameter of droplets and electrical properties of tracks with room temperature sintering

The desired droplet size depends on the application. We have successfully synthesized silver nanoparticles and printed tracks with good conductivity with 50 μm nozzle diameters. While small droplet sizes are perfect for small dimensions and high-resolution applications, however, it was more deflected by air currents. On the other hand, larger droplet sizes are ideal for large-area application and result in quicker printing [14].Therefore, a bigger nozzle diameter was evaluated to discover the difference in conductivity and electrical properties compared with a smaller diameter nozzle.

To investigate the optimum conductivity of the printed pattern printed on photo paper by different nozzle sizes, we produced a linear array of 5 silver-nickel lines with colloidal ink (10 wt% NPs). Tables 4.9 and Figures 4.17 illustrate how printing with a bigger nozzle 80 μm affects conductivity compared with the 50 μm nozzle.

Table 4.9. Comparison of electric properties of printed lines 10% AgNi /PAA (50:50 w/w %) alloy ink on glossy photo paper with a 50µm / 80µm nozzle at room temperature.

Pitch size (mm)	Resistance (Ω)	Width (m)	Thickness (m)	Resistivity (Ω.m)	Resistance (Ω)	Width (m)	Thickness (m)	Resistivity (Ω.m)
	50 µm Nozzle				**80 µm Nozzle**			
0.095	-	-	-	-	**-**	**-**	**-**	-
0.085	-	-	-	-	287	1.03×10^{-4}	3.18×10^{-7}	18.8×10^{-7}
0.075	-	-	-	-	191	1.07×10^{-4}	3.67×10^{-7}	15.001×10^{-7}
0.065	-	-	-	-	118	1.10×10^{-4}	3.70×10^{-7}	9.60×10^{-7}
0.055	-	-	-	-	89	1.17×10^{-4}	3.72×10^{-7}	7.74×10^{-7}
0.045	853	0.97×10^{-4}	2.81×10^{-7}	46.5×10^{-7}	59	1.39×10^{-4}	4.15×10^{-7}	6.80×10^{-7}
0.035	307	1.11×10^{-4}	2.83×10^{-7}	19.2×10^{-7}	39	1.67×10^{-4}	4.89×10^{-7}	6.36×10^{-7}
0.025	209	1.34×10^{-4}	3.39×10^{-7}	18.9×10^{-7}	18	1.99×10^{-4}	5.36×10^{-7}	3.83×10^{-7}
0.015	80	1.74×10^{-4}	3.73×10^{-7}	10.3×10^{-7}	17	2.75×10^{-4}	5.60×10^{-7}	5.23×10^{-7}

Pitch size (mm)	Resistivity (Ω.m)	Relative error in resistivity	Resistivity ± error (Ω.m)	Conductivity (s/m)	Conductivity ± error (s/m)
80 µm Nozzle					
0.095	-	-	-	-	-
0.085	18.8×10^{-7}	0.042	$(18.8 \pm 0.79) \times 10^{-7}$	5.31×10^{5}	$(5.3 \pm 0.22) \times 10^{5}$
0.075	15.001×10^{-7}	0.145	$(15 \pm 2.2) \times 10^{-7}$	6.66×10^{5}	$(6.7 \pm 0.96) \times 10^{5}$
0.065	9.60×10^{-7}	0.329	$(10 \pm 3.2) \times 10^{-7}$	10.4×10^{5}	$(10 \pm 3.4) \times 10^{5}$
0.055	7.74×10^{-7}	0.345	$(8 \pm 2.6) \times 10^{-7}$	12.9×10^{5}	$(13 \pm 4.5) \times 10^{5}$
0.045	6.80×10^{-7}	0.158	$(7 \pm 1.1) \times 10^{-7}$	14.7×10^{5}	$(15 \pm 2.3) \times 10^{5}$
0.035	6.36×10^{-7}	0.178	$(6 \pm 1.1) \times 10^{-7}$	15.7×10^{5}	$(16 \pm 2.8) \times 10^{5}$
0.025	3.83×10^{-7}	0.177	$(3.8 \pm 0.68) \times 10^{-7}$	26.1×10^{5}	$(27 \pm 4.6) \times 10^{5}$
0.015	5.23×10^{-7}	0.168	$(5.2 \pm 0.88) \times 10^{-7}$	19.1×10^{5}	$(19 \pm 3.2) \times 10^{5}$

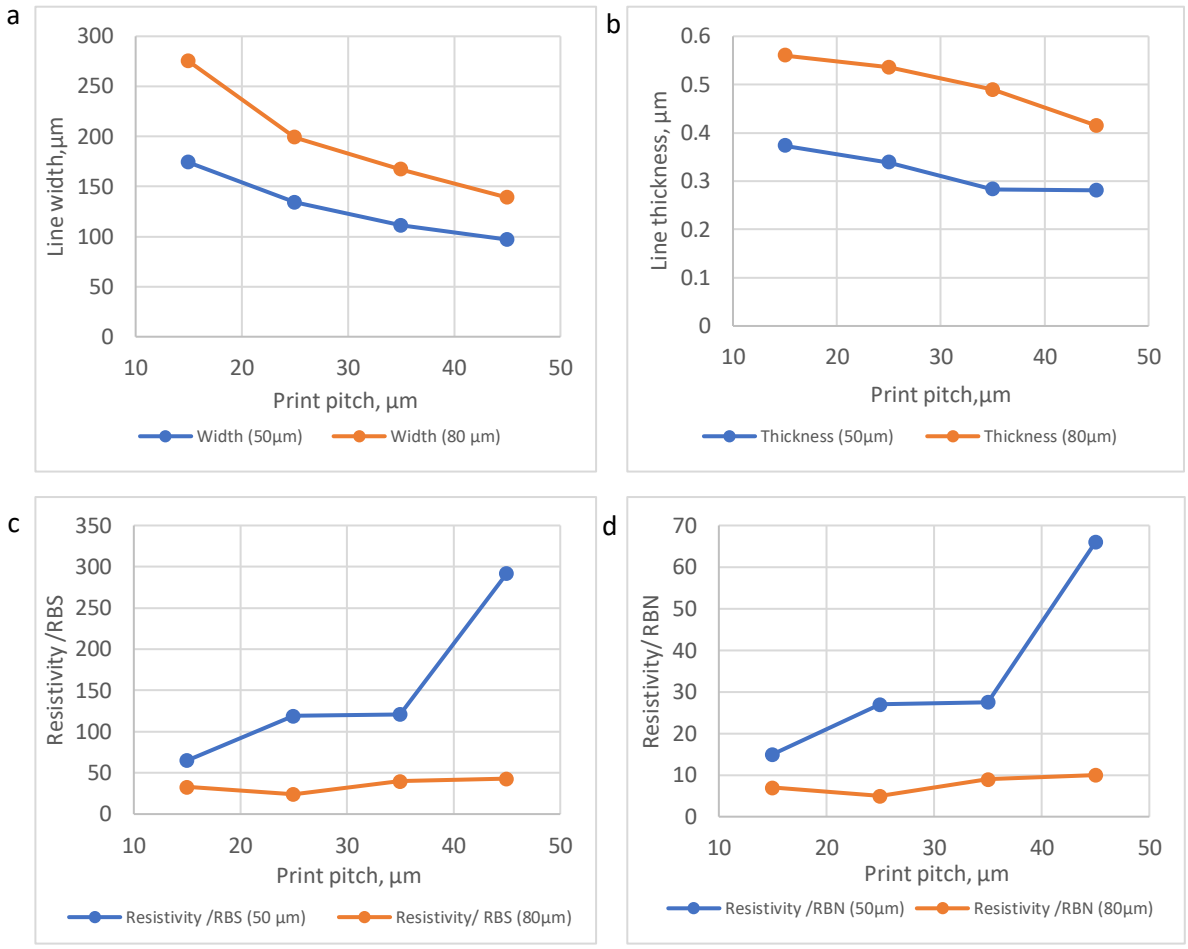

Figures 4.17. Comparison the effect of nozzle size on physical dimension and electric properties of printed lines on glossy photo paper at room temperature (a) on line width, (b) on line thickness, (c) resistivity shown relative to bulk silver, and (d) resistivity shown relative to bulk nickel.

These tables/figures allow for an easy and quick comparison of the electrical properties for printing under the same condition with different nozzle sizes. Our results confirm that a significant decrease in electric resistance is observed by using 80 µm nozzles corresponding to the increase in line thickness /width due to the greater deposition of particles, but once this is corrected for by calculating conductivity, there is little difference between tracks obtained by the 50 µm nozzle and the 80 µm nozzle. This is as would be expected, since the particles and the sintering process have not changed, only the geometric pattern of their deposition.

To compare the homogeneity of the Ag-Ni NPs thin coating on the photo paper, a series of surface morphology SEM images were taken. As shown in Figure 4.18 the silver -nickel ink conformally coated the paper surface and exhibited good adhesion.

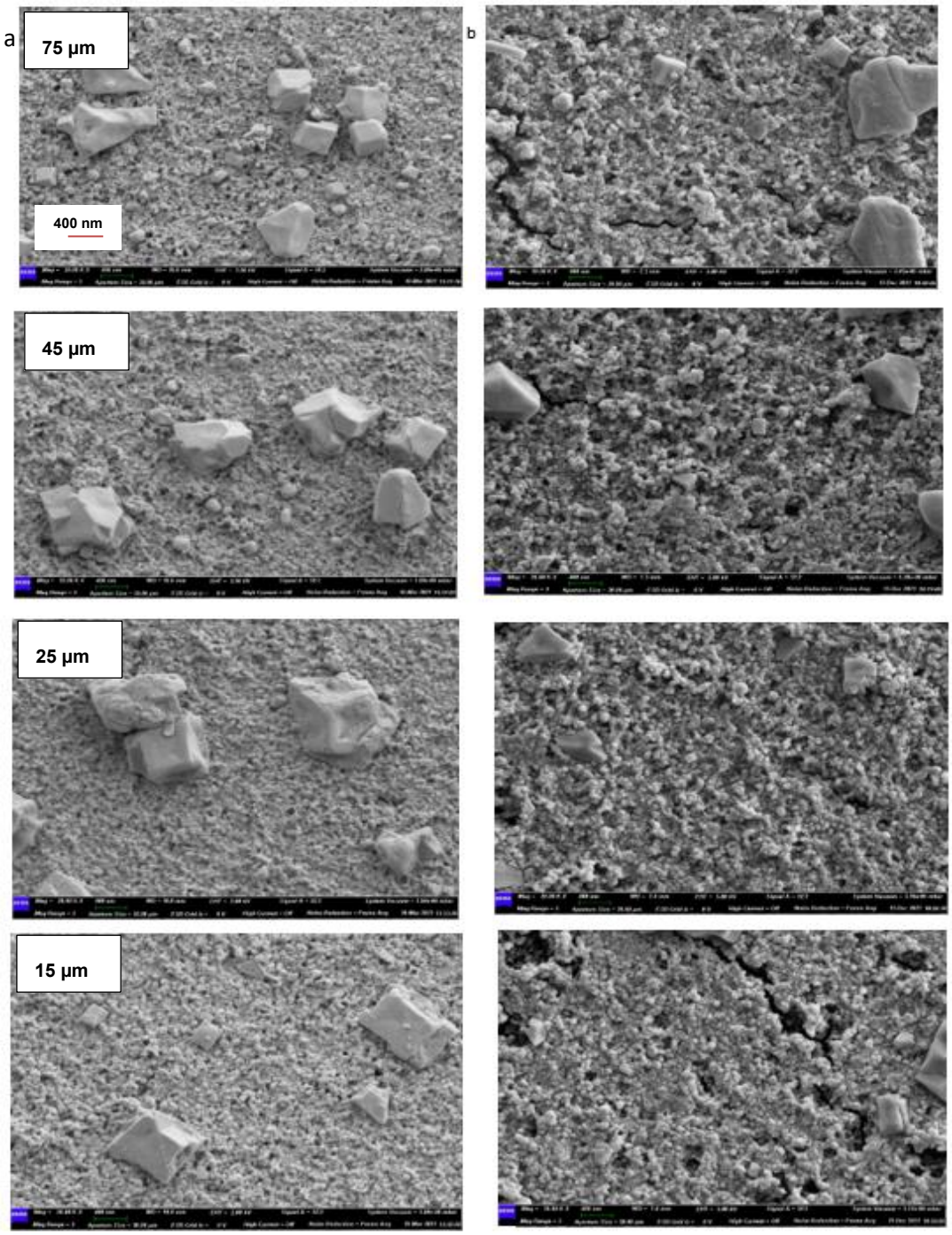

Figure 4.18. Comparison of SEM images of the surface of the 10 wt.% Ag-Ni/PAA (50:50 w/w%) alloy patterns at different pitch size (a) 50µm nozzle (75), (45), (25) and (15) µm, (b) 80 µm nozzle (75), (45), (25) and (15) µm at room temperature respectively.

Figure 4.18 shows some SEM images of coalesced particles printed using different nozzle sizes. With a bigger nozzle (80 µm), the amount of the printing ink increases, which can be seen in the formation of a rougher surface and having more gaps and cracks. As a results of the amount of ink, the top layers of the

printed tracks could be affected, since the Cl^- ion likely struggled to diffuse and reach the top, which makes the cracks and gaps due to the limited mobilisation and redeposition of silver. That was in contrast to the tracks printed by the 50μm nozzle, which had a more uniform, compact surface and the particles show considerably more interconnection. This did not appear to affect the conductivity, however, which was similar in both tracks (see the table above).

4.3.1 Comparison of layer overprinting and print pitch variation on properties

To decide whether the overprinting, geometry and electrical performance of printed lines were also affected by the nozzle diameter, we compared the results from these two nozzles (Tables 4.10 & Figures 4.19). The pitch size was selected at 45 μm and the lines were overprinted up to five times on a photo paper substrate.

Table 4.10. Summary of properties of room-temperature overprinted features on photo paper from a 50 /80µm nozzle at 45µm print pitch.

No. of printed layers	Resistance (Ω)	Width (m)	Thickness (m)	Resistivity (Ω.m)	Resistance (Ω)	Width (m)	Thickness (m)	Resistivity (Ω.m)
	50 µm Nozzle				80 µm Nozzle			
1	854	0.97×10^{-4}	2.81×10^{-7}	46.5×10^{-7}	59	1.40×10^{-4}	4.15×10^{-7}	6.80×10^{-7}
2	522	1.25×10^{-4}	3.44×10^{-7}	44.9×10^{-7}	26	1.99×10^{-4}	5.91×10^{-7}	6.11×10^{-7}
3	245	1.78×10^{-4}	4.32×10^{-7}	37.7×10^{-7}	23	2.50×10^{-4}	6.02×10^{-7}	6.92×10^{-7}
4	115	2.55×10^{-4}	6.02×10^{-7}	35.2×10^{-7}	19	3.08×10^{-4}	6.37×10^{-7}	7.45×10^{-7}
5	134	3.11×10^{-4}	7.02×10^{-7}	58.5×10^{-7}	20	3.70×10^{-4}	6.54×10^{-7}	9.67×10^{-7}

No. of printed layers	Resistivity ± error	Conductivity (s/m)	Conductivity ± error (Ω.m)	Resistivity ± error	Conductivity (s/m)	Conductivity ± error (s/m)
	50 µm Nozzle			**80 µm Nozzle**		
1	$(47 \pm 7.3) \times 10^{-7}$	2.15×10^{5}	$(2.2 \pm 0.34) \times 10^{5}$	$(7 \pm 1.1) \times 10^{-7}$	14.7×10^{5}	$(15 \pm 2.3) \times 10^{5}$
2	$(44.9 \pm 0.49) \times 10^{-7}$	2.22×10^{5}	$(2.22 \pm 0.02) \times 10^{5}$	$(6.11 \pm 0.07) \times 10^{-7}$	16.36×10^{5}	$(16.4 \pm 0.18) \times 10^{5}$
3	$(37.7 \pm 0.87) \times 10^{-7}$	2.65×10^{5}	$(2.65 \pm 0.06) \times 10^{5}$	$(6.9 \pm 0.16) \times 10^{-7}$	14.45×10^{5}	$(14.5 \pm 0.33) \times 10^{5}$
4	$(35 \pm 1.5) \times 10^{-7}$	2.84×10^{5}	$(2.8 \pm 0.12) \times 10^{5}$	$(7.5 \pm 0.31) \times 10^{-7}$	13.42×10^{5}	$(13.4 \pm 0.56) \times 10^{5}$
5	$(59 \pm 2.9) \times 10^{-7}$	1.70×10^{5}	$(1.70 \pm 0.09) \times 10^{5}$	$(9.7 \pm 0.49) \times 10^{-7}$	10.34×10^{5}	$(10.3 \pm 0.53) \times 10^{5}$

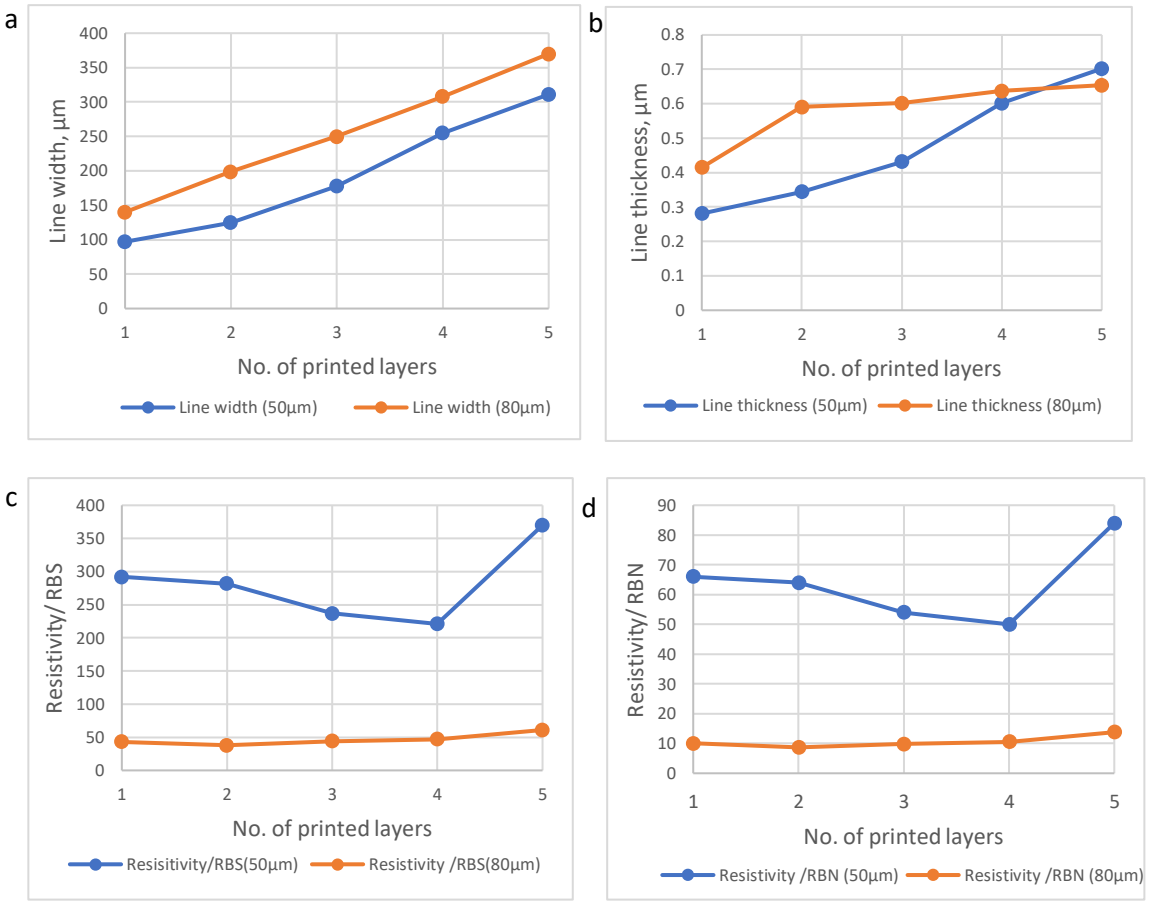

Figure 4.19. Comparison the effect of nozzle size on physical dimension and electric properties of overprinted lines on glossy photo paper at room temperature (a) on line width, (b) line thickness, (c) resistivity shown relative to bulk silver, and (d) resistivity shown relative to bulk nickel.

Obviously, as droplets get bigger, the conductivity increases and is closer to the metal bulk. These bigger droplets are less demanding on printer setup compared with smaller droplet volumes, which require less distance between the print head and the substrate and more energy to break away from the nozzle, as stated in the literature [14].

4.4 Effect of printing 10% AgNi /PAA (75:25 w/w%) alloy ink on photo paper on geometry and electrical properties with room temperature sintering

To date, various Ag-Ni alloy compositions have been investigated by inkjet printing to produce continuous and conducting patterns with high quality. Nickel-

based ink has been restricted in inkjet printing, mainly due to its durability issues (cracking or peeling) occurring in the ink layer after sintering.

It has been found that a uniform layer was successfully printed on the photo paper substrate by the 10% Ag-Ni (75:25 w/w%) ink. However, these printing tracks have suffered from disadvantages such as cracking/ fracturing in the contacting area that caused conductivity loss. Interestingly, the overprinting layers have appeared to give good conductivity and overcome the fracturing issues, unlike a single layer.

By examining the various factors that affect the print interconnects quality and cause this poor printing quality on single layers, substrate-ink interactions and the choosing of the optimal drop pitch can be one of these causes which over-printing layers can overcome by making more particle connections with less porous, thin films, which produces good quality.

Figures 4.20 show SEM-EDS analysis of the nanoparticle dispersion and revealed that (Ag-Ni /PAA) (75:25 w/w%) printing tracks showed the film is not completely covered by ink, so no resistance can be measured across the film. In contrast, the overprinting tracks display better covering of the film and thus give a good resistance (Figure 4.21).

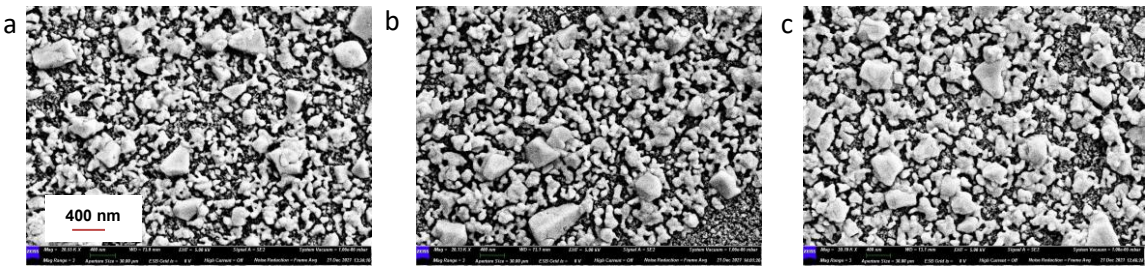

Figure 4.20. SEM images of the film surface of the 10% Ag-Ni/PAA (75:25 w/w%) alloy at different pitch size (a) (45 µm), (b) (25 µm), and (c) (15 µm) at room temperature.

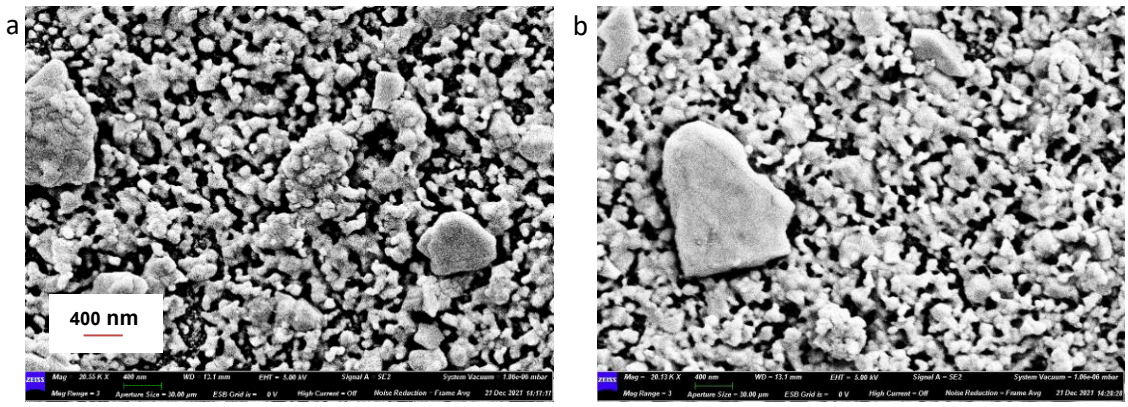

Figure 4.21. SEM images of the surface of the 10% Ag-Ni/PAA (75:25 w/w%) alloy overprinting patterns at pitch size (45 µm) (a) 3 layers, and (b) 5 layers.

Table 4.11 and Figure 4.22 demonstrate that, the conductivity of the overprinted patterns significantly increased as the number of layers printed increased.

Table 4.11. Summary of properties of room-temperature 10% AgNi /PAA (75:25) w/w% alloy ink overprinted features on photo paper from a 50 µm nozzle at 45µm print pitch.

No. of printed Layers	Width (m)	Thickness (m)	Resistance (Ω)	Length (m)
2	2.01×10^{-4}	2.23×10^{-7}	134	0.005
3	2.46×10^{-4}	2.92×10^{-7}	19	0.005
4	3.22×10^{-4}	3.09×10^{-7}	8	0.005
5	3.90×10^{-4}	3.87×10^{-7}	5	0.005

No. of printed layers	Resistivity (Ω.m)	Relative error in resistivity	Resistivity ± error (Ω.m)	Conductivity (s/m)	Conductivity ± error (s/m)
2	12.01×10^{-7}	0.011	$(12.0 \pm 0.13) \times 10^{-7}$	8.32×10^{5}	$(8.32 \pm 0.09) \times 10^{5}$
3	2.72×10^{-7}	0.023	$(2.72 \pm 0.06) \times 10^{-7}$	36.76×10^{5}	$(36.8 \pm 0.85) \times 10^{5}$
4	1.59×10^{-7}	0.042	$(1.59 \pm 0.07) \times 10^{-7}$	62.89×10^{5}	$(63 \pm 2.6) \times 10^{5}$
5	1.50×10^{-7}	0.051	$(1.50 \pm 0.08) \times 10^{-7}$	66.66×10^{5}	$(66 \pm 3.4) \times 10^{5}$

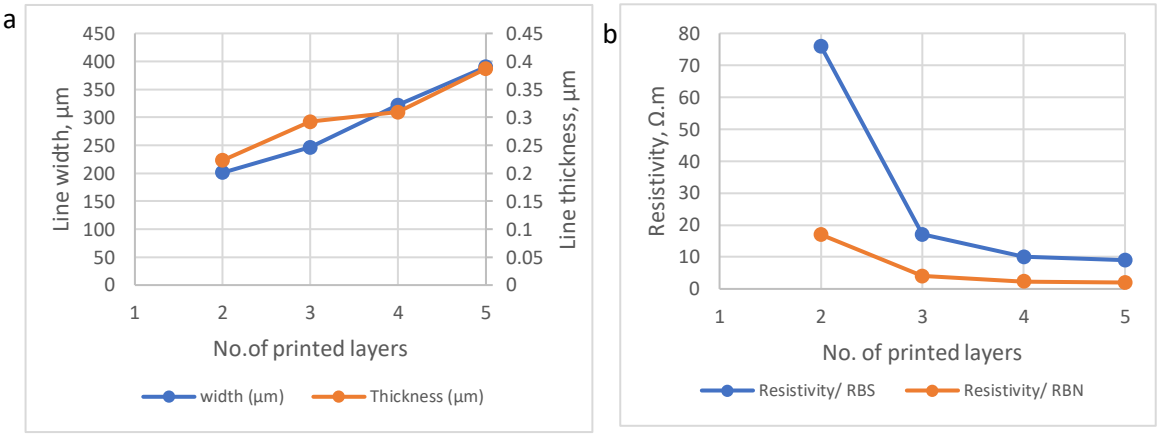

Figure 4.22. Properties of room-temperature overprinted features on photo paper from a 50 µm nozzle at 45 µm print pitch. (a) Effect of number of printed layers on line width/thickness, (b) effect of number of printed layers on resistivity.

As mentioned previously, the thickness and width of the printed lines both increase with overprinting from a thickness of about 2.23×10^{-7} m and width 2.01×10^{4} m with two layers at 45 µm print pitch to a thickness of 3.87×10^{-7} m and width 3.90×10^{-4} m up to five layers.

The resistivity of the overprinted layers showed an incredible conductivity compared with the bulk metal. It was two times that of bulk nickel with 9 times compared with bulk silver up to 5 layers. In a similar way, a steady decrease in resistance is observed as shown in Figures 4.22.

4.5 Characterisation of 10, 20, 30 wt.% Ag-Ni/PAA alloy standard ink

The alloy characteristics of the synthesized Ag-Ni NPs are determined by examining the formulated ink, its printability, and the electric conductivity of the coated film. Based on the available data on Table 4.12, the 10% (50:50 w/w%) composition ink was proven to have highly efficient properties compared with other alloy compositions, as well as displaying a low resistance with good conductivity as pointed out above in section 4.2.

Table 4.12. Summary of characterisation of Ag-Ni/PAA alloy standard ink.

Alloy Ink	Ink Texture	Stability	Resistance	SEM/EDS
10% Ag: Ni (50:50)	Dispersed (printable)	Stable up to 4 months	Great resistance	Continuous line
20% Ag: Ni (50:50)	Non-dispersed (aggregate)	-	-	-
30% Ag: Ni (50:50)	Non-dispersed (aggregate)	-	-	-
10% Ag: Ni (40:60)	Dispersed (printable)	Stable up to 4 months	No resistance	some Cracking (non -continuous line)
10% Ag: Ni (75:25)	Dispersed (printable)	Stable up to 4 months	Resistance just with overprinting	Cracking (non - continuous line)
20% Ag: Ni (75:25)	Non-dispersed (aggregate)	-	-	-
10% Ag: Ni (25:75)	Non-dispersed (aggregate)	-	-	-

Over this compositional range, each ink exhibits different behaviour, which is most pronounced at the highest solids loading, where the ink showed some large particles as they aggregate and become unprintable unlike the 10wt% formulation. Of these compositions, only those inks with 10 wt% silver-nickel nanoparticles are stable for months when stored in properly sealed containers and can flow easily through the nozzle without any blocking issues.

Notably, even though there was some evidence of formulating a printable ink when testing the ink with a smear test, and it showed a good resistance (8-60 Ω) on photo paper, the 10 wt% ink (Ag: Ni) (40:60) and (75:25) exhibited some breaking lines and fracture areas around the contact point when the resistance probe was applied while handling the paper substrate and that caused the absence of the conductivity.

In the absence of conductivity, no more characterizations could be done for the alloy printing tracks. Although significant conductivity was clearly obtained from the 10% (50:50 w/w%) alloy ink around x65 of bulk silver (1.59×10^{-8} Ω m) and only x15 bulk nickel (10.3×10^{-7} Ω m), it should be noted from the elemental composition work that this material actually contained a very small fraction of Ni. Despite this, properties were quite severely affected compared with inks containing no Ni (see chapter 3), leading to poorer conductivity and more difficult ink formulation.

As seen from Figure 4.23, there are lots of cracks and fracturing all over the tracks as a result of handling the substrate and that caused the real problem of losing the conductivity as there was a non-continuous film for measuring the resistance.

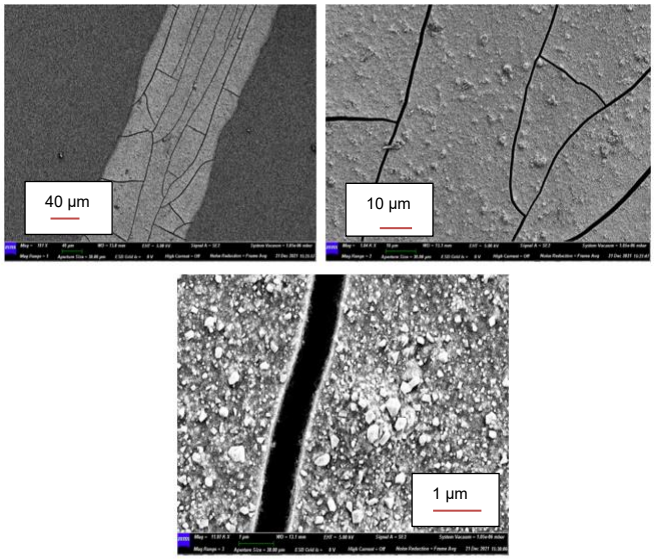

Figure 4.23. SEM images of the surface of the 10% Ag-Ni/PAA (75:25), and (40:60) w/w % printed film on photo paper substrate.

By the comparison between the conductivity of Ag-based ink and Ag-Ni, our results confirm that the existence of Ni alongside Ag could change the ink behaviour and thus cause the absence of conductivity by printing over a flexible substrate. Consequently, the uses of Ni in inkjet printing have some limitations.

Herein, efforts were made to successfully print the alloy-based ink over a flexible substrate but getting conductivity was the real challenge in this study. To address the above issues, our suggestion is either to try a different sintering method or to print on a rigid substrate (glass) to avoid bending so tracks can be handled easily to achieve optimal performance.

By looking at the Table 4.13, surprisingly we got resistance by treating other alloy compositions differently. No noticeable change happened in Ag: Ni (75:25) and (25:75). However, (40:60) displays a good range of resistance by using chemical sintering. In order to expose the film to chemical sintering, firstly, the film was immersed in a solution of 1-amino-2-propanol (MIPA) for 1 min and rinsed with methanol. Afterwards, it was immersed again for 5 min into $NaBH_4$ in pH=12 NaOH solution and finally washed with de-ionized water (more details see Chapter 2). That allowed particles to coalesce together by destabilizing the ligand to achieve effective sintering at room temperature.

Table 4.13. Ag- Ni/PAA alloy ink behaviour applied on different substrate by a smear test and inkjet printing.

10 wt.% Alloy ink (Ag: Ni)	**Smear test on photo paper**	**Smear test on PVOH coated PET film**	**Printed on Photo paper**	**Printed on Photo paper + Chemical Sintering**	**Printed on Photo paper + Cl^- Spray**	**Printed on PVOH coated glass**
40:60	3-18 Ω	No resistance	No resistance	Resistance (240-380 Ω)	Resistance (4-20 Ω)	No resistance
75: 25	1-20 Ω	No resistance	Resistance with overprinting	No resistance	No resistance	No resistance
25: 75	75-250 Ω	No resistance	No resistance	No resistance	No resistance	No resistance

Similarly, a solution with 10% chloride ion was prepared and sprayed toward the printed film and let dry at room temperature. Both sintering methods work well and achieve the desired conductivity.

4.6 Characterisation of 10% Ag-Ni/PAA (40:60 w/w%) alloy standard ink

Table 4.14. Effect of pitch on width, thickness and resistivity of printed lines with Cl^- spray sintering. 10% AgNi /PAA (40:60) w/w% alloy ink was printed with a 50µm nozzle diameter on glossy photo paper at room temperature.

Pitch size (mm)	Width (m)	Thickness(m)	Resistance (Ω)	Length (m)
0.095	0.913×10^{-4}	2.56×10^{-7}	-	0.005
0.085	0.942×10^{-4}	3.94×10^{-7}	48.75 kΩ = (48750 Ω)	0.005
0.075	0.982×10^{-4}	4.35×10^{-7}	23.3 kΩ = (23300 Ω)	0.005
0.065	1.04×10^{-4}	4.61×10^{-7}	282 Ω	0.005
0.055	1.15×10^{-4}	4.62×10^{-7}	7.3 kΩ = (7300 Ω)	0.005
0.045	1.26×10^{-4}	5.10×10^{-7}	274 Ω	0.005
0.035	1.43×10^{-4}	5.42×10^{-7}	242 Ω	0.005
0.025	1.70×10^{-4}	6.03×10^{-7}	228 Ω	0.005
0.015	2.27×10^{-4}	7.20×10^{-7}	56 Ω	0.005

Pitch size (mm)	Resistivity (Ω.m)	Relative error in resistivity	Resistivity ± error	Conductivity (s/m)	Conductivity ± error
0.095	-	-	-	-	-
0.085	3618.6×10^{-7}	0.042	$(3600 \pm 150) \times 10^{-7}$	0.027×10^{5}	$(0.027 \pm 0.001) \times 10^{5}$
0.075	1990.6×10^{-7}	0.145	$(2000 \pm 290) \times 10^{-7}$	0.0502×10^{5}	$(0.050 \pm 0.007) \times 10^{5}$
0.065	27.04×10^{-7}	0.329	$(27 \pm 8.9) \times 10^{-7}$	3.69×10^{5}	$(4 \pm 1.2) \times 10^{5}$
0.055	775.6×10^{-7}	0.345	$(776 \pm 268) \times 10^{-7}$	0.128×10^{5}	$(0.13 \pm 0.04) \times 10^{5}$
0.045	35.2×10^{-7}	0.158	$(35 \pm 5.6) \times 10^{-7}$	2.84×10^{5}	$(2.8 \pm 0.45) \times 10^{5}$
0.035	37.5×10^{-7}	0.178	$(38 \pm 6.7) \times 10^{-7}$	2.66×10^{5}	$(2.7 \pm 0.47) \times 10^{5}$
0.025	46.7×10^{-7}	0.177	$(47 \pm 8.3) \times 10^{-7}$	2.14×10^{5}	$(2.1 \pm 0.38) \times 10^{5}$
0.015	18.3×10^{-7}	0.168	$(18 \pm 3.1) \times 10^{-7}$	5.46×10^{5}	$(5.5 \pm 0.92) \times 10^{5}$

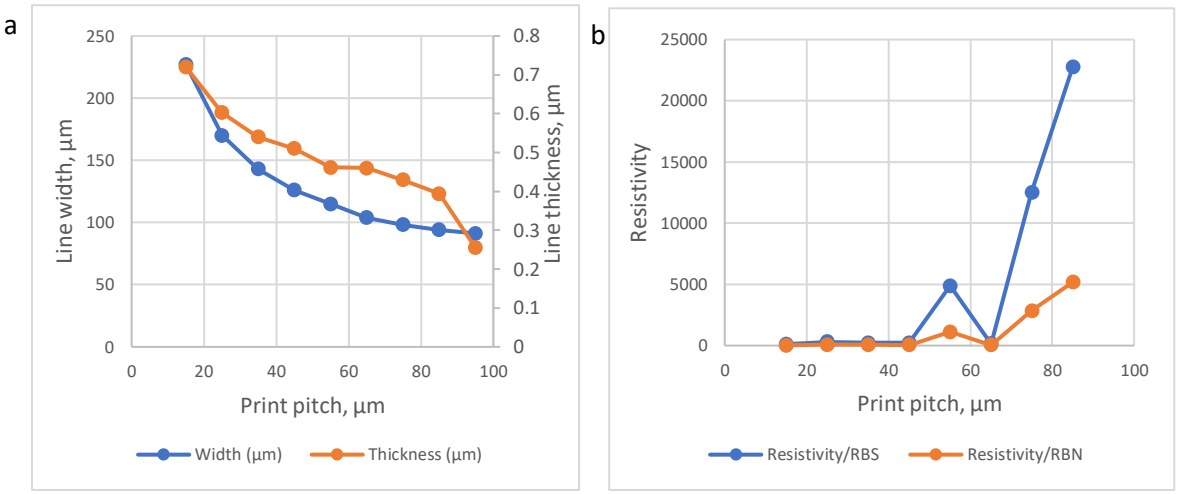

Figure 4.24. Characteristics of printed lines on glossy photo paper with a 50 µm nozzle diameter at room temperature (a) effect of print pitch on the line width/ thickness, (b) effect of print pitch on resistivity.

Table 4.15. Summary of properties of room-temperature 10% AgNi /PAA (40:60) w/w% alloy ink overprinted features on photo paper from a 50 µm nozzle at 45 µm print pitch.

No. of printed layers	Width (m)	Thickness (m)	Resistance (Ω)	Length (m)
1	1.26×10^{-4}	5.10×10^{-7}	274	0.005
2	1.67×10^{-4}	7.37×10^{-7}	175	0.005
3	2.02×10^{-4}	9.80×10^{-7}	80	0.005
4	2.53×10^{-4}	9.11×10^{-7}	52	0.005
5	2.97×10^{-4}	10.04×10^{-7}	34	0.005

No. of printed layers	Resistivity (Ω.m)	Relative error in resistivity	Resistivity ± error	Conductivity (s/m)	Conductivity ± error
1	35.2×10^{-7}	0.158	$(35 \pm 5.6) \times 10^{-7}$	2.84×10^{5}	$(2.8 \pm 0.45) \times 10^{5}$
2	43.07×10^{-7}	0.011	$(43.1 \pm 0.47) \times 10^{-7}$	2.32×10^{5}	$(2.32 \pm 0.03) \times 10^{5}$
3	31.6×10^{-7}	0.023	$(31.6 \pm 0.73) \times 10^{-7}$	3.16×10^{5}	$(3.16 \pm 0.07) \times 10^{5}$
4	23.9×10^{-7}	0.042	$(24 \pm 1.0) \times 10^{-7}$	4.18×10^{5}	$(4.2 \pm 0.18) \times 10^{5}$
5	20.2×10^{-7}	0.051	$(20 \pm 1.0) \times 10^{-7}$	4.95×10^{5}	$(5 \pm 0.25) \times 10^{5}$

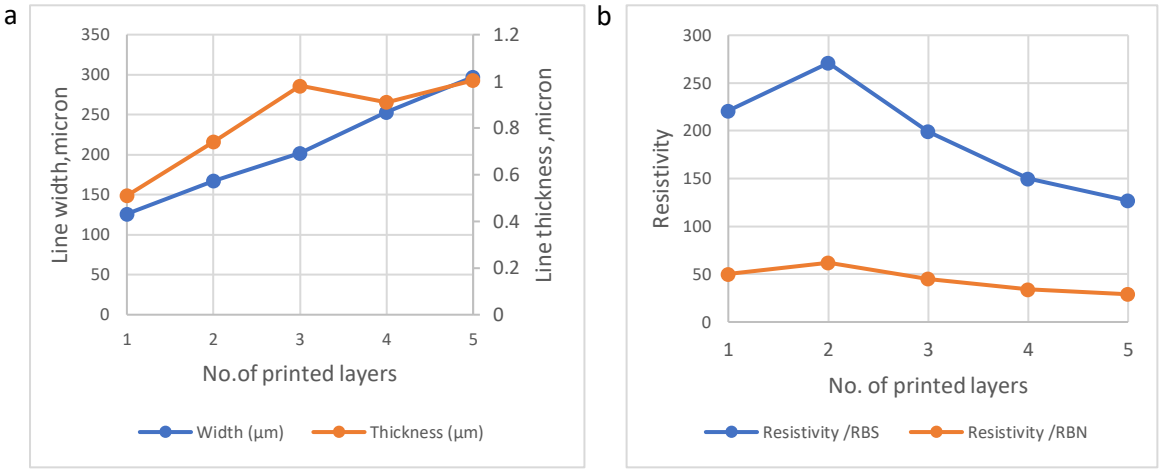

Figure 4.25. Properties of room-temperature overprinted features on photo paper from a 50 µm nozzle at 45 µm print pitch. (a) Effect of number of printed layers on line width/thickness, (b) effect of number of printed layers on resistivity.

Generally, printing with Ag:Ni (40:60) w/w% alloy ink showed a good resistance when increasing the print pitch to 15 µm and with overprinting layers to make the film. That clearly confirmed how chloride ion sprayed on the printed film has effectively destabilized the ligand and allowed particles to be more connected with a continuous line.

4.7 Conclusion

In summary, considerable work was invested in producing and characterising silver /nickel alloy NP and inks formulated from them. A variety of metal ratios were investigated, which can take full advantage of these two materials to enhance the conductivity with improved electronic properties and reduce the cost significantly.

We have successfully prepared highly concentrated and stable suspensions of silver-nickel alloy nanoparticles capped with polymer and containing various ratios of metals by the co-reduction method, although the levels of Ni incorporated were much lower than the stoichiometric ratios in the reactions. Our result confirmed the average size of the alloy nanoparticles in the range of nanoscale and some micro-scale particles regarding particle agglomeration.

On the basis of these finding some of the obtained Ag-Ni alloy NPs can be utilized in conductive ink fabrication, and undergo printing film progress, with particular emphasis on their physical and electrical properties.

As already discussed, a remarkable improvement of resistivity was obtained from 10% (Ag 50: Ni 50) alloy ink printed films about 65 times RBS and 15 times bulk nickel on Photo substrate after sintering at room temperature. It was obvious the alloy conductivity was affected by the nickel resistivity as compared with the Ag films produced using the same formulation and treatment process. Meanwhile, the 10% (Ag75: Ni25) film with overprinted layers showed incredible conductivity compared with the bulk metal. It was 2 times bulk nickel with 9 times compared with bulk silver.

After spending more time discovering the properties of the alloy ink, finally, the 10% (Ag40:Ni60) film displays an optimal resistance by using chemical sintering while increasing the print pitch to 15μm and with overprinting layers. That clearly confirmed how chloride ion has effectively destabilized the ligand and allowed particles to be more connected with a continuous line.

DLS, TGA, TEM and SEM/ EDS were employed to confirm the ink stability, chemical composition, morphologies and thermal decomposition temperature and finally to demonstrate the effect of sintering at room temperature on the microstructure of printing films.

References

(1) Mohammadi, M. M.; Gunturi, S. S.; Shao, S.; Konda, S.; Buchner, R. D.; Swihart, M. T. Flame-Synthesized Nickel-Silver Nanoparticle Inks Provide High Conductivity without Sintering. *Chem. Eng. J.* **2019**, *372 (3)*, 648–655.

(2) Habas, S. E.; Platt, H. A. S.; Van Hest, M. F. A. M.; Ginley, D. S. Low-Cost Inorganic Solar Cells: From Ink to Printed Device. *Chem. Rev.* **2010**, *110 (11)*, 6571–6594.

(3) Kamyshny, A.; Magdassi, S. Conductive Nanomaterials for 2D and 3D Printed Flexible Electronics. *Chem. Soc. Rev.* **2019**, *48 (6)*, 1712–1740.

(4) Pajor-Świerzy, A.; Socha, R.; Pawłowski, R.; Warszyński, P.; Szczepanowicz, K. Application of Metallic Inks Based on Nickel-Silver Core-Shell Nanoparticles for Fabrication of Conductive Films. *Nanotechnology*. **2019**, *30 (22)*, 1-8.

(5) Jang, Y. R.; Jeong, R.; Kim, H. S.; Park, S. S. Fabrication of Solderable Intense Pulsed Light Sintered Hybrid Copper for Flexible Conductive Electrodes. *Sci. Rep.* **2021**, *11 (1)*, 1–15.

(6) Milardović, S.; Ivaniševic, I.; Rogina, A.; Kassal, P. Synthesis and Electrochemical Characterization of AgNP Ink Suitable for Inkjet Printing. *Int. J. Electrochem. Sci.* **2018**, *13 (11)*, 11136–11149.

(7) Kraemer, J. Development of high loading Ag nanoparticle inks for inkjet printing and Ag nanowire dispersions for conducting and transparent coatings . PhD Thesis, *Cranfield University*, **2012**. 1-219.

(8) Alruqi, S. S.; Al-Thabaiti, S. A.; Malik, M. A.; Khan, Z. Role of Surfactants: One Step Facile Synthesis of Hetero Structured Ag-Ni Alloy by Seed Less Approach. *Colloids Surfaces A Physicochem. Eng. Asp.* **2018**, *540 (11)*, 36–47.

(9) Yang, W. Preparation and Characterization of Organic Silver Based Conductive Inks for Flexible Electronics. The degree of Doctor of Philosophy, *Heriot-Watt University*, **2019**. 1-185.

(10) Santhi, K.; Thirumal, E.; Karthick, S. N.; Kim, H. J.; Nidhin, M.; Narayanan, V.; Stephen, A. Synthesis, Structure Stability and Magnetic Properties of Nanocrystalline Ag-Ni Alloy. *J. Nanoparticle Res.* **2012**, *14 (5)*, 868.

(11) Yan, S.; Sun, D.; Tan, Y.; Xing, X.; Yu, H.; Wu, Z. Synthesis and Formation Mechanism of Ag–Ni Alloy Nanoparticles at Room Temperature. *J. Phys. Chem. Solids.* **2016**, *98 (6)*, 107–114.

(12) Kumar, M.; Deka, S. Multiply Twinned AgNi Alloy Nanoparticles as Highly Active Catalyst for Multiple Reduction and Degradation Reactions. *ACS Appl. Mater. Interfaces.* **2014**, *6 (18)*, 16071–16081.

(13) Lee, C. C.; Cheng, Y. Y.; Chang, H. Y.; Chen, D. H. Synthesis and Electromagnetic Wave Absorption Property of Ni-Ag Alloy Nanoparticles. *J. Alloys Compd.* **2009**, *480 (2)*, 674–680.

(14) Cummins, G.; Desmulliez, M. P. Y. Inkjet Printing of Conductive Materials: A Review. *Circuit World.* **2012**, *38 (4)*, 193–213.

Chapter 5. Core- shell results and discussion

5.1 Formation and characterisation of nickel @silver / PAA core-shell nanoparticles

Motivated by studies that have reported Ni as one of the most promising candidates for use as a conductive material as the replacement of Ag, because of its great conductive properties, favourable melting point and lesser cost than noble metals [1,2], a range of nickel/silver alloys were investigated. As seen in the previous chapter, there were promising results from printing the Ag-Ni Alloy. However, nickel incorporation was much lower than expected from the starting recipes and the resulting tracks were not wholly satisfactory (significantly lower conductivity than pure silver), even when only low levels of Ni were present. These materials would need lots of further development to get better results. An alternative approach might be to avoid the complexity of alloy formation and instead use pure Ni NPs, or “hide” the Ni inside a core-shell (CS) NP, which might then behave much more like a pure silver NP in terms of surface ligand behaviour and sintering.

Ni NPs need more effort to prevent their spontaneous oxidization as they readily oxidize with air, which leads to lower or even loss of their electrical conductivity. Several approaches have been suggested to overcome this problem: synthesis of Ni NPs under an inert atmosphere (Ar or N_2) in organic solvents, coating Ni NPs with a dense protective layer, a core–shell NPs structure by formation of an additional shell involving a non-oxidizable conductive material such as (Ag, Au... etc) to obtain oxidation stability of Ni NPs [3].

In previous research [4], the authors have carried out a comparison between different better-quality core-shell systems from an energetic and a kinetic point of view. They confirmed that the Ni-Ag core-shell structures are more favourable than those that contained Ag-Cu and Ag-Pd core-shell structures. In this situation, applying the Ni-Ag core-shell system is worth investigating.

According to our studies presented in Chapter 4, it is also worth mentioning that we obtained better resistivity by using Ag Ni alloy-based ink, compared with the above CS NPs. The lowest resistivity of (Ag 75: Ni 25), (Ag40: Ni 60) w/w%

ink was 2 times and 29 times bulk nickel, respectively after printing 5 layers on photo paper resulting in spontaneous room temperature sintering.

The Ni-Ag core - shell NP is a very attractive system to get around some of the issues encountered with Ni/Ag alloys, however, on account of it minimizing the strain arising from the striking lattice mismatch because of the large difference in size between Ag and Ni atoms [5,6].

In the first part of this chapter, synthesis by different methods and characterization of the as-prepared Ag-Ni core-shell nanoparticles with different compositions were evaluated using a range of techniques. Each technique provides different information that can be used to build up a comprehensive picture of the synthesised material and its ability to form a conductive film with room-temperature sintering. Some preliminary results related to CS NPs with copper will be discussed later in this chapter.

This method was performed by nickel ion reduction with excess of sodium borohydride and finally the $AgNO_3$ solution was added to the Ni suspension as the precursor of the Ag shell by a transmetalation reaction. Polyacrylic acid (PAA) was used as a stabilizer under N_2 atmosphere as well, to assure the Ni NPs stabilization and protect them from oxidation and aggregation.

Core-shell NP were synthesised with a variety of core to shell material ratios. According to the DLS data, the size of Ni-Ag NPs for the concentration of (1:1) metal precursor was slightly bigger than (1:0.1) molar ratio, which indicates that the size of the core-shell NPs can be controlled by choosing the appropriate ions concentration of Ag shell. Table 5.1 shows the summary of the particle size distribution and how it is affected by different metal ratios. The phenomenon was similar to that obtained by other researchers [7] and [8], the core-shell nanoparticle size increased with increasing silver nitrate concentration .

Table 5.1. Summary of the particle size of Ni-Ag-PAA core- shell NPs with different metal molar ratio.

Metal composition	Stabilizing agent	DLS size (d. nm)	TEM range size (nm)
Ni-Ag (1:1)	PAA	72	9-15
Ni-Ag (1: 0.1)	PAA	56	N.D.

TEM image presented in Figure 5.1 showed that, an agglomeration of particles takes place for molar ratio (1:1) with presence of roughly spherical Ni-Ag NPs and their size distribution seems to be homogeneous within the range of 10-16 nm.

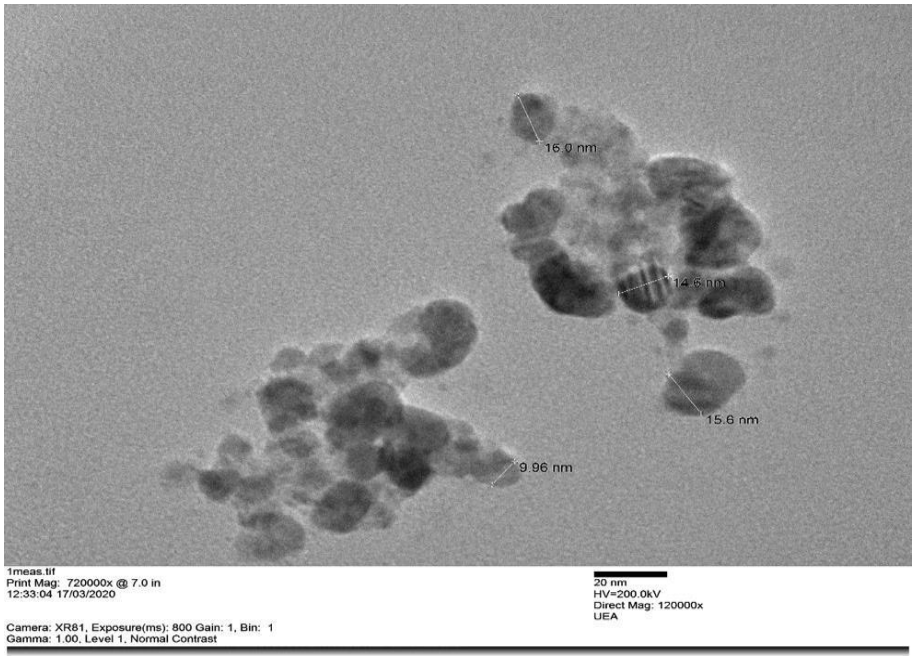

Figure 5.1. TEM image of Ni-Ag (1:1 w%).

It is worth to mention that the prepared Ni- Ag core-shell NPs in both ratios (1:1) and (1:0.1) have shown a high electric resistance about 16-32 MΩ, when we applied the particle suspension in a thin film over a photo epson paper by the 'smear test' for both ratios. This indicates that the materials probably sinter like pure Ag NP do, However, their conductivity will be very poor as they have a very high resistance compared with other Ag NPs we have synthesized. These results stopped us from going forward with these materials and instead we tried different synthetic routes in order to obtain better resistance with a reasonable conductive film compared with bulk metal.

5.2 Synthesis and characterization of nickel-silver /PAA core-shell NPs by Polyol Method

Clearly, using Ni-AgNPs should be more economical than pure silver NPs, based on the costs of the metals. That justifies making more efforts to try different methods with some modification as we have done in this synthesis. Here in this work, lots of redevelopments of Anh T. *et al.* [9] work was made. Ni-Ag core-shell nanoparticles were successfully synthesized by a polyol process.

This polyol method is cheap and accessible in terms of the chemicals and methods involved and hence good for bulk synthesis of Ni-Ag core-shell, and the most common PAA was used as the dispersant for the preparation of metal nanoparticles. To further protect the Ni nanoparticles, Ag shell was deposited onto it in subsequent polyol process by reduction of $AgNO_3$.

The size distribution of Ag and Ni NPs is illustrated in Figure 5.2. As was shown, there was variability in measurements and this is most likely due to the presence of the aggregated material in the sample, coupled with the size distribution making the data a bit unstable and that was shown in the value of the polydispersity index (PDI). The mean particle size distribution provides nanoscale particles of about 20 nm.

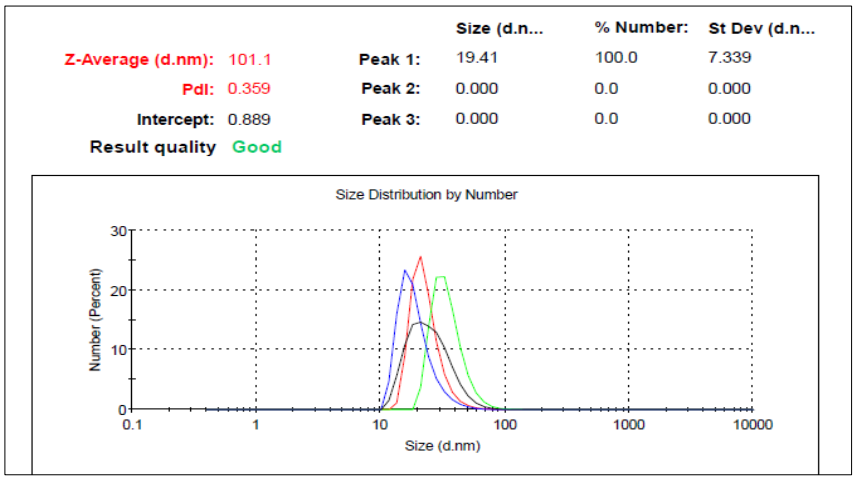

Figure 5.2. The DLS graphs of nickel- silver core-shell nanoparticles.

Thermogravimetric analysis (TGA) was applied at 10 °C/min, to investigate the thermal decomposition behaviour of PAA that adsorbed on the Ag shell (Figure 5.3). There are three significant stages shown as temperature increased. The first stage, between 98.75-100 °C, is due to moisture loss – loss of physically

adsorbed water. This is followed by chemical dehydration at about 100-140 °C - loss of water by two OH groups on adjacent COOH groups from parts of the chain coming together with the elimination of water and formation of an anhydride ring (1% weight loss). The higher temperature between 280 °C and 390 °C was mainly attributed to the loss of PAA absorbed on the Ag shells by breakdown and loss of the organic material as small volatiles.

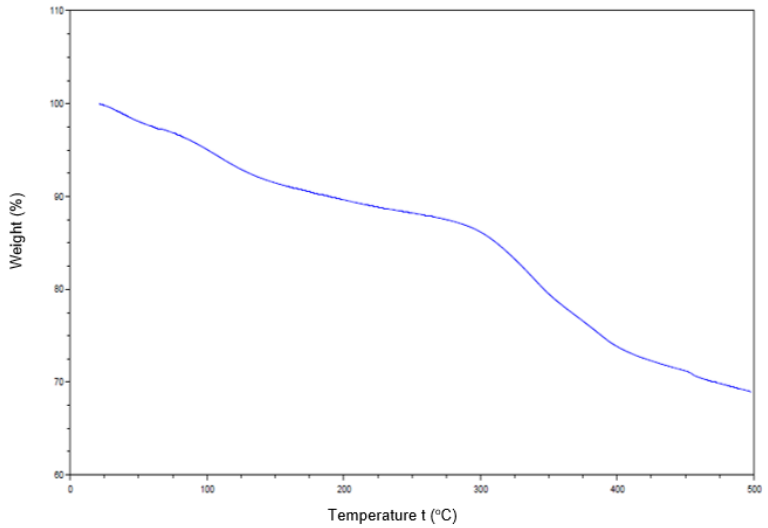

Figure 5.3. TGA of the Ni@ Ag core-shell nanoparticles.

At controlled reaction conditions, the formation of a core-shell structure is observed clearly, and the particle size was further verified using SEM. Figure 5.4 shows the SEM image of the Ni-Ag nanoparticles, which shows the nearly uniform size and shape of the nanoparticles prepared. The average diameter of particles size was between 3–12 nm and that nearly correspond with DLS results. The measurement of zeta potential of the Ni- Ag core-shell NPs confirmed that the particles were negatively charged. A relatively high value of the zeta potential, −19±5 mV, was obtained, which indicated the electrostatic stability of Ni-Ag NPs against aggregation and precipitation.

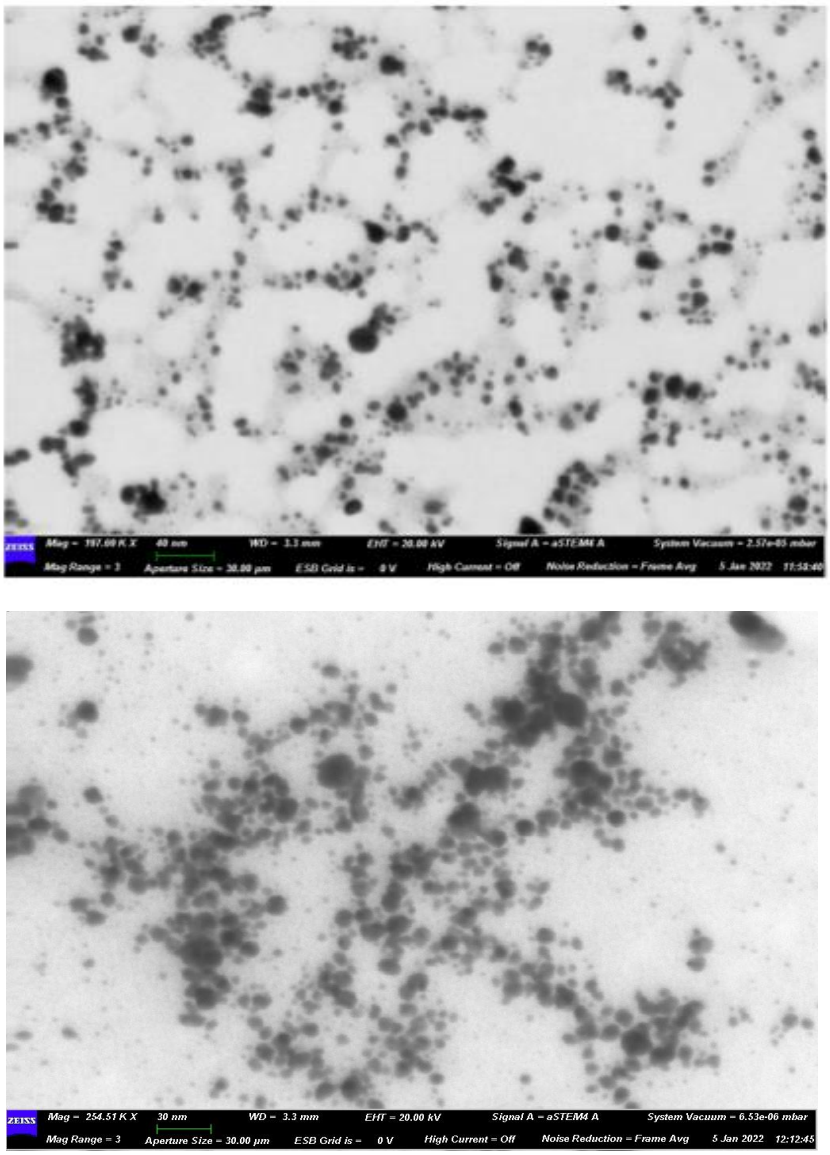

Figure 5.4. SEM images of the Ni@ Ag core-shell.

Further, to confirm the presence of the Ag shell on the Ni nanoparticles (Figure 5.5). Particles were chosen randomly and analysed by EDS. All the particles showed the presence of both Ag and Ni elements. The silver to nickel ratio was similar from multiple regions of analyses and is about 5: 1.

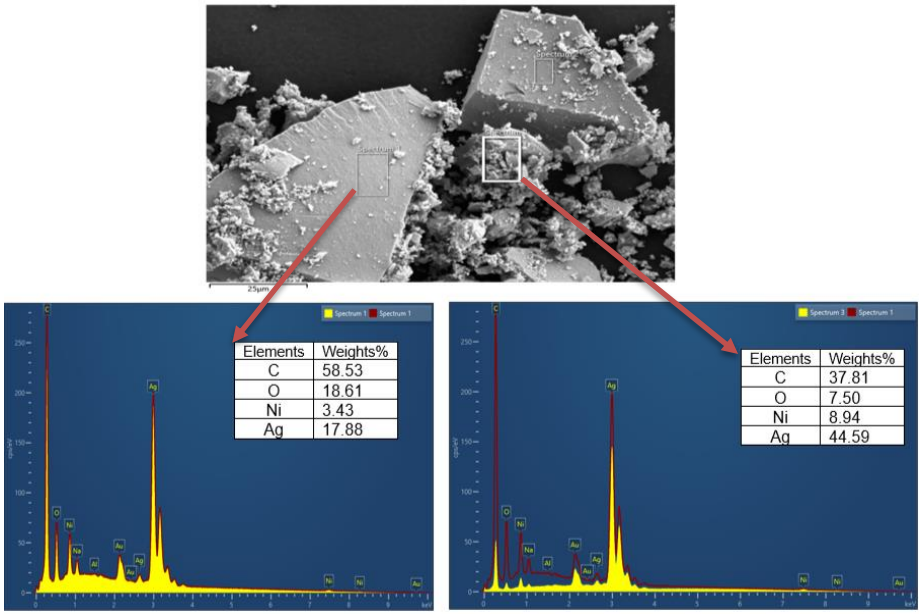

Figure 5.5. EDS results of as-synthesised Ni @ Ag core-shell composite.

Here, in addition to the EDS results, ICP-MS was done in order to confirm the presence of the Ag and Ni in the core-shell structure. From Table 5.2, silver nitrate and nickel acetate salts (the synthetic precursors) were also analysed for reference. This result indicates that the nickel percentage was below the expectation in different samples and also lower than EDS estimate .

Table 5.2. ICP-MS elemental analysis results.

Chemicals	Ni 231.604 (Aqueous-Radial-IFR) %	Ag 338.289 (Aqueous-Axial-IFR) %	Ratio Ag/ion %
$AgNO_3$	0	99.98	
Ni acetate	25.39	0.009	
Ni@ Ag/PAA core-shell	4.56	55.85	12.11

The ICP-MS analysis results showed the atomic ratios of Ni to Ag. This is likely to be more accurate representation than the EDS value. EDS often shows significant variability depending on the exact area analysed and local heterogeneities in the sample, whereas for ICP-MS the whole sample is dissolved, hence it averages such variations .

The purpose of this report is to attain scalable and more economical NPs. This could be achieved either by replacing or mixing the pure Ag with Ni or Cu.

However, the characterization of Ni-Ag core-shell NPs by SEM/EDS and ICP-MS has confirmed that there is a very little percentage of Ni in the final products, so it doesn't reach our intended outcome to save the material cost, especially when considered alongside the increased synthetic complexity.

5.2.1 Ink formulation and inkjet printing of Ni@ Ag core-shell

In order to investigate the applicability of the Ni@ Ag core-shell NPs to printed conductive films on a flexible substrate, the NPs were suspended in a solvent mixture of 33.3% EG: 36.7% deionized water by stirring for 2-4 min. Afterwards, the resultant solution was sonicated for 30 min using sonics & material probe to obtain homogenous ink. Finally, (30%)1-propanol was added to the above solution with continuous stirring for around 3 min. The ink was then ready to undergo inkjet printing.

In principle, Ag and Ni NPs are able to form printable nano ink with an economical cost compared to pure silver ink compositions. Based on that, 10wt.% Ni@ Ag core-shell ink was formulated. Subsequently, printing the Ni@Ag based ink showed its ability for printing with a good appearance. However, the printed film shows lots of cracks and fractures as a result of handling the substrate and that caused the real problem of losing the conductivity as there was a non-continuous line for measuring the resistance. Similar results were acquired with alloy printed films. This behaviour could be attributed to the ink wettability and lots of optimisation may need to be done by replacing the water with less volatile solvents with lower surface tension and testing them again to assess improvements.

Similar problems were found visually in other studies [10], while evaluating suitable solvents and co-solvents for the formulation of conductive metallic inks. For all water-based formulations, the coatings were not uniform, contained numerous cracks and voids and were characterized by very low electrical conductivity. This may result from significant surface tension and viscosity variations during evaporation of the ink.

Pajor-Swiery A. *et al*. [2] have been trying to develop Ni-Ag core-shell-based ink for several years. In 2019, they synthesized Ni-Ag core-shell NPs in two steps, the formation of a dispersion of Ni NPs and then the Ag shell formation by galvanic displacement reaction, using $NaBH_4$ as the reducing agent. The size

distribution (a diameter between 50-210 nm for the Ni core and 10-20 nm Ag shell) was undesirably large for inkjet printing, as it could cause nozzle clogging. They obtained long-term stability against aggregation and oxidation. In 2020, with different scientists, Pajor-Swiery studied the conductive ink formulation and properties of a mixture of Ni-Ag NPs at the size of 70 and 250 nm [3]. The conductivity was about 20% of bulk nickel and it was obtained after thermal sintering at 300 °C. In this context in 2021, they started to develop nanocomposite inks based on nickel–silver core-shell and silver nanoparticles for fabrication of a conductive film using low-temperature sintering. It was found that this nanocomposite ink displayed better conductivity as compared with the original Ni-Ag NPs-based ink. The conductive film based on the nanocomposite coatings doped with 1% of Ag NPs after sintering at 150 °C and 0.5% of Ag NPs sintered at 200 °C showed a high conductivity which corresponds to 35% of bulk nickel [5]. The ongoing process wasn't the best for our work, however, as we are looking for room-temperature sintering with a smaller size distribution that suits the inkjet printing process.

5.3 Formation and characterization of silver @ nickel core-shell nanoparticle by solvothermal hot injection method

Silver/ Nickel NPs were synthesised according to Vykoukal V. *et al.* [11]. In brief, Ag-Ni core-shell NPs were made by simultaneous thermolysis- reduction of the precursors ($AgNO_3$ and $Ni(acac)_2$ in a dry hot mixture composed of oleylamine and octadecene at 230 °C under N_2. Using oleylamine has advantages in reducing the temperature required for silver dissociation to that of Ni and thus assure the appropriate reaction conditions. It is evident that the nature of oleylamine has a high impact on the NPs formation as it acts as a solvent, an electron donor, and capping agent at the same time [11,12]. An inverted Ag @Ni core-shell nanoparticle structure has also been synthesized by a one-pot solvothermal synthesis in oleylamine with similar metal precursors. The size distribution for the as-prepared Ag-Ni core-shell shows a very narrow size distribution between 1.2-14.9 nm [13].

Ag-Ni NPs were dispersed either in hexane or in toluene to prepare the diluted solution for the hydrodynamic diameter measurements by the DLS

technique (Table 5.3). Different solvent was used to get the better dispersity we got. DLS gives the determination of the solvodynamic diameter of particles with size about 11 nm up to above 200 nm. The largest size was attributed to the polydispersity of the particles as shown in the Table 5.3 below.

Table 5.3. The DLS data and size distribution of Ag-Ni NPs prepared with hot injection method.

Ratio % (Ag: Ni)	Size (d. nm) in Hexane	Size (d. nm) in Toluene
25 :75	10.75	270.6
50 :50	12.43	219.5
75 :25	27.91	25.35

TEM was used to confirm the morphology and hetero structured core-shell Ag @Ni nano composition. For TEM analysis, samples were prepared similar to the previous mentioned method except the sample was dispersed in hexane. The nanoparticles were slightly polydisperse (Figure 5.6 (a)) and show a narrow size distribution ranging from 2 to 5 nm for (50- 50%). In low Ni contents (75:25) the shell does not completely cover the core with a nearly spherical shape as shown in Figure 5.6 (b). The size is not completely consistent with the DLS measurements and contradictory with a noticeable difference in values between them and this might be due to aggregation process in reaction where particles are conjoined together and need more sonication time to get well dispersed solution before measurements were done.

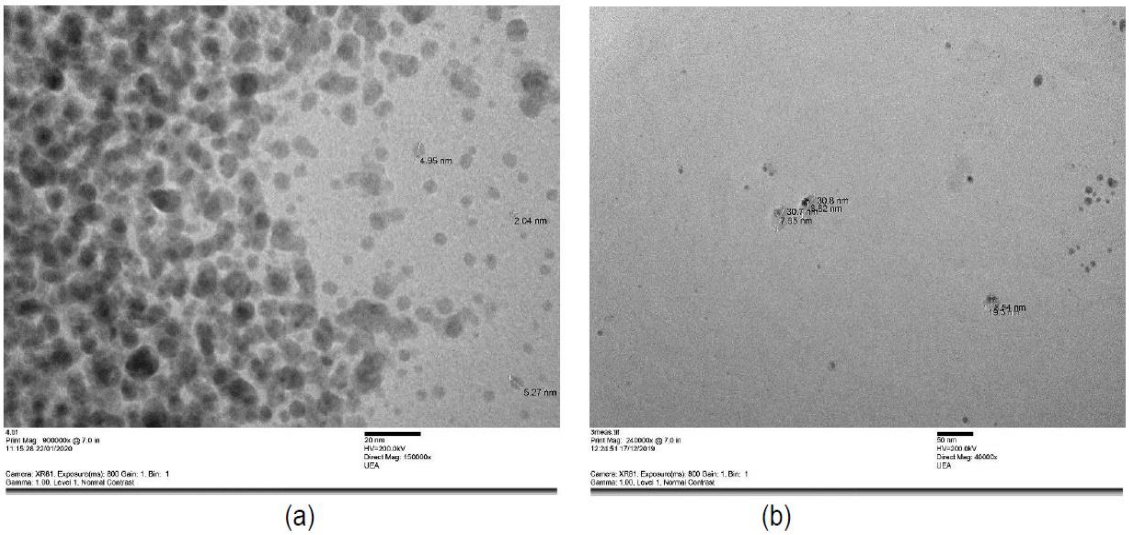

(a) (b)

Figure 5.6. TEM images of Ag-Ni core-shell NPs (a) (50:50), (b) (75:25).

Although the TEM images of Ag-Ni core-shell show a fairly good size range, we struggled to get a desired resistance when we did a simple ‘smear test‘ from their suspension to make a film on photo paper to measure the electrical resistance by multimeter. Therefore, we stopped at this point. Our goal is to get a conductive material that we are able to formulate to a conductive ink, so these materials did not appear to be very promising.

The prepared Ag-Ni core-shell NPs had taken much more effort compared to other methods, with synthesis under N_2 to avoid oxidation and decomposition of Ni. That make it unfavourable with scale-up production in mind.

5.4 Synthesis and characterization of copper@ silver core-shell NPs by thermal decomposition and galvanic displacement

There are several studies using silver conductive inks for inkjet printing for its excellent properties and conductivity. However, from a commercial perspective, silver has a serious drawback in its use as conductive ink. The high price of silver provides the driver to look for another candidate. Therefore, replacing Ag with alternative metals such as copper and nickel has been our goal. Various approaches with nickel have been detailed above.

Copper is also a good candidate for metal replacement for Ag nanoparticles due to its low price, high conductivity and high electromigration resistance [14]. Unfortunately, copper nanoparticles are easily oxidized upon contact with air, particularly for nanosize particles, and also could be oxidised in every step of application (storage, printing and sintering) [14,15,16]. Therefore, it was suggested that forming bimetallic nanoparticles is necessary in this case, for example, core-shell NP or alloy system with another material that possesses higher oxidation resistance such as Ag, Ni and Au could protect the surface.

In order to enhance the oxidation stability of metallic NPs, silver is the most suitable material to protect Cu NPs from oxidation [14,17] at a reasonable price and lower resistivity compared with others. In this regard, it was found that over 22 mol.% coverage of Ag enables Cu@ Ag nanoparticles to attain oxidation resistance in air [14]. Eventually, the presence of Cu is helpful in decreasing the electrical migration encountered by pure silver conducting lines [14,18].

The alloy system cannot typically protect the nanoparticles from oxidation because the Cu atoms at the surface may be exposed to oxidation. Therefore, a core – shell structure is more promising for protecting Cu atoms from oxidation [3].

Among various methods that have been used recently, such as seeded growth and co-reduction methods, galvanic displacement is considered the most effective method to form a core-shell structure. The galvanic displacement method is an electrochemical procedure that includes the oxidation of one metal by ions that have a higher reduction potential [17]. This method is mostly used for the synthesis of bimetallic nanoparticles with different structures, such as alloys and core-shell nanoparticles and showed good oxidation stability [17,19].

Our goal is to develop a simple method to get a fine particle size on a larger scale to formulate conductive inks at a reasonable price. In this study, the Ag shell should enhance the oxidation stability of the copper core. Therefore, we synthesized Cu@ Ag core-shell nanoparticles by a simple two-step process consisting of the thermal decomposition of copper formate by OAM and producing Cu nanoparticles. The colour of the solution changed from green to reddish brown due to the Cu reduction. In the second step, the Ag shell is formed by the galvanic displacement reaction as the $AgNO_3$ chemically decomposes while the electron of Cu^o transfers to Ag (I) ions because of the difference in standard redox potential between Ag (E^o=0.779V) and Cu (E^o=0.46V) [17].

$$Ag^+ + e^- \rightarrow Ag^\circ$$

$$Cu^{2+} + 2e^- \rightarrow Cu$$

Size distribution of particles dispersed in hexane was investigated by dynamic light scattering (DLS). It appears that Cu@ Ag core-shell NPs with an ultra-fine average particle size of 14 nm were achieved with a very consistent measurement (Figure 5.7(b)). The z-average was high as there are a few large particle aggregates, but the size distribution was in a very good range. The Cu core size was measured before adding the Ag shell and it was about 12.57 nm. This is consistent with the formation of the Ag shell that surrounds the Cu core as particles became bigger in size, although the relatively small change leaves some uncertainty, due to small variations in replicate DLS measurements. Ideally, this would have been confirmed by HRTEM measurements to visualise the core-shell structures, but unfortunately, we did not have access to these facilities and

attempts to arrange it via external contacts was unsuccessful for various reasons. Small size NPs could be expected to be good for successful ink formulation and inkjet printing due to the size effect [18], so the physical characteristics of this product seem promising.

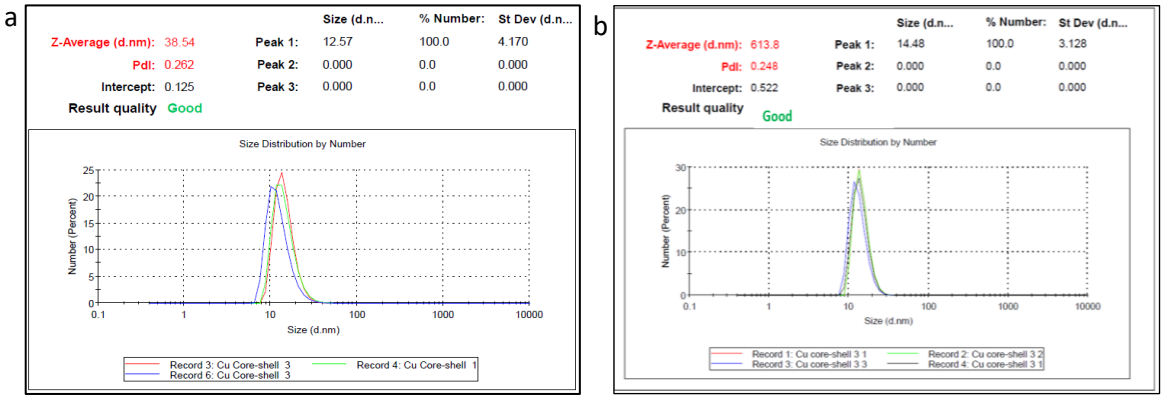

Figure 5.7. The DLS graphs of (a) copper (core) nanoparticle, (b) Cu@ Ag core-shell nanoparticles.

Pajor-Swierzy A. *et al.* [10] obtained the Cu- Ag core-shell NPs in three processes: synthesis of Cu particles, removal of an excess of reducing agent and formation of Ag shell by transmetalation by using sodium formaldehyde sulfoxylate dehydrate (SFS) as the reducing agent. The formulated Cu@ Ag ink was deposited on a glass substrate by using a bar coating with 3 m application rod. Then, the sintering of the deposited layers was performed on a hot plate under N_2 at various temperatures in the range of 200–300 °C for 15 min followed by cooling down at room temperature for 3 min. The obtained particles are significantly large in the range of (600- 1600 nm for the Cu core) and that is attributed to the use of a weak reducing agent like SFS. The fact the SFS makes the reduction and nuclei formation very slow caused the formation of microparticles rather than NPs. This finding can explain why we chose a strong reducing agent like OAM alongside the thermal decomposition and galvanic displacement, which have several advantages of short decomposition time, lower decomposition temperature, simple process and less solvent [14]. Huang Y. *et al.* [20] have prepared a good anti-oxidation Cu-Ag core-shell NPs with a size of 8 nm by a compound method of replacement reaction and chemical reduction reaction. Although, they reached the desired size and structure, this method is time time-consuming and not ideal for large-scale production.

The surface and cross-sectional morphology was investigated using field emission scanning electron microscopy (SEM) with EDS. Figure 5.8 shows SEM images of particles, which are obviously spherical and reasonably monodispersed. The average diameter of particles size was between 5.51-14.68 nm which closely corresponds with the DLS results. The surface of the particle is surrounded by an amorphous layer with a thickness of ~1.84 nm, which is reasonable for the dimensions of an oleylamine surface ligand layer that chemisorbed on the surface. This measured dimension represents two ligand layers, so the thickness of the layer is only half this.

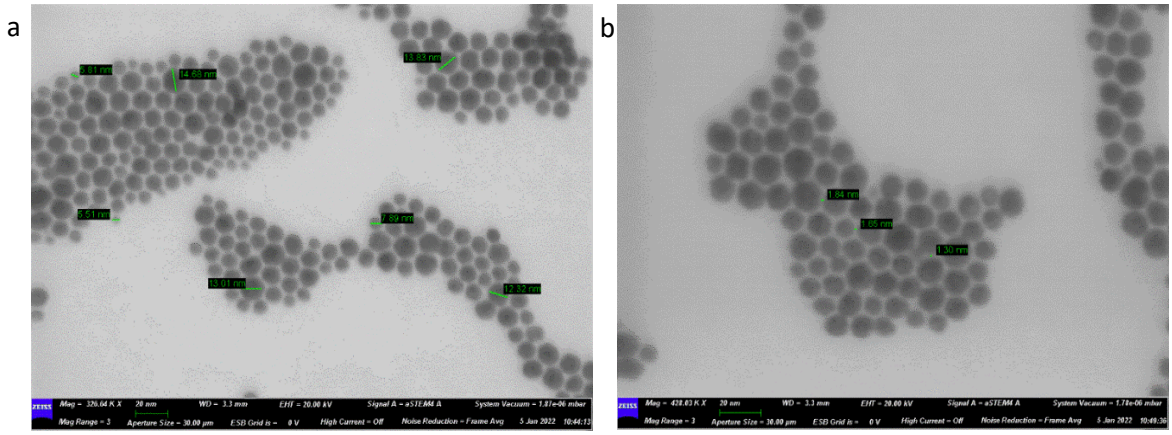

Figure 5.8. (a) SEM images of the Cu@ Ag core-shell nanoparticles (Mag = 428.0 kx), (b) thickness of ligands between particles (Mag = 326.6 kx).

In this regard, it is clear that Cu@ Ag NPs capped with OAM act as an insulator that limits contact and reduces the number of percolation paths between particles. Therefore, the resistivity is high, and the stabilizer cap must be removed. In this case, we are looking for a hydrophobic to hydrophilic transition for improvement if highly conductive tracks are to be generated via printing. More details about this issue in the sintering process have been discussed in Chapter 2.

To give the evidence of oleylamine adsorbed on the Ag shell, we analyzed the particle sample with TGA to investigate the thermal decomposition behaviour of oleylamine (Figure 5.9). There are two significant stages shown as temperature increases. The first stage is between 90-110 °C due to the evaporation of water /solvent that is residual on the core-shell surface. The higher temperature between 120 and 390 ˚C was mainly attributed to the loss of OAM absorbed on the Ag shells and the total mass loss is about 9.8%.

From the TGA the weight ratio of the Cu-Ag is about 90% by weight, the remainder (10%) being the olylamine surface ligand. These data were then used to calculate the density of OAM molecules on the nanoparticles surface, using the method described by Chang Y. *et al.* [21], which was approximately 4.2 nm^{-2}. This represents a quite dense coverage of surface ligands, suggesting that the particle surfaces are very well protected. This influenced the sintering process (see below).

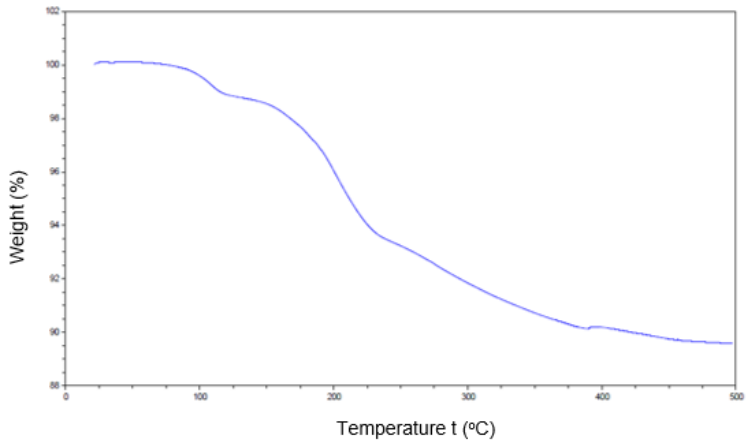

Figure 5.9. TGA of the Cu@ Ag core-shell nanoparticles.

In addition to particle size and distribution, the particle composition of the synthesised nanoparticles was also investigated. The Ag, Cu, C and Cl^- elements were detected by EDS during SEM imaging and compared with the original chemical composition of the compound Cu@ Ag core-shell NPs (Figure 5.10). The measured composition was Cu: Ag = 30: 50 (at. %), compared to the initial precursor concentration Cu:Ag=50: 50 (at. %),. Clearly, the measured composition of Cu was slightly decreased. This decrease in the Cu composition (roughly half of it disappeared) is due to the galvanic displacement method [17]. These results are further evidence that the Cu dissolves as the Ag is deposited. Also, there was a strong peak signal of C which must arise from the oleylamine ligand.

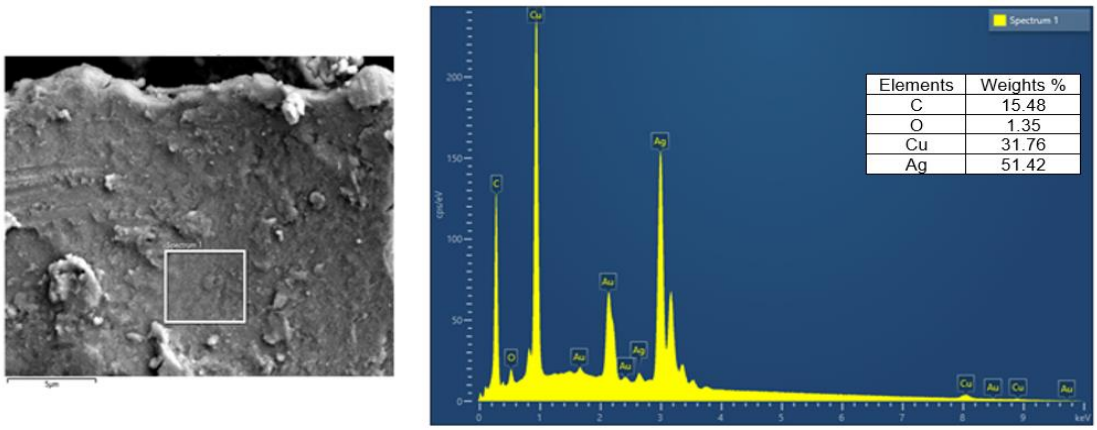

Figure 5.10. EDS results of Cu@ Ag core-shell composite.

The quantity of Ag, Cu and other elements was confirmed by inductively coupled plasma mass spectroscopy (ICP-MS) to check the ratios reflected in the final products indicated from the EDS (Table 5.4). Silver nitrate and copper formate salts were also analysed for the sake of comparison as a reference.

Based on the results from EDS and ICP-MS the metal percentage is about 90% and there is 10% which is estimated to be the organic ligand. This corresponds with the mass loss from TGA. The Cu: Ag ratio was very similar to that obtained from the EDS analysis, further confirming the composition.

Table 5.4. ICP-MS elemental analysis results.

Chemicals	Cu 327.396 (Aqueous-Axial-iFR) %	Ag 338.289 (Aqueous-Axial-iFR) %	Ratio Ag/ion
$AgNO_3$	0	99.98	
Cu formate	28.71	0.002	
Cu@Ag core-shell	35.43	54.85	1.55

5.4.1 Sintering, ink formulation and inkjet printing

In order to study the electrical resistivity of the conductive pattern, the printed Cu-Ag film was sintered at room temperature using a dip chemical sintering process to remove the capping agent and make connection between the nanoparticles. Unfortunately, removing the capping agent on the surface of the Cu- Ag core-shell to obtain conductive film was the main obstacle to using the copper-silver conductive ink, since the spontaneous method using chloride did

not occur. Presumably, the binding of the amine ligands on the surface is too strong, or they are unable to detach and migrate for some other reason. Some researchers have used a high temperature for the sintering process alongside an inert atmosphere, which must be provided to inhibit oxidation of the Cu core [22,23,24].

Increasing the temperature leads to the destruction of the protective shell and causes the instability of core-shell NPs. Since the thickness of the shell is mostly several nanometres and their physicochemical properties are similar to those of NPs, the mobility of the shell atoms increases. Consequently, agglomerates of Ag atoms in the shell are formed and grow on the core surface which gives the oxygen access to the core and oxidizes easily. This destabilization mechanism was discussed in detail in several studies [16,25,26, 27].

Tan S. *et al.* [16] synthesized Cu-Ag core-shell NPs by combining the $NaBH_4$ reduction method with the transmetallation reaction. The conductive ink was deposited on photo paper using a roller pen. For the sintering process, they exposed the film to a different range of temperatures in the air. After sintered for 1 h, it was found that copper oxide was not detected when the conductive patterns were sintered at 90 °C and 110 °C because of the protection of the silver shells. However, CuO was found when conductive patterns were sintered at a higher temperature than 110 °C. The reason was that the Ag shell grew to be silver crystallite, partially exposing the Cu core to air.

Otherwise, using a destabilizing agent that can be a simple electrolyte such as HCl, NaCl, etc. to destabilize the capping agent could be effective as in the Ag nanoparticles conductive ink. However, the Cu-Ag nanoparticles immersed in the electrolyte solution can cause copper oxidation because electrochemical corrosion may happen. This was recorded for an alloy structure in NaOH solution at 25 ˚C [28]. In our work, the silver shell may provide some protection to the Cu core and that will be discussed below.

We successfully synthesized monodispersed Cu-Ag for conductive inks. For the sintering process, we used ($NaBH_4$) as an electrolyte solution to destabilize the capping agent, and to trigger the spontaneous sintering without copper oxidation at room temperature to avoid harsh sintering conditions by high temperature. For more details see Chapter 2 section (2.9.2). Using this approach

should remove the limitation for applications to heat-resistant substrates, allowing use of the substrates that are most used in flexible electronics, such as paper and PET.

As olylamine is a hydrophobic ligand, to get a very dispersed ink with low resistance a solvent must be chosen non-polar enough to disperse the hydrophobic surface ligand. For this purpose, a variety of solvents were chosen (octane, toluene, butanol, 1-propanol, dimethyl formide, butyl acetate and butyl ether). Based on previous studies by different scientists, they have used different solvents to obtain the highly concentrated nano ink. For instance, ethylene glycol [6,27], ethylacetate-terpineol [29], toluene [30], n-butanol, acetone, and propylene glycol monobutyl ether [31]. Solvent choice must also take into consideration the inkjet printing requirements (ink viscosity, surface tension of the solvent), to avoid nozzle blockage and ink drying (due to evaporation before deposition) or unstable droplets .

In the beginning, 10 wt% inks were formulated for the synthesized copper–silver core-shell nanoparticles by dispersing these in the different solvents using sonics & material probe for 30 min to accomplish the formulation of the conductive ink. The inks were then coated by a smear test onto PVOH -coated PET / Photo paper substrate followed by a chemical sintering process and the electrical resistance of the ink layers was measured. The results of this study are clearly shown in Table 5.5 below:

Table 5.5. Cu@ Ag core-shell ink behaviour applied on different substrates by a smear test.

Ink (NPs + Solvent)	Ink dispersion	Resistance before chemical sintering on coated PET	Resistance after chemical sintering on coated PET	Resistance before chemical sintering on Photo paper	Resistance after chemical sintering on Photo paper
Toluene	dispersed	-	44-199 Ω	-	6 MΩ
Octane	dispersed	-	8- 130 Ω	-	95- 102Ω
xylene	dispersed		105 -200 Ω		
Butyl ether	dispersed	-	0.4 MΩ-1K Ω	132 -239 Ω	281Ω-1.2 KΩ
Toluene + Butyl ether (60:40) wt%	dispersed	1.6 M Ω	-	0.8 K Ω	1.4 KΩ
other solvents	Did not disperse	-	-	-	-

The results from the smear test suggest that octane and toluene deposited layers have the lowest resistance with a shiny, metallic coating, however, while printing toluene rapidly evaporates into the air and that caused a dry layer over the nozzle. To overcome this problem xylene has been suggested as it has similar properties to toluene with a slower evaporation rate with more viscosity and by investigation it showed similar appearance to toluene film.

Regarding octane, it worked in a similar way to toluene in a smear test, with a good resistance on coated PET /photo paper after sintering but the chemical sintering tends to damage the paper substrate. Compared with the toluene, layers spread using octane seemed to have much better adherence to the coated PET substrate, possibly due to greater surface interaction/solvation of the alkane's solvent with the saturated hydrocarbons units of the PET chain structure.

Attempts were made to print by inkjet printing using the ink formulation that showed a good range of resistance by smear tests, such as octane and toluene.

However, they didn't act similarly in printing, and it was very difficult to get a nice steady droplet. Of those tested, xylene was the best and we managed to print on coated PET substrate at 90 °C. The film showed a slightly high resistance compared with Ni-Ag alloy film (Table 5.6) (Figure 5.11).

Finally, a conductive ink for printed electronics was produced from the synthesized Cu–Ag core–shell nanoparticles with xylene as a solvent. The formulated ink was printed onto a PVOH coted PET substrate using an inkjet printer. The film was sintered using chemical sintering as mentioned previously. The lowest resistivity of the Cu-Ag core-shell conductive inks was measured to be 2.17×10^{-6} Ω.m, which is approximately 129 times the bulk resistivity of Cu (1.68×10^{-8} Ω.m). This value was relatively consistent for a range of different print pitches, suggesting that the sintering process was consistent for a range of different layer thicknesses (albeit within quite a small range).

In a study done by Lee c. *et al.* [17], the lowest resistivity was measured to be 1.2×10^{-7} Ω.m, which is approximately seven times the resistivity of bulk copper. These results showed a considerably lower resistivity than those in my study. They used a spin coater to deposit the formulated ink onto a glass substrate. Then, the coated film was sintered using a heat treatment (200 °C, 250 °C, 300 °C, and 350 °C) under a N_2 gas atmosphere. Unlike this, we used an inkjet printer and a chemical sintering at room temperature to avoid substrate damage and obtain more scalable nanoparticles. This might be more cost effective in manufacturing, since high temperatures under N_2 are very demanding in terms of required infrastructure.

Table 5.6. Effect of pitch on width, thickness and resistivity of printed lines. 10% Cu Ag /xylene core-shell ink was printed with a 50 μm nozzle diameter on coated PET at 90 ˚C.

Pitch size (mm)	Width (m)	Thickness (m)	Resistance (Ω)	Length (m)
0.095	-	-	-	0.005
0.085	1.66×10^{-4}	1.91×10^{-7}	365	0.005
0.075	1.71×10^{-4}	2.12×10^{-7}	363	0.005
0.065	2.01×10^{-4}	2.17×10^{-7}	295	0.005
0.055	2.26×10^{-4}	2.20×10^{-7}	285	0.005
0.045	2.49×10^{-4}	2.25×10^{-7}	194	0.005
0.035	3.38×10^{-4}	2.32×10^{-7}	177	0.005
0.025	3.45×10^{-4}	2.75×10^{-7}	168	0.005
0.015	The lines were fused together			

Pitch size (mm)	Resistivity (Ω.m)	Relative error in resistivity	Resistivity ± error	Conductivity (s/m)	Conductivity ± error
0.095	-	-	-	-	-
0.085	2.31×10^{-6}	0.042	$(2.31 \pm 0.09) \times 10^{-6}$	4.32×10^{5}	$(4.3 \pm 0.61) \times 10^{5}$
0.075	2.61×10^{-6}	0.145	$(2.6 \pm 0.38) \times 10^{-6}$	3.83×10^{5}	$(3.8 \pm 0.55) \times 10^{5}$
0.065	2.57×10^{-6}	0.329	$(2.6 \pm 0.84) \times 10^{-6}$	3.89×10^{5}	$(4 \pm 1.3) \times 10^{5}$
0.055	2.83×10^{-6}	0.345	$(2.8 \pm 0.98) \times 10^{-6}$	3.53×10^{5}	$(4 \pm 1.2) \times 10^{5}$
0.045	2.17×10^{-6}	0.158	$(2.2 \pm 0.34) \times 10^{-6}$	4.61×10^{5}	$(4.6 \pm 0.73) \times 10^{5}$
0.035	2.77×10^{-6}	0.178	$(2.8 \pm 0.49) \times 10^{-6}$	3.61×10^{5}	$(3.6 \pm 0.64) \times 10^{5}$
0.025	3.18×10^{-6}	0.177	$(3.2 \pm 0.56) \times 10^{-6}$	3.14×10^{5}	$(3.1 \pm 0.56) \times 10^{5}$

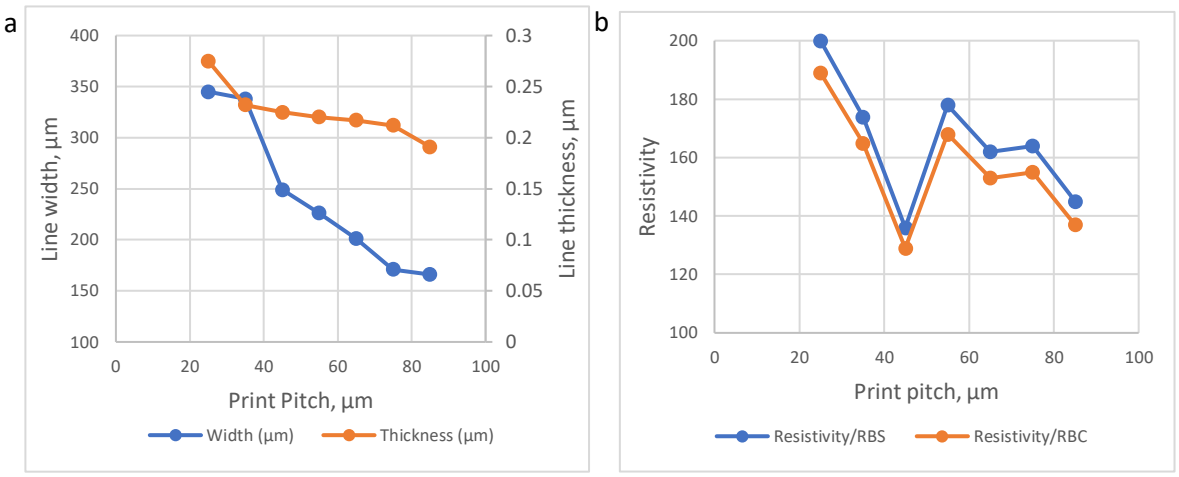

Figure 5.11. Characteristics of printed lines on coated PET at 90˚C by 50 µm nozzle (a) effect of print pitch on the line width/ thickness, (b) effect of print pitch on resistivity.

5.5 Conclusion

The purpose of this chapter is to attain scalable and more economical NPs, where Ag is replaced in part by a less expensive but still conductive and solderable metal. This can be achieved either by replacing or mixing the pure Ag with Ni or Cu. However, the characterization of Ni-Ag core-shell NPs by SEM/EDS and ICP-MS has confirmed that there is a very little percentage of Ni in the final products, so it doesn't reach our outcome to save the material cost. In contrast, copper offers desirable blending values that achieve our goal while being more economical and has a good particles distribution of about 14 nm with spherical and monodisperse particles. However, the main obstacle was with the ink jet printing process and the ink formulation, where choosing the appropriate solvent to get a well dispersed ink was a challenge.

In summary, the prepared Ni-Ag core-shell NPs with different Ag/Ni ratios were successfully synthesised by different methods, such as the polyol method and solvothermal method and completely characterized by different techniques. The nanoparticle size distribution varied between 10 – up to over 200 nm with increasing Ag content.

Even though its ink formulation produced a good appearance in the smear tests and its ability to print by inkjet printer was acceptable, the printed film showed lots of cracks and fractures as a result of handling the substrate and that caused the real problem of losing the conductivity similar to results obtained from

AgNi alloy ink. Thus, there is still plenty of development of nickel conductive inks that need to be done to make it favourable for inkjet printing and scale-up production.

In contrast to the Ni results, for Cu-Ag core-shell, monodisperse nanoparticles were synthesized using a simple two-step process consisting of thermal decomposition and galvanic displacement methods. We used 80°C as the galvanic displacement reaction temperature to produce a very robust galvanic displacement reaction while keeping the core–shell structure.

Compared with Ni-Ag core-shell properties the Cu–Ag core–shell nanoparticles have considerably better oxidation stability under similar conditions. Finally, we also investigated the electrical properties of the Cu–Ag core–shell printed nanoparticles after sintering at room temperature under chemical sintering.

This result is very encouraging because sintering at room temperature is sufficiently low for flexible substrates to remain undamaged and can be used for flexible applications in the future. This approach may thus be worthy of further development.

References

(1) Pajor-Świerzy, A.; Socha, R.; Pawłowski, R.; Warszyński, P.; Szczepanowicz, K. Application of Metallic Inks Based on Nickel-Silver Core-Shell Nanoparticles for Fabrication of Conductive Films. *Nanotechnology*. **2019**, *30 (22)*, 1-8.

(2) Pajor-Świerzy, A.;Gaweł, D.;Drzymała, E.; Socha, R.;Parlińska-Wojtan, M.;Szczepanowicz, K.; Warszyński, P. The Optimization of Methods of Synthesis of Nickel – Silver Core – Shell Nanoparticles for Conductive Materials. *Nanotechnology*. **2019**, *30* (015601), 1-8.

(3) Pajor-Świerzy, A.; Pawłowski, R.; Warszyński, P.; Szczepanowicz, K. The Conductive Properties of Ink Coating Based on Ni–Ag Core–Shell Nanoparticles with the Bimodal Size Distribution. *J. Mater. Sci. Mater. Electron.* **2020**, *31 (15)*, 12991–12999.

(4) Baletto, F.; Mottet, C.; Rapallo, A.; Rossi, G.; Ferrando, R. Growth and Energetic Stability of AgNi Core-Shell Clusters. *Surf. Sci.* **2004**, *566–568 (3)*, 192–196.

(5) Pajor-Świerzy, A.; Szendera, F.; Pawłowski, R.; Szczepanowicz, K. Nanocomposite Inks Based on Nickel-Silver Core-Shell and Silver Nanoparticles for Fabrication Conductive Coatings at Low-Temperature Sintering. *Colloids and Interfaces.* **2021**, *5* (1), 1-12.

(6) Srivastava, C.; Chithra, S.; Malviya, K. D.; Sinha, S. K.; Chattopadhyay, K. Size Dependent Microstructure for Ag-Ni Nanoparticles. *Acta Mater.* **2011**, *59 (16)*, 6501–6509.

(7) Chen, D. H.; Wang, S. R. Protective Agent-Free Synthesis of Ni-Ag Core-Shell Nanoparticles. *Mater. Chem. Phys.* **2006**, *100 (2–3)*, 468–471.

(8) Jing, J. J.; Xie, J.; Chen, G. Y.; Li, W. H.; Zhang, M. M. Preparation of Nickel–Silver Core–Shell Nanoparticles by Liquid-Phase Reduction for Use in Conductive Paste. *J. Exp. Nanosci.* **2015**, *10 (17)*, 1347–1356.

(9) Thu, N. N. A.; Park, J. G.; Kim, S. H. Synthesis of Ni-Ag Core-Shell Nanoparticles by Polyol Process and Microemulsion Process. *Bull. Korean Chem. Soc.* **2013**, *34 (10)*, 2865–2870.

(10) Pajor-Świerzy, A.; Farraj, Y.; Kamyshny, A.; Magdassi, S. Air Stable Copper-Silver Core-Shell Submicron ParticlesSynthesis and Conductive Ink Formulation. *Colloids Surfaces A Physicochem. Eng. Asp.* **2017**, *521 (80)*, 272–280.

(11) Vykoukal, V.; Bursik, J.; Roupcova, P.; Cullen, D. A.; Pinkas, J. Solvothermal Hot Injection Synthesis of Core-Shell AgNi Nanoparticles. *J. Alloys Compd.* **2019**, *770 (8)*, 377–385.

(12) Wakuda, D.; Kim, K. S.; Suganuma, K. Room Temperature Sintering of Ag Nanoparticles by Drying Solvent. *Scr. Mater.* **2008**, *59 (6)*, 649–652.

(13) Guo, H.; Chen, Y.; Chen, X.; Wen, R.; Yue, G. H.; Peng, D. L. Facile Synthesis of Near-Monodisperse Ag@Ni Core-Shell Nanoparticles and Their Application for Catalytic Generation of Hydrogen. *Nanotechnology.* **2011**, *22 (19)*, 1-9.

(14) Dai, X.; Xu, W.; Zhang, T.; Shi, H.; Wang, T. Room Temperature Sintering of Cu-Ag Core-Shell Nanoparticles Conductive Inks for Printed Electronics. *Chem. Eng. J.* **2019**, *364 (10)*, 310–319.

(15) Ishizaki, T.; Watanabe, R. A New One-Pot Method for the Synthesis of Cu Nanoparticles for Low Temperature Bonding. *J. Mater. Chem.* **2012**, *22 (48)*, 25198–25206.

(16) Tan, S.; Zu, X.; Yi, G.; Liu, X. Synthesis of Highly Environmental Stable Copper–Silver Core–Shell Nanoparticles for Direct Writing Flexible Electronics. *J. Mater. Sci. Mater. Electron.* **2017**, *28 (21)*, 15899–15906.

(17) Lee, C.; Kim, N. R.; Koo, J.; Lee, Y. J.; Lee, H. M. Cu-Ag Core-Shell Nanoparticles with Enhanced Oxidation Stability for Printed Electronics. *Nanotechnology.* **2015**, *26 (45)*, 1-9.

(18) Park, B. K.; Jeong, S.; Kim, D.; Moon, J.; Lim, S.; Kim, J. S. Synthesis and Size Control of Monodisperse Copper Nanoparticles by Polyol Method. *J. Colloid Interface Sci.* **2007**, *311 (2)*, 417–424.

(19) Kim, K.; Kim, K. L.; Shin, K. S. Co-Reduced Ag/Pd Bimetallic Nanoparticles: Surface Enrichment of Pd Revealed by Raman Spectroscopy. *J. Phys. Chem. C.* **2011**, *115 (30)*, 14844–14851.

(20) Huang, Y.; Wu, F.; Zhou, Z.; Zhou, L.; Liu, H. Fabrication of Fully Covered Cu-Ag Core-Shell Nanoparticles by Compound Method and Anti-Oxidation Performance. *Nanotechnology* **2020**, *31 (17)*, 1-10.

(21) Chang, Y.; Bai, Y.; Teng, B.; Li, Z. A New Drug Carrier: Magnetite Nanoparticles Coated with Amphiphilic Block Copolymer. *Chinese Sci. Bull.* **2009**, *54 (7)*, 1190–1196.

(22) Magdassi, S.; Grouchko, M.; Berezin, O.; Kamyshny, A. Triggering the Sintering of Silver Nanoparticles at Room Temperature. *ACS Nano.* **2010**, *4 (4)*, 1943–1948.

(23) Grouchko, M.; Kamyshny, A.; Mihailescu, C. F.; Anghel, D. F.; Magdassi, S. Conductive Inks with a 'Built-in' Mechanism That Enables Sintering at Room Temperature. *ACS Nano.* **2011**, *5 (4)*, 3354–3359.

(24) Shi, L.; Layani, M.; Cai, X.; Zhao, H.; Magdassi, S.; Lan, M. An Inkjet Printed Ag Electrode Fabricated on Plastic Substrate with a Chemical Sintering Approach for the Electrochemical Sensing of Hydrogen Peroxide. *Sensors Actuators, B Chem.* **2018**, *256 (10)*, 938–945.

(25) Grouchko, M.; Kamyshny, A.; Magdassi, S. Formation of Air-Stable Copper-Silver Core-Shell Nanoparticles for Inkjet Printing. *J. Mater. Chem.* **2009**, *19 (19)*, 3057–3062.

(26) Tsai, C. H.; Chen, S. Y.; Song, J. M.; Chen, I. G.; Lee, H. Y. Thermal Stability of Cu at Ag Core-Shell Nanoparticles. *Corros. Sci.* **2013**, *74 (4)*, 123–129.

(27) Yu, X.; Li, J.; Shi, T.; Cheng, C.; Liao, G.; Fan, J.; Li, T.; Tang, Z. A Green Approach of Synthesizing of Cu-Ag Core-Shell Nanoparticles and Their Sintering Behavior for Printed Electronics. *J. Alloys Compd.* **2017**, *724 (7)*, 365–372.

(28) Assaf, F. H.; Zaky, A. M.; Abd El-Rehim, S. S. Cyclic Voltammetric Studies of the Electrochemical Behaviour of Copper-Silver Alloys in NaOH Solution. *Appl. Surf. Sci.* **2002**, *187* (1–2), 18–27.

(29) Peng, Y. H.; Yang, C. H.; Chen, K. T.; Popuri, S. R.; Lee, C. H.; Tang, B. S. Study on Synthesis of Ultrafine Cu-Ag Core-Shell Powders with High Electrical Conductivity. *Appl. Surf. Sci.* **2012**, *263 (8)*, 38–44.

(30) Lee, C.; Kim, N. R.; Koo, J.; Lee, Y. J.; Lee, H. M. Cu-Ag Core-Shell Nanoparticles with Enhanced Oxidation Stability for Printed Electronics. *Nanotechnology.* **2015**, *26 (45)*, 1-10.

(31) Titkov, A. I.; Logutenko, O. A.; Vorobyov, A. M.; Yu. Gerasimov, E.; Shundrina, I. K.; Bulina, N. V.; Lyakhov, N. Z. Synthesis of ˜10 Nm Size Cu/Ag Core-Shell Nanoparticles Stabilized by an Ethoxylated Carboxylic Acid for Conductive Ink. *Colloids Surfaces A Physicochem. Eng. Asp.* **2019**, *577 (3)*, 500–508.

Chapter 6. Developing flexible plastic substrates for room temperature silver sintering results and discussion

Fabricating electronic devices and circuits on flexible substrates has gained significant interest over the last decade as a route to achieve cost-effective roll-to-roll processing of lightweight, ecofriendly, disposable and foldable electronic devices, such as an active-matrix electronic ink display [1], solar cells [2], radio frequency identification tags [3,4], biosensors on polyimide (PI) [5] and silver nanowire transparent electrodes [6] on poly(ethylene therephthalate) (PET) [7]. Attention was thus drawn in the direction of preparation of flexible printed electronics using metal nanoparticles (NPs) based conductive nano-inks.

Nevertheless, there are two challenges for the effective printing of nanomaterial-based electronic devices on various substrates [8]. Firstly, some substrates are intolerant of high temperatures, such as, the process temperatures of PET and paper are all less than 180 °C [9]. Therefore, decreasing the sintering temperature of nanomaterials ink is usually more appropriate as discussed previously. Secondly, the wettability of the inks on some substrates cannot satisfy the requirements of printing high-quality patterns. For example, the same silver ink could print fine lines on photo paper but not on PET substrates owning to the different wettability of silver ink on these substrates [10].

This chapter will discuss the requirements to print on thermostable and tough plastics in order to get conductive AgNP printed tracks and the plastic films that are being develop for this application. Herein, the chapter will cover how the surfaces and properties of the plastic substrates are being engineered to make them suitable for Ag spontaneous sintering, with good adhesion and electric performance of the produced tracks, and to produce acceptable flexibility with repeated bending on economically desirable substrates. The PVOH solution and bar coating that are being developed and the issues facing the development of a ‘‘flexible plastic substrate’’ will be discussed.

The plastic substrate needs to be able to offer the properties of Ag spontaneous sintering, thermal stability, solvent resistance, coupled with a smooth surface in terms of being able to develop flexible devices. We will discuss and contrast the leading candidates for plastic based flexible substrates (PET and

PI) and discuss their electrical performance after being developed to meet the demanding targets.

PVOH is a widely studied polymer due to its versatile properties. It is highly water-soluble, has a low cost, and has suitable film-forming properties [11]. A PVOH coating solution mixed with different Cl^- concentrations could ensure the forming of spontaneously sintering patterns owing to its adsorption of ink and the high adhesiveness of PVOH with substrates. So, we envision that this approach could serve as an adaptive method for sintering of Ag NPs based conductive patterns on various substrates at room temperature and promote the manufacture of printed electronics [9]. This unique surface coating of PVOH helps the ink to permeate through the nanopores and also aids absorption along the fibril direction parallel to the surface while retaining the silver nanoparticles on the surface to compete with the initial spreading and final evaporation process [7].

As these substrates are temperature sensitive, they require a relative low sintering temperature to prevent destruction by heating. As we stated in chapter 3, stabilizing Ag NPs with capping agent in dispersion before use, then destabilizing them by some anions during application, leads to a spontaneous coalescence between particles to realize sintering and that makes the sintering of Ag NPs at room temperature possible and also simplifies the sintering procedure. On this basis we have found that PAA or PVP was competent to stabilize Ag NPs by adsorbing on their surface and could be facilely detached by Cl^- on photo paper, which also leads to the spontaneous sintering process. However, no plastic film offers these properties, so plastic substrate will certainly need to be modified to be capable of room temperature sintering [12].

To cope with this need, electrical devices that can be manufactured with high electrical conductivity and mechanical robustness are critical for developing flexible electronics with heat-sensitive substrates [13]. Even under bending or folding, these electric patterns need to constantly maintain a high level of conductivity [14].

Bar coating is considered one of the most popular coating methods. It provides a simple but effective means of printing across a substrate surface to apply some coating solution to the substrate to improve surface properties such as appearance, adhesion, wettability etc. When creating a hydrophilic wetting

area with PVOH, layer thickness can be controlled by the solid content of the solution and the wire diameter/spacing of the wire wound around the bar .

Poly(ethylene terephthalate) (PET) and polyimide (PI) were initially selected as base substrates for printing at the beginning of the coating process. Both these polymers are tough and relatively temperature stable, and widely used in the microelectronics industry [15]. Subsequently, glass was also used as a rigid substrate for more sensitive Ni ink due to its previously demonstrated susceptibility to damage when bent during handling.

This study lays the foundation for greatly improving the properties of the sintered patterns on plastic substrate. The synthesis, conductivity, and bending stability based on our Ag NPs were systematically investigated.

6.1 Aim of this chapter

The aim of the project is to identify how a plastic substrate surface can be improved by applying a suitable PVOH coating formula, in order to develop surface properties suitable for inkjet printing and high printing quality.

The work investigates the AgNP printed tracks on a thermostable and tough plastic substrate compared with photo paper and how to incorporate Cl^- for spontaneous Ag sintering and test the electric performance of tracks by comparing their initial resistance to that after multiple bending cycles.

6.2 Fabrication of PVOH /KCl coated film

A coating is a covering that is applied to the substrate in order to enhance the substrate properties. PVOH is typically applied to improve the quality of a substrate by coating a film layer onto the whole sheet [16].

We have prepared a thick and thin polymer layer with different Cl^- concentrations starting from high concentration to very dilute chloride, and finally zero added chloride as a reference. Coating was carried out using wire -wrapped coating bars. The wet thickness of the coating was controlled by the diameter of the wire on the bars that were used to apply the coating to the surface.

For the present study, a 30 wt% AgPAA ink was tested by a quick smear test with a spatula to see if standard ink stayed well adhered to the PET substrate or whether it tended to peel off. This provided a simple test to verify ink printability onto the coated substrate, and gauge whether or not it was sintered and gave good conductivity, which allowed assessment of different Cl^- concentrations in the PVOH coating layer. After that, a more controlled test was done by spreading some formulated ink onto the film using metering bars with different wire thicknesses and testing the conductivity using a Digital Multimeter.

The coating solution was first applied to the top edge of the substrate, then a layer was spread by pulling the rod firmly over the substrate. The rod is used to manage the excess coating solution and control the coating weight. The wet thickness is controlled by the diameter of the wire on the rod used to apply the ink. The rods are available in a wide variety of sizes to give a range of coating weights. Table 6.1 below gives the wire sizes that have been used and the wet thickness that can be achieved. The dry thickness is determined by the solids concentration of the coating solutions - about 1/10 of wet film thickness with the solutions used in this study. Following preliminary trials, the blue bar with a 1.27 mm wire diameter was selected in this study as it showed the best (lowest) resistance for sintered ink layers.

Table 6.1. Bar metering application chart.

Bar code	Wire diameter	Wet film deposit
Red	0.15 mm	12 µm
Black	0.51 mm	40 µm
Blue	1.27 mm	100 µm

Generally, for this work, bar coating was used to produce thin uniform films of polymer solution for testing purposes. The coating contained (10 wt%) polyvinyl alcohol solution and 0.01 M KCl as a sintering agent. Chloride ions can assist the sintering of AgNP films by displacing capping agents on the surfaces of AgNPs. The hydrophilic ink is able to swell the hydrophilic PVOH film, mobilising the Cl^- ions and allowing them to diffuse into the printed NP film, where they can perform the sintering function (for more details see Chapter 2 (2.10)).

6.3 Assessment of electrical performance of printed tracks

To present the result of inkjet printing of Ag/PAA ink on PVOH coated substrate via bar metering, a series of experiments was conducted in order to determine the most effective Cl^- concentration for ink sintering and its characteristics [16].

Electrical performance of printed tracks was evaluated by measuring the resistance. Resistance was significantly different depending on the Cl^- level. Silver ink was successfully printed on each coated substrate with five different Cl^- concentration (1 M, 0.1 M,0.01 M,0.001 M and 0M). Good resistance is expected when the Cl^- level is low, and the conductive ink is printed consistently and reliably. Only (0.01 and 0.001 M) were verified to have significantly low resistance compared to others, while the difference among them became more apparent with a higher level of Cl^-.

It was observed that the electrical conductivity was higher when using a thicker layer (black & blue bar) with low -chloride (0.01 and 0.001 M) and the track showed a metallic appearance. This compared with high chloride concentrations (1 M and 0.1 M), where the ink is slightly white in colour and this confirms the likely presence of AgCl on the surface, suggesting that some silver at least has been mobilised and reoxidised.

We believe that the formation of AgCl nanocrystals explains the high resistance and inhibited sintering characteristic. As the AgCl nanocrystals are semiconductors, this tends to reduce the number of direct conductive contact points between the nanoparticles in the film, replacing them with AgCl bridges. The high chloride concentration will tend to react rapidly with any mobilised Ag^+ ions, forming these nanocrystals and preventing Ag^+ diffusion and redeposition

on new particles to create the sintering process. Also, it is a reason for slower drying of the ink over several minutes.

This finding is also consistent with the results obtained by Ohlund T. *et al*. [17]. Their results showed an increase in resistivity when PVP-capped AgNPs were inkjet-printed on papers containing (0.3 wt%) KCl. By investigating the AgNP printed film nanostructure in detail, they found that the resistivity increased because of the formation of AgCl nanocrystals on the surface of AgNPs. That confirms that chloride can play an opposite role as a sintering inhibitor on absorptive media if the concentrations and kinetics are not favourable.

As we faced some problems with getting conductive printing with Ag-Ni NPS due to cracking or peeling (track bending) occurring in the ink layers after printing and handling when doing the characterization on a flexible, uncoated substrate, a protective rigid substrate is necessary to try. Therefore, microscope slides (glass) were suggested for coating and discovering their efficiency with printing tracks (for details see chapter 4 (Table 4.13)).

These results reveal that the modified substrate is effective and offers a potential way to fabricate inkjet materials with better conductivity and Cl^- sintering was transferred successfully to plastic substrate to enable spontaneous Ag sintering.

The preparation of coating solution / fabrication of PVOH/KCl coated film and the explanation of how the chloride sintering method has been transferred to plastic substrates was presented in detail in Chapter 2 section (2.10) and chapter 6 (6.3). The following section focuses on testing the robustness of the produced silver tracks on two different flexible substrates (polyethylene terephthalate (PET) /Polyimide (PI)) and the approaches used, and the results of this work will be discussed here.

6.4 Testing the robustness of the produced silver tracks on flexible substrates

Due to the flexibility of the polymer substrate, researchers rely on a wide range of mechanical deformation conditions such as bending, stretching modes, scratch testing, or peel testing. All of these approaches are used to get different information about the mechanical stability of the printed materials, but in this

study, we assessed the durability of printed patterns via an automated bending test. Testing of track adhesion and stability on substrates through flexing tests is describe below [4,15].

The term "flexible" is used to describe bendability and foldability of planar electronic structures or components. Bending can disturb the connections between particles, causing crack formation and detachment of the conductive material in the printed layers and cause an increase in resistance over the entire length of the printed pattern. As a result, the performance of electronic devices will fail, so all of these obstacles should be addressed when fabricating flexible electronic devices. To ensure the printed patterns' stability to bending, performance is usually tested by measuring the resistance of the printed tracks after several bending cycles [15].

6.4.1 Mechanics of bending /stretching-mode

Figure 6.1 shows the experimental setup for the cyclic bending deformation of flexible electronics with Ag NP printed track. We have designed a novel and custom-built rig to give more reliable data than manual bending/stretching experiments. An image (Figure 6.1) illustrates the custom rig and from the images, the rig parts can be understood.

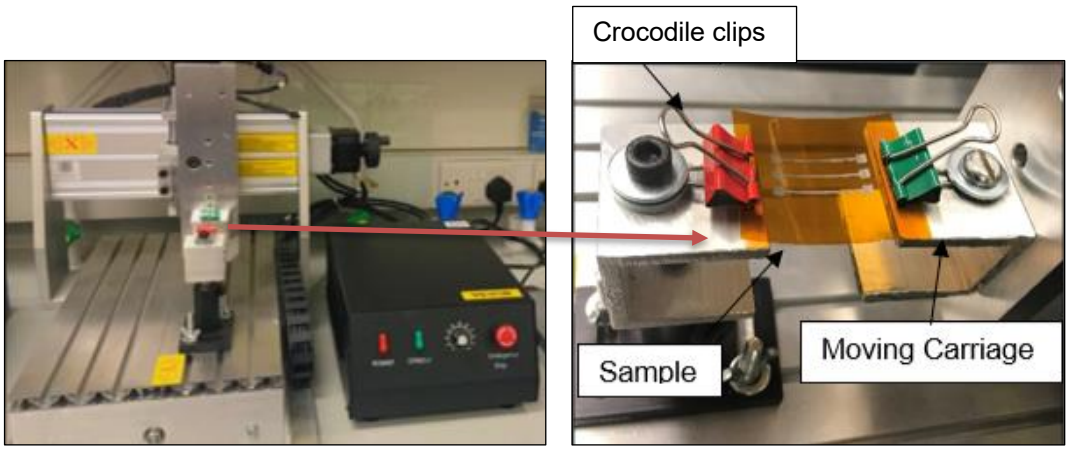

Figure 6.1. Photograph of bending rig (novel and custom built) with the parts labelled.

The printed tracks are bent in two directions (i.e. tension /compression). In a bending process, bending the tracks toward the substrate imparts compressive bend (Figure 6.2 (a)) while bending the tracks away from the substrate imparts a tensile bend (Figure 6.2(b)). In each direction, simple before/ after cyclic bend measurements have been done in which performance (via measured resistance) is assessed during many bend cycles and variable experimental parameters (e.g. speed of bending) to evaluate resistance against bending.

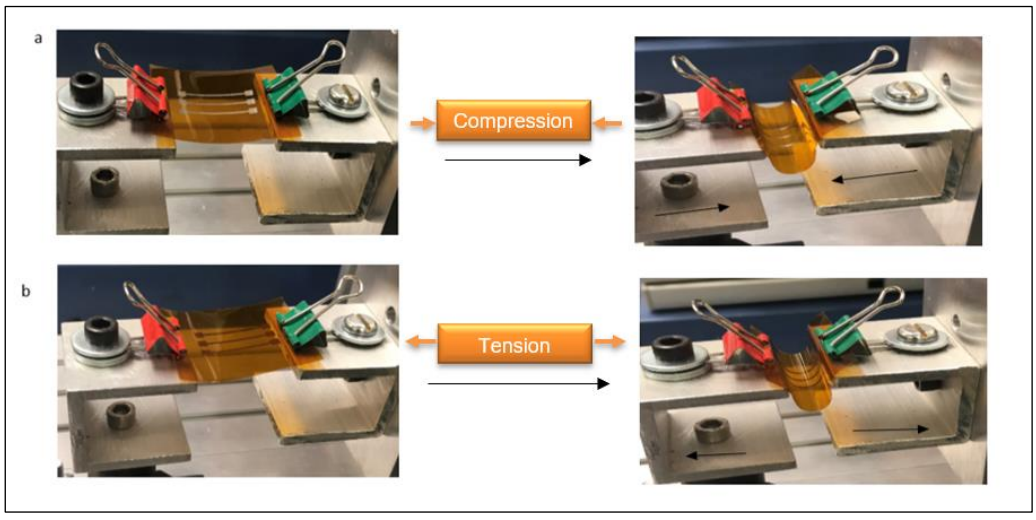

Figure 6.2. Simple drawing/images of forces in (a) compressive (printed track on top surface) and (b) tensile (printed track on bottom surface) bending.

For bending experiments, we followed two major steps starting by:

1. Establish a protocol for transferring pattern designs to the printer software in order to create a bitmap with 2 mm wide and 20 mm long tracks terminated by 3x3mm square contact pads (Figure 6.3).

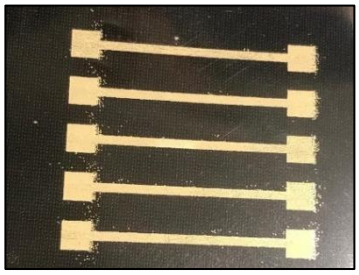

Figure 6.3. Optical microscope image of the inkjet silver track on PVOH/KCl coated PET substrate.

The bitmap design starts with creating a pattern design in paint software, then it is saved as a monochrome bitmap (BMP) file. After that a script (printing recipes can be written in separate text files by the user and then read and executed by the jet lab printer program) is created containing the actual print parameter instructions. After the script is selected, its tittle is displayed under the file name. The needed action is to click on “start“ to do the actual printing. A simple description is shown below to achieve these variables (Figure 6.4).

a

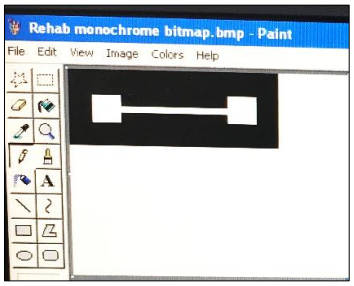

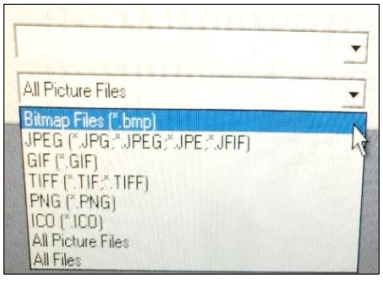

b

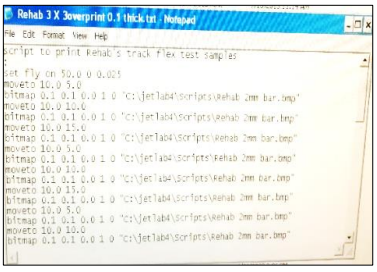

Figure 6.4. (a) Illustration of bitmap creating steps, (b) example of a script file for printing.

2. Several variables should be set up (Figure 6.5 -) to describe the robustness of the printed track, and the most common of these is bending angle (which is the angle formed between the two ends of the bent sample, bending cycle repeats and bending speed). Then, samples were mounted between crocodile clip holders on a fixed platform and a moving carriage on a motorised stage (Figure 6.2). The moving carriage was moved to bend the sample by 10°

and 20°, either in compression or tension, hold it for 2 s and then moved back to the original position. The speed in both directions was adjusted (10, 50 and 100 mm/min). Finally, the resistance was measured with a digital multimeter at the end of the cycle to evaluate the result of the deformation of printed silver tracks on a flexible substrate.

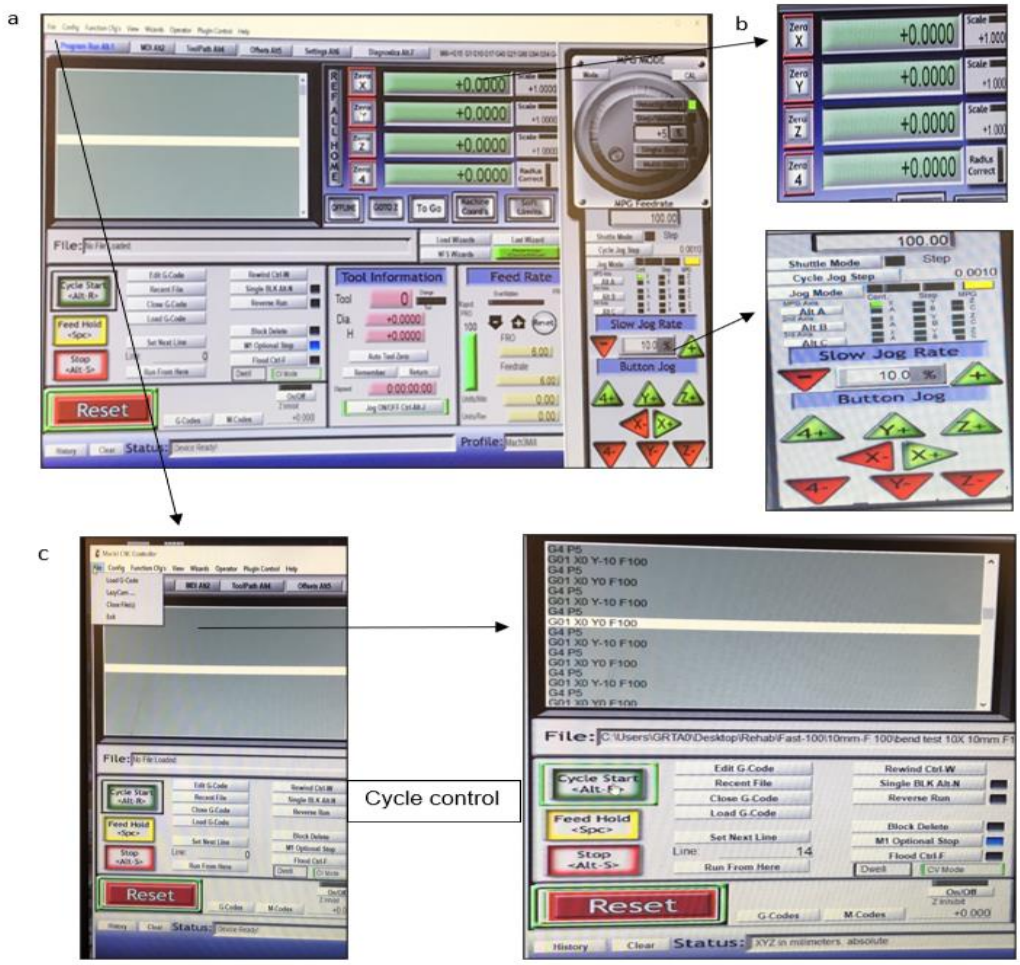

Figure 6.5. A simple illustration of bending software setting, using Mach 3 software to control the motion of the micro engraving rig. (a) Overall software, (b) axes (X, Y) control, (c) load / control cycle.

6.4.2 Assessment of electrical properties of tracks on PVOH-KCl substrate after bending test

The profilometer was used to measure the physical dimension based on vertical scanning interferometry and evaluated by Vision 64 (Bruker) analysis software of the 3-layer overprinting silver track (5 replica lines) on these different substrates. The print pitch between droplets was adjusted identically in all printed tracks (0.055 mm). These measurements make it possible to calculate the

conductivity on photo paper, PET and PI substrates after bending is performed (Tables 6.2-6.9).

Table 6.2. 30 wt% AgPAA ink on PET coated substrate (tension) with 0.055 mm print pitch.

No. of bends	Width (m)	Thickness (m)	Resistance (Ω)	Length (m)	Resistivity (Ω.m)	Resistivity/ RBS	Conductivity (s/m)
0	9.61×10^{-4}	1.25×10^{-6}	12.6	0.02	7.56×10^{-7}	47.5	1.32×10^{6}
100	9.61×10^{-4}	1.25×10^{-6}	13.2	0.02	7.92×10^{-7}	49.8	1.26×10^{6}
200	9.61×10^{-4}	1.25×10^{-6}	13.4	0.02	8.04×10^{-7}	50.5	1.24×10^{6}
300	9.61×10^{-4}	1.25×10^{-6}	13.4	0.02	8.04×10^{-7}	50.6	1.24×10^{6}
400	9.61×10^{-4}	1.25×10^{-6}	13.5	0.02	8.10×10^{-7}	50.9	1.23×10^{6}
500	9.61×10^{-4}	1.25×10^{-6}	13.6	0.02	8.16×10^{-7}	51	1.22×10^{6}

Table 6.3. 30 wt% AgPAA ink on PET coated substrate (compression) with 0.055 mm print pitch.

No. of bends	Width (m)	Thickness (m)	Resistance (Ω)	Length (m)	Resistivity (Ω.m)	Resistivity/ RBS	Conductivity (s/m)
0	9.61×10^{-4}	1.25×10^{-6}	6	0.02	3.60×10^{-7}	22.6	2.77×10^{6}
100	9.61×10^{-4}	1.25×10^{-6}	6.5	0.02	3.90×10^{-7}	24.5	2.56×10^{6}
200	9.61×10^{-4}	1.25×10^{-6}	6.7	0.02	4.02×10^{-7}	25.2	2.48×10^{6}
300	9.61×10^{-4}	1.25×10^{-6}	6.8	0.02	4.08×10^{-7}	25.3	2.23×10^{6}
400	9.61×10^{-4}	1.25×10^{-6}	7.5	0.02	4.50×10^{-7}	28.3	2.22×10^{6}
500	9.61×10^{-4}	1.25×10^{-6}	8	0.02	4.80×10^{-7}	30.2	2.08×10^{6}

Table 6.4. 30 wt% AgPAA ink on PI coated substrate (tension) with 0.055 mm print pitch.

No. of bends	Width (m)	Thickness (m)	Resistance (Ω)	Length (m)	Resistivity (Ω.m)	Resistivity/ RBS	Conductivity (s/m)
0	9.53×10^{-4}	1.49×10^{-6}	12.2	0.02	8.66×10^{-7}	54	1.15×10^{6}
100	9.53×10^{-4}	1.49×10^{-6}	12.4	0.02	8.79×10^{-7}	55	1.13×10^{6}
200	9.53×10^{-4}	1.49×10^{-6}	12.5	0.02	8.86×10^{-7}	55.7	1.12×10^{6}
300	9.53×10^{-4}	1.49×10^{-6}	12.8	0.02	9.08×10^{-7}	57	1.10×10^{6}
400	9.53×10^{-4}	1.49×10^{-6}	12.9	0.02	9.15×10^{-7}	57.5	1.09×10^{6}
500	9.53×10^{-4}	1.49×10^{-6}	13	0.02	9.22×10^{-7}	58	1.08×10^{6}

Table 6.5. 30 wt% AgPAA ink on PI coated substrate (compression) with 0.055 mm print pitch.

No. of bends	Width (m)	Thickness (m)	Resistance (Ω)	Length (m)	Resistivity (Ω.m)	Resistivity/ RBS	Conductivity (s/m)
0	9.53×10^{-4}	1.49×10^{-6}	18.5	0.02	13.1×10^{-7}	82	0.76×10^{6}
100	9.53×10^{-4}	1.49×10^{-6}	18.7	0.02	13.2×10^{-7}	83	0.75×10^{6}
200	9.53×10^{-4}	1.49×10^{-6}	18.9	0.02	13.4×10^{-7}	84	0.74×10^{6}
300	9.53×10^{-4}	1.49×10^{-6}	22	0.02	15.6×10^{-7}	98	0.64×10^{6}
400	9.53×10^{-4}	1.49×10^{-6}	23	0.02	16.3×10^{-7}	102	0.61×10^{6}
500	9.53×10^{-4}	1.49×10^{-6}	30	0.02	21.3×10^{-7}	134	0.47×10^{6}

Table 6.6. 30 wt% AgPAA ink on photo paper/ wide line (2 mm) (compression) with 0.055 mm print pitch.

No. of bends	Width (m)	Thickness (m)	Resistance (Ω)	Length (m)	Resistivity (Ω.m)	Resistivity/ RBS	Conductivity (s/m)
0	9.52×10^{-4}	5.83×10^{-7}	7	0.02	1.94×10^{-7}	12	5.15×10^{6}
100	9.52×10^{-4}	5.83×10^{-7}	9	0.02	2.50×10^{-7}	16	4.00×10^{6}
200	9.52×10^{-4}	5.83×10^{-7}	14	0.02	3.89×10^{-7}	24	2.57×10^{6}
300	9.52×10^{-4}	5.83×10^{-7}	16	0.02	4.44×10^{-7}	28	2.25×10^{6}
400	9.52×10^{-4}	5.83×10^{-7}	17	0.02	4.72×10^{-7}	30	2.11×10^{6}
500	9.52×10^{-4}	5.83×10^{-7}	18	0.02	4.99×10^{-7}	31	2.00×10^{6}
600	9.52×10^{-4}	5.83×10^{-7}	20	0.02	5.55×10^{-7}	35	1.80×10^{6}
700	9.52×10^{-4}	5.83×10^{-7}	21	0.02	5.83×10^{-7}	37	1.72×10^{6}
800	9.52×10^{-4}	5.83×10^{-7}	27	0.02	7.49×10^{-7}	47	1.34×10^{6}
900	9.52×10^{-4}	5.83×10^{-7}	29	0.02	8.05×10^{-7}	51	1.24×10^{6}
1000	9.52×10^{-4}	5.83×10^{-7}	33	0.02	9.16×10^{-7}	58	1.09×10^{6}

Table 6.7. 30 wt% AgPAA ink on photo paper/ wide line (2 mm) (tension) with 0.055 mm print pitch.

No. of bends	Width (m)	Thickness (m)	Resistance (Ω)	Length (m)	Resistivity (Ω.m)	Resistivity /RBS	Conductivity (s/m)
0	9.52×10^{-4}	5.83×10^{-7}	21	0.02	5.83×10^{-7}	37	1.72×10^{6}
100	9.52×10^{-4}	5.83×10^{-7}	22.2	0.02	6.16×10^{-7}	39	1.62×10^{6}
200	9.52×10^{-4}	5.83×10^{-7}	22.9	0.02	6.35×10^{-7}	40	1.57×10^{6}
300	9.52×10^{-4}	5.83×10^{-7}	23	0.02	6.38×10^{-7}	40.1	1.57×10^{6}
400	9.52×10^{-4}	5.83×10^{-7}	24	0.02	6.66×10^{-7}	42	1.50×10^{6}
500	9.52×10^{-4}	5.83×10^{-7}	25	0.02	6.94×10^{-7}	44	1.44×10^{6}
600	9.52×10^{-4}	5.83×10^{-7}	26.6	0.02	7.38×10^{-7}	46	1.35×10^{6}
700	9.52×10^{-4}	5.83×10^{-7}	26.7	0.02	7.41×10^{-7}	46.6	1.35×10^{6}
800	9.52×10^{-4}	5.83×10^{-7}	27	0.02	7.49×10^{-7}	47.1	1.34×10^{6}
900	9.52×10^{-4}	5.83×10^{-7}	27.8	0.02	7.71×10^{-7}	48.5	1.30×10^{6}
1000	9.52×10^{-4}	5.83×10^{-7}	28	0.02	7.77×10^{-7}	48.9	1.29×10^{6}

Table 6.8. 30 wt% AgPAA ink on photo paper/ narrow line (1 mm) (tension) with 0.055 mm print pitch.

No. of bends	Width (m)	Thickness (m)	Resistance (Ω)	Length (m)	Resistivity (Ω.m)	Resistivity/ RBS	Conductivity (s/m)
0	3.26×10^{-4}	3.66×10^{-7}	45	0.02	2.68×10^{-7}	17	3.73×10^{6}
100	3.26×10^{-4}	3.66×10^{-7}	51	0.02	3.04×10^{-7}	19	3.29×10^{6}
200	3.26×10^{-4}	3.66×10^{-7}	60	0.02	3.58×10^{-7}	23	2.79×10^{6}
300	3.26×10^{-4}	3.66×10^{-7}	68	0.02	4.06×10^{-7}	26	2.46×10^{6}
400	3.26×10^{-4}	3.66×10^{-7}	79	0.02	4.71×10^{-7}	30	2.12×10^{6}
500	3.26×10^{-4}	3.66×10^{-7}	98	0.02	5.85×10^{-7}	37	1.71×10^{6}
600	3.26×10^{-4}	3.66×10^{-7}	110	0.02	6.56×10^{-7}	41	1.52×10^{6}
700	3.26×10^{-4}	3.66×10^{-7}	120	0.02	7.16×10^{-7}	45	1.40×10^{6}
800	3.26×10^{-4}	3.66×10^{-7}	129	0.02	7.69×10^{-7}	48	1.30×10^{6}
900	3.26×10^{-4}	3.66×10^{-7}	138	0.02	8.23×10^{-7}	52	1.22×10^{6}
1000	3.26×10^{-4}	3.66×10^{-7}	174	0.02	1.03×10^{-6}	65	0.970×10^{6}

Table 6.9. 30 wt% AgPAA ink on photo paper/ narrow line (1 mm) (compression) with 0.055 mm print pitch.

No. of bends	Width (m)	Thickness (m)	Resistance (Ω)	Length (m)	Resistivity (Ω.m)	Resistivity/ RBS	Conductivity (s/m)
0	3.26×10^{-4}	3.66×10^{-7}	69	0.02	4.12×10^{-7}	26	2.43×10^{6}
100	3.26×10^{-4}	3.66×10^{-7}	0	0.02	-	-	-

Reporting track performance against bending is the norm in testing the ink adhesion /robustness to the different substrates. With these calculations, the performance of the track (resistance) can be plotted against the number of bends and enables convenient comparisons across different substrates (Figures 6.6 and 6.7).

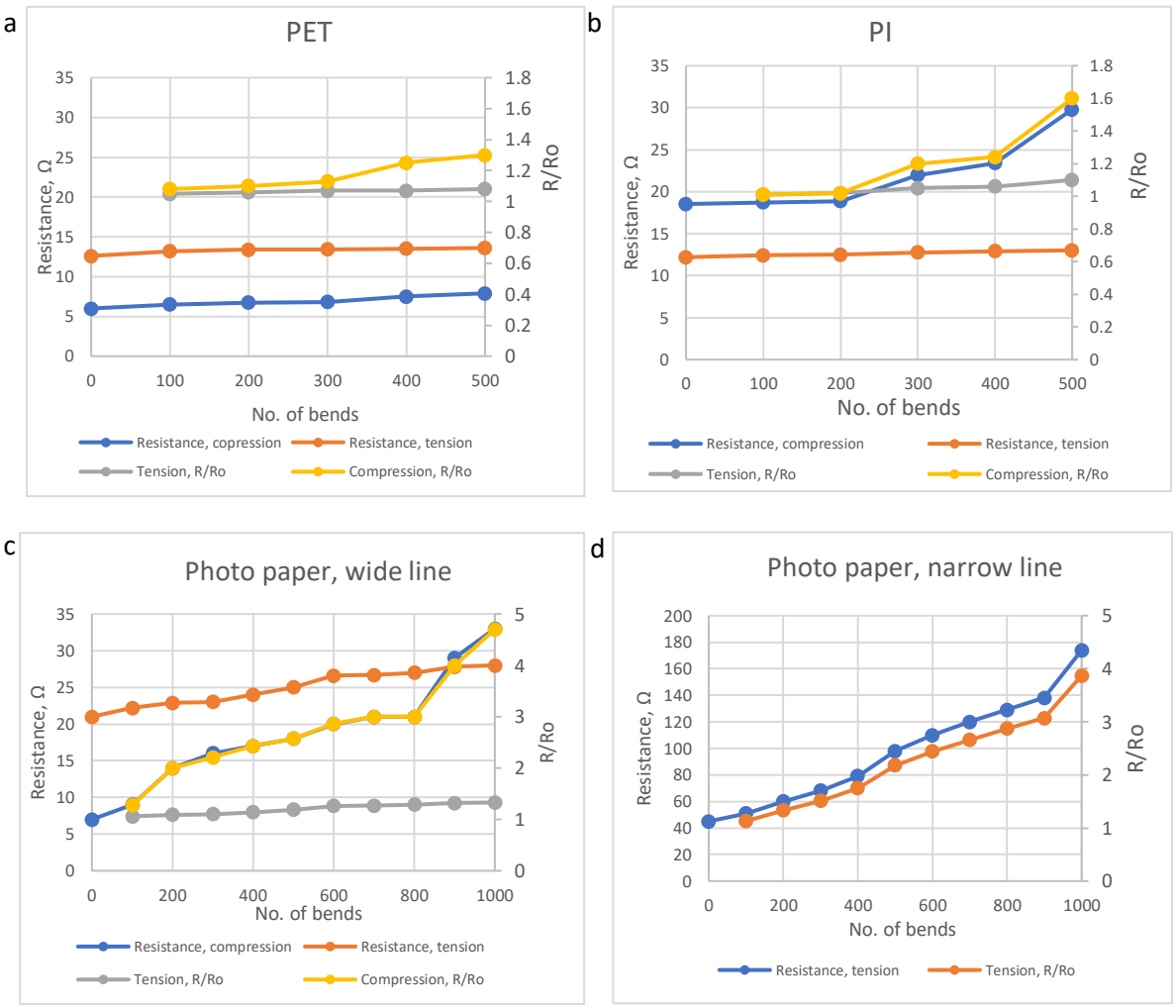

Figure 6.6 The electrical resistance vs the change in resistance between the initial resistance and the resistance after number of bending cycles on (a) PET, (b) PI, (c) photo paper(wide line), and (d) photo paper (narrow line).

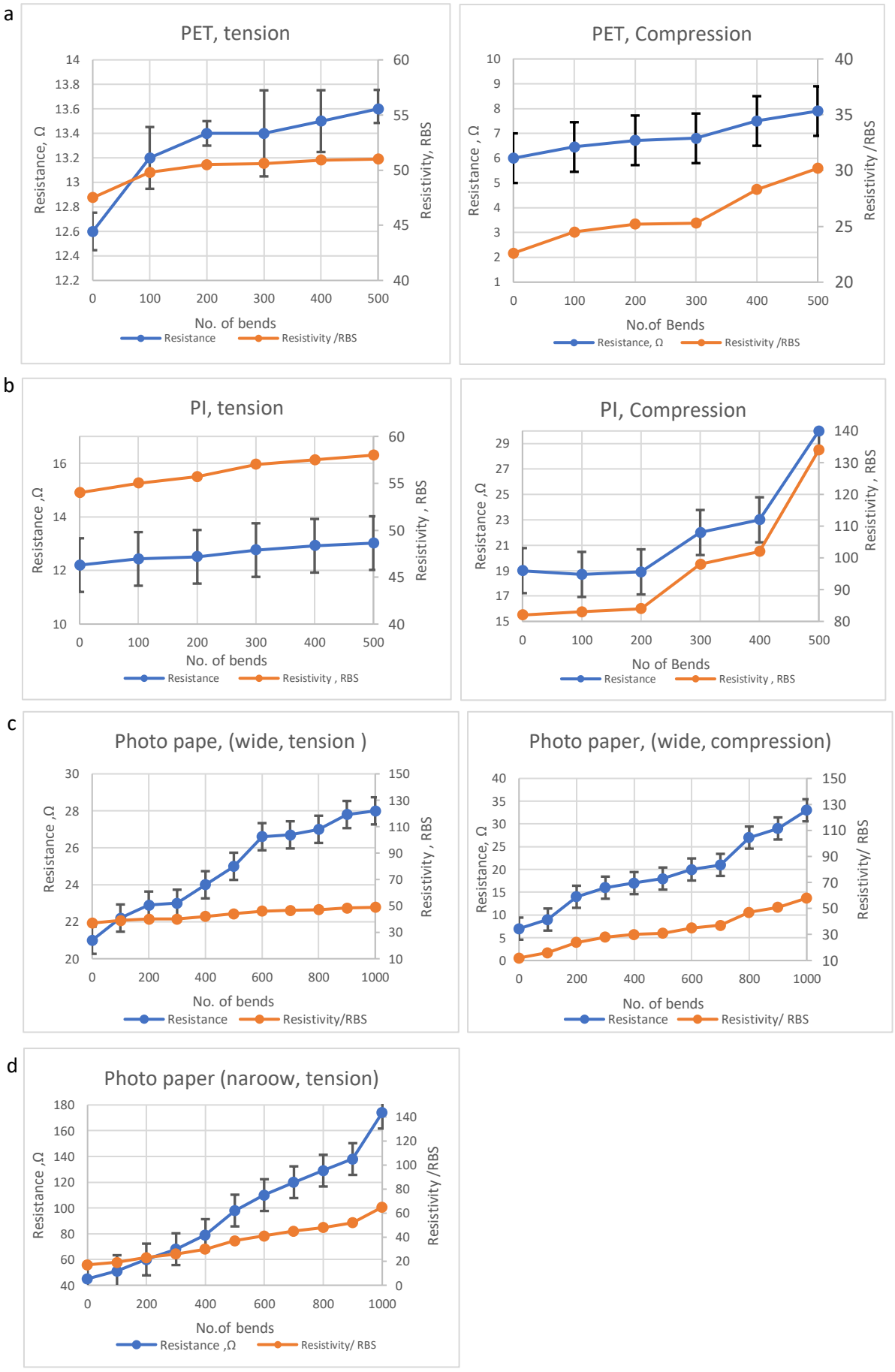

Figure 6.7. The electrical resistance of the printed silver vs bendability on (a) PET (tension, compression); (b) PI (tension, compression); (c) photo paper (wide line, tension, compression); (d) photo paper (narrow line, tension) bending. Error bars show the resistance S.D. for the 5 tracks tested simultaneously side by side in a bending test.

It is important to note that nonuniformities in the sample measurements tend to arise from print history, a different batch of ink or a different day. These variations can have a significant effect on measured properties. Consequently, measurements were repeated three times, and the results were averaged (the mean and standard deviation) represented in Figures (6.7) above. However, as the substrate and overlayer have similar mechanical properties then equal thickness/width will be ensured.

By looking at the tables/ figures above, it is notable that the chloride sintering method has been successfully transferred to plastic substrates (PET/PI) and showed an excellent influence on the printability and sintering afterward. The tables and figures above show the change in resistance and resistivity before and after bending of the 30wt.% AgPAA ink printed patterns under multiple bending cycles. All substrates have similar mechanical properties which means that their thickness and width are equal for the same printed track with repeating bending cycles. We define the change in resistance by R/R_o, where R is the resistance after different bending cycles and R_o is the initial resistance before bending. The mechanical flexibility of the inkjet printed AgNP conductive tracks on PET, PI or photo paper was determined by bending tests. The electrical resistance property (R/R_o) as a function of the number of bend cycles is shown in the figures above.

Typically, the electrical resistance of the printed AgNP tracks increased gradually with repeated bending cycles of the test specimens. This slight increase in electrical resistance comes from cracks that form in the conductive track at the point of bending. Crack formation was obtained due to repeated bending, which caused breaking of the 3D-network and breaking of the interparticle contacts of Ag NP [7].

Particularly, the silver tracks printed on the PET show 1-fold and 1.3-fold increases in electrical resistance in tension and compression bending mode after 500 bending cycles. The resistivity was nearly 51%, and 30% higher than the RBS in tensile and compressive mode respectively after 500 bending times.

On the other hand, the printed AgNP track on PI was also tested for comparison. The conductive track resists bending up to 500 cycles showed a similar increase in resistance as the track on PET 1-fold in tensile mode and 1.6-fold in compressive mode relative to the initial resistance. We observed that the conductive tracks on both substrates (PET and PI) could resist repeated bending

of up to 500 cycles with a slight difference in electrical response. When applying a similar bending mode on printed pattern on PI, the increase in resistivity reached 58% in tensile mode, with a higher increase in compressive mode of nearly 134% compared with RBS.

We then investigated the electrical resistance response further on the printed AgNP-wide tracks on photo paper. It exhibits a good electrical performance over 1000 bending cycles, with only a slight increase in their electrical resistance of 5-fold and 1-fold increase relative to their initial resistance in compressive mode and tensile mode with wide tracks respectively. Photo paper with wide track around 9.516×10^{-4} m showed resistivity higher by 57% of bulk silver by compressive bending and 49% by tensile bending with 1000 bending times and that showed a better ink adhesion compared to PI.

In contrast, the printed conductive narrow tracks on photo paper exhibit 4-fold increases in their electrical resistance relative to the initial, as-printed state, after 1000 repeated bending cycles. However, the conductive narrow track underwent full breakage failure after 100 compressive bending cycles and resistance became infinite.

Obviously, the printed AgNP narrow tracks on the photo paper substrate are much more fragile upon repeated bending when compared with those wide tracks on the PET and PI and photo paper, where a relatively sharp fracture is observed at the fold point on the nanostructured paper after 100 cycles on the narrow track.

A rather large fragile area of the AgNP conductive track around the bend point on the photo paper is related to the narrow-printed track under strain and the smooth photo surface. Also, the repeated bending cycles lead to severe crease formation in the underlying substrates in a direction perpendicular to the printed conductive tracks.

From SEM image observation of wide track on photo paper samples, there is no noticeable crack formation or delamination after 1000 cycles. It is clear that the printed conductive tracks on the photo paper could maintain their electrical function even after repeated bending cycles with a wide track at different bending speeds of 10, 20 and 50 mm/min (image not shown for photo paper and similar image for track on PET was shown Figure 6.8). However, it is observed that Ag film on photo paper with a narrow track in compressive bending encountered

small cracks and slight deformations in the track as shown in (Figure 6.9). Therefore, the resistance was infinite (no conductivity) after 100 times bent, while the same track structure in tensile mode maintained its resistance after 1000 cycles and it was 4 times higher relative to the initial resistance. Likewise, in a study done by Liu Z. *et al*. [18], in the compression, more cracks were formed at the interface between the sintered AgNP printed pattern and the photo paper, and then, damage near the pattern side was caused by the limited endurance of the photo paper substrate after 400 bending cycles.

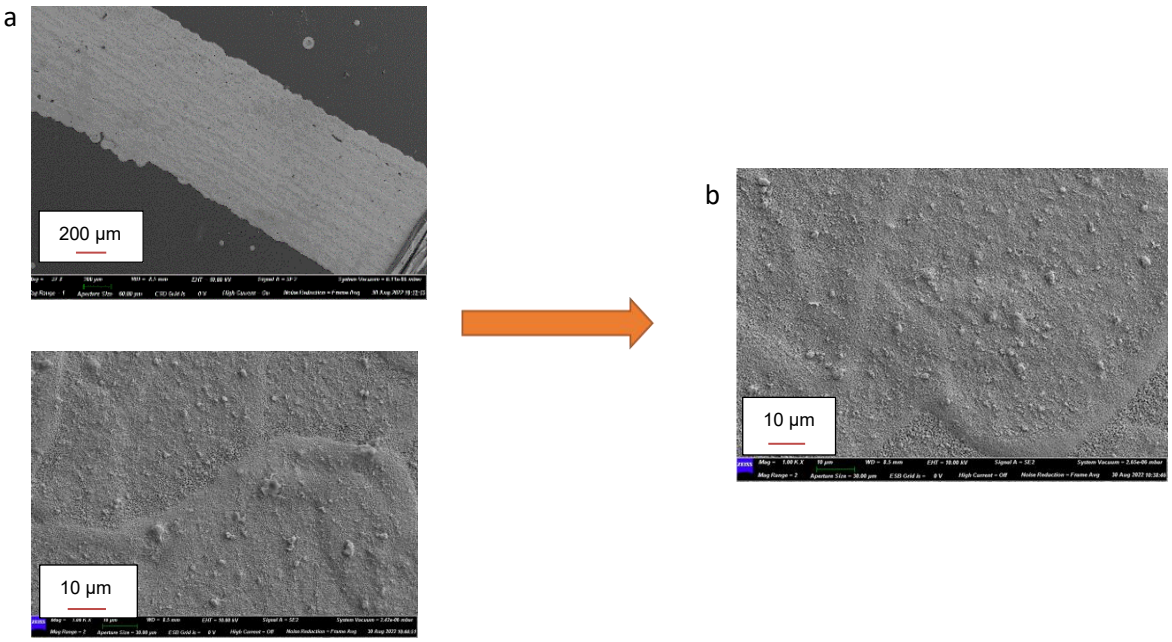

Figure 6.8. SEM images (a) before, (b) after bending test on coated PET.

Before performing the mechanical bending test, the track surface was investigated using SEM, as shown in Figure 6.8 (a), to use as a reference at the end after the bending test. Then, a smooth bending (approximately 20° bending angle), was carried out as presented in Figure 6.2 above. SEM images in Figure 6.8 compare the Ag NP track on PET substrate before and after 500 cycles of bending deformation. The nanostructure maintained the same surface morphology with no observable development of cracks or change of surface roughness after 500 cycles of bending deformation. This indicates that flexible plastic substrate can bear bending up to 500 times and recover with no obvious peeling or cracking.

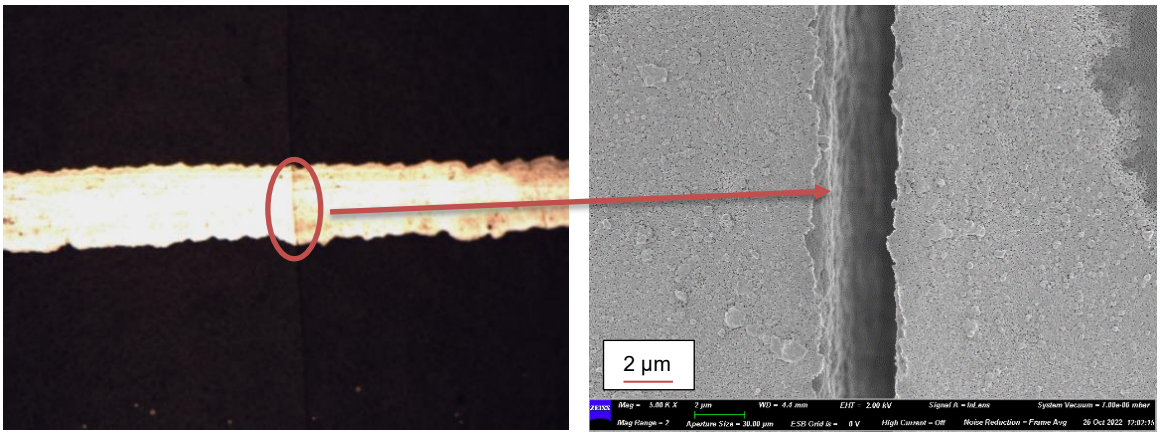

Figure 6.9. SEM image after compressive bending for printed silver track on photo paper, showing a catastrophic crack right across the narrow track.

A similar finding was achieved by other researchers [4], they have printed nanoimprinted gold microstructures (line array, hole array) on PI substrate. They ran bending cycles from zero to 65000 cycles without any sign of any cracks or change of surface roughness afterwards after examining the SEM images before and after. The resistivity values do not show any changes through the course of bending deformation cycles too and that is comparable with our finding.

Stability to multiple bending cycles is a critical characteristic to be used in flexible electronic devices. By reviewing the literature, we have noted that it is not easy to compare the report outcome on the mechanical stability of printed structure because it depends on several factors, like ink composition, adhesion of the various inks to different substrates, thickness of the printed pattern, quality of sinter, etc. Consequently, we will discuss some examples of printed pattern stability and their retention/decreasing of resistivity upon bending.

For instance, in contrast to our work, Nge T. *et al*. [7] have printed AgNP tracks on nanostructured paper made from cellulose and on PI. The experimental width of the AgNP conductive tracks on nanostructured paper (419± 12 μm), PI (399± 9 μm) with a drop spacing of 20 μm was set to print. In contract , we have set the print pitch at 55 μm with a much wider track (952 μm). Firstly, the silver tracks printed on the nano-structured paper showed a good electrical performance after 5000 bending cycles, with a small bending radius of 2.5 mm. There was a slight increase in their electrical resistance with no noticeable crack formation after 5000 bending cycles. After that, more extreme folded states were done for both printed tracks on paper and PI for comparison. The tracks were folded to -180° and returned to 0° and then folded to +180°.The practical results showed that the printed AgNP tracks on the PI substrate are much more fragile upon repeated folding when compared with those on the nanostructured paper. Meanwhile, a relatively sharp fracture is observed at the fold point on the nanostructured paper after 15 cycles, although the PI substrate did not break apart in this instance. They refer the large fragile area of the printed track around the fold point on PI to the yield of the polymer film under strain and the weak support from the smooth PI surface. However, in our work, we coated the PI with a PVOH polymer which obviously enhanced the capacity of the bending strain and bending lifetime and improved the mechanical properties of the sintered patterns [7].

He P. *et al.* [19], have conducted bending tests on printed patterns of graphene and silver on PI, PET, and paper substrates with post-annealing and compressive rolling. They found that the printed graphene patterns on all three substrates exhibit no observable loss in relative resistance (R/R_o) after deformation through various radii of bending from 18 to 2.5 mm and under a constant bending radius after 1000 bending cycles. However, the printed silver patterns show a clear increase in the relative resistance after 1000 bending cycles. By measuring the SEM images, they confirmed that the printed graphene patterns on PI and PET substrates have almost no breakages after the bending test, while some cracks appeared in the paper-based pattern because of the mechanical deformation.

6.5 Conclusion

In this study, we presented a strategy for developing a plastic substrate, which can lead to the high-quality formation and room temperature sintering of the Ag NPs ink patterns. That potentially provides a promising route toward the large-scale fabrication of low-cost flexible printed electronic devices. Using the wire-wrapped coating bars technique, thick and thin polymer layers of PVOH solution with different Cl^- concentrations were fabricated. We found previously that Cl^- can detach the stabilizer from the Ag NPs and enable the coalescence and spontaneous sintering of the Ag NPs. We believe that the approach presented here could be a simple and significant way to fabricate conductive patterns on various substrates at room temperature. They showed excellent adhesion, electrical properties and resistance to peeling and cracking after facing multiple bending cycles.

The PVOH/KCl properties could likely be further tuned to optimise sintering and conductivity, but the work presented here clearly demonstrates a viable approach to transfer spontaneous Cl^- induced sintering at room temperature to more robust flexible plastic substrates of interest in electronics fabrication.

In conclusion, we successfully developed a flexible substrate by transferring the chloride sintering method to PVOH-coated PET or PI plastic substrates to allow spontaneous room-temperature sintering. The morphology, and electrical properties were studied for comparison on PET, PI and photo paper which represent the substrates most commonly used in printed electronics.

In terms of the mechanical flexibility of AgNP conductive tracks after repeated bending tests, the printed AgNP tracks on (PET) plastic substrate showed similar bending resistance performance compared with printed tracks on photo paper after 500 bending cycles, while tracks on PI showed a great performance in tensile bend with less performance efficiency in compressive bend compared with PET and photo paper. This reliability despite repeated bending confirms the potential of PET and PI for use as flexible substrates for printed electronics.

Considering practical application, in the tensile mode with 100 mm/min and a large bending strain, the Ag NP ink patterns exhibited smaller relative R/R_o electric resistance, not more than 2.2-fold the initial resistance in the photo paper

narrow line after 500 bending cycles. Under the compressive mode, the Ag pattern exhibits a lower relative change in resistance about 1.3-fold to the initial resistance.

The resistivity of the printed pattern on PET demonstrated the best performance with a resistivity of 30% to RBS in compressive mode after 500 bending cycles, which was lower than the resistivity of the PI and photo paper.

Notably, our AgNP ink patterns reached a great electrical conductance and showed a good endurance with a bending speed of 100 mm/min, 20^{o}bending angle and 500 bending cycles in plastic substrate and 1000 bending cycles on photo paper and could likely endure more bending cycles although this was not investigated due to time limitations. This finding indicates the potential of plastic substrate and photo paper as a printable material, with the particular aim of producing low-cost disposable and recyclable consumer electronics to reduce the environmental impact.

References

(1) Chen, Y.; Au, J.; Kazlas, P.; Ritenour, A.; Gates, H.; Mc Creary, M. Flexible Active-Matrix Electronic Ink Display. *Nature.* **2003**, *423 (6936)*, 136.

(2) Otte, K.; Makhova, L.; Braun, A.; Konovalov, I. Flexible Cu (In, Ga) Se2 Thin-Film Solar Cells for Space Application. *Thin Solid Films.* **2006**, *511–512*, 613–622.

(3) Komoda, N.; Nogi, M.; Suganuma, K.; Kohno, K.; Akiyama, Y.; Otsuka, K. Printed Silver Nanowire Antennas with Low Signal Loss at High-Frequency Radio. *Nanoscale.* **2012**, *4 (10)*, 3148–3153.

(4) Park, I.; Ko, S. H.; Pan, H.; Grigoropoulos, C. P.; Pisano, A. P.; Fréchet, J. M. J.; Lee, E. S.; Jeong, J. H. Nanoscale Patterning and Electronics on Flexible Substrate by Direct Nanoimprinting of Metallic Nanoparticles. *Adv. Mater.* **2008**, *20 (3)*, 489–496.

(5) Li, C.; Han, J.; Ahn, C. H. Flexible Biosensors on Spirally Rolled Micro Tube for Cardiovascular in Vivo Monitoring. *Biosens. Bioelectron.* **2007**, *22 (9–10)*, 1988–1993.

(6) Tokuno, T.; Nogi, M.; Karakawa, M.; Jiu, J.; Nge, T. T.; Aso, Y.; Suganuma, K. Fabrication of Silver Nanowire Transparent Electrodes at Room Temperature. *Nano Res.* **2011**, *4 (12)*, 1215–1222.

(7) Nge, T. T.; Nogi, M.; Suganuma, K. Electrical Functionality of Inkjet-Printed Silver Nanoparticle Conductive Tracks on Nanostructured Paper Compared with Those on Plastic Substrates. *J. Mater. Chem. C.* **2013**, *1 (34)*, 5235–5243.

(8) Choi, S. J.; Kim, S. J.; Jang, J. S.; Lee, J. H.; Kim, I. D. Silver Nanowire Embedded Colorless Polyimide Heater for Wearable Chemical Sensors: Improved Reversible Reaction Kinetics of Optically Reduced Graphene Oxide. *Small.* **2016**, *12 (42)*, 5826–5835.

(9) Liu, Z.; Ji, H.; Yuan, Q.; Ma, X.; Feng, H.; Zhao, W.; Wei, J.; Xu, C.; Li, M. Nano Oxide Intermediate Layer Assisted Room Temperature Sintering of Ink-Jet Printed Silver Nanoparticles Pattern. *Nanotechnology.* **2019**, *30 (49)*, 1-10.

(10) Shen, W.; Zhang, X.; Huang, Q.; Xu, Q.; Song, W. Preparation of Solid Silver Nanoparticles for Inkjet Printed Flexible Electronics with High Conductivity. *Nanoscale.* **2014**, *6 (3)*, 1622–1628.

(11) Monne, M. A.; Howlader, C. Q.; Mishra, B.; Chen, M. Y. Synthesis of Printable Polyvinyl Alcohol for Aerosol Jet and Inkjet Printing Technology. *Micromachines.* **2021**, *12 (2)*, 1–16.

(12) Tang, Y.; He, W.; Wang, S.; Tao, Z.; Cheng, L. New Insight into the Size-Controlled Synthesis of Silver Nanoparticles and Its Superiority in Room Temperature Sintering. *CrystEngComm.* **2014**, *16 (21)*, 4431–4440.

(13) Gong, S.; Lai, D. T. H.; Wang, Y.; Yap, L. W.; Si, K. J.; Shi, Q.; Jason, N. N.; Sridhar, T.; Uddin, H.; Cheng, W. Tattoolike Polyaniline Microparticle-Doped Gold Nanowire Patches as Highly Durable Wearable Sensors. *ACS Appl. Mater. Interfaces.* **2015**, *7 (35)*, 19700–19708.

(14) Wei, Y.; Chen, S.; Li, F.; Lin, Y.; Zhang, Y.; Liu, L. Highly Stable and Sensitive Paper-Based Bending Sensor Using Silver Nanowires/Layered Double Hydroxides Hybrids. *ACS Appl. Mater. Interfaces.* **2015**, *7 (26)*, 14182–14191.

(15) Kamyshny, A.; Magdassi, S. Conductive Nanomaterials for 2D and 3D Printed Flexible Electronics. *Chem. Soc. Rev.* **2019**, *48 (6)*, 1712–1740.

(16) Gaaz, T. S.; Sulong, A. B.; Akhtar, M. N.; Kadhum, A. A. H.; Mohamad, A. B.; Al-Amiery, A. A.; McPhee, D. J. Properties and Applications of Polyvinyl Alcohol, Halloysite Nanotubes and Their Nanocomposites. *Molecules.* **2015**, *20 (12)*, 22833–22847.

(17) Öhlund, T.; Hummelgård, M.; Olin, H. Sintering Inhibition of Silver Nanoparticle Films via AgCl Nanocrystal Formation. *Nanomaterials.* **2017**, *7 (8)*, 1–13.

(18) Liu, Z.; Ji, H.; Wang, S.; Zhao, W.; Huang, Y.; Feng, H.; Wei, J.; Li, M. Enhanced Electrical and Mechanical Properties of a Printed Bimodal Silver Nanoparticle Ink for Flexible Electronics. *Phys. Status Solidi Appl. Mater. Sci.* **2018**, *215 (14)*, 1–9.

(19) He, P.; Cao, J.; Ding, H.; Liu, C.; Neilson, J.; Li, Z.; Kinloch, I. A.; Derby, B. Screen-Printing of a Highly Conductive Graphene Ink for Flexible Printed Electronics. *ACS Appl. Mater. Interfaces.* **2019**, *11 (35)*, 32225–32234.

Chapter 7. Design and characterization of a simple temperature sensor obtained by inkjet printing on photo paper /flexible substrate results and discusion

To explore the thermal stability and conductive properties of silver tracks produced by inkjet printing of silver nano-ink, a simple low-cost resistive temperature sensor was designed, produced by inkjet printing and characterized by different techniques (profilometer, SEM). The sensor was printed on different substrates (photo paper, polyester, polyimide). A brief explanation of the inkjet printing process / physical characterization will be given, followed by studies of the electrical properties of the sensor during thermal cycling.

Choosing suitable flexible substrates is not an easy task. There are lots of factors that need to take into consideration, such as good flexibility, thermal expansion, transparency, thickness, solvent absorption rate, etc.

The photo paper substrate was chosen in the beginning as it is a well-known material used for inkjet printing because of its high quality of printed patterns and its environmentally friendly recyclable and renewable properties. In order to keep possession of the printed electronic device without losing conductivity and other performance by printing on flexible film, an alternative to paper is to use plastic substrates such as polyethene terephthalate (PET) or polyimide (PI).These plastics offer a low-cost alternative as well as excellent characteristics of flexibility (bending or stretching) of the used substrate while continuing to provide conductive properties [1] (see chapter 6). Besides, they present enhanced thermal stability when exposed to a high temperature (up to 360 °C in PI and long-term use temperature up to 150 °C in PET).

The purpose of this work is to explore the stability of my materials and better understand how they behave against rising temperatures. This is important for the device itself, but it also has much wider importance for understanding the relevance of thermal stability and thermal history if these techniques were used to print electrical interconnects for other devices.

7.1 Fabrication process

This work starts with the synthesis of the silver nanoparticles and their formulation into effective printing inks (following my previous method which is explained in detail in Chapter (2)).

The typical fabrication process of flexible sensors based on inkjet printing technology includes device design, fabrication and characterization. A prototype-designed pattern for a simple resistive temperature sensor device was generated as a bitmap image and was transferred onto the inkjet printer software. This study resulted in the achievement of the final prototype sensor with the characteristics of 4 Ag layers overprinted. The sensor length was 0.189 m on photo paper, with a width of 7.167×10^{-4} m and an average thickness of 4.43×10^{-7} m. In contrast, the printed device on the flexible substrate had a similar physical dimension with 0.099 m length. The length was only half as long as the sensor on photo paper because the quality of printing was lower, and we didn't want to risk a fault that would make the device useless. The physical measurements were done using a mechanical profilometer across the tracks of the Ag-printed devices.

It was reported by Htwe Y. *et al.* [2], that increasing the number of printing layers helped to maintain a connection between the conductive films with fewer pore and gap structures. Consequently, the conductivity improves in the printed patterns if multiple layers are printed. This agreed with results reported in chapter 3.

The fabrication stage starts with substrate pre-treatment in the plastic substrate case, to meet the requirements of the subsequent steps, in order to improve the manufacturing quality and the performance of the flexible sensors without increasing their cost substantially. That includes either physical or chemical modification. Physical modification means changing the physical properties of the substrates like roughness, cleanliness, and water absorption by different technical methods. On the other hand, chemical modification changes the chemical properties of the substrate, such as hydrophobicity, interface energy, or other chemical parameters involved in the subsequent manufacturing process [3]. In the current research, we applied a coating solution to the substrate to improve surface properties by creating a hydrophilic wetting area with PVOH, with different Cl^- concentrations added in order to assist the sintering process.

The inkjet printing parameters were studied to achieve reproducible and well-defined patterns. Printing was performed at a jetting frequency of 350 Hz with a print pitch 55 µm between droplets at ambient temperature in photo paper and fixed at 90 ˚C for flexible substrate. This elevated temperature was found to

give the most consistent prints with good conductivity properties, ideal for the extended homogenous patterns required in this work.

The resulting printed devices were then tested in an extended temperature range (19-130 °C) over 30 min to investigate their stability during temperature change. The maximum temperature should be lower than the stability temperature of the substrate material, reducing the risk of their damage due to substrate degradation (photo paper / PET lower than 130 °C, PI less than 250 °C, and PVOH less than 200 °C before it decomposed) [3]. The electrical resistance of the Ag printed pattern was measured every 1 min during a 30 min period using a digital multimeter, while heating the printed device (attached to an aluminium block to ensure even heating) in the oven. Silver epoxy was used to connect the printed contact pads to wires that were connected to the multimeter using crocodile clips (Figure 7.1). Silver epoxy has its own minor resistivity and does not affect the contact resistance for the printed tracks.

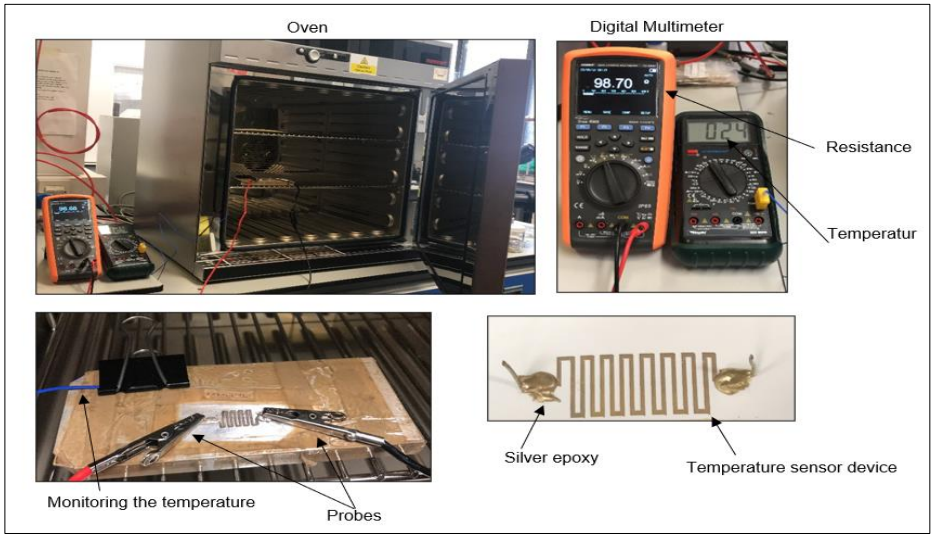

Figure 7.1. Images showing the setup for the temperature cycling experiments. The close-up images show the digital multimeter connected to the printed pads using wire connects attached with conductive silver epoxy. The aluminium block was coated with plastic packaging tape to insulate it electrically and avoid short-circuits.

7.2 Theory and fabrication of temperature sensor inkjet printed on paper substrate

In the beginning of this study, a final prototype of the silver printed lines was discussed. During our previous study, it was determined that the optimal print pitch between droplets for the best homogeneity was 55 µm. Therefore, this led to the achievement of the final prototype sensor with a two-pixel wide zigzag line in between two 3x3 mm conductive pads on each side. From these results, we chose the length depending on the substrate yielding the best results on resistance and fabricated printed temperature sensors with 189 / 99 mm length in photo paper or PET/PI respectively. The target length for the device was estimated using the resistivity values from previous work to calculate the likely resistance, and a length chosen to give a resistance where reasonably small changes could still be measured with adequate precision (1%) using the multimeter. The average width of lines was 7.167×10^{-4} m with thickness about 4.43×10^{-7} m (Figure 7.2).

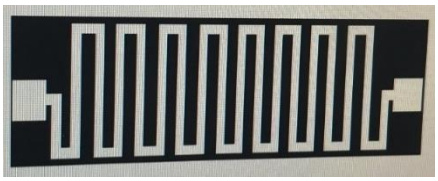

Figure 7.2. Photograph of the temperature sensor design for photo paper.

Generally, the relationship between the measured resistance and the temperature change for a conductor can be expressed as:

$R = R_o (1+ AT+BT^2+CT^3)$ (7. 1)

R_o is the value of the resistance at an initial temperature, T represent the temperature in °C. The relation (7. 1) can be linearized for small temperature variation ΔT around T. This relation becomes:

$R= R_o [1+ \alpha (T-T_o)]$ (7. 2)

The relative resistance variation ($\Delta R/R_o$) is a function of temperature.

The slope of the fitting line is the temperature coefficient of resistance (α) used to indicate the sensitivity of the sensor in unit of $°C^{-1}$, and can be expressed by the following equation:

$$\alpha = \frac{1}{R_o}\frac{\Delta R}{\Delta T} \quad (7.\ 3) \qquad [4]$$

The temperature coefficient of resistance refers to the extent of resistance change per unit temperature variation [5].

Better measurement accuracy of a temperature sensor is achieved if the temperature coefficient of resistance is similar to the standard value of bulk silver ($3.8x10^{-3}$ $°C^{-1}$) [6]. This is shown by a dotted line in the figures that refers to the linearity of the sensor output resistance value as a function of temperature. In other words, it shows the maximum deviation of the ideal fit straight line in the operating temperature range of the sensor.

To monitor the variation of results over time, the temperature was characterized in a range between 19 (room temperature) and 130 °C and the resistance was measured as a function of increasing temperature. This measurement was made within a 30 min time (the heating time of the oven) and repeated 2-4 cycles for the same device then the average was taken (Table 7.1). The utilized temperature / time range in the experiments was chosen depending

on testing done under constraints within the possible temperature window for photo paper.

Table 7.1. Summary of the measured resistance, temperature, and temperature coefficient (with SD in brackets) on photo paper over 30 min time.

	$\Delta R = R - R_o$(Ω)	$\Delta T = T - T_o$ (°C)	α (°C $^{-1}$)
Cycle 1	23.91	110	2.011x10^{-3}
Cycle 2	24.08	109	1.997x10^{-3}
Average	23.99	109.5	(2.00 ± 0.01)x10^{-3}

At times higher than 30 min at 150 °C, the paper started to turn yellow (Figure 7.3), and that was in a good agreement with the result of Coubat J. *et al.* [7]. Similarly, a study done by Huang Q. *et al.* [8], highlighted some voids and cracks on the surface of the printed Ag film at high temperature (150 °C). To avoid degradation of the paper substrate, lower temperature should be used. Consequently, the time and temperature were defined to a maximum temperature of 130 °C for 30 min during this work.

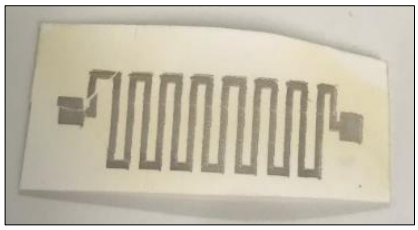

Figure 7.3. Image of a test device on photo paper showing the effect of high temperature on photo paper causing yellowing.

The initial resistance of the Ag temperature sensor on photo paper varies between 108.04 and 110.6 Ω in cycles 1 & 2 respectively. Increasing the T of the sensor, the resistance reached over 130 Ω in both cycles (Table 7.2 & Figure 7.4).The sensitivity of this sensor is 2.004x10^{-3} °C $^{-1}$with a nominal resistance of 109.32 Ω at 19 °C (room temperature). That was lower by a factor of 2 compared with the temperature coefficient of Ag in the bulk material (3.8x10^{-3} °C^{-1}).This variation showed a good linearity between 22 °C and 100 °C. However, beyond 100 °C it showed a poor linearity behaviour of the sensor, and this might be explained by the paper stability limitations when the temperature increases too far. It may also be due to material changes to the silver track. With the continuous

increase in temperature, the kinetic energy of the electrons inside the metal increases, thereby increasing the resistance of the metal material [7].

Table 7.2. Summary of the assessment of electrical properties of a temperature device on photo paper.

Width (m)	Thickness (m)	Resistance (Ω)	Length (m)	Resistivity (Ω.m)
7.17 x10^{-4}	4.43x 10^{-7}	133	0.189	2.24 x10^{-7}

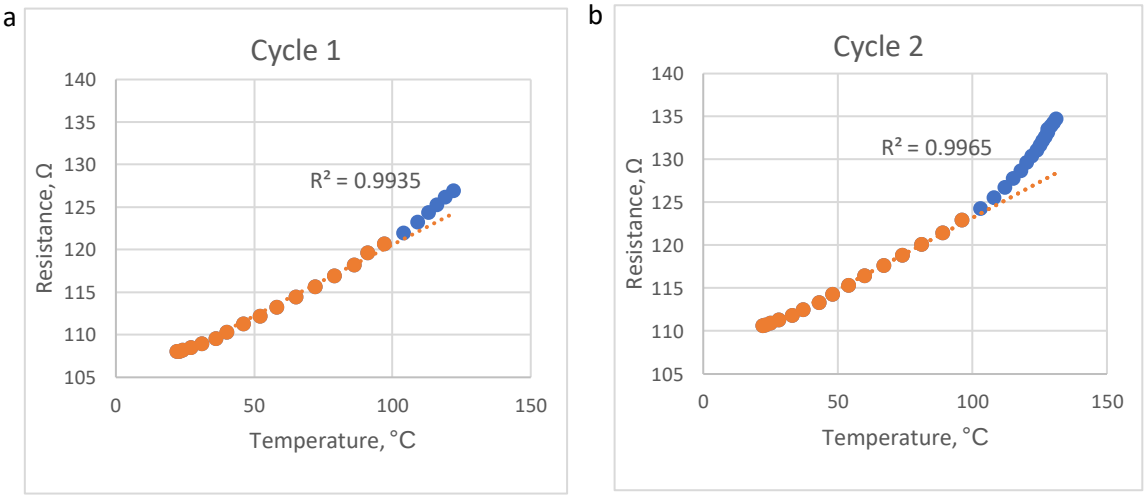

Figure 7.4. Resistance versus temperature (during a 30 min heating ramp) of the printed temperature sensor on photo paper (a) cycle 1, (b) cycle 2. R^2 is the linearity, which was calculated using only the data points up to approximately 100 °C (orange data points on the graph).

As is apparent from the SEM image (Figure 7.5), the temperature sensor printed on paper shows smooth and uniform layers of sintered Ag nanoparticles where the NPs start forming a percolation network all around and that explains its excellent electrical conductivity. However, a slight change happened after being heated. It is possible that residual water or EG bound to the structures are evaporated and the particles are clustered into small agglomerates and uneven track surfaces can be observed from initiating the fusion of Ag NPs.

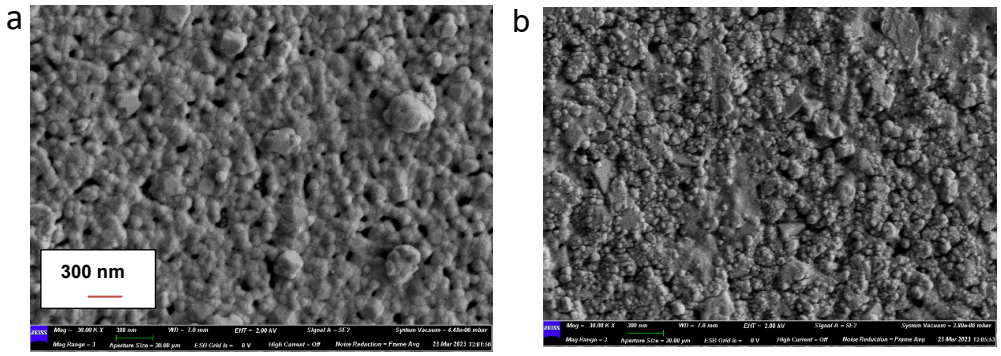

Figure 7.5. SEM images of printed temperature sensor on photo paper (a) before heating, (b) after heating in oven for 30 min.

More than one sensor was tested in order to confirm its stability. All tested sensors on one type of substrate showed very similar behaviour, so only one of these sensors is presented here in detail [9].

An overview of the characteristics of all tested sensors between 20 °C and 130°C on photo paper are summarised in Table 7.3.

Table 7.3. Overview of the characteristics of all tested sensors on photo paper.

Sensor	R_o in Ω	α ($°C^{-1}$)
1	102	1.06×10^{-3}
2	82	1.74×10^{-3}
3	114	1.40×10^{-3}

Clearly, the R_o of all fabricated sensors varied, even though all sensors had been designed, printed and heated in the exact same way. As a result, R_o needs to be determined separately. This can be explained by many different factors such as, the change in ink composition over time, evaporation of solvents, printhead is prone to degradation over time and that could cause clogging of nozzles, resulting in different drop size, so affecting the amount of conductive ink that is deposited [9]. Despite this variation, however, the alpha value was slightly consistent which are about 3/10, 1/2, and $2/5^{th}$ that of bulk silver. The absolute value can be compared with 3.8×10^{-3} $°C^{-1}$ for bulk silver, indicating that the

somewhat porous sintered structure changes resistance with T less than bulk silver.

Shen W. *et al.* [10] printed AgPAA ink 14 times on Kodak photo paper and then dried it at room temperature. The resistivity of the printed pattern was $8x10^{-8}$ Ω.m and by increasing the sintering temperature to 180 °C for only 15 min the resistivity decreased to 3.7 $x10^{-8}$ Ω.m. This indicates that room temperature sintering was incomplete - maybe because it was quite a thick layer and chloride from the paper did not fully diffuse and assist the sintering. It is possible that the Kodak paper has less chloride ion [discussed previously; see chapter3].

7.3 Resistive temperature sensor on PVOH/KCl coted polyester substrate (PET)

To characterize the temperature sensitivity (α) of our printed temperature sensor on coated PET substrate, the devices first had to be produced. The substrate temperature was fixed at 90 °C while printing. Printing multiple layers cause substantial ink ejection on the substrate, which results in the spreading of ink. Printing at a higher temperate helps the removal of solvent from the multilayer printing allowing it, to form a conductive pattern without line merging. It does, however, mean that the devices were exposed to a somewhat higher temperature than the paper devices, which might lead to some differences in sintering beyond those that might have occurred due to the change of substrate surface alone. The printed devices on PET film were treated in two different ways. Some were tested directly after printing under a change in temperature over time and the other devices were heated for 1 h at 190 °C in an oven to enhance ink stability (sintering) after printing and evaporate any excess solvent before testing. This would hopefully allow nanoparticles to fuse with fewer pores to obtain improved track density, stability and linearity. It is made possible by the greater thermal stability of PET.

As mentioned above, the change in resistance as a function of temperature can be approximated linearly as shown in equation [7. 1], Table 7.4. For this purpose, a True RMS Datalogging multimeter (TENMA, 72-3540) was employed for resistance measurements.

Table 7.4. Summary of the measured resistance, temperature, and temperature coefficient on PVOH/PET substrate over 30 min time.

	$\Delta R = R\text{-}R_o\ (\Omega)$	$\Delta T = T\text{-}T_o$**(°C)**	α **(°C $^{-1}$)**
Cycle 1	7.89	88	7.95 x10^{-4}
Cycle 2	9.57	111	7.91 x10^{-4}
Cycle 3	7.42	84	8.25 x10^{-4}
Average	8.29	94.33	(8.03 ± 0.186) x10^{-4}

All sensors were measured in the temperature range between (20 °C ≤137 °C), however, there was a sharp increase in resistance above 100 °C for photo paper. The resistance went down above120 °C for plastic substrate. To be consistent, the only results up to 130 °C are presented. We can infer that the higher temperature improves sintering, and reduces resistance and resistivity as a result. This would be consistent with the reduced starting resistance for cycles 2 and 3 in each sensor on plastic substrates.

During the test, the sensor on coated polyester (PET) shows a good response to temperature increases between 20 and 100 °C without substrate distortion. The resistance obtained at T_o was 112.72, 108.93 and 107.09 °C in cycles 1, 2 & 3 respectively. This sensor exhibits a temperature sensitivity of 8.038 x10^{-4} °C $^{-1}$ which is about 1/5th that of bulk silver.

The resistivity was higher by 24 times than the value usually reported for bulk silver (1.59x10^{-8} Ω.m) (Table 7.5) and was higher compared with the Ag sensor printed on photo paper that was just 14 times higher than RBS.

Table 7.5. Summary of the assessment of electrical properties of temperature device on coated polyester (PET).

Width (m)	**Thickness (m)**	**Resistance (Ω)**	**Length (m)**	**Resistivity (Ω.m)**
7.17 x10^{-4}	4.43 x10^{-7}	118	0.099	3.78 x10^{-7}

Plots of resistance versus temperature for temperature sensors on PVOH/ PET are shown in Figure 7.6. Clearly, the resistance-temperature curves show good linearity over time in all cycles.

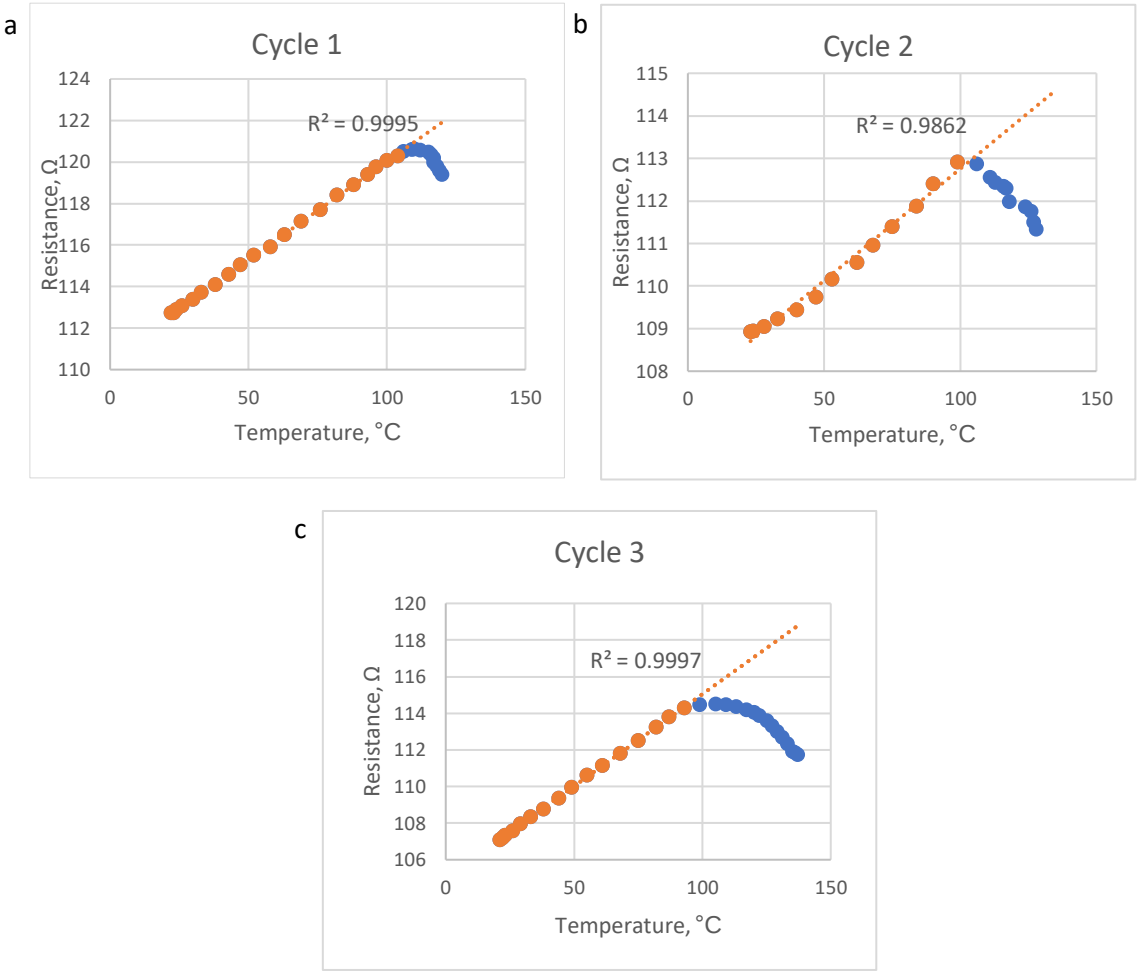

Figure 7.6. Resistance versus temperature (during a 30 min heating ramp) of the printed temperature sensor on PVOH/PET substrate (a) cycle 1; (b) cycle 2; and (c) cycle 3. R^2 is the linearity, which was calculated using only the data points up to approximately 100 °C (orange data points on the graph).

7.4 Resistive behaviour of pre-heated temperature sensor on PVOH/PET substrate

Table 7.6. Summary of the measured resistance, temperature, and temperature coefficient for pre-heated temperature sensor on coated polyester (PET) over 30 min time.

	$\Delta R = R\text{-}R_o(\Omega)$	$\Delta T = T\text{-}T_o$**(°C)**	α **(°C $^{-1}$)**
Cycle 1	3.64	99	1.42×10^{-3}
Cycle 2	3.94	101	1.53×10^{-3}
Cycle 3	4.02	102	1.56×10^{-3}
Cycle 4	3.95	102	1.54×10^{-3}
Average	3.88	101	$(1.51 \pm 0.063) \times 10^{-3}$

Table 7.7. Summary of the assessment of electrical properties of the pre-heated temperature sensor on PVOH/PET substrate.

Width (m)	**Thickness (m)**	**Resistance (Ω)**	**Length (m)**	**Resistivity (Ω.m)**
7.17×10^{-4}	4.43×10^{-7}	29	0.099	9.30×10^{-8}

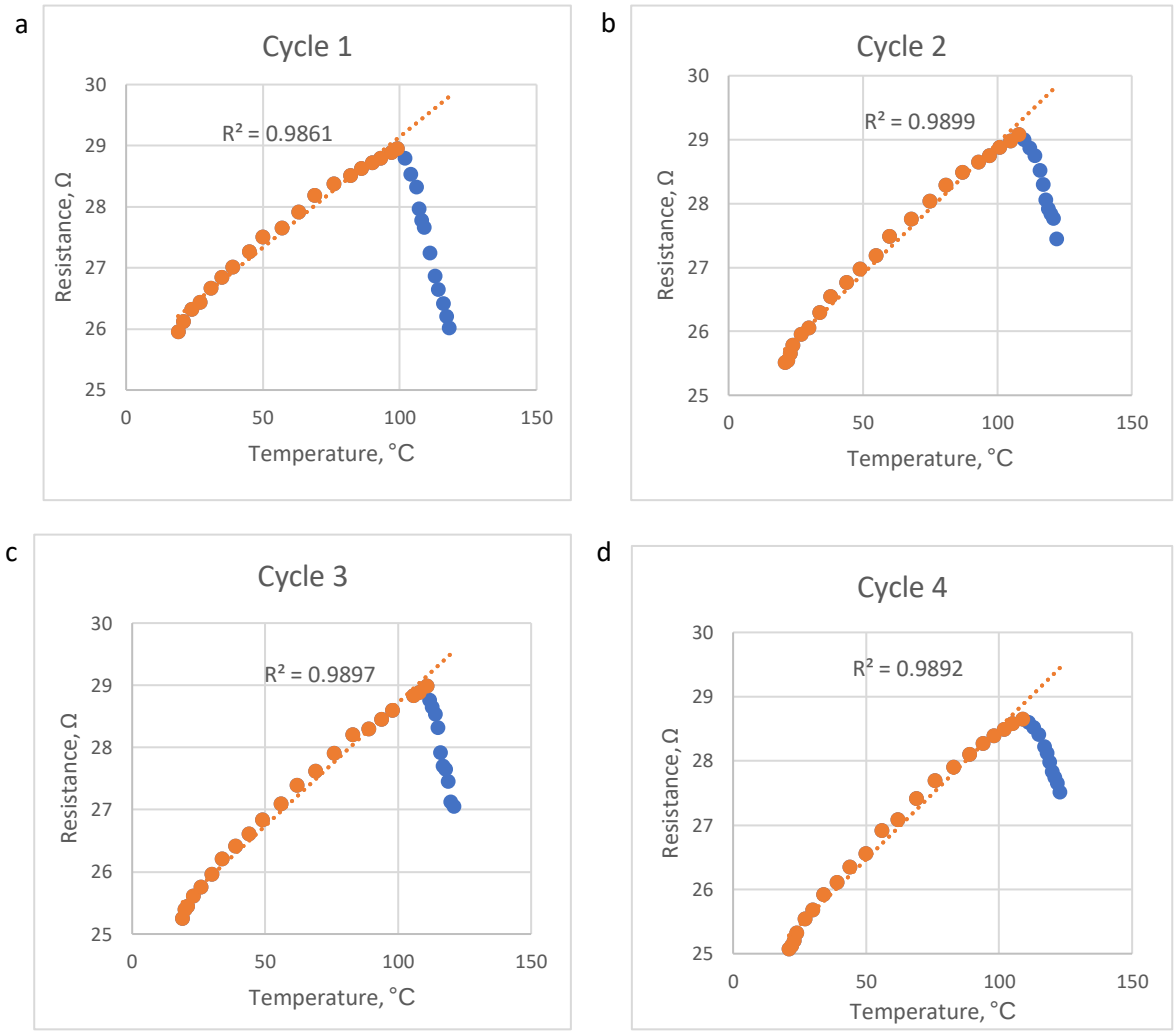

Figure 7.7. Resistance versus temperature (during a 30 min heating ramp) of the pre-heated printed temperature sensor on PVOH/PET substrate (a) cycle 1; (b) cycle 2; (c) cycle 3; (d) cycle 4. R^2 is the linearity, which was calculated using only the data points up to approximately 100 ºC (orange data points on the graph).

Obviously, the measurement of the pre-heated sensor on coated PET shows a good near-linear behaviour over time with the same starting resistance about 25 Ω in each cycle. Comparing to bulk silver resistivity, it is 6 times higher than bulk silver, in contrast to the non-pre-treated sensor on PET, which was 24 times worse. That is acceptable and comparable to other research [11] based on the thermal behaviour of printed silver citrate conductive ink on PET substrate. The electrical resistivity of the printed patterns on PET substrate cured at 150 °C for 50 min showed a decrease from $7x10^{-7}$ Ω.m to $1.7x10^{-7}$ Ω.m and that was approximately 11 times RBS [11].

Besides, the temperature sensitivity about $1.512x10^{-3}$ °C $^{-1}$, this is roughly double the value for non-pre-treated devices on PET. We believe this increase in temperature coefficient can be explained by increasing the exposure time to a high temperature which occurred twice in this case, before and after heating. That is enough to enlarge the grain size and to reduce the lattice defects. This produces a much more notable reduction of resistance (R) and gives rise to an enhanced temperature coefficient [12].

Wang S. *et al.* [5] reported a resistive flexible temperature sensor fabricated on polyethylene terephthalate (PET) substrates with silver nanoparticles-based ink using an inkjet printer. The temperature sensor with a droplet spacing of 20 µm and curing condition of 150 °C for 30 min showed a high sensitivity of 0.084 $°C^{-1}$ with high linearity over time. Their temperature sensor has a much higher sensitivity compared with our device, presumably due to their device having very different preparation conditions, including the printing parameters and the pre-conditioning. These process parameters affect the surface morphology and the electrical properties of the sensors. The post-processing process was also affecting the performance of the sensors. The PET substrate was treated with an atmospheric plasma machine for 5 min to make the substrate more hydrophilic for bonding the ink on the surface. A five-arm serpentine temperature sensor with an overall size of 10 × 10 mm^2 was designed. The temperature sensors were printed using a microelectronic printer and a heating table was used to measure the electrical properties. Silver pastes were used to connect the ends of the printed temperature sensor. The sensor was encapsulated with PDMS, which was dispensed on the top to protect the sensing layer and the two electrodes. The silicone pre-polymer was heated at 80 °C for 1 h to ensure complete curing. This exemplifies how a device could be improved if the aim was to maximise the performance and robustness of an actual component. In our work the sensors were rather used as a means to study thermal behaviour of the printed materials, so no attempt was made to improve or optimise them as devices.

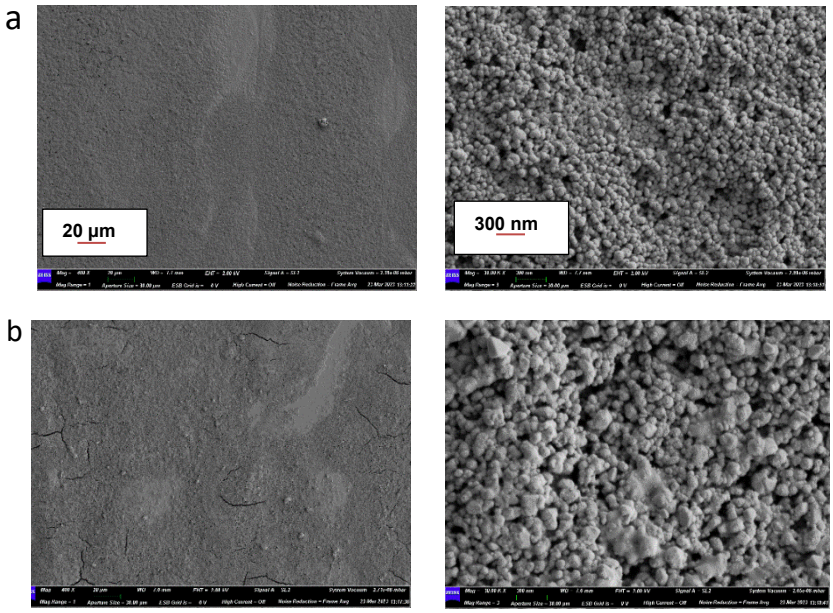

Figure7.8. SEM images of printed temperature sensor on PVOH/PET (a) before heating, (b) after heating in oven for 1h/ 190 °C,then heating cycle for 30 min reaching a temperature of 130-137 °C for testing.

Figure 7.8 shows the SEM images of printed sensors on coated PET before and after heating. It shows how the silver film topography can change and affect the printed pattern conductivity. Clearly, before heating the printed layer was quite homogeneous with small spherical particles visible in the close up and no obvious defects. However, the high temperature has caused multiple small cracks in the printed layer, clearly seen in Figure 7.8 (b). However, the conductivity has improved, whereas the heat-treating improved sintering and particle connectivity overall, even though the cracks might suggest damage to conductivity - better connections in the pathways that do not have cracks occurred. It is also apparent from the close-up image that the particle size has increased significantly on heating, suggesting the fast evaporation rate of solvent led to fast growth of grains and produced large particles eventually. So, substantial fusion and material redeposition happened as a result of the thermal as well as chemical sintering.

Riheen M. *et al*. [13] have optimized the inkjet printing properties by using silver nanoparticles to realize highly conductive and stable printed patterns on polyethylene terephthalate (PET) substrate, using a Fujifilm Dimatix Materials Printer (DMP-2831). In order to investigate its electrical conductivity, the optimum

parameters were adjusted to be $2x10^{-5}$ m print pitch, three overprinted layers and subsequent post-heat treatment of 120 °C curing temperature for 30 min. After curing, the resistivity was found to be $5.25x10^{-8}$ Ωm, that is, three times higher than bulk silver. Further increases in printing layers (quadruple layers) didn't improve the conductivity and it remained almost the same as with three printed layers, with some cracks in the printed track after 120 °C. In contrast , the sensor printed on PVOH/PET substrate in this work with 55 µm print pitch size and 4-printed layers showed a resistivity of $3.78x10^{-7}$ Ω.m and that is higher by 24 times than the value usually reported for bulk silver ($1.59x10^{-8}$ Ω.m) after heating for 30 min at 130 °C. likewise, it showed multiple small cracks in the printed layer after heating (see Figure 7.8).

7.5 Resistive temperature sensor on PVOH/KCl coated polyimide substrate (PI)

In order to investigate the influence of rising temperature on silver temperature sensor device stability, the resistance and temperature coefficient measurements have also been carried out using polyimide film as substrate.

Table 7.8. Summary of the measured resistance, temperature, and temperature coefficient on coated Polyimide (PI) (during a 30 min temperature ramp).

	$\Delta R = R\text{-}R_o(\Omega)$	$\Delta T = T\text{-}T_o$**(°C)**	α **($°C^{-1}$)**
Cycle 1	5.35	79	$7.19x10^{-4}$
Cycle 2	5.61	106	$6.24x10^{-4}$
Cycle 3	6.2	109	$7.02x10^{-4}$
Average	5.72	98	$(6.8 \pm 0.51)x10^{-4}$

Table 7.9. Summary of the assessment of electrical properties of temperature device on PVOH/PI substrate.

Width (m)	**Thickness (m)**	**Resistance (Ω)**	**Length (m)**	**Resistivity (Ω.m)**
$7.17\ x10^{-4}$	$4.43\ x10^{-7}$	92	0.099	$2.95\ x10^{-7}$

As can be observed from Tables 7.8 and 7.9, the resistance obtained from the Ag temperature sensor printed on PI varies between 94.25, 84.78 and 81.02 Ω in cycles 1 & 2 & 3 respectively. The trend of reducing resistance for each cycle, suggesting that further thermal sintering is occurring as a result of the treatment history. The resistivity is higher by 18.6 times compared with the value usually reported for bulk silver ($1.59x10^{-8}$ Ω.m) (Table 7.9) and the resistance is measured from 20 °C to137 °C with a relatively linear response between 20~ 120 °C (Figure 7.9). This sensor exhibits a temperature sensitivity of $6.82x10^{-4}$ $°C^{-1}$, which is about $1/5^{th}$ that of bulk silver and that was similar to the sensor on PVOH/PET. Plots of resistance versus temperature for temperature sensors on PI are shown in Fig 7.9.

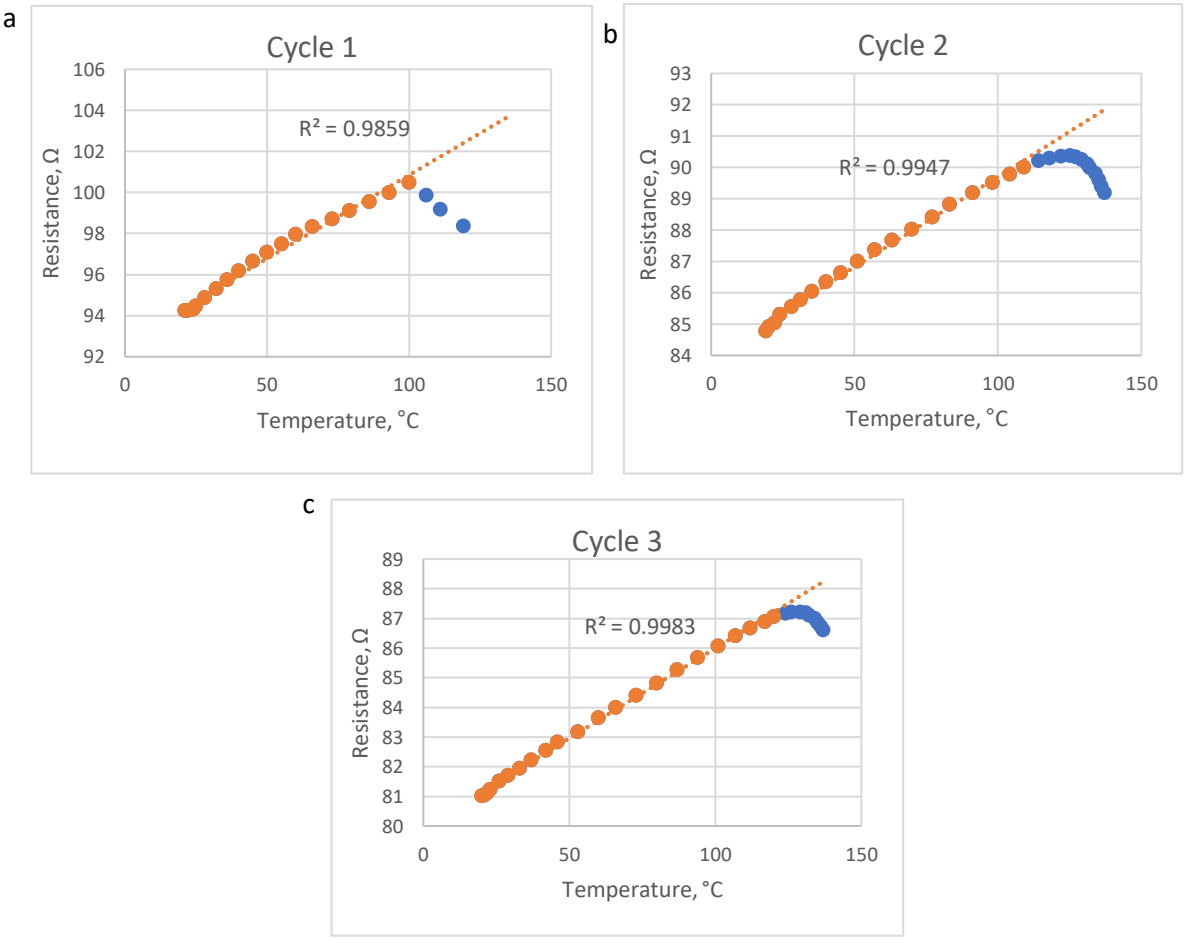

Figure 7.9. Resistance versus temperature (during a 30 min heating ramp) of the printed temperature sensor on PVOH/PI substrate (a) cycle 1; (b) cycle 2; and (c) cycle 3. R^2 is the linearity, which was calculated using only the data points up to approximately 100 °C (orange data points on the graph).

7.6 Resistive behaviour of pre-heated temperature sensor on PVOH/PI substrate

Table 7.10. Summary of the measured resistance, temperature, and temperature coefficient on pre-heated temperature sensor on coated (PI) over 30 min time.

	$\Delta R = R\text{-}R_o$ **(Ω)**	$\Delta T = T\text{-}T_o$ **(°C)**	α **(°C $^{-1}$)**
Cycle 1	26.4	120	$35x10^{-3}$
Cycle 2	3.65	95	$6x10^{-3}$
Cycle 3	12.66	95	$22x10^{-3}$
Cycle 4	6.72	67	$17x10^{-3}$
Average	12.35	94	$(20 \pm 12)x10^{-3}$

It is interesting that the sensitivity (slope of resistance v temp line) decreases with each heating cycle, although cycle 2 is a clear anomaly. This suggests that each cycle improves the sintering and hence conductivity of the tracks, leading to lower sensitivity moving towards that of bulk metal. This sensor exhibits an average temperature sensitivity of 20 $x10^{-3}$ $°C^{-1}$ which is higher than bulk silver by a factor of 5.3, but it transitioned from 9.2 times bulk silver in cycle 1 to 4.5 times bulk silver in cycle 4. This high sensitivity may be due to that the upper layers are less well-sintered and less dense, and hence the track overall shows a higher sensitivity to temperature. This contrasts with the behaviour of tracks on preheated PET, where the sensitivity hardly changed at all from one cycle to the next (although it had a very low sensitivity of only 0.4 times bulk silver).

Table 7.11. Summary of the assessment of electrical properties of the pre-heated temperature device on PVOH/PI substrate over 30 min time.

Width (m)	**Thickness (m)**	**Resistance (Ω)**	**Length (m)**	**Resistivity (Ω.m)**
$7.17\ x10^{-4}$	$4.43\ x10^{-7}$	17	0.099	$5.45\ x10^{-8}$

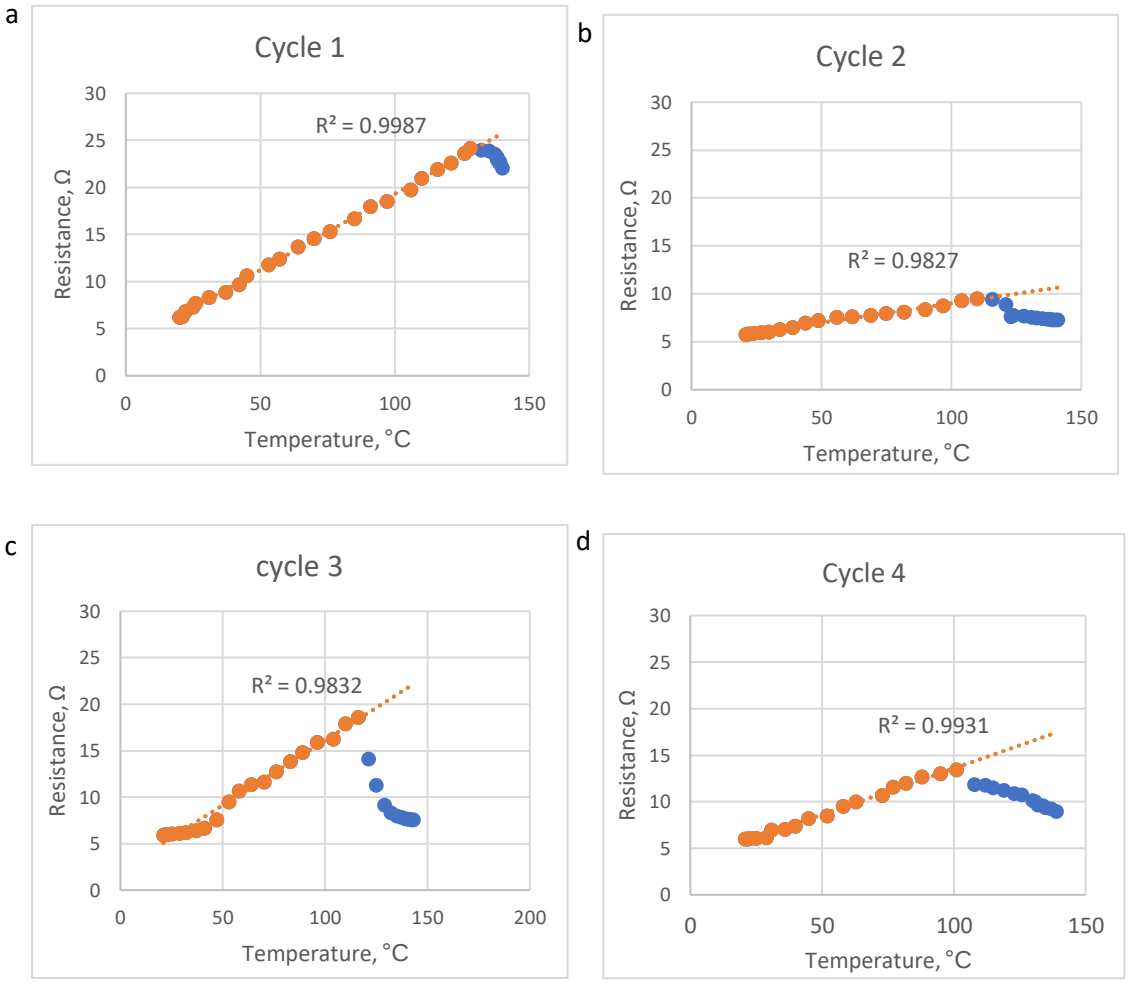

Figure 7.10. Resistance versus temperature (during a 30 min heating ramp) of the pre- heated printed temperature sensor on PVOH/PI substrate (a) cycle 1; (b) cycle 2; and (c) cycle 3. R^2 is the linearity, which was calculated using only the data points up to approximately 100 ºC (orange data points on the graph).

Dankoco M. *et al.* [14] used an organic silver complex ink, inkjet printed on PI (Kapton substrate). The final prototype sensor was printed with a droplet spacing of 90 µm. The printed lines have a width of 306 µm, and thickness of 365 nm. The sensor was characterized at ambient temperature before (just dried on a hotplate at 130 °C for 10 min) to remove solvent and get a continuous structure and after further annealing at 150 °C for 30 min in an oven to obtain a conductive structure. The resistivity for two Ag-printed layers was 5.9×10^{-8} Ω.m. The sensitivity of the printed temperature sensor obtained in the range of 20–60 °C was 2.19×10^{-3} °C^{-1}. They observed a good linear response over time. Compared with our results for the printed sensor on PVOH/PI under similar annealing conditions, the resistivity of our device was about 3.4 times bulk silver with different physical dimensions (width=717 µm, thickness= 443 nm, droplet spacing= 0.055 mm). The sensitivity for 4 printed layers was much higher; about

20 x10^{-3} °C^{-1}. This may be caused by the increasing number of printed layers and the relative difficulty of mobilising the Cl^- ions throughout the layers to achieve efficient and uniform sintering.

The conducted tests demonstrate that all sensors on both flexible substrates PET and PI show a good linear temperature/resistance behaviour, but the multiple cycles of measurement showed a notable difference compared with the data for photo paper. On all substrates the response showed good linearity up to 100 °C, but beyond this temperature there was an obvious deviation from linearity. For photo paper the resistance went up, suggesting the higher temperatures were causing some material damage (e.g. cracking or voids forming). This led to a higher starting resistance in subsequent cycles. For the plastic substrates, the curve bent downwards at higher temperatures, suggesting that the track became better sintered and more conductive as a result of the higher temperature. This resulted in the starting resistance being reduced for subsequent cycles. The size of the change became smaller with more cycles, suggesting that the material was progressively equilibrating towards a stable structure.

However, the pre-heated devices that were printed on PI/PET showed much lower resistance. This is attributed to the heat treatment, as printed films on the PI /PET substrates sometimes show distinct layered morphology, holes etc. Heating the film, however, results in the elimination of water /solvent which in turn destroys the layered pattern and a denser printed track result. Thus, the conductivity improves, and resistance becomes lower. By forcing the material changes due to heating using one high temperature heating step, the gradual changes seen with the unheated samples from cycle to cycle were not really apparent and the starting resistance returned almost to the same value each time.

Figure 7.11 displays the SEM images of the printed Ag pattern before and after heating in an oven. It is clear that the layers of the printed Ag NP are disrupted by cracking all over the surface, both before and after heating. The cracks are quite small and fine before heating, but after heating they are large and prominent, looking like contraction cracks from drying mud. The close-up image also reveals major changes, with the small spherical particles appearing to have “melted” and fused into much larger-scale globular worm-like structures. The cracking did not destroy the conductivity; indeed, in most cases the conductivity actually improved after heating, despite the crack formation. This suggests that the benefit of particle fusion and sintering actually outweighed the damaging effect of the cracks, leading to better conductivity overall.

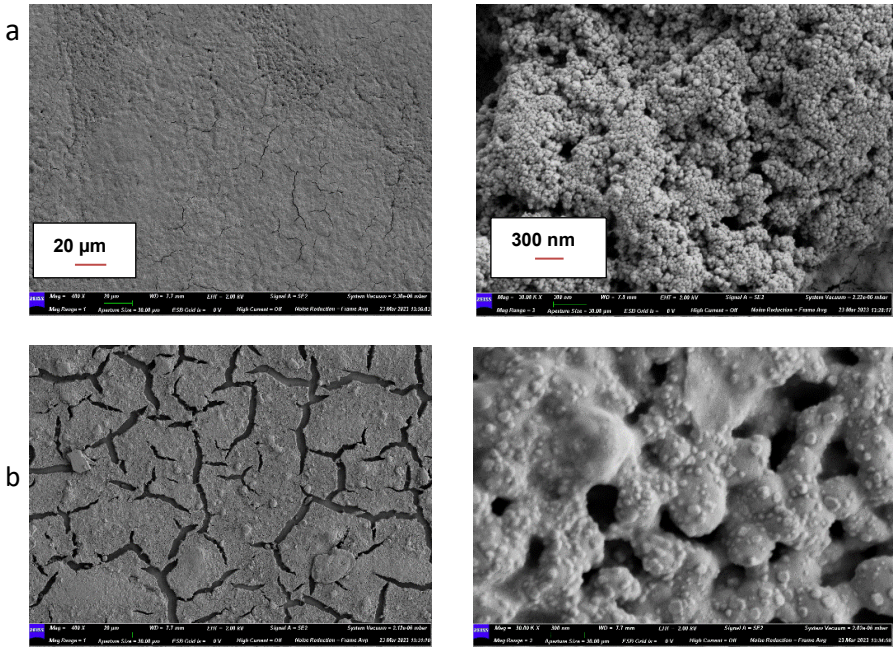

Figure7.11. SEM images of printed temperature sensor on PVOH/PI (a) before heating, (b) after heating in oven for 1h/ 190 °C, then heating cycle for 30 min reaching a temperature of 130-137 °C for testing.

Generally, on comparing SEM images of the Ag track on paper/PET and PI after being exposed to the oven heat, most of the boundaries between the nanoparticles disappeared. However, in PI/ PET , there are clearly some cracks and voids formed within the track. This may be attributed to the coated PVOH layer over the substrate under the printed layer, which could influence the printing process, such as wettability and ink adhesion. It can be seen in Figure 7.12 below,

that the PVOH-coating decomposed at the high temperature and that may worsened the ink adhesion [2].

In contrast, the surface of the printed track on photo paper is highly compacted, and no obvious cracks or voids can be observed, which suggests the tracks have a densely packed structure with most of the nanoparticles fused together. The difference in behaviour between the photo paper and the plastic substrates is interesting, and would merit further investigation, since it is not clear exactly why the materials behave so differently and whether or not the PVOH interlayer is really responsible.

The thermal decomposition of PVOH was studied using thermal gravimetric analysis (TGA) to support the observation above and the results are displayed in fig 7.12. There are three distinct weight loss stages:150-200 °C, 200-300 °C and 350-450 °C.

The first stage occurring around 150 °C is mainly attributed to the physical elimination of strongly bound water. The next weight loss stages noticed were related to PVOH thermal decomposition. The second stage, which occurred between 200 °C and 300 °C, is mainly dehydration caused by the elimination of hydroxyl side groups, which in turn enhances the alignment order of the polymeric chains through the formation of polyene. As a result, the PVOH loses its polar nature and the solubility of the polymer in water decreases too. In the third stage, with a higher temperature, the decomposition of PVOH occurs as the polymer backbone breaks down at 350-450 °C, and carbon and hydrocarbons are produced [15,16,17].

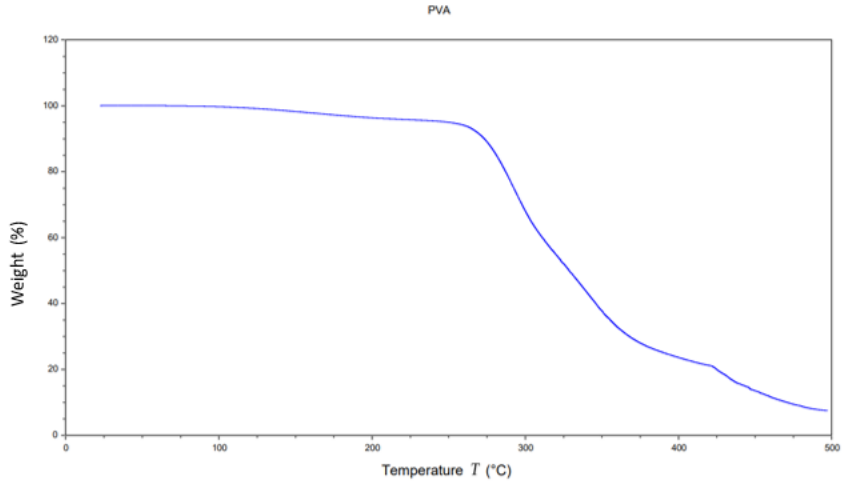

Figure 7.12. Thermogravimetric analysis for polyvinyl alcohol.

The adhesion between the pattern and the substrate is an important factor to ensure the stability and service life of the flexible sensor. Through my study of the nano-silver film performance (such as resistance), the results showed that the chemical sintering was effective in photo paper and showed an optimal resistance about two times the RBS. However, there is a certain problem that has been shown in the case of printing on PET/PI. After drying at room temperature, some inks still need post-processing to obtain the final conductive structures or functions as they showed a high resistance in the range of kΩ/MΩ in some films, depending on the printing quality. In this case, two convenient and intuitive methods were proposed to alleviate this problem. Firstly, some of the PVOH-coated PI/PET substrates were pre-heated in the oven for 2 h at 200 °C, then the device was printed over the substrate. This high-temperature pretreatment was to make sure that any chemical changes to the PVOH film had already occurred before the tracks were printed, to avoid the gradual change during temperature cycling that I have observed. This was a good hypothesis/strategy, but obviously, the changes made the surface much more hydrophobic (elimination of OH groups), so the ink did not then stick, and it was easy to wipe the printed film off (Figure 7.13 (a)). Secondly, the other devices were printed on non-heat-treated PI/PET substrate then heated afterward for (1h/190 °C) and that showed a downward trend from KΩ/MΩ to ohm, so the sintering temperature/time has a great impact on its resistance and the final conductivity and uniformity.

Therefore, from this exploration of the optimal resistance, the results indicate that this would not also cause partial decomposition/rearrangement of the PVOH (referring to the TGA result). We presume the difference here is that the PVOH and the PAA from the ink could interact with one another (e.g. ester formation), which might covalently link the ink layer and the PVOH layer, leading to really GOOD adhesion. In contrast, poor adhesion happens when the PVOH is heated first, and the ink applied later (without heating). It also allows the ink to be printed normally on a nice hydrophilic PVOH layer, where it spreads and dries well, though it seems that maybe the Cl^- is not diffusing and sintering the layers well (since the resistance was initially k-ohm).

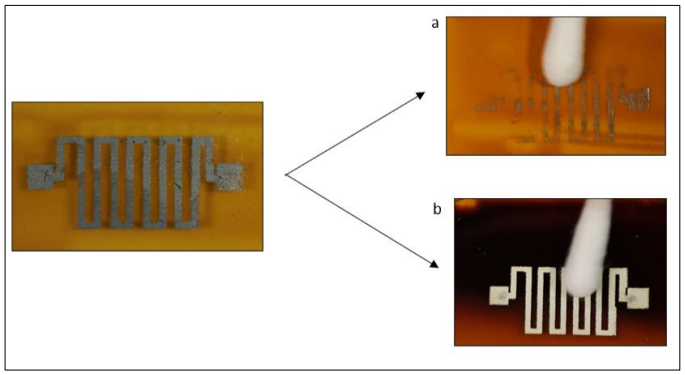

Figure 7.13. Images of Ag printed device on coated PI substrate (a) printed device on pre-heated PI/PVOH substrate, (b) printed device on non-heat-treated PI/PVOH, substrate then heated afterwards.

Infrared absorption spectra of PVOH coated PET/PI were obtained with a Bruker Vertex 70 FT/IR spectrometer fitted with a special diamond ATR attachment at room temperature. Spectra were collected at a resolution of 4cm^{-1} at wavenumbers between 500 cm^{-1} and 4000 cm^{-1}. The IR absorbance spectra of PVOH on PET / PI before and after heating exhibited characteristic bands of stretching and bending vibration of the functional groups (see Figure 7.14 and explanation below). That may explain their similarity after printing and supports the observations obtained from the practical work and TGA study. The selected PVOH has a degree of hydrolysis of 98-99% [17].

The present study clarified that after coating the PET/PI film with polyvinyl alcohol, all substrates showed only the characteristics of PVOH film and the vibrational frequencies of absorption bands in the IR spectra confirm that. This demonstrates that the PVOH layer is" thick" compared with the evanescent field penetration depth of the single-pass diamond ATR crystal (i.e.,>~1/3 of the IR wavelength). This is to be expected for the coated films, which should be in the region of 100 μm thick, based on the coating bar and solid content of the polymer solution used. The top coatings contained (10 w%) polyvinyl alcohol solution, 0.1 M KCl as a sintering agent and the wire diameter (1.27 mm) (100 μm) wet film deposit, respectively. The dry thickness is determined by the solid concentration of the coating solutions; ~ 1/10 of wet film thickness.

During the thermal decomposition of the PVOH film, some changes in its IR spectra are observed Figure 7.14(b). Clearly, there are changes happened in

the bands' intensity, position, and new absorption bands. The table / figure below shows the most characteristic bands of PVOH and their respective assignment.

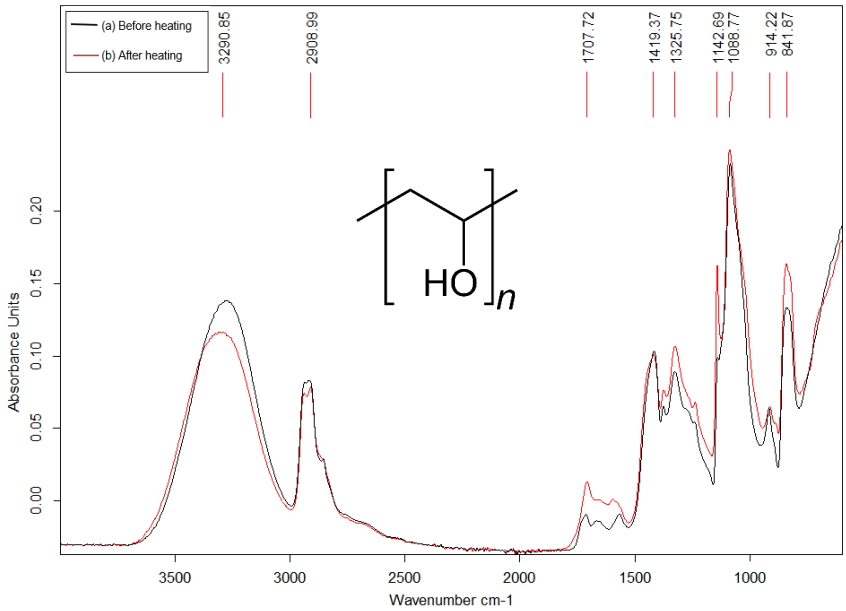

Figure 7.14. FT-IR spectra of PVOH coated on PET /PI film (a) spectrum of the sample before heating, (b) after heating for 1 h, 190 °C.

Table 7.12 Assessment of IR spectroscopy functional groups of PVOH coated on PET /PI film before and after heating.

Absorption frequency (cm^{-1})	**Vibration mode**	**Functional group**
3290	O-H	Alcohol
2920	C-H stretch	alkyl
2857	O-H stretch	of -COOH
1707/1096	C=O/ C-O	Vinyl acetate (ester)
1668	C=C	polyene
1088	O-H	Secondary alcohol
1142	C-O	Crystallinity
1378	CH_2 wagging	CH- and CH_2 aliphatic bending groups
1325	-C- O	C-O stretch
916-841	-CH2-	Deformation vibration

The assignments given in Table7.12 will be discussed in more detail below: Initially, a very strong broad band is observed from 3000-3600 cm^{-1}, which may

be assigned to O-H stretching due to the strong hydrogen bond of intramolecular and intermolecular type in PVOH. This is similar, but with less intensity and a slight shift to longer wavenumber for the heated coated substrate. This shift is usually associated with greater order and crystallinity in carbohydrates and is probably indicative of similar behaviour here.

The absorption band at 1707.72 cm^{-1} -1096 cm^{-1} indicates the presence of the C=O and C-O of the remaining nonhydrolyzed vinyl acetate group in the virgin PVOH. However, after heating a new peak at 2857 cm^{-1} for stretching of acetic acid (-COOH) showing possible ester cleavage but retention (e.g. through strong H-bonding) of the acetic acid within the heat treatment. There is also a band at 1378 cm^{-1} due to CH_2 wagging and at 1328 cm^{-1} due to -C-H- and O-H bending in both spectra of PVOH with more intensity after heating [17].

There are isolated and conjugated C=C bonds appearing with more intensity in the vicinity of the C=O group after heat treatment because of the elimination of water and formation of PVOH chains with a mono-ene or poly-ene structure. The absorption bands with maxima at 1088.77 cm^{-1} and 1330 cm^{-1} can be referred to O-H deformation and C-O valence bond vibrations of secondary alcohols of which PVOH contains many.

According to [18], the new peak at 1142 cm^{-1} serves as a measure of PVA crystallinity and bands at (914.22/841.87 cm^{-1}) give information about a ratio of syndiotactic and isotactic sequences in PVA, although this will not change upon heating in this case.

In summary, all assignments are consistent with the known structure and composition of PVOH, and the most obvious and likely chemical losses/transformations that might be predicted to occur upon heating i.e., condensation of OH groups to form ethers, elimination of water to form C=C, possible migration of acetate groups towards the outer surface and a general increase in crystalline order and packing. All these processes would increase the hydrophobicity of the film, compared with the starting PVOH, which is also consistent with observations and printing behaviour [19,20].

This analysis must be based on a definite molecular structure of the coated film, without any signals arising from the underlying substrate layer, so we are

here considering the structure of PET/PI also, to confirm that these features are NOT visible in the PVOH spectrum (i.e. it is “thick” – see above).

The infrared spectrum of polyethylene terephthalate / Polyimide, with the interpretation of some of their features, are listed in the tables below.

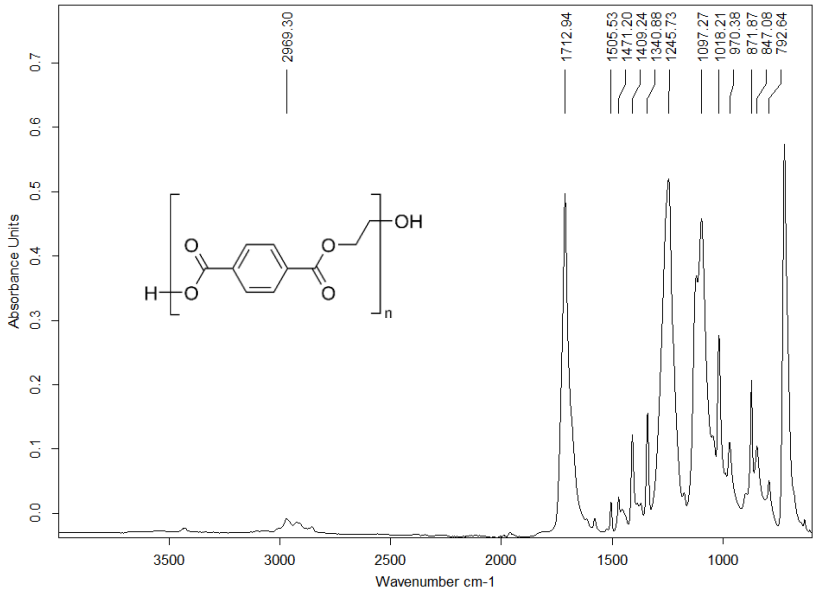

Figure 7.15 FT-IR spectra of polyethylene terephthalate (PET) Films.

Table 7.13. Assessment of IR spectroscopy functional groups PET substrate.

Absorption Frequency (cm^{-1})	**Vibration modes**
2969	C-H aromatic stretching
1712	-C=O bending
1097-1247	O=C-O-CH_2
1340 -1370	-CH_2
871 - 970	C_2H_2O
1505	C=C stretching
1471	CH_2 bending
1409	C-C stretching
1018	CH
847	CH_2 rocking
792 - 813	(C=O) rocking + (CCO) bending + (COC) bending

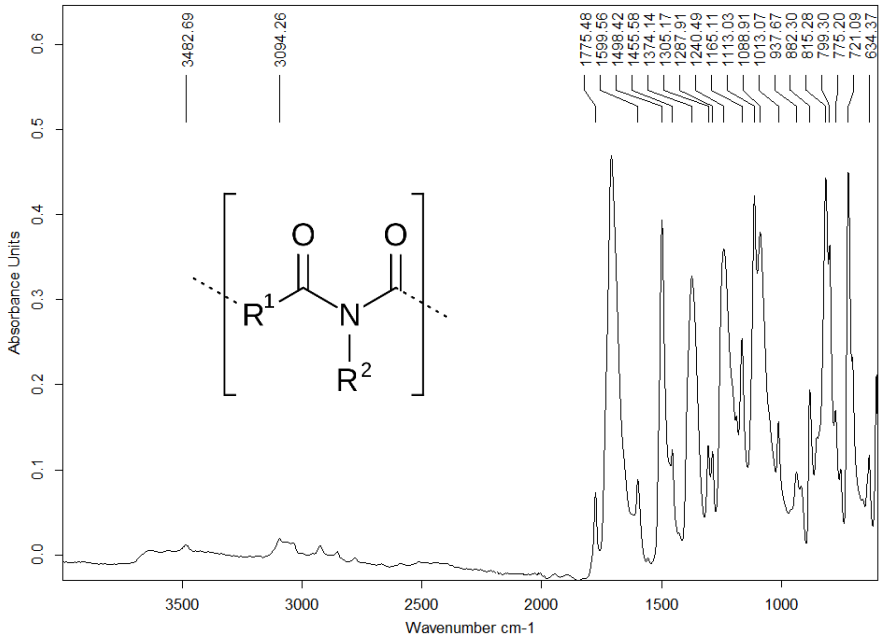

Figure 7.16 FT-IR spectra of Polyimide Films.

Table 7.14 Assessment of IR spectroscopy functional groups PI substrate.

Absorption frequency (cm^{-1})	Vibration mode
3482	Aromatic N-H stretching band
3094	Aromatic C-H stretching band
1775	symmetrical C=O stretching
1720-1740	asymmetrical C=O stretching
1374	C-N stretch
1088	C-H bending
721	C=O bending
1599	N-H bend
1240	C-O-C stretching ether bond

These assignments show the major difference between the infrared spectrum of PET and PI film before and after PVOH coating [21,22,23,24,25].

7.7 Conclusion

In this work, we fabricated a temperature sensor through inkjet printing of Ag NPs layer. The presented sensor has been printed on photo paper or PVOH-coated PET or PI, which is suitable for printed electronic devices and other printed

applications. Inkjet droplet spacing, pre-printing conditions, physical dimensions and post-processing have been investigated to optimize the electrical properties of the sensors.

Comparing the substrates, printing on photo paper results in a much higher resistance and temperature sensitivity compared to PVOH-coated PET or PI considering the coating surface and good line quality. The substrate had a large influence on both the resistance as well as the temperature sensitivity of silver ink.

With the optimized process parameters, the sensitivity of the temperature sensor on photo paper has a high sensitivity of 2.004×10^{-3} °C^{-1} which is lower than bulk silver by a factor of 2 in the tested temperature range of 20 °C -130 °C on photo paper. These sensors possessed a good linearity, fast response time between 22 -100 °C. The R^2 value is (0.9935) in first cycle and (0.9965) in the second cycle at a time of 30 min when the temperature was 100 °C. The reproducibility of the sensor was demonstrated, which is strongly required for manufacturing high quality flexible temperature sensors. The conducted tests demonstrated the performance of Ag printed sensors on PET/PVOH and PI/PVOH after being exposed to the oven heat. Generally, they showed good linear temperature/resistance behaviour. However, the pre-heated devices that were printed on PI/PET showed much lower resistance. This is attributed to the heat treatment, evaporating any excess solvent, fusing nanoparticles and improving stability, linearity and final conductivity.

After heat treatment, the temperature sensor printed on PI/ PET showed clearly some cracks and voids formed within the track. This may be attributed to the coated PVOH layer over the substrate but under the printed layer, because it is chemically altered when heated to high temperature, so that actually, the temperature sensor is still only stable to about 100 °C, even though the base substrates are stable at a much higher temperature. At the temperatures used in the cycling experiments, however, the maximum temperature was barely enough to cause significant changes to the PVOH structure, so the explanation for this observation may lie elsewhere.

References

(1) Maslik, J.; Andersson, H.; Forsberg, V.; Engholm, M.; Zhang, R.; Olin, H. PEDOT:PSS Temperature Sensor Ink-Jet Printed on Paper Substrate. *J. Instrum.* **2018**, *13 (12)*, 1-11.

(2) Htwe, Y. Z. N.; Hidayah, I. N.; Mariatti, M. Performance of Inkjet-Printed Strain Sensor Based on Graphene/Silver Nanoparticles Hybrid Conductive Inks on Polyvinyl Alcohol Substrate. *J. Mater. Sci. Mater. Electron.* **2020**, *31 (18)*, 15361–15371.

(3) Wang, X.; Zhang, M.; Zhang, L.; Xu, J.; Xiao, X.; Zhang, X. Inkjet-Printed Flexible Sensors: From Function Materials, Manufacture Process, and Applications Perspective. *Mater. Today Commun.* **2022**, *31 (103263)*, 1-21.

(4) Sui, Y.; Kreider, L. P.; Bogie, K. M.; Zorman, C. A. Fabrication of a Silver-Based Thermistor on Flexible, Temperature-Sensitive Substrates Using a Low-Temperature Inkjet Printing Technique. *IEEE Sensors Lett.* **2019**, *3 (2)*, 1–4.

(5) Wang, S.; Hu, Y.; Ma, L.; Cui, X.; Peng, Y.; Zheng, J.; Qiao, L.; Ma, H.; Wang, R.; Zhang, H. Preparation and Performance Optimization of Resistive Flexible Temperature Sensors Prepared by Inkjet Printing Method. *Flex. Print. Electron.* **2023**, *8 (2)*, 1-11.

(6) Wan Hassan, W. M. S.; Tamuri, A. R.; Yaacob, M. Z.; Zainal, R. Current and Resistance. *Physics—Problems, Solut. Comput. Calc.* **2023**, 191–208.

(7) Courbat, J.; Kim, Y. B.; Briand, D.; De Rooij, N. F. Inkjet Printing on Paper for the Realization of Humidity and Temperature Sensors. *Solid-State Sensors, Actuators Microsystems Conf. TRANSDUCERS'11.* **2011**, 1356–1359.

(8) Huang, Q.; Shen, W.; Xu, Q.; Tan, R.; Song, W. Properties of Polyacrylic Acid-Coated Silver Nanoparticle Ink for Inkjet Printing Conductive Tracks on Paper with High Conductivity. *Mater. Chem. Phys.* **2014**, *147 (3)*, 550–556.

(9) Zikulnig, J.; Hirschl, C.; Rauter, L.; Krivec, M.; Lammer, H.; Riemelmoser, F.; Roshanghias, A. Inkjet Printing and Characterisation of a Resistive Temperature Sensor on Paper Substrate. *Flex. Print. Electron.* **2019**, *4 (1)*, 15008.

(10) Shen, W.; Zhang, X.; Huang, Q.; Xu, Q.; Song, W. Preparation of Solid Silver Nanoparticles for Inkjet Printed Flexible Electronics with High Conductivity. *Nanoscale.* **2014**, *6 (3)*, 1622–1628.

(11) Nie, X.; Wang, H.; Zou, J. Inkjet Printing of Silver Citrate Conductive Ink on PET Substrate. *Appl. Surf. Sci.* **2012**, *261 (8)*, 554–560.

(12) Jiao, R.; Wang, K.; Xin, Y.; Sun, H.; Gong, J.; Yu, L.; Wang, Y. Enhancing the Temperature Coefficient of Resistance of Pt Thin Film Resistance-Temperature-Detector by Short-Time Annealing. *Ceram. Int.* **2023**, *49 (8)*, 12596–12603.

(13) Riheen, M. A.; Saha, T. K.; Sekhar, P. K. Inkjet Printing on PET Substrate. *J. Electrochem. Soc.* **2019**, *166 (9)*, B3036–B3039.

(14) Dankoco, M. D.; Tesfay, G. Y.; Benevent, E.; Bendahan, M. Temperature Sensor Realized by Inkjet Printing Process on Flexible Substrate. *Mater. Sci. Eng. B Solid-State Mater. Adv. Technol.* **2016**, *205 (11)*, 1–5.

(15) Peng, Z.; Kong, L. X. A Thermal Degradation Mechanism of Polyvinyl Alcohol/Silica Nanocomposites. *Polym. Degrad. Stab.* **2007**, *92 (6)*, 1061–1071.

(16) He, Z.; Xia, Z.; Hu, J.; Ma, L.; Li, Y. Thermodynamic Properties of Polyvinyl Alcohol Binder of Electrically Controlled Solid Propellant. *J. Polym. Res.* **2019**, *26 (9)*, 10–12.

(17) Gohil, J. M.; Bhattacharya, A.; Ray, P. Studies on the Cross-Linking of Poly (Vinyl Alcohol). *J. Polym. Res.* **2006**, *13 (2)*, 161–169.

18) Prosanov, I. Y.; Matvienko, A. A. Study of PVA Thermal Destruction by Means of IR and Raman Spectroscopy. *Phys. Solid State*. **2010**, *52 (10)*, 2203–2206.

(19) Voronova, M. I.; Surov, O. V.; Guseinov, S. S.; Barannikov, V. P.; Zakharov, A. G. Thermal Stability of Polyvinyl Alcohol/Nanocrystalline Cellulose Composites. *Carbohydr. Polym.* **2015**, *130 (5)*, 440–447.

(20) Liang, C. Y.; Krimm, S. Infrared Spectra of High Polymers Part IX. Polyethylene Terephthalate. *Journal of Molecular Spectroscopy*. **1959**, *3*, 554-574 .

(21) Grime, D.; Ward, I. M. The Assignment of Infra-Red Absorptions and Rotational Isomerism in Polyethylene Terephthalate and Related Compounds. *Trans. Faraday Soc.* **1958**, *54*, 959–971.

(22) Mecozzi, M.; Nisini, L. The Differentiation of Biodegradable and Non-Biodegradable Polyethylene Terephthalate (PET) Samples by FTIR Spectroscopy: A Potential Support for the Structural Differentiation of PET in Environmental Analysis. *Infrared Phys. Technol.* **2019**, *101* (5), 119–126.

(23) Dhakshnamoorthy, M.; Vikram, S.; Vasanthakumari, R. Development of Flexible Low Dielectric Constant Polyimide Films Based on Iso-Propylidene , Aryl-Ether Linked Dianhydride / Diamine. *Int. J. Sci. Eng. Res.* **2012**, *3 (5)*, 5.

(24) Diaham, S.; Locatelli, M. L.; Lebey, T.; Malec, D. Thermal Imidization Optimization of Polyimide Thin Films Using Fourier Transform Infrared Spectroscopy and Electrical Measurements. *Thin Solid Films.* **2011**, *519 (6)*, 1851–1856.

(25) Guerra, G.; Choe, S.; Williams, D. J.; Karasz, F. E.; Macknight, W. J. Fourier Transform Infrared Spectroscopy of Some Miscible Polybenzimidazole/Polyimide Blends. *Macromolecules.* **1988**, *21 (1)*, 231–234.

Chapter 8. Conclusion and recommendations for future research

8.1 Conclusion

In summary, we have prepared highly concentrated and stable suspensions of silver nanoparticles by different chemical reduction methods of silver nitrate by EG, or $NaBH_4$ with PAA /or PVP/or PVA as a stabilizer and protective agent. Our result confirmed that PAA/PVP were found to be very effective stabilizers for the dispersion of silver NPs. The average size of the Ag particles is in range of nanoscale and some micro-scale particles due to particle agglomeration. A stable Ag ink was formulated by dispersing as-prepared Ag NPs in a combination of solvent (ethylene glycol, water, and 1-propanol) under vigorous stirring. Then it being treated with ultrasound to ensure it is well dispersed and achieving continuous ink throwing without nozzle clogging during the inkjet printing process.

One purpose of this study was to attain scalable and more economical NPs, where Ag is replaced in part by a less expensive but still conductive and solderable metal. This was achieved either by replacing or mixing the pure Ag with Ni or Cu. We have successfully prepared highly concentrated and stable suspensions of these nanoparticles capped with polymer and containing various ratios of metals by the co-reduction method, hot injection, polyol method, and galvanic displacement methods ,although the levels of Ni incorporated were much lower than the stoichiometric ratios in the reactions. The copper offers desirable blending values and has a good particle size distribution centred at about 14nm. However, the main obstacle was with the ink jet printing process and the ink formulation, where choosing the appropriate solvent to get a well dispersed ink without metal oxidation was a challenge.

Our results confirm that using Ni-Ag, either in alloy or CS ink formulation, produced a good appearance in simple smear tests and its ability to print by inkjet printer was acceptable. The printed film showed lots of cracks, however, and that caused the loss of conductivity. Thus, there is still plenty of development of nickel conductive inks that need to be done to make it favourable for inkjet printing and scale-up production. Compared with the above results the Cu–Ag core–shell

nanoparticles have considerably better oxidation stability under similar conditions.

DLS, TGA, TEM and SEM/ EDS were employed to confirm the ink stability, chemical composition, morphologies and thermal decomposition temperature and finally to demonstrate the effect of sintering at room temperature on the microstructure of printed films.

As already discussed, a remarkable improvement of resistivity was obtained from Ag/PAA or PVP films, about 2 times RBS ($1.59x10^{-8}$ Ω) on photo substrate after sintering at room temperature. Meanwhile, the 10% (Ag75:Ni25) film with overprinted layers showed an excellent conductivity of only two times bulk nickel ($6.99x10^{-8}$ Ω) or nine times compared with bulk silver, although the actual Ni content was much lower than expected from the synthetic stoichiometry. After spending more time discovering the properties of the alloy ink, the 10% (Ag40:Ni60) film displays a good resistance 29 times bulk nickel by using Cl^- spray post-treatment sintering at room temperature.

Finally, a conductive ink for printed electronics was produced from the synthesized Cu–Ag core–shell nanoparticles with xylene as a solvent. The formulated ink was printed onto a PVOH coted PET substrate using an inkjet printer. The film was sintered using dip-post treatment chemical sintering as mentioned previously in Chapter 2 (section 2.9.2). The lowest resistivity of the Cu–Ag core–shell conductive inks was measured to be $2.17x10^{-6}$ Ω.m, which is approximately 129 times the bulk resistivity of Cu. While this result shows some promise, much further optimisation work would be required to improve conductivity for practical use.

Chapter 6 and 7 reported the successful transfer of Cl^- sintering to plastic substrate and investigation of the effect of coating substrates on the electrical and mechanical performance of printed layers using silver ink. By applying PVOH coating solution with known and varying chloride content, the same type of spontaneous room temperature sintering could be achieved as was seen on photo paper. In principle, this approach allows the Cl^- concentration to be varied over a very wide range. It might be assumed that this would result in a significant improvement in overprinting conductivity (since Cl^- availability would not be a limiting factor for sintering the overlayers), but in practice it seems that this process is controlled by complex dissolution, mobilisation and diffusion aspects,

so careful optimisation is required to improve the quality of printing in general. There is considerable scope to adjust the PVOH thickness, molecular weight, degree of hydrolysis etc., which all have an effect on solvent penetration and Cl^- mobilisation. Systematic exploration of these parameters would be useful for future optimisation.

After successfully printing over these coated substrates, this study explored the durability of printed patterns through flexing tests, as described in chapter 6. The printed silver patterns showed great mechanical stability on both plastic and paper substrates, suitable for flexible electronic applications in tension and compression mode after 500 bending cycles in the plastic substrate and up to 1000 bending cycles on photo paper. This work potentially provides a promising route toward the large-scale fabrication of low-cost yet flexible printed electronic devices. Therefore, further appropriate tests are required to meet the needs of the upcoming era of the flexible electronics industry with excellent electrical conductance and mechanical properties. For instance, adhesive lift-off, stretching of substrates, and varying Ag printing film thickness should be done to ensure their ability to constantly maintain a high level of conductivity afterwards.

A prototype-designed pattern of 4 overprinted Ag layers of silver ink was generated as a bitmap image and was transferred onto the inkjet printer software to create a simple resistive temperature sensor device. The sensor length was about 0.189 m on photo paper, with a width of about 7.167×10^{-4} m and an average thickness of 4.43×10^{-7} m. A similar device about half the length was printed on the PET and PI substrate. This was because the printing quality was poorer, and the chance of faults would make the device useless by breaking the tracks and destroying conductivity.

The resulting printed devices were tested in an extended temperature range (19-130 °C) over 30 min to investigate their stability over temperature change. Our results confirmed that the resistance of the Ag temperature sensor on photo paper was reasonable; about 110 Ω. When increasing the temperature up to 150 °C, it showed some heat limitation, highlighted some voids and cracks on the surface of the printed Ag film. The sensitivity was lower by a factor of 0.52 compared with the temperature coefficient of Ag in the bulk material (3.8×10^{-3} °C^{-1}).

The measurement of the Ag printed sensor on non-heated PET/PVOH or PI/PVOH shows a good response to temperature increase with a resistivity 24 times and 18 times RBS respectively with a high resistance. However, the pre-heated temperature sensor on PET/PVOH and PI/PVOH show good near-linear behaviour over time compared to bulk silver resistivity which is 6 times and 3.4 times worse than bulk silver. The sensitivity for the sensor on pre-heated PET/PVOH was about 1.512×10^{-3} $°C^{-1}$; this is roughly double the value for devices on non-pre-treated PET and 20×10^{-3} $°C^{-1}$ for PI/PVOH pre-heated device which is higher than bulk silver by a factor of 5.3. This increase in temperature coefficient might be a result of increasing the exposure time to a high temperature which occurred twice in this case, before testing and during measurement. That is enough to enlarge the grain size and to reduce the lattice defects, with a much more notable reduction of resistance (R) and gives rise to an enhanced temperature coefficient. Thus, the poor-quality device printed on the pre-heated PET/PVOH or PI/PVOH was transformed into an excellent device by heating it again.

8.2 Recommendations for future research

There is still plenty of development of nickel conductive inks that needs to be done to make it favourable for inkjet printing and scale-up production.The implementation of the alloy / CS nickel ink could have real cost or quality benefits if it could be made to work effectively. As achieved in this study, there were promising results from printing the Ag-Ni Alloy. However, nickel incorporation was much lower than expected from the starting recipes and the resulting tracks were not wholly satisfactory. Thus, these materials would need lots of further development to get better results. An alternative synthesis method might be used or a different sintering method to achieve optimal performance, especially when considered alongside the increased synthetic complexity.

We have investigated the electrical properties of the Cu–Ag core–shell printed nanoparticles after sintering at room temperature under dip chemical sintering. In this study, $NaBH_4$ was used as an electrolyte solution to destabilize the olylamine capping agent, and to trigger the spontaneous sintering without copper oxidation at room temperature to avoid harsh sintering conditions by high temperature. Using this approach should remove the limitation for applications to

heat-resistant substrates, allowing use of the substrates that are most used in flexible electronics, such as paper and PET. This result is very encouraging because sintering at room temperature is sufficiently low for flexible substrates to remain undamaged and this approach can be used for flexible applications in the future. However, the main obstacle was with the inkjet printing process and the ink formulation, where choosing the appropriate solvent to disperse the hydrophobic surface ligand and to meet the inkjet printing requirements was a challenge, so further developments are needed at this point.

This work takes some first steps towards introducing simple printed resistive temperature sensors. The prototype devices under heating testing were implemented in the late stages of the research and due to the restrictions of the PhD time scale, real sensor devices were not properly investigated. The prototypes were implemented and shown to work broadly as expected from an electrical viewpoint. Therefore, further in-depth investigation is suggested as further optimisation could improve the quality and consistency of the printed devices. The true values of these sensors, however, was not so much as real temperature measuring devices but rather as tools to investigate the underlying stability and behaviour of the printed tracks themselves. These were shown to have excellent adhesion properties on robust flexible substrates and could be flexed extensively with little damage. Although the Cl^--doped PVOH coating was effective, it showed some chemical instability above 100 °C, the likely origin of which was discussed. For applications where higher temperatures will be used, alternative polymers should be investigated, which do not have the tendency to chemically rearrange or degrade in the required temperature window. They still need to be hydrophilic enough to allow aqueous ink printing however, and swell to mobilise Cl^- for sintering, so careful polymer choice/design may be required.

Chapter 9. Appendix

A. **Chapter 2 :** More examples of “cross- sectional” scans of the stylus profilometer trace across a printed track

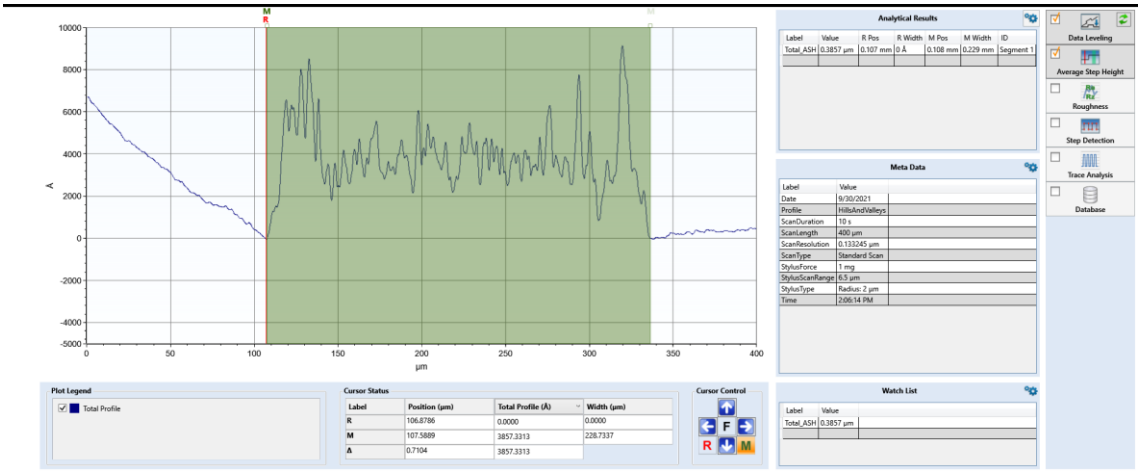

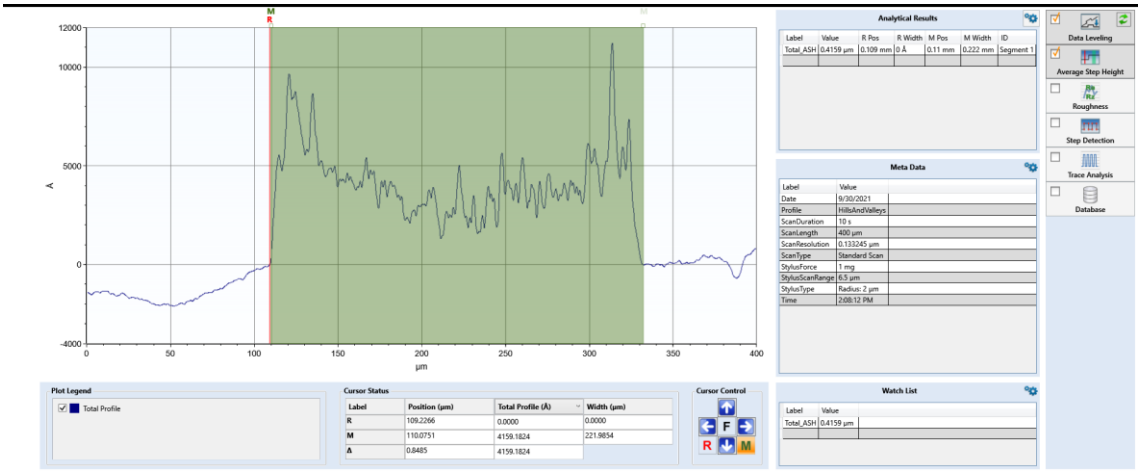

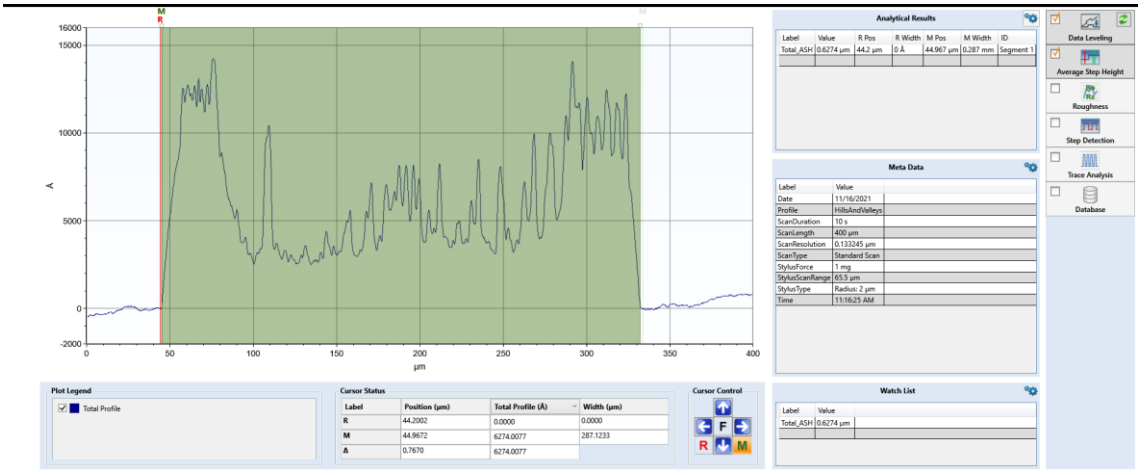

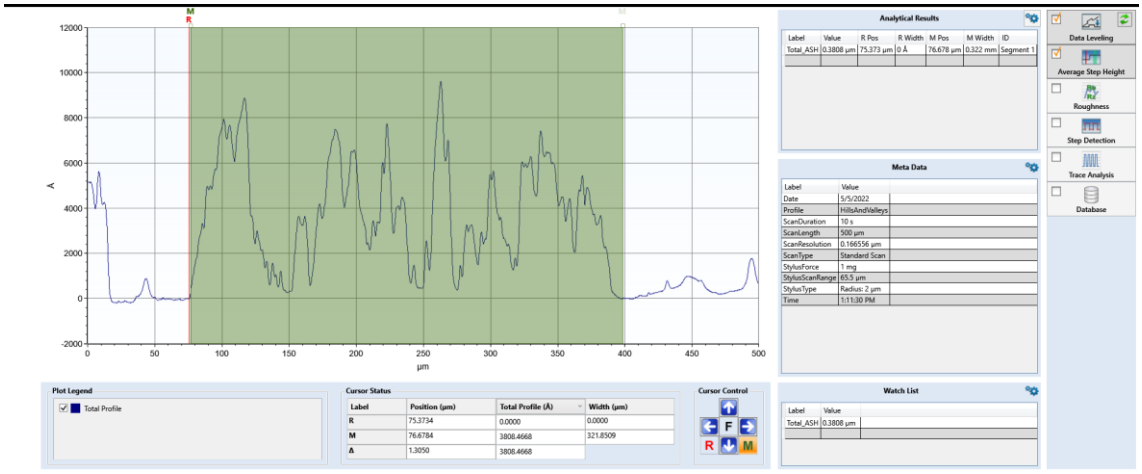
Analytical Results
Meta Data
Watch List
Plot Legend
Total Profile
Cursor Status
Cursor Control
Data Leveling
Average Step Height
Roughness
Step Detection
Trace Analysis
Database
µm
Å

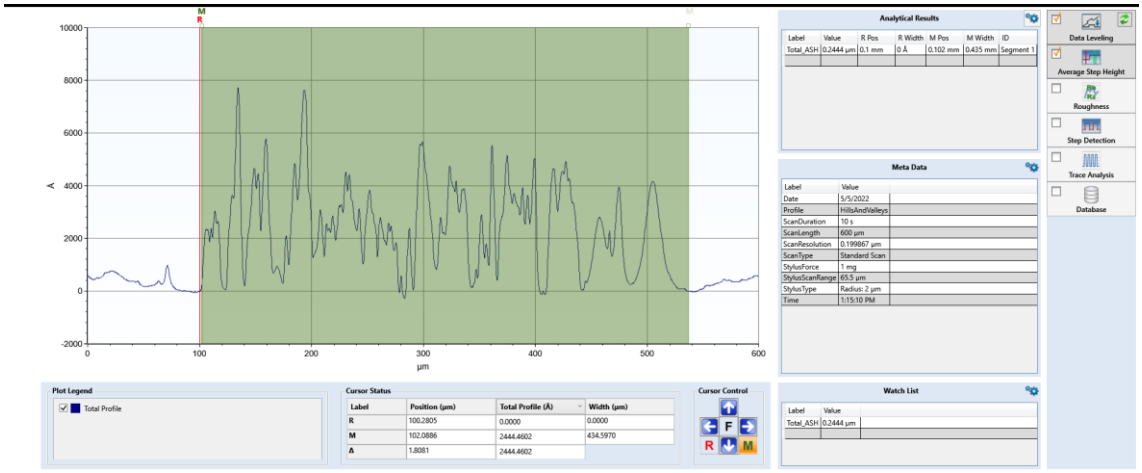
Analytical Results
Meta Data
Watch List
Plot Legend
Total Profile
Cursor Status
Cursor Control
Data Leveling
Average Step Height
Roughness
Step Detection
Trace Analysis
Database
µm
Å

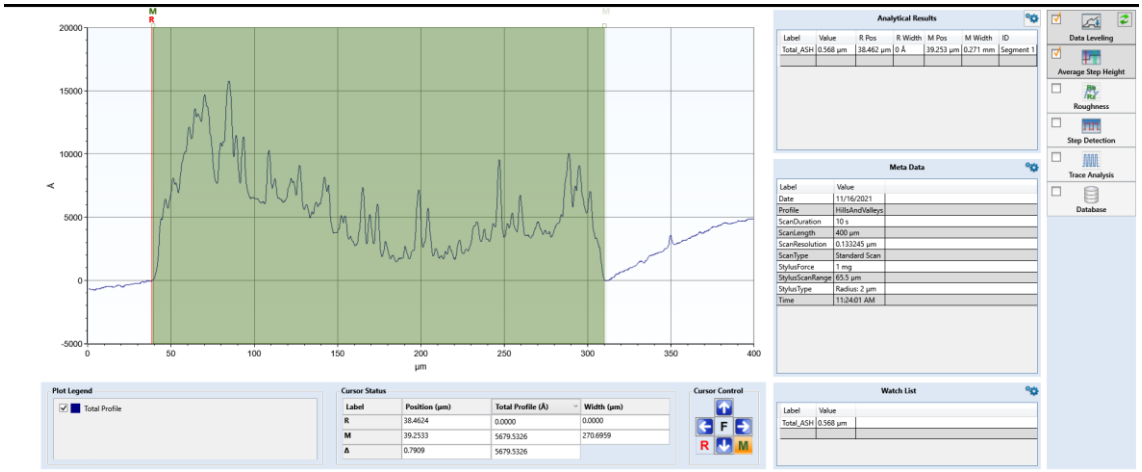
Analytical Results
Meta Data
Watch List
Plot Legend
Total Profile
Cursor Status
Cursor Control
Data Leveling
Average Step Height
Roughness
Step Detection
Trace Analysis
Database
µm
Å

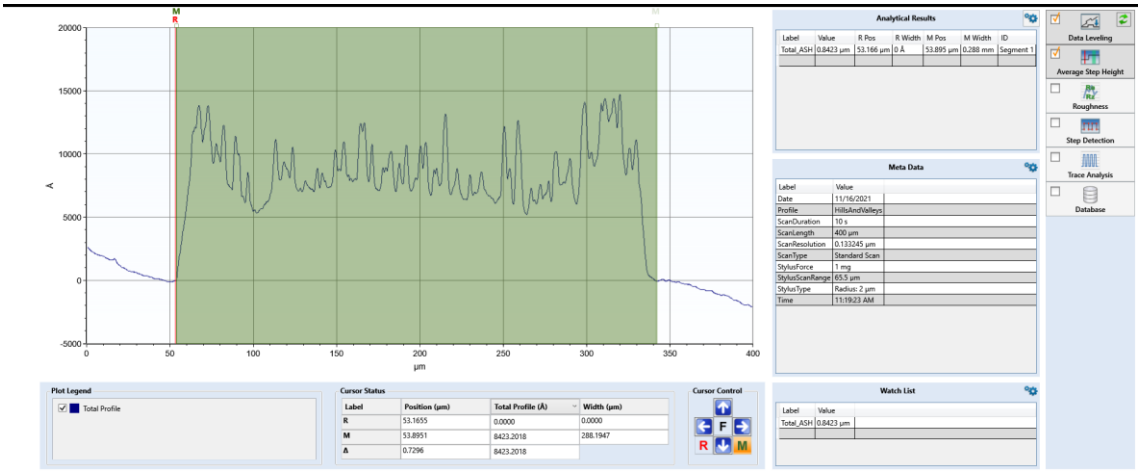
Analytical Results
Meta Data
Watch List
Plot Legend
Total Profile
Cursor Status
Cursor Control
Data Leveling
Average Step Height
Roughness
Step Detection
Trace Analysis
Database
µm
Å

B. Chapter 3: SEM images of the surface of the 30 wt.% AgPAA printed tracks at different pitch size (a)75 µm; (b) 55 µm; (c) 35 µm; (d) 15 µm; (e) overprinting x2(65 µm); and (f) overprinting x4 (65 µm) at room temperature.

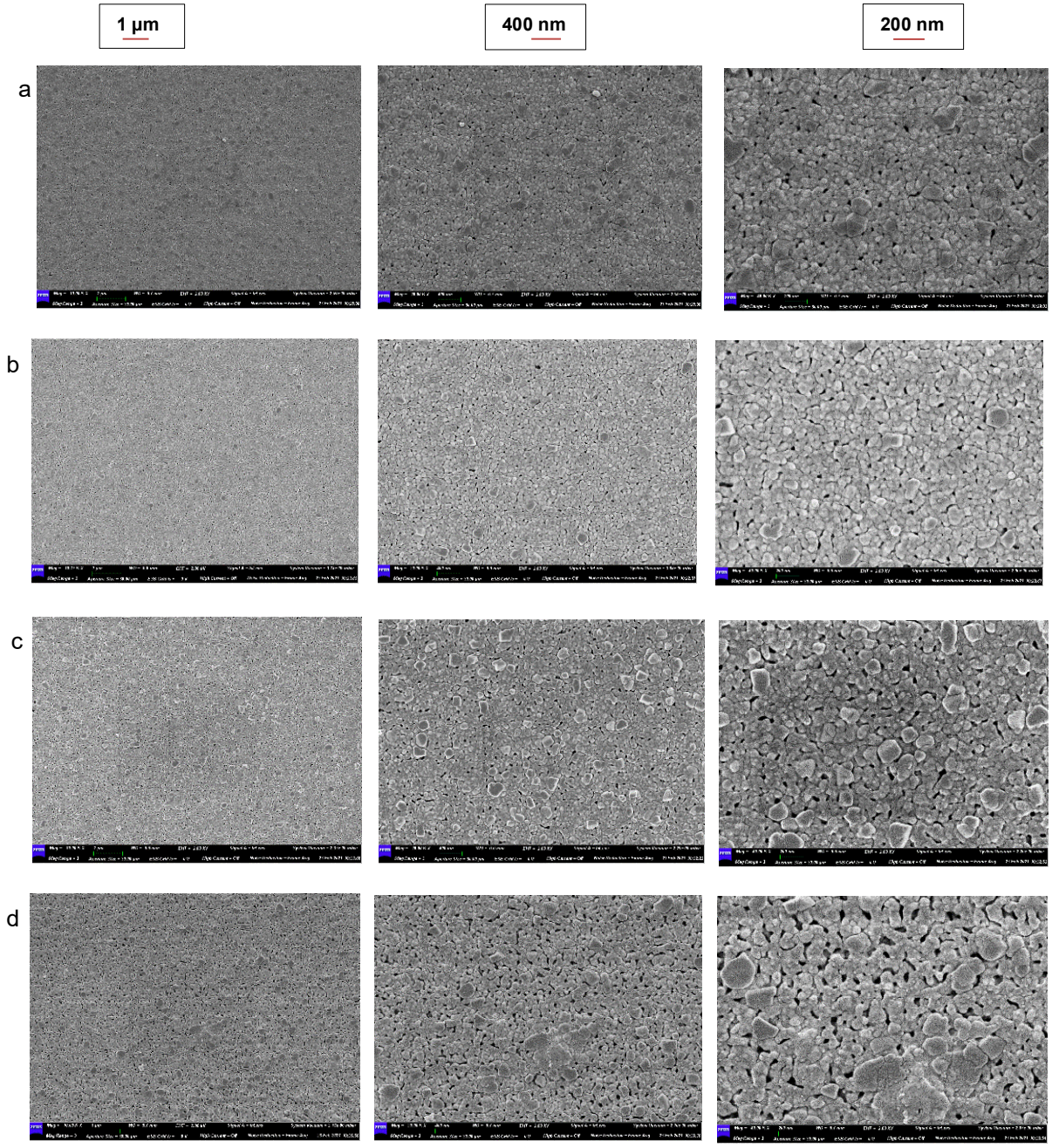

e

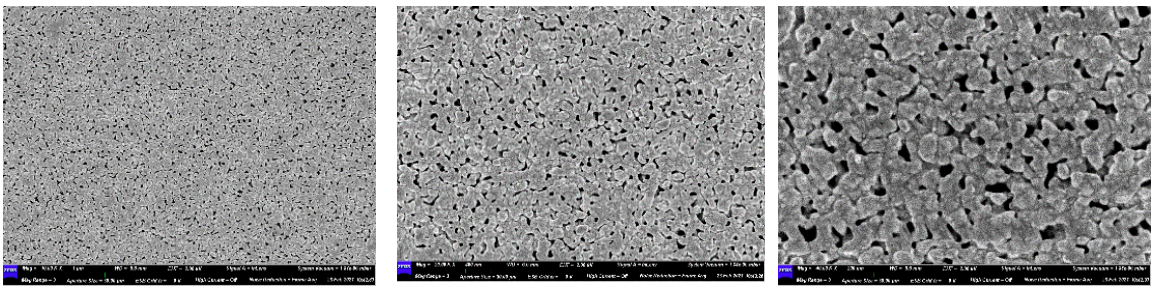

f